Refractometric Platforms for Label-Free Biochemical Sensing

Carlos Avelino de Jesus Gouveia

Centro de Ciências Exactas e da Engenharia

Universidade da Madeira

A thesis submitted for the degree of Ph.D.

in Electrical Engineering

Funchal 2013

This thesis was conducted under the supervision of

Jose Manuel Teixeira Rocha Baptista

Associate Professor, Center of Exact and Engineering Sciences, University of Madeira

and

Pedro Alberto da Silva Jorge,

Senior Researcher, Institute for Systems and Computer Engineering of Porto

This thesis was **unanimously approved** on **January 6th, 2014**

Jury President

Mikhail Benilov, Full Professor, Center of Exact and Engineering Sciences, University of Madeira

Members of the Committee (in alphabetical order):

Henrique Manuel de Castro Faria Salgado, Associate Professor, Department of Electrical and Computer Engineering, Faculty of Engineering, University of Porto

Luís Armando de Aguiar Oliveira Gomes, Assistant Professor, Center of Exact and Engineering Sciences, University of Madeira

Jose Luis Santos, Full Professor, Department of Physics and Astronomy, Faculty of Sciences, University of Porto

Jose Manuel Teixeira Rocha Baptista, Associate Professor, Center of Exact and Engineering Sciences, University of Madeira

Paulo Sérgio de Brito André, Associate Professor, Department of Electrical and Computer Engineering, Instituto Superior Técnico

Pedro Alberto da Silva Jorge, Senior Researcher, Institute for Systems and Computer Engineering of Porto

Bolsa de investigação da Fundação para a Ciência e a Tecnologia com a referência SFRH/BD/63758/2009, financiada pelo POPH – QREN – Tipologia 4.1 – Formação Avançada, comparticipada pelo Fundo Social Europeu e por fundos nacionais do MEC.

"A blue glass appears to be blue when light shines through it because it absorbs all colors and thus does not let them pass. That is to say, we call a glass 'blue' precisely because it does not retain the blue waves, It is named not for what it possesses, but for what it gives out"

Max Hunziger

to my beloved wife, Desiree,

for her love, support, and encouragement in every moment;

to my loving parents, Avelino and Lucia,

for their love, values and principles instilled;

and

to my sisters, Ana and Adriana,

have never left my side and are very special.

Acknowledgements

It is a great pleasure to thank all those who were present during the last four years and who in some way contributed to making this work possible.

First and foremost, praises and thanks to God, for the wisdom and perseverance that he has been bestowed upon me during this research project, and indeed, throughout my life: "I can do everything through him who give me strength." (Philippians 4:13).

I would like to thank my supervisors Jose Manuel Baptista and Pedro Jorge for their guidance, friendship and help, for availability always demonstrated, for the valuable lessons passed down over the last few years, useful critiques and advice that helped me to grow both, professionally and personally, and also, for all the time and effort spent in reviewing this document. This dissertation would not have been possible without their contribution.

I also thank Orlando Frazão, Manuel Joaquim Marques, Paulo Moreira and Ramiro Fernandes for their suggestions in completion of laboratory work and valuable scientific support. I also thank Paulo Marques and Ireneu Dias for their support.

I want to express my gratitude to Joel Carvalho for the work done together, for his support and friendship.

A special thanks to Katalyn Balogh and Raquel Queirós for all the knowledge shared regarding biochemical sensors and for all the help in experimental work.

To my colleagues and friends from INESC Porto Jaime Viegas, Judyta Tillak, Rita Ribeiro, João Ferreira, Filipe Magalhães, Askari Ghalam, Dionisio Pereira, Susana Silva, Diana Viegas, Paulo Caldas, Luís Coelho, Ivo Nascimento, Ricardo Melo, Manuel Jorge Marques, Javier de la Cruz and Yonny Barcelay for their many valuable discussions, support, shared knowledge and mainly for their friendship.

A special thanks to Luísa Mendonça for being so kind, professional and helpful.

Thanks to Carlos Gaspar, Pedro Cruz, Carlos Torres and Fernando Santos for their technical support.

I would like to acknowledge Fundação para a Ciência e para a Tecnologia for the PhD grant SFRH/BD/63758/2009, for the financial support to this PhD work, and also for funding the research project in which this work was framed.

I would also like to acknowledge, INESC Porto and FCUP for the facilities to support this work, without which this research would not be possible.

I would like to convey my thanks to Barna Kovács for the great time he provided in the University of Pécs (PTE) during my stay and for the means they made available in the lab, also for the productive cooperation between both institutes, as well as for the friendship and wonderful time in Hungary. I would like to extend my gratitude to others members of the group Àkos Markovics and Alexander Széchenyi.

I am also very grateful to Cristiano Cordeiro for receive me in Universidade Estadual de Campinas (UNICAMP) and for all the resources available in the lab. Also to colleagues from UNICAMP Giancarlo Chesini, Felipe Beltrán, Jonas Osório, Marcelo Alonso, Claudecir Biazoli and José Aparecido dos Santos.

I would like to express my gratitude to my family and all my friends that in many instances contributed with friendship, love, support and incentive for successfully complete this thesis.

Finally, to Desiree I want to thank for being a source of endless love and support and to say I am sorry for all the quality time we have lost.

Abstract

Optical fiber technology, which is well-known for having revolutionized the telecommunications industry, is currently proving to have important roles in applications such as sensing, biomedicine and industry. The sensing technology based on optical fibers has attracted considerable interest due to its unique features. High sensitivity, immunity to electromagnetic interferences, chemically and biologically inert, small size, and capability for *in-situ*, real-time, remote, and distributed sensing are some of the most appealing characteristics that motivate a growing scientific community.

The principle behind optical fiber sensing is the interaction between radiation traveling into the optical fiber and the parameter of interest. The measurand acts over the material, the waveguide or, depending on the sensing structure, directly in the optical signal and this action will infer variations in one or few parameters of the radiation such as: intensity, wavelength, frequency, phase or polarization.

This work fits within this area, specifically on fiber optic refractometric sensors for label-free biochemical sensing. It is presented a review about the most relevant works in this field, results associated with the study, development and characterization of few types of optical fiber sensors based on fiber Bragg gratings, long period gratings, multimode interference and fiber tapers. Also, a differential interrogation system, based on white light interferometry is exposed for high resolution refractive index sensing. In all cases, it was also a main objective of the developed work to evaluate the potential application of the new sensing structures and systems researched, particularly in the context of food industry and environmental monitoring.

Keywords: fiber optic sensors, refractive index measurement, label-free platforms, biochemical sensing, fiber gratings, cross-sensitivity.

Sumário

A tecnologia da fibra ótica, bem conhecida por ter revolucionado a indústria das telecomunicações, atualmente está a desempenhar um papel importante em outros campos como o do sensoriamento, a biomedicina e a indústria. A tecnologia de sensores baseados em fibras óticas tem sido alvo de considerável interesse devido às suas características únicas. Elevada sensibilidade, imunidade a interferências eletromagnéticas, química e biologicamente inerte, tamanho e peso reduzido, e capacidade sensoriamento remoto, distribuído, *in-situ* e em tempo real; são são alguns dos benefícios mais relevantes que motivam a uma crescente comunidade científica.

O princípio por trás dos sensores de fibra ótica, é a interação entre a radiação que viaja no interior da fibra óptica e parâmetro de interesse. O mensurando atua sobre o material, guia de onda ou, dependendo da estrutura sensora diretamente no sinal ótico, resultando na alteração de uma ou mais propriedades da radiação, tais como a sua intensidade, comprimento de onda, frequência, fase ou polarização.

Este trabalho enquadra-se nesta área, especificamente no ramo dos sensores de fibra ótica refratométricos para medição direta (sem utilização de indicadores de cor) de parâmetros bioquímicos. Inicialmente é apresentada uma revisão dos os trabalhos mais relevantes neste domínio científico; seguidamente e exposto o conjunto de sistemas sensores desenvolvidos e caracterizados, baseados em diversas estruturas como redes de difração, *tapers* e dispositivos de interferência intermodal. Adicionalmente, é também descrito um sistema de leitura diferencial com base em interferometria de luz branca, desenvolvido para medição de índice de refração com elevada resolução. Em todos os trabalhos, um dos principais objetivos foi avaliar o potencial de aplicação das novas estruturas e sistemas de sensoriamento desenvolvidos, em particular no contexto da indústria alimentar e monitorização ambiental.

Palavras-chave: sensores em fibra ótica, sistemas refratométricos, sensoriamento bioquímico, redes em fibra, sensibilidade cruzada.

Resumen

La tecnología de la fibra óptica, conocida por haber revolucionado la industria de las telecomunicaciones, desempeña actualmente un papel importante en diversos campos, siendo en la sensorización, biomedicina e industria ejemplo de ello. Los sensores de fibra óptica han despertado considerable interés por sus características únicas, siendo la sensibilidad elevada, inmunidad a interferencias electromagnéticas, química y biológicamente inerte, tamaño y peso reducidos, capacidad para monitorización remota, distribuida, *in-situ* y en tiempo real, algunas de los beneficios mas relevantes que motivan a una comunidad científica creciente.

El principio subyacente de los sensores de fibra óptica, es la interacción entre la radiación que viaja en el interior de la fibra óptica y el parámetro pretendido. El mesurando actúa sobre el material, guía de onda o, dependiendo de la estructura sensora directamente en la señal óptica, resultando en la alteracion de una o mas propiedades de la radiación, tales como su intensidad, longitud de onda, frecuencia, fase o polarización.

El presente trabajo pertenece a esta área, mas específicamente en el ramo de los sensores de fibra óptica refractométricos para la medición directa (sin utilización de indicadores de color) de parámetros bioquímicos. Inicialmente se presenta una revisión sobre los trabajos mas relevantes en el área, seguidamente se exponen los sistemas sensores desarrollados y caracterizados, basados en diversas estructuras como redes de difracción, *tapers* y dispositivos multimodales. Finalmente, se describe también un sistema diferencial basado en interferometría de luz blanca, desarrollado para medición de índice de refracción con elevada resolución. A lo largo de todo el trabajo, fue también objetivo primordial, identificar potenciales aplicaciones para las nuevos sistemas de sensorización desarrollados, principalmente en el ámbito de la industria alimentar y la monitorización ambiental.

Palabras-clave: sensores de fibra óptica, sistemas refractométricos, monitorización bioquímica, redes de fibra, sensibilidad cruzada.

Acronyms

CDM Core diameter mismatch

CMF Coreless multimode fiber

DCF Double-clad fiber

ECA Escherichia coli aptamer

EcOMP Escherichia coli outer membrane protein

EFBG Etched FBG

FBG Fiber Bragg grating

FFPI Fiber Fabry-Perot interferometer

FWHM Full width at the half maximum

HiBi High-Birefringence

HRI High refractive index

LPG Long period grating

MFBG Microfiber FBG

MMF Multimode fiber

MMI Multimode interference

MZ-LPG Mach-Zehnder LPG

NATOF Nonadiabatic tapered optical fiber

OPD Optical path difference

OSA Optical spectrum analyzer

PAA Polyacrylic acid

PAH Polyallylamine hydrochloride

PC Polarization controller

PCF Photonic crystal fiber

PMF Polarization-maintaining fiber

PS Polystirene

PS-LPG Phase-shifted long period grating

RI Refractive index

RIU Refractive index unit

SEM Scanning electron microscopy

SLD Superluminescent diode

SMF Singlemode fiber

SMS singlemode–multimode–singlemode

SPR Surface plasmon resonance

SRI Surrounding refractive index

TCF Thin core fiber

TFBG Tilted fiber Bragg grating

UV Ultra-violet

WLI White light interferometry

WLS White light source

Contents

List of Figures

Chapter 1

Introduction

Summary

In this chapter, the need for *in-situ* and real-time analytical tools for chemical and biological parameters in several fields, ranging from industry, environment and biomedical applications is exposed. A description of the main objectives and contributions of the research performed in the PhD programme is given. The layout of the thesis is also presented.

1.1 Motivation

The measurement of chemical and biological parameters in diversified environments is currently recognized as an important issue for a diversity of complex systems ranging from industrial processes, environmental and biochemical applications. For instance, in the case of the air and water quality control, the on-line monitoring of chemical compounds (e.g. greenhouse gases) and biological agents (e.g. toxins, bacteria), respectively, is crucial. On the other hand, in several industrial circumstances, namely in anaerobic digesters, aquaculture tanks, food industry among others, the real-time monitoring of chemical parameters is critical to the economic viability of these facilities. However, in a wide variety of situations, adequate technology is not available, or the employed techniques often require sample pre-treatment and are time demanding. Long waiting times between sample collection and results often compromise any effective corrective actions. In this context, optical fiber technology has many benefits that makes it a promising alternative to standard technologies: high sensitivity,

immunity to electromagnetic interferences, chemically and biologically inert, small size, and capability for *in-situ*, real-time, remote, and distributed sensing are some of the most appealing characteristics that motivate a growing scientific community. Nevertheless, while optical fiber sensing technology is already in the market, this is mostly true for the measurement of physical parameters such as strain or vibration in structural health monitoring applications. In this regard, the measurement of biochemical parameters is intrinsically more complex as it typically requires interaction of light with the measurand in a gaseous or liquid phase. Therefore a great deal of challenges is still at hand making this a fertile research field.

In this PhD programme, refractometric based configurations suitable for label-free chemical and biological sensing are aim of study. Refractometric label-free systems, allow the direct detection of biological or chemical analytes, without using any colorimetric marker. It requires, instead, the design of sensitive layers that experience a refractive index change in presence of the target. It is achieved using biomolecules with a natural affinity to the target, or chemical species having analyte specific ligands. Along this work several refractometric platforms will be studied and new sensing configurations will be presented.

1.2 Objectives

The main goal of this PhD work was to establish a platform based on fiber optic refractometric configurations, together with adequate interrogation schemes, based on virtual instrumentation, for implementation of advanced analytical instruments aiming online monitoring of chemical and biological parameters. The specific and operational objectives were;

- Conception, design, fabrication and characterization of new fiber optic configurations with enhanced evanescent field interaction for refractometric sensing;
- Study of new approaches to overcome cross sensitivity effects, particularly from temperature;
- Conception, implementation and characterization of advanced interrogation schemes, with virtual instrumentation for interferometric sensors;
- Test of sensing systems with chemically and biologically selective membranes in selected applications.

1.3 Scientific Contribution

The main scientific contributions regarding the work developed during the research activities are summarized below.

New developments on fiber Bragg gratings were reported. Initially, a Fabry-Perot cavity based on a Bragg grating written in a polarization maintaining fiber was developed and demonstrated as refractometer and potentially as a multi-parameter sensing device. Following, the cladding modes of a simple fiber Bragg grating were excited for the first time by using a misaligned splice in the upstream direction of the photonic device. Although, the excited modes did not show sensitivity to the external index, the sensing configuration was used for the measurement of curvature independent from temperature and for the simultaneous measurement of strain and temperature.

Long period gratings were studied as a sensing probe for biochemical applications. The response to the refractive index of different gratings with distinct characteristics were investigated. A huge increment in the sensitivity to the external index was achieved by using high refractive index coatings of polystyrene and silane based materials. Long period gratings based interferometers were also the subject of study. Due to the well-known high sensitivity to the thermal variations of those devices, all the sensing configurations were also characterized in temperature. The application of these devices to the measurement of chemical (CO_2) and biological (*E. coli*) analytes was also demonstrated with innovative sensing layers.

One of the major constraints of fiber optic sensors arises from its intrinsic sensitivity to temperature, which implies that, the simultaneous measurement of temperature and index is crucial when high sensitivity of refractive index is being carried out. A new configuration based on the combination of a multimode interference device inside of a high-birefringent loop mirror is reported for the unambiguous measurement of refractive index and temperature.

Finally, a differential sensing platform for biochemical sensing is presented. The system consists on a white light interferometry based readout device with electrically generated carrier allowing accurate phase measurement. The readout interferometer is used to interrogate two non-adiabatic tapers and a high resolution to measure the refractive index is achieved, the highest so far reported for tapered fiber devices.

1.4 List of Publications

The research and development on fabrication and characterization of optical fiber sensing structures and interrogation techniques reported on this thesis originated the following publications in peer-reviewed journals;

1. C. Gouveia, M. Zibaii, H. Latifi, M.J.B. Marques, J.M. Baptista, P.A.S. Jorge. "High resolution temperature independent refractive index measurement using differential white light interferometry", (2013) Sensors and Actuators B: Chemical, 188, pp. 1212-1217.

2. C. Gouveia, G. Chesini, C.M.B. Cordeiro, J.M. Baptista, P.A.S. Jorge. "Simultaneous measurement of refractive index and temperature using multimode interference inside a high birefringence fiber loop mirror" (2013) Sensors and Actuators, B: Chemical, 177, pp. 1717-1723.

3. J.H. Osório, L. Mosquera, C. Gouveia, C.R. Biazoli, J.G. Hayashi, P.A.S. Jorge, C.M.B. Cordeiro. "High sensitivity LPG Mach-Zehnder sensor for real-time fuel conformity analysis" (2013) Measurement Science and Technology, 24 (1), art. no. 015102.

4. P.A.S. Jorge, S.O. Silva, C. Gouveia, P. Tafulo, L. Coelho, P. Caldas, D. Viegas, G. Rego, J.M. Baptista, J.L. Santos, O. Frazão. "Fiber optic-based refractive index sensing at INESC Porto" (2012) Sensors, 12 (6), pp. 8371-8389.

5. C. Gouveia, P.A.S. Jorge, J.M. Baptista, O. Frazão. "Fabry-Pérot cavity based on a high-birefringent fiber bragg grating for refractive index and temperature measurement" (2012) IEEE Sensors Journal, 12 (1), art. no. 5699902, pp. 17-21.

6. C. Gouveia, P.A.S. Jorge, J.M. Baptista, O. Frazão. "Temperature-independent curvature sensor using FBG cladding modes based on a core misaligned splice" (2011) IEEE Photonics Technology Letters, 23 (12), art. no. 5742678, pp. 804.

A review on evanescent wave based structures for label-free sensing was also published in a book chapter published in international peer-reviewed scientific book;

1. Carlos A. J. Gouveia, Jose M. Baptista, Pedro A.S. Jorge, "Refractometric Optical Fiber Platforms for label-free Sensing" in "Current Developments in Optical Fiber Technology" (2013) InTech, Croatia. ISBN: 978-953-51-1148-1.

Results reported in this thesis were also presented in international conferences;

1. R.B. Queirós, C. Gouveia, J.R.A. Fernandes, P.A.S. Jorge. "Evanescent Wave DNA-Aptamer Biosensor based on Long Period Gratings for the Specific Recognition of *E. coli*". Proceedings of SPIE vol. 8794, pp. 879414–879414–4, 5th European Workshop on Optical Fiber Sensors (EWOFS). Kraków (Poland), May 2013.

2. C. Gouveia, M. Zibaii, H. Latifi, M.J. Marques, J.M. Baptista, P.A.S. Jorge. "Temperature Independent Refractive Index measurement using White Light Interferometry". Proceedings of SPIE vol. 8421, pp. 84216O, 22nd International Conference on Optical Fiber Sensors (OFS-22), Beijing (China) , October 2012.

3. C. Gouveia, G. Chesini, J.M. Baptista, C.M.B Cordeiro, P.A.S. Jorge. "Simultaneous Measurement of Refractive Index and Temperature Based on Multimode Interference inside a Fiber Loop Mirror". Proceedings of SPIE vol. 8421, pp. 84216M, 22nd International Conference on Optical Fiber Sensors (OFS-22), Beijing (China), October 2012.

4. C. Gouveia, K. Balogh, J.M. Baptista, B. Kovacs, P.A.S. Jorge. "LPG based fiber optic sensor for carbon dioxide". Proceedings of SPIE vol. 8421, pp. 84216L, 22nd International Conference on Optical Fiber Sensors (OFS-22), Beijing (China), October 2012.

5. Ricardo M. Silva, G. Chesini, C. J. Gouveia, A.B. Lobo Ribeiro, O. Frazão, C.M. B. Cordeiro, P.A.S. Jorge. "Magnetic field sensor with Terfenol-D thin-film coated FBG". Proceedings of SPIE vol. 8421, pp. 84213C, 22nd International Conference on Optical Fiber Sensors (OFS-22), Beijing (China), October 2012.

6. J.P. Carvalho, C. Gouveia, J.L. Santos, P.A.S. Jorge, J. M Baptista. "Optical time-domain reflectometer based multiplexed sensing scheme for environmental sensing". Proceedings of SPIE Vol. 8439, pp. 84390B (2012), SPIE Photonics Europe 2012, Brussels (Belgium), April 2012.

7. K. Balogh, A. Markovics, C. Gouveia, J.M. Baptista, P.A.S. Jorge, B. Kovacs. "Phenol Derivative Based Carbon Dioxide Sensor for Environmental Monitoring". Europtrode XI, Barcelona (Spain), April 2012.

8. K. Balogh, I. Kindnera, C. Gouveia, P.A.S. Jorge, B. Kovacs. "Poly(p-Nitrophenol) Derivatives as Optical pH Carbon Dioxide Sensors". Europtrode XI, Barcelona (Spain), April 2012.

9. M.I. Zibaii, C. Gouveia, J.R.A. Fernandes, P. Martins-Lopes, L. Pereira, D. Pratas, H. Latifi, P.A.S. Jorge. "Real Time Monitoring of DNA Hybridization with Long Period Fiber Grating for Food Industry Applications". Europtrode XI, Barcelona (Spain), April 2012.

10. B. Kovacs, S. Szechenyi, A. Markovics, K. Balogh, C. Gouveia, P.A.S. Jorge. " Fluorescent Optical Sensors For Carbon Dioxide Using the Quenching Effect of 4-Nitrophenol". Europtrode XI, Barcelona (Spain), April 2012.

11. J.P. Carvalho, C. Gouveia, P.A.S. Jorge, D. Chamorro, M. A. Martinez, M. T. R. Giraldi, A. P. Barbero, J. M. Baptista. "Refractive Index Remote Sensing based in an Optical Time-Domain Reflectometer". 22nd General Congress of the International Commission for Optics (ICO 22), Puebla (Mexico), August 2011.

12. C. Jesus, P.A.S. Jorge, J.M. Baptista, O. Frazão. "Cladding modes FBG curvature sensor based on a core misaligned splice" Proceedings of SPIE vol. 7753, pp. 77538U. 21th International Conference on Optical Fibre Sensors (OFS-21), Otawa (Canada), May 2011.

13. C. Gouveia, P.A.S. Jorge, J.M. Baptista, O. Frazão. "Simultaneous measurement of strain and temperature using the FBG cladding modes based on a core misaligned splice". Proceedings of SPIE vol. 8001, pp. 80013U. International Conference on Applications of Optics and Photonics (AOP - 2011), Braga (Portugal), May 2011.

14. C. Gouveia, A. Markovics, J.M. Baptista, B. Kovács, P.A.S. Jorge. "Colorimetric and refractometric measurements of carbon dioxide" Proceedings of SPIE vol. 8001, art. no. 80013C,806. International Conference on Applications of Optics and Photonics (AOP - 2011), Braga (Portugal), May 2011.

15. J.P. Carvalho, C. Gouveia, P.A.S. Jorge, D. Chamorro, M.A. Martinez, M.T.R. Giraldi, P. Barbero, J.M. Baptista. "Remote Sensing of Refractive Index with an Optical Time-Domain Reflectometer". International Conference on Applications of Optics and Photonics (AOP - 2011), Braga (Portugal), May 2011.

16. C. Gouveia, A. Markovics, J.M. Baptista, B. Kovacs, P.A.S Jorge. "Measurement of CO2 using refractometric fiber optic sensors". Advances in Sensors, Signals and Materials - 3rd WSEAS International Conference on Sensors and Signals (SENSIG 2010), pp. 169-173. Faro (Portugal), November 2010.

17. C. Gouveia, P.A.S. Jorge, J.M. Baptista, O. Frazão, "Optical refractometer based on high birefringence Bragg grating Fabry-Perot cavity". Proceedings of the SPIE vol. 7653, pp. 76530O. 4th European Workshop on Optical Fibre Sensors (EWOFS 2010), Porto (Portugal), September 2010.

1.5 Thesis Organization

This thesis is organized along eight chapters, described as follows. In this first chapter the motivation, the main objectives and the scientific contribution were presented.

In Chapter 2, the basic principles of the optical fiber refractometers and the most relevant developments of the technology are described. Advantages and disadvantages of the different structures are discussed and, wherever possible, a comparison between them in terms of performance is presented.

Chapter 3 presents a thorough discussion of all the relevant topics regarding fiber gratings. Fiber Bragg gratings and long period gratings are described. Topics such as: principle of operation, manufacture and sensing characteristics, with special emphasis given to refractive index sensing capability are addressed. The impact of high refractive index coatings in long period gratings is also detailed.

In Chapter 4, two experimental works based on fiber Bragg gratings are described. A Fabry-Perot cavity is presented for refractive index sensing and a multi-parameter sensor based on cladding modes of a simple Bragg grating, excited by misaligned splice is reported.

Chapter 5 presents an extensive experimental study, regarding long period grating devices for refractive index sensing. Few structures with different features and configurations are characterized and compared. The impact of high refractive index overlays on the sensitivity to the external medium is also evaluated. Finally, two applications are described. An LPG coated with p-nitro-phenol based material is presented for CO_2 sensing, and a LPG biosensor for detection and quantification of *E. coli* is also reported.

In Chapter 6, one of the main issues that affects fiber optic refractometers is addressed: the temperature cross-sensitivity. The problem is described and a solution

based on a combination of a multimode interference device inside of a high birefringence fiber loop mirror is studied. The main concepts of both mechanisms are described and the new configuration is presented.

The aim of Chapter 7 is to present a differential scheme for interrogation of optical fiber interferometers for refractive index sensing. The scheme consists in a readout interferometer based on white light interferometry with pseudo-heterodyne detection, used to measure two similar non-adiabatic tapers, one used as a sensor and the other as reference. The concepts behind this setup are covered and the experimental work is shown.

Chapter 8 is devoted to the conclusion and final remarks arising from the PhD work as well as proposals and guidelines towards the future research work.

In short, the experimental results obtained along the PhD work are presented in chapters 4, 5, 6 and 7. Chapter 3 contains the main theoretical concepts to understand the work presented in chapters 4 and 5. Chapters 6 and 7 start by providing a brief overview of the basic concepts relevant for the understanding of the optical fiber devices and structures proposed therein.

Chapter 2

Refractometric Platforms for Label-Free Optical Fiber Sensing

Summary

It is currently recognized that label-free optical sensing based on the measurement of refractive index is an important technology for the detection and/or quantification of chemical and biological parameters in diversified environments, ranging from industrial processes, medicine to environmental applications, where the need for complete and real-time information about a variety of parameters is present. Fiber optic sensors represent an interesting solution due to their high sensitivity, small size, and capability for *in-situ*, real-time, remote, and distributed sensing. In this chapter it is exposed the set of basic principles of the technology, the most relevant developments of fiber optic refractometers and some examples of its application. Different structures will be presented, including but not limited to those based in surface plasmon resonance, fiber gratings and modal interferometers. Emphasis will be given to the description of fiber optic devices and their sensing mechanism, advantages and disadvantages and wherever possible, the sensing performance of each sensing configuration will be compared in terms of sensitivity and detection limit.

2.1 Introduction

The *in-situ* and real-time measurement of a variety of chemical and biological parameters is important in diversified environments ranging from industrial processes, medicine to environmental applications. In this context, the demand for novel sensing platforms capable of multiplexing, real-time and remote operation in electromagnetic or chemically hazardous environments, has increased significantly in recent years. The combination of fiber optic technology with optical sensing mechanisms has many benefits that make it a promising alternative to standard technologies.

An optical fiber sensor can be defined as a device through which a physical, chemical or biological parameter interacts with light, guided within the optical fiber (intrinsic sensor) or guided by the optical fiber to the interaction region (extrinsic sensor). This interaction results in the modulation of one or more parameters of the guided light (intensity, phase, polarization, wavelength), thereby, the resulting optical signal will be related to the measurand of interest. Fiber sensors can be designed in such way, that the measurand interacts with one or few optical parameters of the guided light. Independently of the sensor type, the light modulation must be processed into an optical intensity signal at the receiver, which subsequently performs a conversion into an electric signal. In general, the main interest in this type of sensor comes from the fact that the optical fiber itself offers great advantages [1]. High sensitivity, immunity to electromagnetic interferences, chemically and biologically inert, small size, and capability for *in-situ*, real-time, remote, and distributed sensing are some of the most appealing characteristics that motivate a growing scientific community.

Biochemical fiber optic sensors, typically requires that optical signal interacts with the external media, either directly with a given analyte or through an auxiliary membrane, which contains an indicator dye. Some of the most appealing techniques regarding sensitivity and specificity rely on the use of colorimetric or fluorescent indicator dyes. Although some of the intrinsic problems of indicator based sensors like, leaching, photobleaching and temperature dependence have reported solutions, some limitations restrict further developments. A variety of excitation sources, detectors and filters are needed to deal with the large variety of spectral characteristics of dye based sensors. Moreover, these wavelength ranges demand for the use of special optical fibers and optoelectronics, severely limiting its multiplexing capability and compatibility with the standard telecom optical fiber technology.

In this context, label-free optical sensing based on the measurement of refractive index (RI) represents an interesting solution. Such approaches do not interfere

with the analyte properties and require, instead, the design of sensitive layers that experience a refractive index change in its presence. This can be achieved by using biomolecules with a natural affinity to the target, or chemical species having analyte specific ligands. The combination of such membranes with refractive index sensors can therefore provide attractive solutions for biochemical sensing.

The aim of this chapter is to expose the basic principles of fiber optic refractometers, suitable to biosensing field and capable to remote and real-time operation. Initially, the principle of the refractometric sensors based on the evanescent field is described. Thereafter, recent progress of the technology is presented where several fiber optic devices will be detailed, ranging from the high sensitive surface plasmon resonances, the well-known fiber Bragg gratings, the popular long period gratings, a variety of modal interferometers including tapers, mismatched fiber sections, multimode interference structures and also Fabry-Perot based devices. Emphasis will be given to the description of the sensing structures and its sensing mechanism, advantages and disadvantages and wherever possible, the sensing performance of each sensing device will be compared in terms of sensitivity and detection limit.

2.2 Fiber Optic Refractometer: The Principle

An optical fiber consists of a coaxial waveguide with a core and a cladding having different refractive indices. The refractive index of the core n_{co} is higher than the refractive index of the cladding n_{cl}. Snell's law can describe the propagation of light in optical fibers by the principle of total internal reflection. In optical fibers, the total internal reflection occurs when light is incident from the core to the cladding, at incident angle θ_i, greater than the critical angle θ_c, which can be calculated by the following equation;

$$\theta_c = \arcsin\left(\frac{n_{cl}}{n_{co}}\right). \tag{2.1}$$

Since light is totally reflected inside the core, no electromagnetic field is propagating into the cladding. Nevertheless, the electromagnetic field actually penetrates a short distance into the lower refractive index medium, propagating parallel to the core-cladding interface and decaying exponentially with the distance from the interface (see Figure 2.1). The physical explanation for this phenomenon is that, when applying Maxwell equations to the interface between two dielectrics, the tangential components of both the electric and magnetic fields must be continuous across the interface, this is, the field in the less dense medium cannot abruptly become zero at the interface and a

small portion of light penetrates into the reflecting medium. This boundary condition can only be satisfied if the electromagnetic field crosses the interface, creating the so-called evanescent wave [2]. The penetration depth d_p of the evanescent wave is a key parameter for sensing purposes. It is the distance from the interface at which the amplitude of the electric field is decreased by a factor equal to $1/e$ and, following the approximation of geometrical optics, it can be expressed by the equation;

$$d_p = \frac{\lambda_0}{2\pi\sqrt{n_{co}\sin^2(\theta_i) - n_{cl}}}, \tag{2.2}$$

where λ_0 is the radiation wavelength. The penetration depth of the evanescent field varies from 50 nm to 1000 nm depending on the wavelength, the refractive indices of the core and the cladding, and the angle of incidence. It is worth mentioning that the equation (2.2) can be used for step index multimode fibers, where the geometrical optics approach is valid. For singlemode fibers the electromagnetic wave theory should be considered.

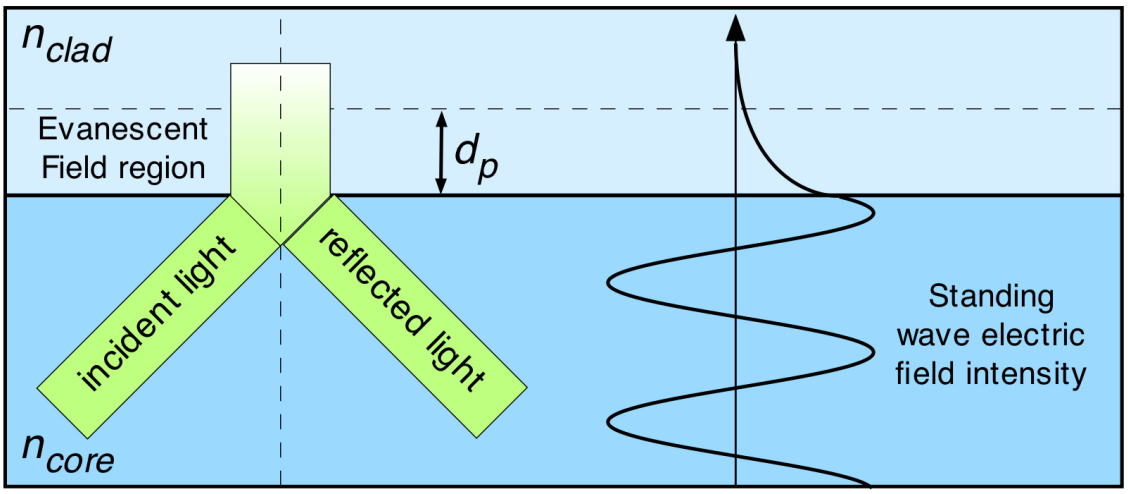

Figure 2.1: Evanescent field in the core/cladding interface of an optical fiber.

The majority of the fiber refractometers are based on evanescent field interactions. However, fibers were originally designed for optical communications. A typical single-mode fiber (SMF) has a core diameter between 8 and 10.5 μm, a cladding diameter of 125 μm and light propagates confined in the core. Therefore, the penetration depth is far smaller than the cladding thickness and there is almost no interaction between the optical signal and the external medium. Strategies must be devised in order to provide interaction with the surrounding medium. Typically, the evanescent field can

be exposed by removing partially or totally the cladding of the optical fiber. This can be done by chemical etching, tapering or side polishing techniques. In alternative, it is possible to use specific tools capable to transfer energy from the fundamental core mode to cladding modes. Fiber gratings are an example of such devices. In these cases the optical radiation can interact with the external environment due to the evanescent field formed at the cladding/external medium interface. In this situation, the penetration depth is given by [3];

$$d_p\left(m\right) = \frac{\lambda_0}{2\pi n_{cl}\sqrt{\sin^2\left(\theta_{(m)}\right) - \sin^2\left(\theta_c'\right)}}, \tag{2.3}$$

where $\theta_{(m)}$ is the incident angle of the geometrical ray associated with the m^{th} cladding mode and θ_c' is the critical angle at the interface between the fiber cladding and the external environment. Clearly, $\theta_{(m)}$ is different for each cladding mode and decreases with the increment of the order of the cladding mode. It is important to observe that the d_p changes as a function of the coupled cladding mode as well as of the external refractive index. The dependence of dp on the external refractive index n_{ext} is implicitly contained within θ_c', which can be expressed as;

$$\theta_c' = \arcsin\left(\frac{n_{ext}}{n_{cl}}\right). \tag{2.4}$$

Biochemical sensors based on fiber optic refractometers rely on the change on the external index induced by a chemical/biochemical interaction in the sensitive surface, that induces a change in the optical signal, allowing the determination of the analyte. In the next section, a brief description of different approaches typically used for the measurement of chemical and biological parameters is presented.

2.3 Optical Fiber Label-Free Biochemical sensing

There are two main cases of refractometric based biochemical sensors. On the first case, a biochemical reaction takes place in the liquid surrounding the bare sensitive structure, and the whole evanescent field is modified by the analyte. A different situation is when a layer is deposited on such structure and the biochemical interaction takes place within this layer or on its surface. In this case, only a portion of the optical radiation which comes out of the fiber device is modulated by the analyte, depending on the thickness of the sensitive region.

The first case, the simplest one, the fiber refractometer is used to measure the concentration of a certain chemical substance. The first example was demonstrated

using an etched fiber grating to measure the concentration of sucrose [4]. Since then, it has been applied to measure the concentration of ethylene glycol, isopropyl alcohol, glycerine, ethanol, glucose among others [3]. Other possibility is to measure a RI change in the solution due to a biochemical reaction that can provide information related with the analyte [5].

It is worth to say that this approach, clearly has the drawback of measuring any RI changes occurring in a solution within which the optical evanescent field extends and, therefore, is highly affected by interfering species different from the parameter of interest. Thus, the use of a selective layer, capable to capture the analyte or that experience a RI change in presence of that substance, is essential for the development of a reliable biochemical sensor. This can be achieved by using biomolecules with a natural affinity to the target, or chemical species having analyte specific ligands. When exposed to an analyte, a chemical/biochemical interaction takes place within this layer or on its surface. In this case, only a portion of the optical radiation which reaches out of the sensor (evanescent field) is modulated, depending on the thickness of the interaction region.

Biological sensing is based on the specific binding between biorecognition molecules (antibodies, oligonucleotides, aptamers or phages) immobilized on the sensor surface and the target biological species, which causes a change in the effective thickness or density at the surface of the fiber and consequently a change on the optical signal. In this case, high selectivities can be achieved, depending on the affinity between the biorecognition element and the target. Figure 2.2 conceptually shows an example of a label-free fiber optic biosensor. A functional coating is used to support and enhance the attachment of the bioreceptor molecules, which bind to the analyte [6].

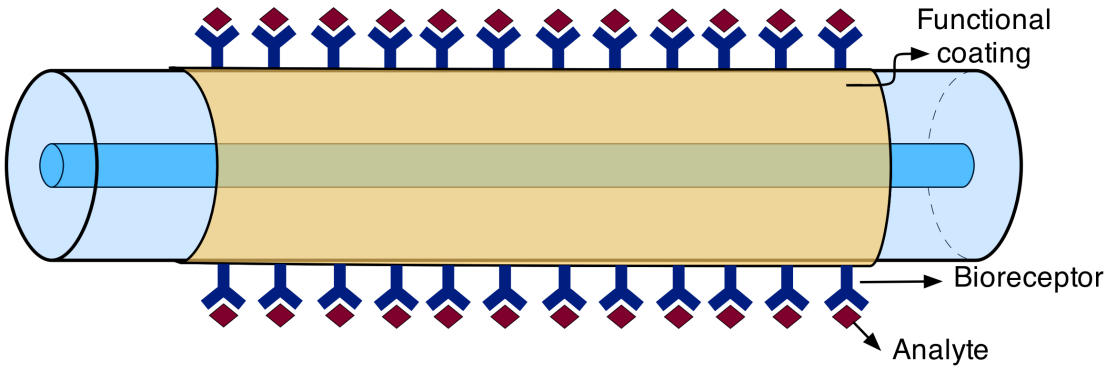

Figure 2.2: Label-free fiber optic biosensor schematic representation.

One critical aspect for biological sensing is the fact that, the sensitivity of evanescent field refractometers is higher when the external index approach the cladding index, whilst, is scarcely sensitivity for indices close to the water index. Nevertheless, the bioassays are usually performed in aqueous solution, with an RI close to the water index, where the sensitivity is quite low. This issue can be solved by using a high refractive index overlay between the cladding and the biologically functionalized surface [3]. This subject will be addressed in further detail later in this chapter.

Chemical sensing relies in the deposition of a sensitive material in the RI sensitive region. This material contains chemical species with specific ligands to the analyte, that in its presence induce a change in the index or density of the related material, and therefore, a change in the optical signal. For these kind of sensors, seems clear that, the thickness of the layer within which the analyte is adsorbed is critical and plays a fundamental role. Thicker layers provide higher sensitivities of the sensor, since a larger fraction of the optical radiation is modulated by the analyte. On the other hand, the thickness of the layer is limited by the d_p at the cladding/layer interface and the response time of the sensor, which, clearly, increases with the increment of the layer thickness. Therefore, a compromise between the sensitivity and the response time should be made [3].

In the following sections the most relevant fiber refractometric platforms based on evanescent field interactions and suitable for label-free biochemical sensing will be presented, including their measurement principle and some examples of most important works presented so far.

2.4 Fiber Bragg Gratings

Fiber Bragg grating (FBG) sensors have generated great interest in recent years because of their many industrial and environmental applications. FBGs are simple, versatile, and small intrinsic sensing elements that can be written in optical fibers and which consequently have all the advantages normally attributed to fiber sensors. In addition, due to the fact that typically the measurand information is encoded in the resonant wavelength of the structure, which is an absolute parameter, these devices are inherently self-referenced. Moreover there are several intrinsic advantages associated with FBG technology such as operation in reflection mode, narrowband spectral response and their compatibility with standard telecom technology. Therefore, they can be easily multiplexed, which is particularly important in the context of remote, multi-point and multi-parameter sensing [7]. Based on diffraction mechanism,

they consist on the periodic perturbation of the core of the optical fiber (typically half-wavelength) that is induced by exposing the fiber to an interference pattern of ultra-violet (UV) light or femtosecond radiation. They are characterized by the periodicity Λ of the refractive index modulation and by the effective refractive index of the waveguide mode n_{eff}. The grating constitutes a wavelength selective mirror or rejection filter defined by the Bragg resonance wavelength λ_B.

The full width at the half maximum (FWHM) of the resonant peak of the Bragg grating is typically a few hundred picometers. It depends on the physical length of the grating, which is usually few millimeters. Figure 2.3 illustrates the principle of operation of an FBG. When a broadband optical signal reaches the grating, a narrow spectral fraction is reflected and the remaining is transmitted. The peak wavelength of the reflected signal is defined by the Bragg resonance wavelength.

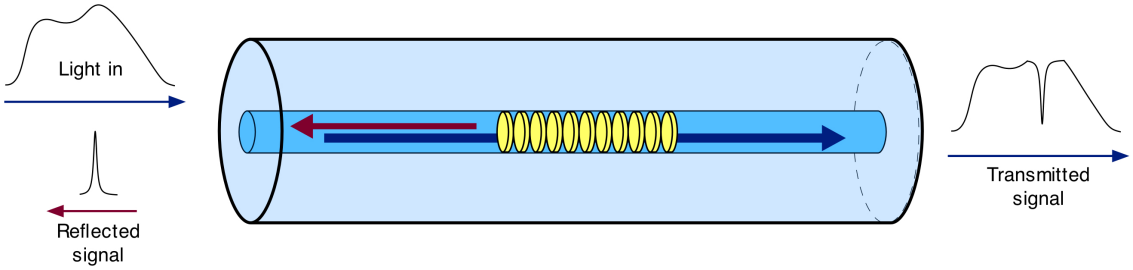

Figure 2.3: Operation principle of fiber Bragg grating.

FBG sensors have been widely used for strain and temperature measurement [8]. Bragg gratings work mainly with radiation confined to the fiber core, this way strategies have to be devised in order for the radiation to interact with the external medium. Typically, FBG based refractometers rely on the evanescent field of the core mode under fiber etching conditions, which enables interaction with the surrounding medium. The first demonstration of a FBG as a refractometer was done in 1997 by Asseh *et al.* [4], and it was based on the application of chemical etching to the fiber region where the grating was located. A 42 mm long FBG was written into a boron-germanium co-doped silica SMF with a cut-off wavelength of 1310 nm. The etching process was done by immersing the fiber in a solution of 40% hydrofluoric acid (HF) for approximately 50 min. After etched, the fiber had a diameter of 11 μm; thus 1 μm of cladding still remained. The sensor was subjected to a variation of refractive index between 1.333-1.345 RIU , by using solutions of water with different concentration of sucrose. The estimated sensibility was 1 nm/RIU and the measured resolution was $\pm$ 5×10^{-4}

RIU. Figure 2.4 illustrates an FBG based refractometer, when the cladding of the optical fiber was partially etched. Thus, the wavelength of the reflected signal depends on the external refractive index.

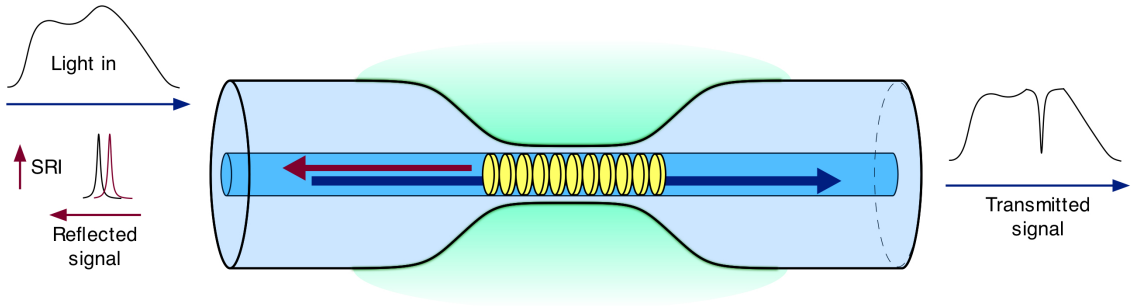

Figure 2.4: Etched fiber Bragg grating refractometer.

Regarding sensitivity enhancement and temperature compensation, Schroeder *et al.* [9] presented in 2001 a configuration with two in-line FBGs written on a single-mode depressed-cladding optical fiber with a cut-off wavelength of 750 nm. One of the gratings was side-polished to become sensitive to the surrounding refractive index (SRI) and the second one was a standard FBG used for thermal compensation. The effect of high refractive index (HRI) overlays was studied in order to shift the mode field to the surface of the sensor and to enhance the sensitivity for low refractive index analytes. Operation in wavelengths far above the cut-off wavelength was also explored resulting in an improvement of the sensitivity of the sensor. The response of the sensor to the SRI was obtained by immersing the sensing element in different solutions with different refractive indices in a range between 1.30-1.46 RIU. The maximum sensitivity for an external refractive index close to 1.45 was found to be 300 nm/RIU and the measured resolution was $\pm$ 2$\times$10^{-6} RIU. It is worth to note that due to the asymmetry induced by the polishing process, the SRI sensitivity becomes polarization dependent. A simpler solution for thermal compensation was published by Iadicicco *et al.* (2005), where a single grating was half-etched and used for simultaneous measurement of refractive index and temperature. The operation principle relies on the splitting of the original grating spectral response in two different peaks due to a selective etching over the grating length, where one of them becomes sensitive to the external refractive index and the other one is just sensitive to temperature [10]. Concerning enhancements in sensitivity, in 2005 Chryssis *et al.* [11] has shown that an effective solution is provided by etching the core of a FBG. A maximum sensitivity of 1394 nm/RIU is achieved as the surrounding index approaches the core index when the residual diameter was reduced to 3.4 μm.

In the past few years, microfibers have attracted increasing interest due to their intrinsic advantages such as large evanescent field, small effective mode field diameter and low-loss interconnection to single mode fibers. Microfibers can be produced by the use of standard flame brushing technique [12]. Bragg gratings written in microfiber (MFBG - Microfiber FBG) have been also explored for refractive index sensing. In 2010 Fang *et al.* [13] presented FBGs written in microfibers with diameters ranging from 2 μm to 10 μm by using femtosecond pulse laser irradiation. The maximum sensitivity obtained was 231.4 nm/RIU for refractive index values near 1.44 for a microfiber with 2 μm diameter. However, femtosecond laser Bragg grating inscription relies in the physical deformation of the fiber surface, which can weaken even more the micrometric structure. Looking for a possible solution to this problem, later in the same year, Zhang *et al.* [14] demonstrated a MFBG fabrication using a KrF excimer laser in a highly Ge-doped photosensitive microfibers with diameters of 6 μm and 6.5 μm, respectively. Two reflection peaks were observed in the spectrum of FBG. The reflected peak induced by the higher-order mode was used to monitor RI variations, because the higher-order mode has a larger evanescent field outside the microfiber and thus it is more sensitive to the SRI, compared with the fundamental mode reflection. The other peak was used for temperature referencing. The maximum sensitivity was about 102 nm/RIU at a RI of 1.378, in the 6 μm diameter fiber.

Etched FBG (EFBG), side polished FBG or MFBGs are interesting devices that exploit the influence of the SRI (by the evanescent field interaction) on the effective index of the core mode, and consequently on the Bragg wavelength. However, in order to enable the interaction with the external medium, the fiber diameter should be reduced, removing the cladding and in some cases partially the core. The sensitivity of the FBG is highly dependent on the diameter of the fiber in the region of the grating. Nevertheless, this process introduces fragility in the fiber sensor especially in cases where maximum sensitivity is required. A different approach to develop fiber optic refractometers based on FBG technology was proposed in 2001 by Laffont *et al.* [15]. The sensing configuration relies on the use of a tilted FBG (TFBG) as refractive index sensor by using the changes in the transmission spectrum, arising from the sensitivity to the external medium of the excited cladding modes resonances. In TFBGs the modulation pattern is blazed (tilted) by an angle θ with respect to the fiber axis. This asymmetry enables the coupling to circularly and non-circularly symmetric contra-propagating cladding modes and reduces the energy coupling to the contra-propagating core mode. The cladding modes are guided by the cladding boundary, and as a result, their effective index depends on the external index. The sensitivity

of the cladding modes to variations of the SRI increases with mode order, since the penetration depth of the evanescent field increases for higher-order modes. With the increment of the SRI, the center wavelength of the resonances experiences a shift to higher wavelengths. In addition to their spectral shift, the intensity drops progressively, to fit a smooth loss curve. Thus, monitoring the shifts of the cladding modes relative to the Bragg resonance or measuring the normalized envelope of the cladding mode resonances in the transmission spectrum can yield an accurate measurement of the SRI. Figure 2.5 shows a conceptual representation of a TFBG.

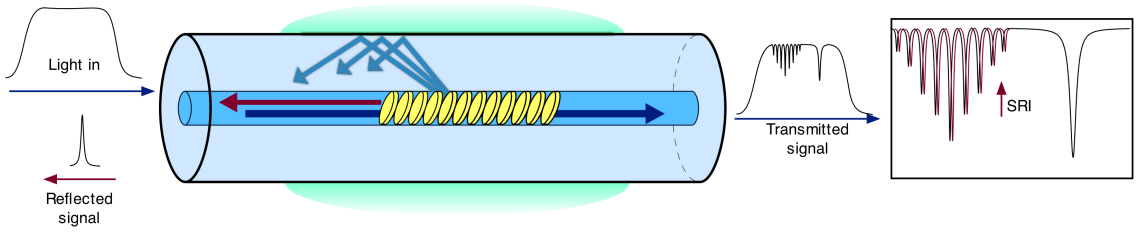

Figure 2.5: Refractometer based on a tilted fiber Bragg grating.

The TFBGs used in the experiment of Laffont *et al.* were written in a standard single mode fiber using a Lloyd mirror interferometer. The measurement of SRI was based on the normalized envelope of the cladding mode resonances spectrum observed in transmission. It was also shown that this parameter was relatively insensitive to temperature. Another reason for using the envelope of the resonance spectrum is that, choosing the proper tilt angle, this parameter can change monotonically and smoothly for RI values between 1.32-1.42, with a small change in sensitivity. Using the normalized area parameter and a 16° TFBG, a resolution of $\pm$ 10^{-4} RIU was achieved. In 2007 Chan *et al.* [16] proposed a relative measurement of refractive index, based on the separation distance between certain cladding modes, that were dependent on the refractive index and temperature, and the core mode, which is refractive index independent. A 4° TFBG was used and a RI sensitivity of 10 nm/RIU was obtained, achieving a resolution of $\pm$ 10^{-4} RIU. TFBGs are a suitable option for refractometric sensing in terms of performance and robustness of the fiber structure. However, a TFBG couples the core mode to a number of cladding modes in a large wavelength bandwidth, which renders difficult the signal readout and multiplexing. In addition, the fact that the measurement must be made in transmission, requiring access to the sensor from both sides, can represent a difficulty in some applications.

Recently some authors have been exploring the possibility to excite the cladding modes of standard FBG by transferring power from the fundamental core mode to

the cladding modes in the upstream direction of the FBG. Thereby, the FBG will couple back the light to the fundamental core mode. This arrangement enables the possibility to read the cladding modes of the Bragg grating in the reflected spectrum. In 2010 Han *et al.* [17] have shown for the first time this method by concatenating a long period grating (LPG) and a FBG. The LPG partially couples light from the core mode to a cladding mode, both of which are reflected by the FBG. A refractive index sensitivity of 2.3 nm/RIU was obtained. Recently, based on the same principle, Wu *et al.* [18] presented a singlemode–multimode–singlemode fiber structure (SMS) assisted FBG to measure the SRI. This structure utilizes multimode fiber (MMF) to excite cladding modes of an FBG written on the SMF and recouples reflected cladding modes to the input SMF. The maximum achieved sensitivity was 7.33 nm/RIU in the range from 1.324 to 1.439 RIU. Fiber refractometers based in cladding modes of standard FBGs represent an interesting opportunity for label-free sensing, especially by using all-grating devices which enable the possibility of efficiently transfer power from the fundamental mode to certain high order modes to excite specific cladding modes of an FBG. However, work has still to be done concerning the enhancement of sensitivity, which is still far from ideal.

Owing to the reflective nature of these devices a few FBG based Fabry-Perot cavities were presented for refractive index measurement. In 2005 Liang *et al.* [19] reported a refractive index sensor based on an etched fiber Fabry-Perot interferometer (FFPI) with a fiber radius of 1.5 μm. The sensor showed a sensitivity of 71.2 nm/RIU and a variation of refractive index of $\pm$ 1.4×10^{-5} RIU could be detected. Later in 2008, Silva *et al.* [20] studied a Fabry-Perot cavity formed between the reflection of a low reflectivity FBG (4%) and the Fresnel reflection from the cleaved fiber end. The refractive index information is derived from the interferometer fringe visibility. The sensor was characterized by immersing the fiber tip in a solution of distilled water with different concentrations of ethylene glycol. A resolution of $\pm$ 10^{-3} RIU was obtained.

Table 2.1 summarizes the most relevant FBG based refractometers presented to date and their performance parameters.

Applications

Several FBG based refractometers have been described that are based on the measurement of the refractive index changes for the measurement of sucrose, salt, ethylene glycol, isopropyl alcohol among others [4, 9, 21, 22]. Just few works were presented using functional layers. The first demonstration of the concept of biosensor based

Configuration	Param.[a]	Year	RI Range	Sensitivity	Res. (RIU)[b]	Ref.[c]
EFBG	$\Delta\lambda$	1997	1.330-1.345	1 nm/RIU	1.4×10^{-5}	[4]
EFBG	$\Delta\lambda$	2005	@ 1.44	1394 nm/RIU	7.2×10^{-6} [d]	[11]
Polished FBG	$\Delta\lambda$	2001	@ 1.45	300 nm/RIU	10^{-6}	[9]
MFBG	$\Delta\lambda$	2010	@ 1.44	230 nm/RIU	5×10^{-6} [d]	[13]
MFBG	$\Delta\lambda$	2010	@ 1.45	110 nm/RIU	10^{-5} [d]	[14]
TFBG	Area	2001	1.320-1.420		10^{-4}	[15]
TFBG	$\Delta\lambda$	2007	@ 1.32	11.2 nm/RIU	10^{-4}	[16]
LPG/FBG	$\Delta\lambda$	2010	@ 1.45	2.32 nm/RIU	10^{-4} [d]	[17]
MMF/FBG	$\Delta\lambda$	2010	1.40-1.45	7.33 nm/RIU	10^{-4} [d]	[18]
FFPI FBG	$\Delta\lambda$	2005	@ 1.33	71.4 nm/RIU	1.4×10^{-5}	[19]

Table 2.1: Most relevant FBG based refractometers

[a]Parameter
[b]Resolution
[c]Reference
[d]Estimated value, considering the maximum resolution of the readout device

on FBG, was done by Chryssis *et al.* (2005) [23], based on an EFBG, where single stranded DNA oligonucleotide probes of 20 bases were immobilized on the surface of the fiber grating using relatively common glutarahyldehyde based chemistry procedure. Hybridization of a complimentary target single strand DNA oligonucleotide was monitored *in-situ* and successfully detected. Later, Maguis *et al.* [24] presented a biosensor based on a TFBG refractometer enabling direct detection, in real-time, of the target molecules. Thus, bovine serum albumin (BSA) (antigen) and anti-BSA (antibody) were used to study the reaction kinetics of the antigen-antibody recognition by changing the antibody concentration in different configurations for the antigen immobilization. In 2009, Jesus *et al.* [25] showed an FBG based Fabry-Perot cavity for determination of acetic acid. The sensing probe was based on a FBG Fabry–Perot cavity, formed between the reflection of a low reflectivity FBG and the Fresnel reflection from the cleaved fiber tip [20]. The distal end of the fiber was coated with a thin film of sol–gel–PVP (polyvinylpyrrolidone) composite material. Figure 2.6 shows the scheme of the sensing probe. The polymeric thin film renders the interferometric output sensitive to the presence of carboxylic acid species. Results showed that the interferometric peaks change with acetic acid concentration, enabling its quantification.

In next section, another kind of fiber optic gratings is presented, like FBG, LPG is also a diffraction structure with a periodicity few orders of magnitude higher, which results in a different operating principle.

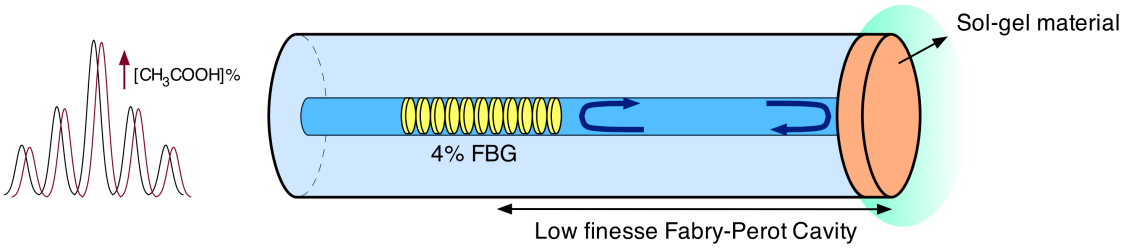

Figure 2.6: FBG based Fabry-Perot cavity for acetic acid measurement.

2.5 Long Period Gratings

An LPG is one of the most popular fiber optic refractive index sensor and it has been widely used for chemical and biological sensing. A LPG is also a diffraction structure, where the refractive index of the fiber core is modulated, with a period between 100 μm to 600 μm that is induced in the optical fiber using different techniques: UV laser irradiation, CO_2 laser irradiation, femtosecond laser irradiation, electric-arc discharge, mechanical processes and periodic etching [26]. This periodic perturbation satisfies the phase matching condition between the fundamental core mode and a forward propagating cladding mode of an optical fiber. Therefore, in an LPG, the core mode couples into the cladding modes of the fiber, resulting in several attenuation bands centered at discrete wavelengths in the transmitted spectrum, where each attenuation band corresponds to the coupling to a different cladding mode. The spectral width of the resonant dip varies from few nanometers up to tens of nanometers depending on the physical length of the grating.

LPGs are intrinsically sensitive to external refractive index exhibiting changes in the position of the resonance wavelength. The resonant wavelength of light coupling into a particular cladding mode is given by the phase matching condition [27];

$$\lambda_R^m = \left(n_{eff,co} - n_{eff,cl}^m\right) \Lambda, \tag{2.5}$$

where Λ is the grating period, and $n_{eff,co}$, $n_{eff,cl}^m$ are the effective indices of the core and m^{th} cladding mode, respectively. As a consequence of the phase matching condition, a change in the SRI will induce a shift in the resonance wavelength due to the variation of the $n_{eff,cl}^m$, which is dependent on the SRI. The first LPG inscribed successfully in an optical fiber was reported in 1996 by Vengsarkar *et al.* [28] for implementing band-rejection filters. In the same year Bhatia *et al.* [29] presented the first application of LPGs for refractive index sensing, reporting a wavelength shift of 62 nm for a RI change between 1.40-1.45 and an average resolution of ± 7.69×10^{-5}

RIU in the same range; for an LPG with period of 320 μm written by UV radiation exposure in a Corning standard 1310 nm fiber. Figure 2.7 illustrates the principle of operation of LPGs.

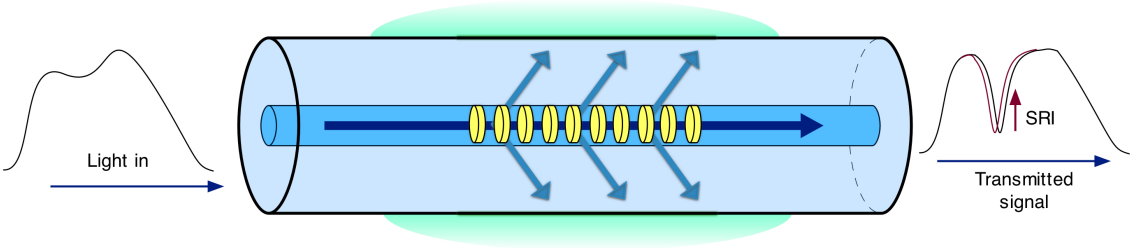

Figure 2.7: Fiber long period grating.

Shu *et al.* [30] reported in 2002 a LPG written in B–Ge co-doped fiber by UV laser irradiation technique, with a period of 202 μm. For the 11^{th} cladding order mode, a RI sensitivity of 1481 nm/RIU was shown in the range between 1-1.36 RIU, which is according with our knowledge the best sensitivity for a bare LPG reported for this range. Electric-arc induced LPGs are attractive due to its simplicity and flexibility, as well as the low cost of the fabrication process and its applicability not only to commonly used photosensitive fibers, but also to photonic crystal fibers, which are made of pure silica. In 2011 Smietana *et al.* [31] published a work on gratings with periods of 345 μm and 221 μm, respectively, for LPGs based on the SMF-28 and PS1250/1500 fibers. There are the shortest periods achieved for this type of fibers using the electric-arc manufacturing technique. Results showed RI sensitivities of 302 nm/RIU and 483 nm/RIU in the range between 1.33-1.41, representing also the highest sensitivity reported for a bare LPG made by electric-arc technique for the specified measuring range.

The sensitivity of an LPG is then typically defined as a shift of the resonant wavelength induced by a measurand. Figure 2.8 shows the typical behavior of resonance wavelength (a) and its optical power (b) to refractive index changes, respectively. The sensitivity characteristic of a bare LPG to SRI changes has an increasing (in modulus) non-linear monotone trend. The result is that the maximum sensitivity is achieved when the external index is close to the cladding index while for lower refractive indices (around 1.33) the LPG is scarcely sensitive. This standard behavior can be changed when a thin layer of sub-wavelength thickness (few hundreds of nanometers) and with higher refractive index than the cladding is deposited thereon. The use of HRI overlays in fiber optic refractometers based on evanescent wave was explored initially by Schroeder *et al.* [9] for a polished FBG. The use of coated LPGs with thin HRI layers

was firstly proposed by Rees *et al.* [32] and since then, several authors have explored its use for LPG RI sensitivity enhancement [32–37] and to develop highly sensitive biochemical sensing devices [38, 39].

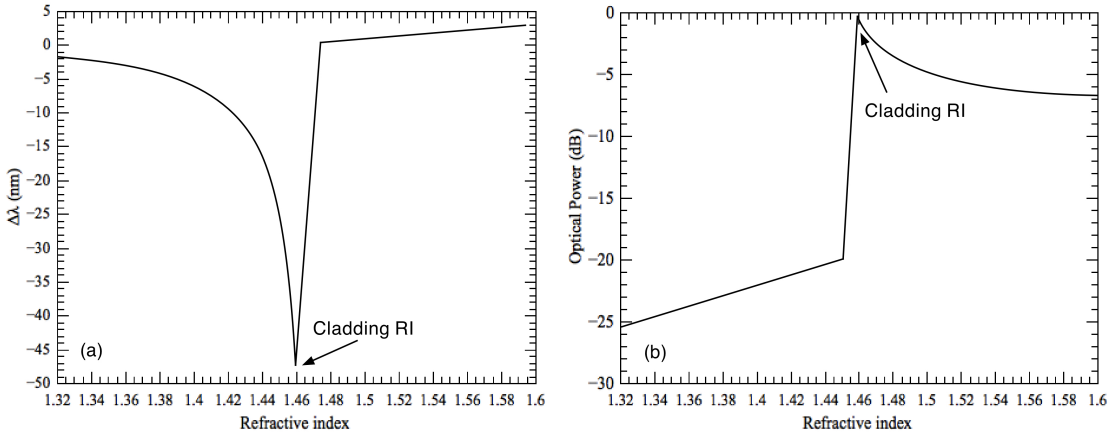

Figure 2.8: Refractive index response of a LPG resonant wavelength (a) and optical power (b).

The HRI overlay draws the optical field towards the external medium extending its evanescent wave. As a result there is an increased sensitivity of the device to the surrounding RI. Due to the refractive-reflective regime at the cladding-overlay interface, the cladding modes in a HRI coated LPG are bounded within the structure comprising the core, the cladding and the overlay. This means that a relevant part of the optical power carried by the cladding modes is radiated within the overlay. The field enhancement in the overlay depends strongly on the overlay features (thickness (Th) and refractive index (n) - nTh) and the SRI. For a fixed overlay thickness and refractive index, by increasing the SRI, the transition from cladding to overlay modes occurs: the lowest order cladding mode (cladding mode with highest effective refractive index) becomes guided into the overlay. At the same time, the higher order modes move to recover the previous effective indices distribution. This is reflected through the phase matching condition in the shift of each attenuation band toward the next lower one [35]. It results from this modal transition that the attenuation bands can exhibit a sensitivity of thousands of nanometers per refractive index unit for a particular RI operation range.

Pilla *et al.* reported in 2009 [36] a polystyrene (PS) coated LPG ($\Lambda = 460$ μm). For a 5^{th} order resonance, sensitivities of $\sim$ 5000 nm/RIU (near 1.41) and $\sim$ 2500 nm/RIU (near 1.38) were achieved for coating thicknesses of 270 nm and 320 nm, respectively. The reported data showed how by changing the overlay thickness it is

possible to tune the sensitivity characteristic, for a considered cladding mode, in the desired refractive index range. High order cladding modes that strongly penetrate the external medium, on the other hand, offer higher sensitivity, and obviously these are the most desirable for sensing purposes. An increase in the order of the coupled cladding mode can be obtained by decreasing the grating period [40]. Pilla *et al.* [41] reported recently in 2012 a PS coated LPG with a period of 200 μm. The coating thickness was approximately 245 nm. For an 11^{th} order resonance, sensitivity over 9000 nm/RIU near 1.347 was achieved, which is so far the best sensitivity obtained for a fiber device for this range of RI. This result shows HRI coated LPGs as a promising technology for high-performance label-free sensing applications.

LPGs show great sensitivity to the SRI, but also at the same time to temperature. On the other hand, the measurement of the refractive index is strongly dependent of the temperature due to thermo-optic coefficient. Thus, measurement and compensation of this parameter is an important issue for this kind of platforms. A number of techniques have been proposed in order to get rid of the temperature cross-sensitivity mainly based on the use of a second grating sensitive only to temperature or with different sensitivities to each measurand [42–45]. In this context, Han *et al.* [46], proposed a simultaneous measurement of the SRI and temperature by using a single grating written on a section of spliced SMF and DCF with the CO_2 laser point-by-point irradiation technique. As result, two resonances appear in the spectrum, for each mode, each of them corresponding to a section of the fiber. The section of the LPG in the SMF is both sensitive to temperature and surrounding RI, while the LPG section in the DCF is solely sensitive to temperature. This characteristic will affect the response of each resonance, permitting the simultaneous measurement of both parameters. Also, Huang *et al.* [47] presented a reflection based phase-shifted LPG (PS-LPG) for simultaneous measurement of temperature and refractive index. The PS-LPG was firstly proposed by Ke *et al.* [48], and generally, is fabricated by changing the index modulation amplitude or the length between the two adjacent grating sections to induce a phase shift. Spectrally, this results in two peaks symmetrically located (or not, depending on the phase shift) around a central wavelength. The grating was written in a standard SMF-28 optical fiber and the authors demonstrated the feasibility of the unambiguous measurement of temperature and SRI due to different sensitivities of the resonant peaks of the PS-LPG.

LPG based interferometers have shown that, it is possible to attain higher resolution in the RI measurement when used instead of a single LPG. The advantage of

using those structures lies on their interferometric nature and its principle of operation, where the coupled core and cladding modes from one LPG combine again at a second matched LPG to form interference fringes. The core and cladding optical paths constitute the arms of an all fiber Mach–Zehnder interferometer [49]. In 2002, Allsop *et al.* [50] presented an LPG based Mach-Zehnder as a refractometer. Using a pair of LPG ($\Lambda = 270$ μm, coupling 9^{th} order cladding mode) apart 100 mm from each other, interrogated by phase generated carrier technique; a resolution of $\pm$ 1.8×10^{-6} RIU was achieved for a RI range between 1.37-1.40 RIU. Later, in 2004 Swart *et al.* [51] presented a refractometer based on Michelson interferometer, by using a single LPG located 45 mm away from the mirrored tip. Compared with the Mach-Zehnder layout, the presented configuration has potential advantages such as reflection operation and compactness, it just need half interaction path length for the same sensitivity. Figure 2.9 show the LPG based interferometers in the Mach–Zehnder (a) and Michelson (b) layout.

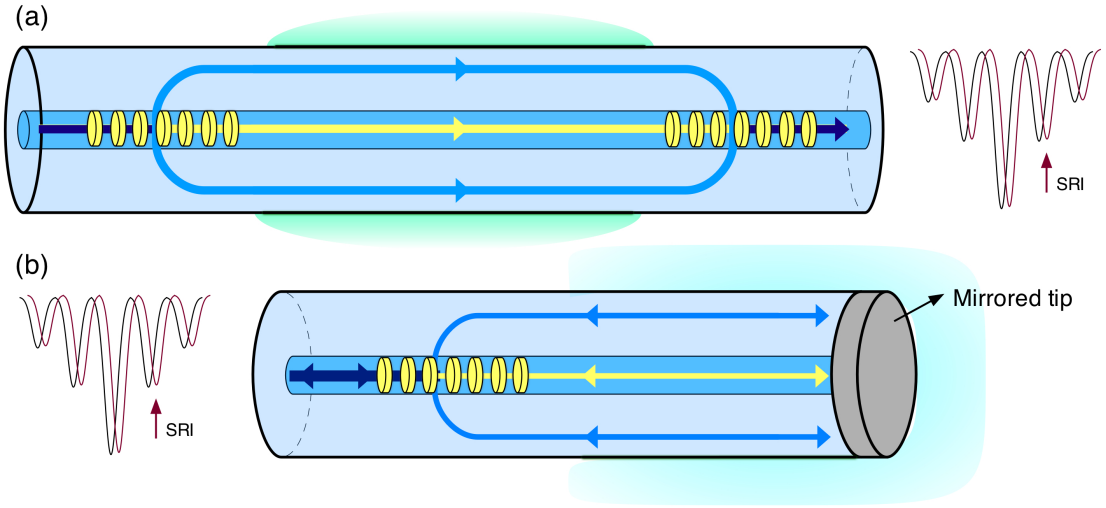

Figure 2.9: LPG based interferometers (a) Mach-Zehnder and (b) Michelson configuration.

More recently, in 2010 Mosquera *et al.* [52], presented an optical fiber refractometer based on a Fabry–Perot resonator that incorporates an intracavity LPG that couples and recovers energy to the fiber cladding after being phase shifted by the SRI. Figure 2.10 shows the sensing head configuration. The resonator is formed by two high reflectivity ($\sim$ 95%) FBGs separated by 47.5 mm. The SRI is monitored by the resonant frequencies of the Fabry–Perot interferometer, which can be measured either in transmission or in reflection. Results give a detection limit of $\pm$ 2.1×10^{-5} RIU at n=1.33.

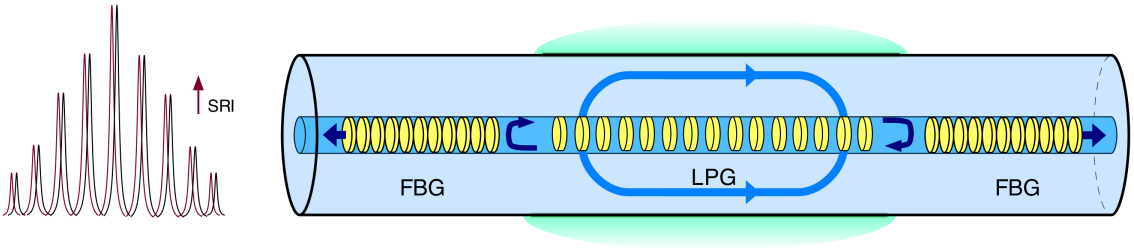

Figure 2.10: Intracavity LPG Fabry-Perot resonator.

Applications

LPGs are the most popular fiber optic sensor for label-free sensing. Since in 1996 Bhatia *et al.* [29] presented the first LPG based refractometer, many refractive index sensors have been reported along the years, using the refractometric ability to measure parameters such as the concentration of ethylene glycol, sucrose, salt, ethanol among others [40, 53–58]. This approach is not the most reliable due to the possible interference of other chemical species present in the solution, which are different from the analyte of interest. Thus, the deposition of sensitive thin layers that can change their own refractive index in presence of a specific analyte have opened a very interesting niche of applications. However, as mentioned above, the thickness and refractive index of the overlay are critical aspects that strongly affect the sensitivity of the device. LPGs coated by functional layers have been successfully exploited for chemical sensing.

Gu *et al.* [38] reported a LPG with a sol-gel derived coating of SnO_2 with optimized thickness. In presence of specific gases, the semiconductor surface energy changes, which leads to the change of conductivity and refractive index. The sensor was tested for ethanol vapor detection. Corres *et al.* [39] used the electrostatic self-assembled method to create pH sensitive films with an optimal overlay thickness. Two coatings were presented; the first one is based on polyallylamine hydrochloride (PAH), polyacrylic acid (PAA), and the second one was done incorporating the pigment prussian blue (PB) in the PAH/PAA matrix. Faster response was obtained with the introduction of PB particles in the polymeric matrix. Barnes *et al.* [59] presented a LPG functionalized with a polymethylsiloxane coating, able to perform solid-phase micro-extraction of organic solvents such as xylene and cyclohexane. The grating was interrogated using cavity ring down spectroscopy. Improvements regarding sensitivity and miniaturization of the sensing probe were studied recently by the same authors [60]. An LPG coated with a zeolite thin film was used to detect the presence of toluene and isopropanol vapors by Zhang *et al.* [61]. Recently, Korposh

et al. [62] reported a LPG multilayer film assembled with silica nanoparticles and the subsequent infusion of a porphyrin into the porous coating for ammonia sensing. The infusion of a functional material into the base mesoporous coating, chosen to be sensitive to a specific analyte, represents the novelty of this work. Two possible sensing mechanisms were shown, based upon changes in the refractive index of the coating. Chemically induced refractive index changes of the mesoporous coating at the adsorption of the analyte to the functional material (PAA), and chemically induced desorption of the functional material (tetrakis-(4-sulfophenyl)porphine), from the mesoporous coating.

LPG has been also widely used for biochemical sensing; on this case a biomolecule with affinity to a target can be used as functional coating. The earliest demonstration of biomolecule detection using this structure was done by DeLisa *et al.* [63], where the LPG was used for sensitive detection of antibody-antigen reactions. Goat anti-human immunoglobulin G (antibody) was immobilized on the surface of the LPG, and detection of specific antibody-antigen binding was shown. Later, several works were reported regarding antibody-antigen interaction [36, 64–72] and also DNA hybridization [73–76]. LPGs applied for label-free detection of specific bacteria using physically adsorbed bacteriophages were presented for the first time by Smietana *et al.* [77], where T4 phages immobilized onto the surface of an LPG were used as recognition element for *E. coli* detection. Recently, improvements in sensitivity in a similar work was presented by Tripathi *et al.* [78]. Lately, an enzyme coated LPG was used for glucose detection by Deep *et al.* [79]. The authors demonstrated the successful immobilization of glucose oxidase on to the 3-aminopropyl-triethoxysilane (APTES) silanized LPG fibers for the development of a new glucose sensing technique.

In this chapter, modal interferometers based on LPG were presented, in the next section different modal interferometers are detailed, including tapers, multimodal devices among others.

2.6 Modal Interferometers

Fiber modal interferometers have recently concentrated the focus of research because of their potential sensing capabilities and, in some cases, the reduced cost and simplicity of fabrication. In the previous section an LPG based modal interferometer was introduced. The LPGs were used as mechanism to couple light from core to cladding and subsequently from cladding to core. There are different mechanisms through which the high order modes could be selectively excited, by tapering a SMF,

through a core diameter mismatch structure (larger or thinner) or by a simple misaligned splice. Other kind of devices rely on multimode interference, in such cases a small section of MMF is properly inserted between SMFs. The aim of this section is to describe the sensing mechanism of these kind of devices and to address the most relevant contributions for chemical and biosensing field.

2.6.1 Tapered Singlemode Fiber

Tapering a SMF involves reducing the cladding diameter along with the core and it is made by heating a section of the fiber and pulling on both ends of the fiber in the opposite directions, either using a constant speed, force or tension. The heat source can be a gas burner flame, a focused CO_2 laser beam or an electric-arc formed between a pair of electrodes. When the optical fiber is tapered, the core–cladding interface is redefined in such a way that the light propagation inside the core penetrates to the cladding and its confined by the external medium. A fiber taper consists of three contiguous parts: one taper waist segment with small and uniform diameter, and two conical transition regions with gradually changed diameter. Depending on the pulling conditions it is possible to fabricate tapers with different shapes and properties.

Fiber tapers may be divided into two distinct categories: adiabatic and non-adiabatic. An adiabatic fiber taper is characterized by a very smooth change in the profile (small taper angle) in order to ensure a smooth mode conversion without significant losses in the transmitted signal. In this case, the main portion of the radiation remains in the fundamental mode ($LP_{0,1}$) and does not couple to higher order modes as it propagates along the taper. On the other hand, non-adiabatic fiber tapers (abrupt taper angle) can be done in such a way that coupling occurs primarily between the fundamental mode of the un-pulled fiber and the first two modes of the taper waveguide ($LP_{0,1}, LP_{0,2}$), where due to the large difference of the refractive indexes of air and fiber cladding, the taper normally supports more than one mode. Figure 2.11 shows a conceptually representation of a non-adiabatic fiber taper. The light propagates at the air/cladding interface of the taper waist region and the SMF is converted into a multimode waveguide. The result of back and forth coupling between the single mode of the fiber and the two (or more) modes of the taper is an oscillatory spectral response. The efficiency of this last coupling is dependent on the relative phase of the participating modes.

This device behaves as a Mach-Zehnder modal interferometer. When there are only two modes, the relative phase is $\Delta\varphi = \Delta\beta L$, where $\Delta\beta$ and L are the difference in propagation constants of the two modes and the interaction length along

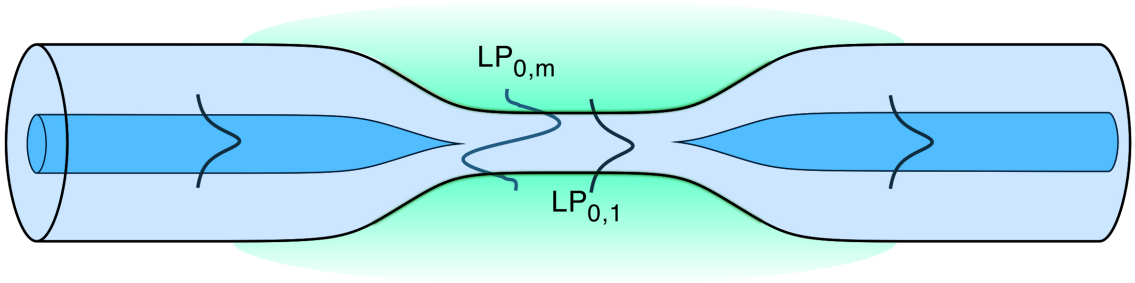

Figure 2.11: Abrupt tapered optical fiber.

the taper, respectively [80]. Therefore, the spectral response of the taper will shift correspondingly by changing the above terms. For instance, if the refractive index of the surrounding environment of the taper changes, the difference in propagation constants and the relative phase would be modified leading to a shift of the spectral response. Usually, these devices present a length ranging from few millimeters to tens of millimeters, and a waist diameter of few microns, promoting high interaction of the optical signal with the surrounding medium; thereby they are very sensitive to SRI. It is worth to refer that, the first fiber optic refractometer, was based on a tapered MMF and it was reported in 1984 by Kumar *et al.* [81].

Applications

Fiber refractometers based in non-adiabatic tapers have been proposed recently as platform for label-free sensing. Zibaii *et al.* [5] presented a singlemode non-adiabatic tapered optical fiber sensor, for monitoring the variation in refractive index with concentration of D-glucose in deionized water and measurement of the RI of amino acids (AAs) in carbohydrate solutions. This method showed a rewarding ability in understanding the basis of biomolecular interactions in biological systems. The fiber tapers were fabricated using heat-pulling method with waist diameter and length of 7 μm and 9 mm respectively. The limit of detection of the sensing probe was 55 ppm for a D-glucose concentration ranging from 0 to 80 mg/ml. Regarding refractive index measurements a sensitivity of approximately 1150 nm/RIU in the range between 1.3330-1.3447 was obtained. A resolution of $\pm$ 8.2×10^{-6} RIU was also estimated.

Zibaii *et al.* [82] presented also a similar sensing probe for real-time monitoring of the *E. coli* K-12 growth in an aqueous medium. The taper length and waist diameter were 7-9 μm and 3 mm respectively. The bacteria were immobilized on the tapered surface using poly-L-lysine as a binding agent. By providing the proper conditions, bacterial population growth on the tapered surface increased the average

surface density of the cells, and consequently, the refractive index of the tapered region would increase. The adsorption of the cells on the tapered fiber lead to changes in the optical characteristics of the taper. This affected the evanescent field leading to changes in optical power throughput. Concerning improvements in refractive index sensitivity, the same author showed that a singlemode non-adiabatic tapered optical fiber sensor inserted into a fiber loop mirror, enabled sensitivity tuning. Adjusting the polarization controllers inserted in the loop allowed to excite different cladding modes in the interferometric taper resulting in different optical paths for the clockwise and the counterclockwise beams. The variation of the polarization settings provided a tuning of the RI sensitivity in a range between 800 nm/RIU - 1200 nm/RIU for indices in the range from 1.3380 to 1.3510 [83].

Later, Tian *et al.* [84] reported a tapered optical fiber biosensor that enabled the label-free detection of biomolecules. The amount of biomolecules bonded on the taper surface were determined by demodulating the resulting transmission spectrum phase shift. The taper waist diameter and length were approximately 10 μm and 12 mm respectively. A tapered optical fiber biosensor was evaluated with an immunoglobulin G antibody-antigen pair.

Abrupt Tapered devices show high sensitivity to refractive index measurements. However, after tapering, due to the reduced fiber diameter, the structure becomes very fragile and special handling is needed. Recently, a different approach based on core spliced mismatched sections have been investigated. The next section is devoted to this kind of structures.

2.6.2 Core Mismatch

Mismatched sections are proposed as valid alternatives as mode-coupling mechanisms to transfer optical power between core and cladding modes in optical fibers. The idea is to couple and recouple the fundamental mode and high order cladding modes through two mismatched sections. It can be done by using a misaligned splice of two standard SMF or by inserting a short section of a special fiber between two SMF. The principle behind this configurations is the same of modal interferometers exposed in previous sections. The volume of the reported works using this technique is small, employing different coupling mechanisms; and to the best of our knowledge they were just used to measure the RI of a solution, still no reported applications.

A spliced core offset refractometer configuration was presented by Tian *et al.* (2008) [85]. Higher order cladding modes were excited by fusion splicing two SMF sections with a certain core offset. Due to the asymmetric nature of a core offset

splice, coupling mainly occurs between the $LP_{0,m}$ and $LP_{1,m}$ modes. Two layouts were presented, a Mach-Zehnder configuration obtained by concatenating two misaligned splices and a Michelson configuration, realized by a single core offset splice and a layer of 500 nm gold coating at the tip of the optical fiber acting as a mirror. The Michelson interferometer was tested as refractometer. The response of the device to external variations of refractive index was evaluated by using dimethyl sulfoxide solutions with different concentrations. The sensitivity for a device with 38 mm of interaction length was 33 nm/RIU in the range of refractive index between 1.315-1.362.

The core-offset technique presents difficulties in the precise control of the amount of light power splitting. In alternative, Pang *et al.* [86] presented a Mach-Zehnder configuration based on a standard SMF sandwiched between two DCF sections. Standard SMF were used for both light input and output of the Mach-Zehnder device. The DCF consists of three layers, the core, inner cladding and external cladding. The inner cladding is thin and its refractive index is lower than that of the core and the external cladding. The DCFs serve as the in-fiber couplers that split and combine light propagating in the core and the outer cladding region. Because of the depressed inner cladding structure, the light wave propagating in the core can be partially coupled to the outer cladding through the evanescent wave. Therefore, the DCF can be employed as a core-cladding modes coupler to construct in-fiber interferometers. The DCF reported length was approximately 5 mm (on both sides), and the interferometer interaction length was 93 mm. Sensitivities of 31 nm/RIU and 823 nm/RIU were obtained for the lower refractive index (1.34 range) and the higher refractive index (1.44 range), respectively.

The idea of using a fiber core diameter mismatch (CDM) based interferometer for refractive index sensing has been reported by Rong *et al.* [87]. The sensing probe was constituted by a 9 mm section of SMF sandwiched between two 2 mm segments of thin core fiber (TCF). This TCF has a core diameter of 5 μm. The two TCF sections act as core-cladding modes coupling and recoupling, and the SMF middle section acts as the interference arm. The first TCF couples part of the core-guided fundamental mode into forward propagating cladding modes of the upstream SMF via CDM. Thus, the cladding modes propagating in the SMF middle section become sensitive to the SRI. Finally, the cladding modes are coupled back to the fiber core of the lead-out SMF via the second TCF, mixing with the original core mode and generating the interference signal. The studied refractometer exhibited sensitivity up to 159 nm/RIU over low refractive index values from 1.33 to 1.38. Similar work was later presented by the same group [88]. It was based on the same principle, but using

two sections of MMF as a core-cladding modes coupling and recoupling mechanism. Figure 2.12 shows schematically the MMF assisted Mach-Zehnder interferometer. The sensing probe was constituted by a 40 mm section of SMF sandwiched between two 5 mm segments of MMF. The device showed sensitivity up to 188 nm/RIU over low RI values from 1.33 to 1.40.

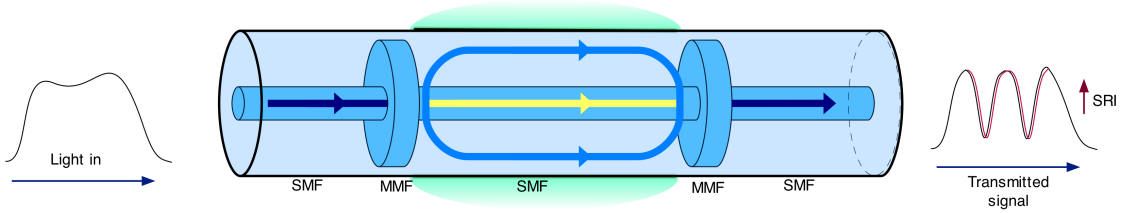

Figure 2.12: Mach-Zehnder interferometer based on core diameter mismatch.

In the next section, devices based on the interfering waves of several modes in MMF structure are described.

2.6.3 Multimodal Interference

Modal interference involving more than two modes has also been studied, resulting into a spectral transfer function that is no co-sinusoidal but instead show sharp peaks at specific wavelengths. It is common to refer this approach as multimode interference (MMI). MMI devices in optical fiber are usually obtained by splicing a MMF section between two SMFs, thus forming a SMF-MMF-SMF (SMS) fiber configuration. Based on multimodal interference and self-imaging or re-imaging effects, the SMS structure acts as an optical band filter that has been widely explored for optical communication and sensing applications. The SMS fiber concept relies on the fact that when the light field coming from the input SMF enters the MMF, excites several high order modes, generating a periodic interference pattern along the MMF section. Depending on the wavelength and geometrical length, the light into the MMF can interfere constructively or destructively resulting, at the end, in a device with different spectral characteristics [89]. Therefore the length of the MMF determines the spectral features of the MMI device. Depending where the interference pattern is 'intersected', constructive or destructive interference results, at different wavelengths yielding the transmission of resonant peaks or resonant losses, respectively. The transmitted spectral power distribution is, therefore, highly sensitive to the optical path length of the MMF section. It is important to refer that in MMI devices based on standard MMF,

the optical signal does not access the external medium. Therefore, they are insensitive to the SRI. MMI based refractometers usually relies on etched cladding MMF, tapered MMF or coreless multimode fiber (CMF). Figure 2.13 shows conceptually a SMS device based in a CMF, where constructive interference is present resulting in a resonant peak in the transmitted spectrum. MMI fiber devices are very attractive due to their high potential for refractive index sensing.

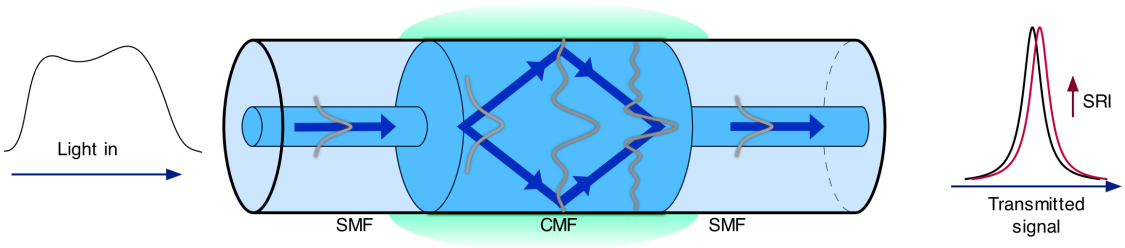

Figure 2.13: Singlemode-Multimode-Singlemode (SMS) multimodal interferometer.

In 2006, Jung *et al.* [90] presented the first MMI based fiber refractometer. The sensing structure was based in a 125 μm diameter CMF spliced between two step index 50/125 μm MMF sections. The advantage of using MMF instead SMF is the efficient power coupling and recoupling due to the large core diameter. The refractive index resolution was estimated to be ± 4.4×10^{-4} RIU for a refractive index range from 1.30 to 1.44. Later, Wu *et al.* [91] investigated the influence of using etched MMF with different core diameters on the sensitivity of an SMS fiber based refractometer. They have shown that refractive index sensitivity is highly dependent on the MMF diameter. The SMS fiber structure based refractometer with a core diameter of 80 μm has an estimated sensitivity of 180 nm/RIU in the RI range from 1.342 to 1.352 and 1815 nm/RIU in the RI range from 1.431 to 1.437. In another perspective, Biazoli *et al.* [92] studied a tapered SMS structures for high sensitivity index sensing. The device relies on a coreless MMF, part of which was tapered down by flame brushing technique. For a 55 μm MMF taper waist diameter the results showed that in the lower index range of 1.30–1.33, a sensitivity of 148 nm/RIU was achieved, while in the high sensitivity index region of 1.42–1.43, a value of 2946 nm/RIU was attained.

Applications

Good sensitivity, ease of fabrication and possibility to build robust devices are some of the advantages of SMS structures for label-free sensing. However, these structures produce a broad optical band spectrum, resulting in a small Q factor and thus poor resolution in the measurement of spectral shift. Concerning improvements in the

interrogation scheme, Lan *et al.* [93] proposed a SMS fiber structure coated with a zeolite thin film, interrogated by a fiber ring laser for highly sensitive chemical vapor detection. The zeolite-coated SMS structure was used as a bandpass filter and inserted into an erbium fiber loop to generate a laser line with narrow linewidth and high signal-to-noise ratio. The nanoporous zeolite coating adsorbs chemical molecules from the surrounding environment that increase its effective refractive index, producing a wavelength shift of the SMS filter and a corresponding change in the laser wavelength. The sensor has been demonstrated for detection of ethanol.

A different approach for multimodal interference devices was presented by Xia *et al.* [94]. The authors investigated a fiber modal interferometer constituted by a TCF sandwiched between two SMF. The designed TCF modal interferometer was made with a commercial TCF (Nufern 460-HP) whose cut-off wavelength was around three times shorter than normal SMF. In such structure, the high order cladding modes are excited when the light reaches the first heterocore interface. The excited high order cladding modes then interfere with the core mode at the second heterocore interface due to the existing optical path difference between the two modes. The constructive or destructive interference takes place and determine if the output spectrum presents an intensity maximum or minimum. Both transmissive and reflective TCF modal interferometers were experimentally demonstrated, and showed a good sensitivity to a small change of external refractive index, about 100 nm/RIU in the range between 1.34-1.39. Gu *et al.* [95] presented a pH sensor based on a TCF modal interferometer with electrostatic self-assembled nanocoating. The surface of the sensor is coated with PAH and PAA nanocoating. A fast and linear response was obtained in either acid or alkaline solution (in the pH range 2.5 to 10) with resolution of $\pm$ 0.013 pH unit.

In the next section, an interferometric optical structure based on the direct interaction of the radiation with the external medium or sensitive layer is presented. Fiber Fabry-Perot cavities have been widely used for refractive index sensing, usually based on the Fresnel reflection at the fiber tip.

2.7 Fabry-Perot

Fiber Fabry–Perot interferometer have been extensively explored for sensing applications due to their high sensitivity, compactness and easy fabrication. Monitoring changes in the optical cavity, can be a mechanism that allows some environmental parameters to be measured with high resolution and accuracy. In a FFPI sensor, the

sensing element consists on two partially reflective interfaces separated by a distance L. Thus, the reflections at the interfaces of the cavity, result in multiple waves, that form an interference signal at the output. If the reflectivity of the interfaces is low, the behavior of the cavity can be approximated by a two-beam interferometer model;

$$I = I_1 + I_2 + 2\sqrt{2I_1 I_2}\cos\left(\frac{4\pi Ln}{\lambda} + \phi_0\right), \tag{2.6}$$

where I is the intensity of the interference signal; I_1 and I_2 are the reflected intensities at the interfaces; ϕ_0 is the initial phase; n the refractive index of the medium filling the cavity and λ the radiation wavelength. Changes in the cavity due to external perturbations cause a phase shift in the interference signal that can be retrieved through the wavelength shift of the channeled spectrum or more accurately by tracking the phase of a carrier signal generated using a readout interferometer. FFPI based refractometers usually are based on the reflection in the silica/air (liquid) interface on the distal end of the optical fiber. In those cases, the refractive index measurement is based in the Fresnel reflection obtained from the fiber-liquid interface that will change according to the refractive index of the liquid. The refractive index information is derived from the visibility of the fringes of the channeled spectrum. Ran *et al.* [96] proposed a refractive index sensor by adding a sealed Fabry-Perot cavity near the tip of a single mode fiber, by using femtosecond laser micromachining. The external refractive index is determined according to the maximum fringe contrast of the interference fringes in the reflected spectrum. This technique provides temperature-independent index measurement and offers a RI resolution of $\pm$ 3.7×10^{-5} RIU and $\pm$ 4.2×10^{-5} RIU for the linear ranges between 1.33 - 1.441 and 1.456 - 1.62, respectively. A different approach is based on a micro gap in an optical fiber or between optical fibers in case of an extrinsic Fabry-Perot interferometer. Here, the cavity is filled with the liquid; changes on the refractive index of the fluid will induce variations in the optical path of the interferometer. The refractive index information can be obtained through the wavelength shift of the channeled spectrum. Wei *et al.* [97] reported a FFPI, with an open micro-notch cavity fabricated by one-step femtosecond laser micromachining, in a standard telecom fiber, for refractive index measurement. The cavity was 60 μm long and 72 μm depth. For the measurements the cavity was exposed to the different refractive indices of various liquids, as well as the temperature-dependent refractive index of deionized water from 3 ℃ to 90 °C. The sensitivity obtained in the measurement of the refractive index changes induced by the variations in the water temperature was 1163 nm/RIU at the wavelength of 1550 nm.

Applications

FFPI biochemical sensors are obtained by introducing sensitive layers with biomolecules with natural affinity to the target, or chemical species with analyte specific ligands. In presence of the target or analyte, these membranes experience changes in its thickness or in its effective RI. In FFPI biochemical sensors, the design of the sensing layer is crucial, not just regarding with the specificity and sensibility aspects but also with its optical properties. If the refractive index contrast between the layer and core of the optical fiber is large enough, the sensitive material itself can form an optical cavity. However, the film thickness should be comparable with the wavelength of the light source, usually in a micrometer range. If the contrast is too small, the sensing layer can become a part of the cavity. In the first case, the sensitivity to the analyte is higher once the entire cavity is sensitive. The optical quality is also important to avoid high optical losses, which reduce the visibility and decrease the signal to noise ratio. Numerous FFPI were presented for biochemical parameters. In 1999, Arregui *et al.* [98] presented a FFPI formed in the tip of the fiber, depositing successive bilayers by using ionic self-assembly monolayer process. This technique is based on the electrostatic attraction between opposite charges on molecules that form each of the deposited monolayers. Changes in the refractive index or thickness of the layer can be monitored by the reflected power of the cavity. This configuration was used to measure ammonia [99] by depositing zirconia (ZrO_2) nanoclusters and poly(sodium-4-styrenesulfonate) salt; hydrogen peroxide [100] by using Meldola's blue and a catalyst hemin deposited in a polymeric structure formed by PAH and PAA; and volatile organic compounds [101] by using PAH and PAA doped with a vapochromic material. Liu *et al.* [102] presented a FFPI for detection of dissolved organics in water. The cavity was developed by fine-polishing a thin layer of polycrystalline nanoporous mordenite framework inverted (MFI) zeolite synthesized on the cleaved end face of a single mode fiber. The measurements were done by monitoring the optical thickness changes of the zeolite thin film caused by the adsorption of organic molecules into the zeolite channels.

Zhang *et al.* have presented in 2005 [103], a multicavity FFPI immunosensor. The multicavity is formed by a small section of hollow core fiber (HCF) sandwiched between two sections of standard SMF (Figure 2.14). Changes in the thickness of the optical cavity can be measured precisely by monitoring the reflected power. A multilayered polyelectrolyte film was self-assembled onto the fiber distal end. The immobilization of proteins such as immunoglobulin G was done. The binding of antibody and the corresponding antigen was observed and the nonspecific binding

characteristics were investigated. From the same group, in 2006, Wang *et al.* [104] used the same configuration for DNA detection. The captured DNA was immobilized on the cavity end by layer-by-layer electrostatic self-assembly. The sensor was able to detect the hybridization of target DNA with complementary capture DNA by observing the cavity optical thickness variation. Later in 2008, Wang *et al.* [105] presented a similar approach also for DNA detection, based on a micro-gap structured Fabry–Perot interferometer. In this case the optical cavity was formed by a micro-gap sealed between a single mode fiber and the fiber tip where the DNA was immobilized.

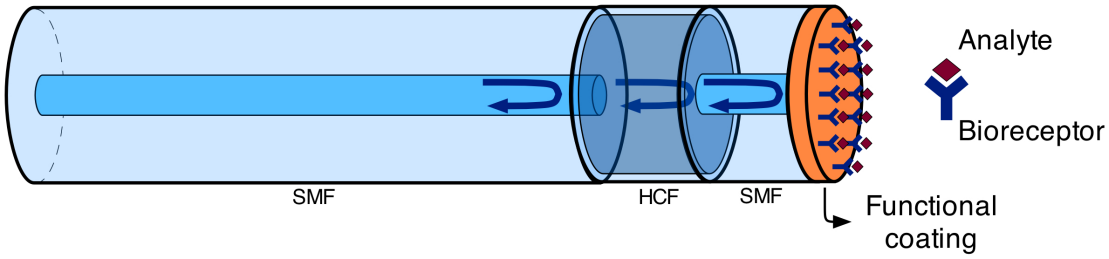

Figure 2.14: Biosensor based on a Fabry-Perot cavity presented by Zhang *et al.* [103].

Queirós *et al.* [106] published a FFPI sensing probe based on an optical fiber tip coated with a microcystin-LR selective thin film. The membrane was developed by imprinting microcystin-LR in a sol–gel matrix that was dip coated on the tip of the fiber. In this case, the cavity was formed by the sensitive layer itself, whose change in refractive index was correlated with the presence of the bacteria.

In the next section, fiber surface plasmon resonance based devices are described. Plasmonic structures are capable to achieve the higher resolution to the external index.

2.8 Surface Plasmon Resonance

The evanescent field intensity at the interface between two transparent materials is relatively weak. Thus, it is interesting to modify the interface in order to enhance the field intensity, therefore increasing the sensitivity of sensors based on these effects. In a previous section the use of an HRI overlay was exposed as a mechanism to enhance the evanescent field. Another possibility is to use the phenomenon of surface plasmon resonance (SPR). SPR is one of the most successful and sensitive mechanisms for label-free sensing. In this structure a metallic thin layer of few tens of nanometers induces a resonant loss in the propagation of light in the waveguide.

Surface plasmons are an optical phenomena that take place when total internal reflection of light occurs at a thin metal film-dielectric interface. SPR occurs when the real part of the thin film permittivity is negative and higher in magnitude than both its own imaginary part and the permittivity of the material surrounding the thin film. Surface plasmons will be excited when the following condition is accomplished [107];

$$k_{sp} = \frac{2\pi}{\lambda}\sqrt{\frac{\varepsilon_d \varepsilon_m}{\varepsilon_d + \varepsilon_m}}, \tag{2.7}$$

where ε_m is the real part of the dielectric constant of the metal, ε_d the dielectric constant of the medium and λ the radiation wavelength. Plasmon excitation strongly depends on the refractive index of the surrounding medium, thereby, all these sensors can be considered to be refractometers. Most of the proposed SPR configurations are made up of bulk optic components. The first optical fiber SPR device was proposed by Jorgenson and Yee [108] in 1993. In this work the sensing element was built by removing a section of the fiber cladding and depositing an SPR active thin metal layer symmetrically around the fiber core. This work was based on a resonant wavelength interrogation, and this sensing structure was capable of detecting variations in the SRI within the operating range between 1.2-1.4 RIU with a resolution up to $\pm$ 5×10^{-5} RIU in the high refractive index range (corresponding to a resonant wavelength resolution of 0.5 nm). This work represented the beginning of a new concept of compact and robust SPR devices. In particular, side polished fibers [109], tapered fibers [110–112] and D-type [113] fibers have constituted useful alternatives to the classical configurations [114]. Figure 2.15 shows the scheme of a singlemode tapered optical fiber as a coupling mechanism to excite the SPR.

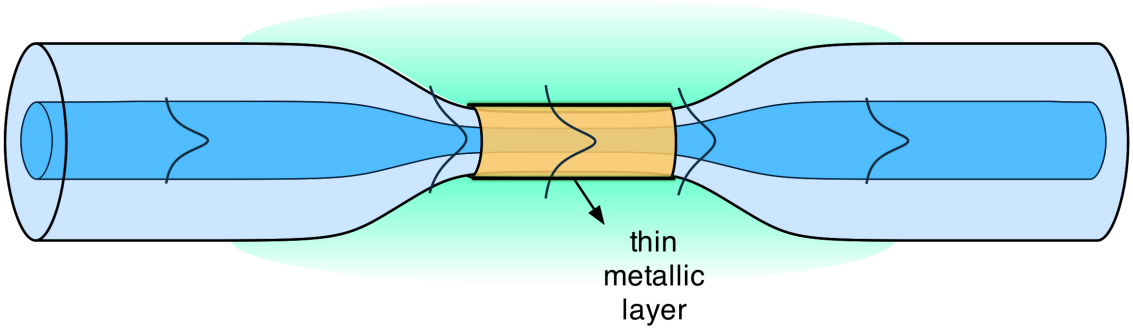

Figure 2.15: Tapered based surface plasmon resonance fiber optic sensor.

Taking advantage of all the devices for optical communications available at the spectral window around 1500 nm, Diaz-Herrera *et al.* published in 2010 [115] a new

SPR optical fiber sensor operating at 1500 nm and based on doubly deposited tapered fiber structures, well-known to exhibit small or zero sensitivity to polarization. It was shown that this configuration allows a substantially higher sensitivity compared to the ones obtained with the same elements in the 800 nm region (typically 5000 nm/RIU at 1500 nm vs. 3000 nm/RIU at 800 nm).

Applications

In 2001 Slavík *et al.* [109] presented a fiber optic SPR sensing device in a side-polished fiber using depolarized radiation. A laboratory prototype of the sensor has been proved to be able to measure refractive index variations as small as ± 5×10^{-7} RIU. Suitability of the sensor for biosensing was demonstrated by detecting immunoglobulin G via respective monoclonal antibodies immobilized on the SPR sensor surface. The lowest detected antibody concentration was ± 40 ng/ml. In 2009, Pollet *et al.* [116] investigated a fiber optic SPR biosensor for measuring DNA hybridization and DNA–protein interactions. The fibers were sputtered with a 50 nm gold layer which was subsequently coated with a protein repulsive self-assembled monolayer of mixed polyethylene glycol (PEG). Streptavidin was attached to the PEG's carboxyl groups to serve as a versatile binding element for biotinylated single stranded DNA (ssDNA). The ssDNA coated SPR fibers were first evaluated as a nucleic acid biosensor through a hybridization assay for a random 37-mer ssDNA. This single stranded DNA showed a 15 nucleotides overlap with the receptor ssDNA on the SPR fiber. In a second assay the fiber optic SPR biosensor was functionalized with ssDNA aptamers against human immunoglobulin E. Limits of detection (± 2 nM) and quantification (6 nM) in the low nanomolar range were observed. Recently, Delport *et al.* [117] reported a fiber optic SPR sensor used to analyze the melting process of DNA linked to silica nanoparticles. The SPR sensor platform, with silica nanobead signal amplification, allowed sensing inside a standard polymerase chain reaction thermocycler, allowing high resolution DNA melting curve analysis. This combination was used to characterize the hybridization and melting events between DNA immobilized on the sensor surface and DNA probes on silica nanoparticles. In a SMF, the optical power is guided by the fiber core, and in most of the sensing concepts proposed, the evanescent field access is achieved by removing partially the cladding of the optical fiber; by tapering or side polishing. In these processes, the fiber becomes very fragile; moreover in the case of the side polishing, it will increase the polarization dependence.

Recently, few authors proposed to use fiber grating technology to compensate for the lack of access to the evanescent field caused by the fiber cladding. Bragg gratings coupling into counter-propagating surface plasmon wave or LPGs coupling into co-propagating surface plasmon wave. Schuster *et al.* (2011) [118] presented a LPG to achieve SPR of a single cladding mode at the gold-coated tip of a SMF. The grating was written in a standard Nufern HP630 fiber. A LPG with period of 114 μm was found to couple in to the designated $LP_{0,20}$ cladding mode at a wavelength of around 660 nm, which was subsequently coupled to a SPR wave. The sensor combines a high level of sensitivity, a miniaturized sensing area and simple intensity based interrogation. The results indicate that a refractive index resolution of $\pm$ 10^{-5} RIU can be achieved. Shevchenko *et al.* [119] presented a FBG based SPR biosensor. The probe used in this study utilizes a TFBG to excite the SPR on the surface of the sensor over a large range of external medium refractive indices. TFBG-SPR sensor is obtained because the grating is imprinted in the fiber core at a certain angle relative to the longitudinal axis of the fiber. This results in the excitation of tens of cladding modes, each at a specific well defined wavelength, over a relatively large spectral window. Some of the excited cladding modes were coupled to a SPR wave on the surface of the fiber when the SPR phase matching condition was satisfied. The label-free biorecognition scheme used demonstrated that the sensor rely on the functionalization of the gold-coated fiber with aptamers, synthetic DNA sequences that bind with high specificity to a given target. In addition to monitoring the functionalization of the fiber by the aptamers in real-time, the results also showed how the fiber biosensor could detect the presence of the aptamers target, in various concentrations of thrombin in buffer and serum solutions.

2.9 Conclusion

In this chapter, a review of the most relevant fiber optic evanescent field based refractometric sensors for label-free sensing was given. Several aspects regarding the implementation of label-free biochemical sensors using standard optoelectronics were address. Different structures were described, including fiber gratings, modal interferometers, Fabry-Perot cavities and surface plasmon resonance devices. Emphasis was given to the description of fiber optic device and their sensing mechanism, advantages and limitations and the sensing performance of each sensing technology was evaluated. Table 2.2 summarizes the main features of the referred refractometric configurations.

Optical fiber gratings, including FBGs and LPGs, have been explored for refractive index sensing. Typically, FBG based refractometers rely on the evanescent field of the core mode using etched fiber configurations. FBGs based devices are more attractive for the purpose of multipoint sensing due to their very narrow spectral response. Nevertheless, the etching process introduces fragility in the fiber sensor. Tilted FBG do not require etching therefore maintain the fiber integrity. Although, a TFBG couples the core mode to a number of cladding modes in a large wavelength bandwidth, it results in difficulties for accurate readout and multiplexing. The refractive index sensitivity of these devices (FBG and TFBG) in the biological range is quite low which means that these configurations are not the most promising for the field of biochemical sensing.

Technology	Advantages	Limitations
EFBG	Well developed technology Multiplexing capability Narrow band peak	Fragility Low sensitivity High cost manufacturing
TFBG	Well developed technology Narrow band peak	Low sensitivity High cost manufacturing Broader spectral range
LPG	High sensitivity Low cost manufacturing[a]	High temperature cross-sensitivity Fabrication reproducibility[a]
LPG-I[b]	High Sensitivity	Fabrication Device length (long)
Abrupt taper	High Sensitivity	Fragility
CDM-I[c]	Low cost	Reproducibility
MMI	Low cost Low temperature sensitivity[d]	Sensitivity Reproducibility Broader resonance
SPR	Great sensitivity Low temperature sensitivity	High cost Fragility Broader resonance
FFPI	Compact	Low sensitivity

[a]Depending on the fabrication technique, for instance electric-arc.
[b]Long period grating based interferometer
[c]Core diameter mismatch based interferometer
[d]Depending on the MMF fiber, for instance pure silica coreless fiber.

Table 2.2: Summary of the advantages and limitation of the studied technologies.

LPGs, on the other hand, provide evanescent interaction by exciting cladding modes, and are therefore intrinsically sensitive to external refractive index changes.

They maintain fiber integrity and probably represent the most popular device for label-free sensing. They present high sensitivity to refractive index measurement, which can be increased and tuned by using HRI overlays. The HRI overlay draws the optical field towards the external medium extending its evanescent wave. As a result there is an increased sensitivity of the device to the SRI. The field enhancement in the overlay depends strongly on the overlay thickness and refractive index. This technique allows the coupling of the optical design and sensitivity optimization of the device, together with the functionalization. The careful design by means of proper choice of the grating period, the overlay RI and a very controlled deposition method, together with the integration on the HRI of sensitive materials or biological active agents, provide a powerful platform for advanced optical label-free biochemical sensing. However, LPGs are also highly sensitive to temperature and they need an extra mechanism to compensate temperature changes.

LPG interferometers based on Michelson or Mach-Zehnder layouts or even Fabry-Perot intracavity were also presented showing high sensitivity when compared with single bare LPG, having great potential for biosensing applications. Nevertheless, the typical device length (few tens of centimeters) can be a constraint for some applications. Fiber tapers, due its highly reduced cladding diameter have an enhanced evanescent interaction and have long been explored for refractive index measurements by monitoring the transmitted optical power. In spite of high sensitivity and very compact size (few millimeters), however, these structures are very fragile and special packaging is needed. On the other hand, new configurations using special fibers provide new sensing opportunities.

Modal interferometers based on CDM, by using TCF or MMF used as cladding coupling mechanism have shown good sensitivity, ease of fabrication and potential low cost. Nevertheless, these configurations are difficult to reproduce and to control the mode excitation and the amount of power transferred. MMI based refractometers are also interesting solutions that rely on the concept of re-imaging effects of MMI patterns present in multimode waveguides. In these devices, the transmitted spectral power distribution is highly sensitive to the optical path length of the MMF and its SRI. Usually based on SMS structures, they can be easily fabricated and applied in different situations. However, these configurations are also difficult to reproduce and present very broad spectral resonance making for instance multiplexing a very difficult task.

Surface plasmon resonance is based on metal nano layers deposited on the surface of the optical fiber. The metallic layer induces losses in the propagation of light in

the fiber. This kind of sensors are very sensitive to external refractive index and they are scarcely sensitive to temperature, thereby, they are very appealing for biosensing applications. However, they are usually based on polished or tapered fibers that are fragile structures. Also they present very broad spectral resonances making multiplexing a very hard task.

Finally, Fabry-Perot cavities are simple and compact, often the fabrication is easy and low cost. Depending on the type of cavity, the optical signal can interact with the external medium either through the evanescent field or directly through the Fresnel reflection at the fiber tip. The latter presents low sensitivities to the external index when compared with other devices studied. The case is different when a biological or chemical active layer is deposited on the tip. In this case, the phase of the interfering pattern can be highly sensitivity to the parameter of interest. Table 2.3 shows the most relevant fiber optic based refractometers.

Configuration	Param.[a]	RI Range	Sensitivity	Res. (RIU)[b]	Ref.[c]
MFBG	$\Delta\lambda$	@ 1.45	110 nm/RIU	10^{-5}[d]	[14]
TFBG	$\Delta\lambda$	@ 1.32	11.2 nm/RIU	10^{-4}	[16]
Bare LPG	$\Delta\lambda$	1-1.36	1481 nm/RIU	-	[30]
Coated LPG	$\Delta\lambda$	@1.347	9000 nm/RIU	-	[41]
LPG/FBG	Optical Power	1.33-1.35	-	$\pm 2\times10^{-5}$	[43]
MZ-LPG	Phase	1.37-1.40	-	$\pm 1.8\times10^{-6}$	[50]
FP-LPG	$\Delta\lambda$	@1.33	-	$\pm 2.1\times10^{-5}$	[52]
Abrupt Taper	$\Delta\lambda$	1.33-1.35	1200 nm/RIU	$\pm 8.2\times10^{-6}$	[83]
CDM-MZ	$\Delta\lambda$	1.33-1.40	188 nm/RIU	-	[88]
MMI	$\Delta\lambda$	1.30-1.33	148 nm/RIU	-	[92]
SPR	$\Delta\lambda$	1.32-1.38	5000 nm/RIU	-	[115]

Table 2.3: Most relevant fiber optic refractometers.

[a]Parameter
[b]Resolution
[c]Reference
[d]Theoretical Value

Overall, evanescent field fiber refractometers are very attractive due to their immunity to electromagnetic interferences, small size, and capability for *in-situ*, real-time, remote, and distributed sensing. Most of the applications, however, focus on the measurement of parameters such as the concentration of ethylene glycol, sucrose, salt, ethanol, among others. Nevertheless, this approach is not the most reliable due

to the possible interference of other species present in the solution, which are different from the analyte of interest. Thus, the use of sensitive materials containing biomolecules with a natural affinity to the target, or chemical species having analyte specific ligands, has increased in the last years, mainly based in LPGs. Several works were reported regarding antibody-antigen interaction and also DNA hybridization. Regarding chemical application several sensing probes were presented to measure pH, ethanol vapor and ammonia.

Chapter 3

Fiber Grating Sensors

Summary

Fiber grating sensors have generated great interest in recent years because of their many industrial, structural health and environmental monitoring applications. Based on a diffraction mechanism, these periodic micro structures can be used as an in-fiber filter for fiber optic sensing or communications. Depending on the range of its period, they can be classified in Bragg gratings (or short period gratings) and long period gratings. In this chapter, a thorough discussion of all the relevant topics regarding fiber gratings operation, manufacture and sensing characteristic, with special emphasis given to refractive index sensing is addressed.

3.1 Introduction

The photosensitivity in optical fibers was firstly observed by Hill *et al.* in 1978 [120], more or less accidentally. Hill and co-workers were carrying out an experimental work on Brillouin scattering in optical fibers, they launched light from an argon laser emitting a spectral line at 488 nm into the core of an optical fiber doped with germanium. After a few minutes, a substantial portion of the injected optical power started to be reflected by the fiber, this portion gradually increased until it became almost all of the light injected. Subsequent spectral measurements made indirectly by application of temperature and strain, revealed that, a very narrow spectral filter,

had been produced along the total length of fiber of approximately one meter. The formation of this filter was due to the presence of a pattern of standing waves caused by the interference of the coherent light propagated in the optical fiber and reflected at the end face, through a non-linear effect called photosensitivity; that caused a periodic change in the refractive index of the fiber core. The first fiber grating had been written.

The photosensitivity is particularly observable in silica fibers, with high levels of doped core with impurity atoms such as boron or germanium [121] or standard optical fibers subjected to a treatment with high pressure hydrogen load [122]. The mechanisms involved include reactions between hydrogen and germanium, forming OH and deep UV absorbing species, inducing a large change of the refractive index [122].

The experiment of Hill and colleagues, brought the discovery of the photosensitivity of optical fibers and the possibility of writing periodic structures on its core, that signified an important advance in fiber optic technology for communications and later for sensing. However, limitations in the fabrication were a significant drawback in the early stage around 1980. The real breakthrough occurred in 1989 by Meltz *et al.* [123] through the demonstration of a fiber grating fabrication technique by external (side) UV exposure. From that moment on, the scientific research in this area shows a huge development. Fiber gratings were successfully fabricated in spectral regions of interest for fiber optic communications, for filtering and sensing, raising the general interest towards the practical applications of these fiber periodic structures. In the next section, the physical concept well-known from optical diffraction gratings will be exposed.

3.2 Principle

A fiber grating is an optical diffraction grating and corresponds to a periodic modulation of the refractive index in the fiber core, that satisfies a phase matching condition between a guided mode and other modes that can be core modes, cladding modes or radiation modes. Fiber gratings allow the transfer of power between modes of an optical fiber. Figure 3.1 represents an optical uniform diffraction grating and its effect upon a light wave incident on the grating at an angle θ_1. The effect of the grating in the light wave can be described by the familiar grating equation [124];

$$n \sin(\theta_1) = n \sin(\theta_2) + m\frac{\lambda}{\Lambda}, \tag{3.1}$$

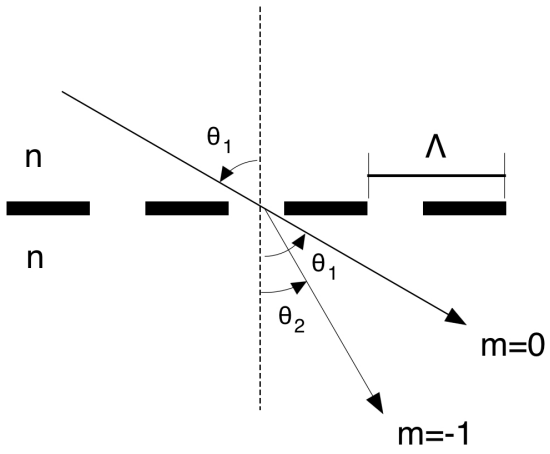

Figure 3.1: The diffraction of a light wave by a grating.

where θ_2 is the angle of the diffracted wave, m determines the diffraction order and Λ is the grating periodicity. In fiber gratings generally dominates the first order diffraction, m =-1, and since the propagation constant of a mode is $\beta = \frac{2\pi}{\lambda} n_{eff}$, where $n_{eff} = n \sin(\theta)$, the equation 3.1 can be re-written in function of the guided modes;

$$\beta_1 - \beta_2 = \frac{2\pi}{\Lambda}. \tag{3.2}$$

Which is phase matching condition for uniform fiber gratings. Fiber gratings can be broadly classified into two types: Bragg gratings (also called short period gratings), in which coupling occurs between modes traveling in opposite directions; and long period gratings, in which the coupling is between modes traveling in the same direction. FBGs are usually designed to diffract light into the same spatial mode as the exciting mode, unlike the LPGs, which act as intermodal couplers. Figure 3.2(a) illustrates the reflection from a Bragg grating. In this case, a mode with an incidence angle of θ_1 is reflected into the same mode but traveling in the opposite direction with an angle of $\theta_2 = -\theta_1$. Thus, considering $\beta_2 = -\beta_1 = \beta_{co}$ the equation 3.2, can be re-written as;

$$2\beta_{co} = \frac{2\pi}{\Lambda}. \tag{3.3}$$

This condition is illustrated on the β axis shown in Figure 3.2(b), where the circles represents the bound co-propagating and counter-propagating core modes. The propagation constant for the fundamental guided mode is given by $\beta_{co} = \left(\frac{2\pi}{\lambda}\right) n_{eff,co}$, with $n_{eff,co}$ the effective index of the core, therefore substituting in equation 3.3, the

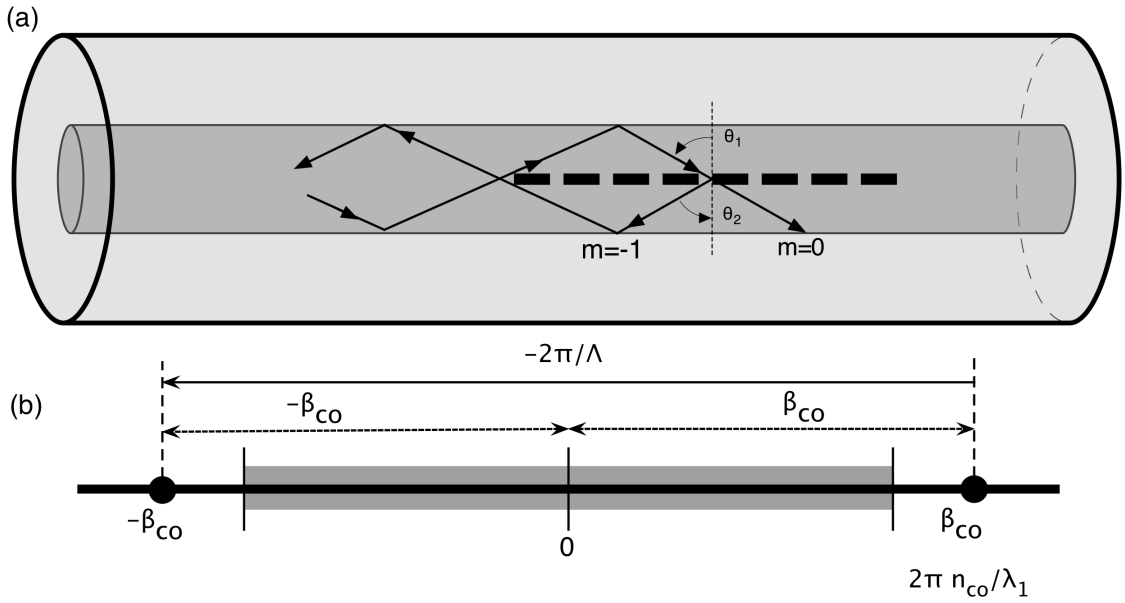

Figure 3.2: Ray-optics illustration of core-mode Bragg reflection by a fiber Bragg grating and (b) the β axis diagram demonstrating the grating coupling condition for m =-1.

resonant wavelength of the back-reflected peak, the so-called Bragg wavelength (λ_B), is defined by Bragg grating condition [125];

$$\lambda_B = 2n_{eff,co}\Lambda. \tag{3.4}$$

Diffraction by a LPG of a mode with a bounce angle θ_1 of into a co-propagating mode with a bounce angle of θ_2 is shown in Figure 3.3(a). In this situation the first mode is the fundamental core mode while the second is a m^{th} cladding mode. Using the same reasoning as before, and considering $\beta_1 = \beta_{co}$ and $\beta_2 = \beta_{cl}^m$, the equation 3.2, can be re-written as;

$$\beta_{co} - \beta_{cl}^m = \frac{2\pi}{\Lambda}. \tag{3.5}$$

Again, this condition is illustrated on the β axis shown in Figure 3.3(b), where the circles represents the bound co-propagating core mode and co-propagating m^{th} cladding mode. Substituting $\beta_{co} = \left(\frac{2\pi}{\lambda}\right) n_{eff,co}$, $\beta_{cl}^m = \left(\frac{2\pi}{\lambda}\right) n_{eff,cl}^m$, the propagation constants for core and m^{th} cladding mode, respectively, with n_{eff}^m being the effective index of the m^{th} cladding mode; the resonant wavelength for a certain cladding mode λ_R^m, is given by;

$$\lambda_R^m = \left(n_{eff,co} - n_{eff,cl}^m\right)\Lambda. \tag{3.6}$$

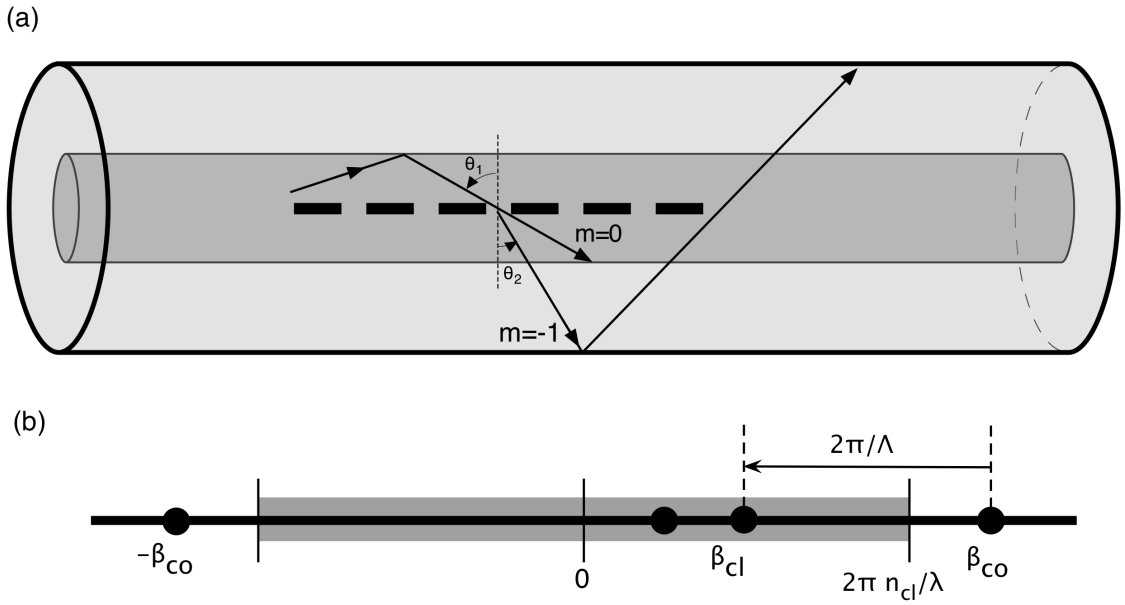

Figure 3.3: Ray-optics illustration of the cladding mode coupling by a long period grating and (b) the β axis diagram demonstrating the grating coupling condition for m =-1.

For co-propagating coupling at a certain wavelength, clearly a much longer grating period is required than for counter-propagating coupling. In the next sections the most relevant concepts and details regarding fiber gratings operation, fabrication and sensitivity to external parameters will be exposed, starting by the FBGs.

3.3 Fiber Bragg gratings

FBGs sensors have generated great interest in recent years because of their many industrial and structural health monitoring applications. The fiber grating can be used as fiber mirror or in-fiber filter for fiber optic sensing or communications. Bragg grating sensors have been widely used and commercialized for strain and temperature measurement. In this section, a detailed discussion of all the relevant topics regarding Bragg gratings operation, manufacture and sensing characteristic, with special emphasis given to refractive index sensing is addressed.

A FBG is a microstructure of small dimensions, general few millimeters, that is written in the core of an optical fiber, through different techniques frequently using UV laser radiation. This photonic structure consists, in a sub-micron localized and periodical modulation of the refractive index in the order of 0.1%, which has its origin in a physical mechanism called photosensitivity described in the section 3.1.

The result is a structure with a narrow spectral reflection band, that can be used as filter for optical communications and sensing applications. The FWHM of an FBG resonant peak is around 200 pm, it may vary depending on the physical length of the grating.

3.3.1 Theory

When light from a broadband source, guided by an optical fiber, as shown in Figure 3.4, incides in the diffraction structure, for a certain wavelength, light scattering occurs in the consecutive planes of the grating, where each plane acts as a localized mirror, which reflects the light guided along the core of the fiber. In a simplified way, it is possible to affirm that for every grating, there is a particular wavelength for which is satisfied the resonance condition, the Bragg condition, where the waves generated at each plane are all in phase, resulting in a strong back reflection. Hence, when Bragg condition is satisfied, the contributions of reflected light from each plane add constructively in the backward direction to form a back-reflected peak with a center wavelength defined by the grating parameters. Therefore, there is a coupling between the fundamental core mode and its respective counter-propagating mode.

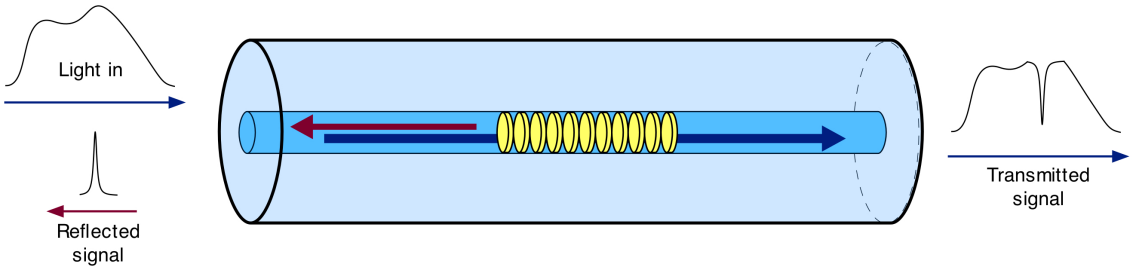

Figure 3.4: Operation principle of an FBG.

Hence, when Bragg condition is satisfied, the contributions of reflected light from each plane add constructively in the backward direction to form a back-reflected peak with a center wavelength defined by the grating parameters. Thus, there is a coupling between the fundamental core mode and its respective counter-propagating mode. The resonant wavelength of this back-reflected peak, the Bragg wavelength, was already defined in the section 3.2 is given by $\lambda_B = 2n_{eff,co}\Lambda$ (equation 3.4). Through the coupled-mode theory, an analytical description of the reflection properties of Bragg gratings can be obtained. The reflectivity of a grating with a constant modulation amplitude and period is given by [126];

$$R = \frac{k^2 \sinh^2(SL)}{\Delta\beta \sinh^2(SL) + S^2 \cosh^2(SL)}, \tag{3.7}$$

where L represents the physical length of the grating, $\Delta\beta = \beta - \frac{\pi}{\Lambda}$, where $\beta = \frac{2\pi n_{eff,co}}{\lambda}$ is the propagation constant of the fundamental guided mode and $S = \sqrt{k^2 - \Delta\beta^2}$. The coupling coefficient, k, for the sinusoidal variation of index along the fiber axis is given by;

$$k = \frac{\pi \Delta n}{\lambda} \eta, \tag{3.8}$$

where $\triangle n$ is the induced modulation amplitude in the index, η is the confinement factor of the guided mode. The maximum reflectivity occurs for $\lambda = \lambda_B$, hence, the expression for the reflectivity becomes;

$$R_{max} = \tanh^2(kL). \tag{3.9}$$

Depending on the variation of few parameters, for instance, grating length and magnitude of induced index change, it is possible to obtain narrow-band transmission, as well as high reflectivity of the resonant peak.

3.3.2 Fabrication

The first Bragg grating written into an optical fiber was reported in 1978 by Hill *et al.* [120]. It was made with visible laser light propagating along core of the waveguide. In 1989, a more versatile technique was developed by Meltz *et al.* [123]. In this experiment the fiber was irradiated from the side with two intersecting coherent UV laser beams. The transverse holographic method worked since fiber cladding is transparent to UV light, whereas fiber core is highly absorbing of this radiation. Currently, the two UV beams are usually generated by exposing the coherent radiation through a periodic phase mask with a single UV beam [127], the writing is made by using two first-order diffracted rays.

Figure 3.5 illustrates the phase-mask technique [126], which is one of the most effective methods to fabricate FBGs. The phase-mask is a diffractive element, made from a slab of silica glass, transparent to UV light where a periodic structure is etched on one of the surfaces with a pattern like a square wave. When the UV laser light incides perpendicularly on the phase-mask, it is diffracted by its periodic corrugations. Most of the diffracted light is contained in the 0, +1 and -1 diffracted orders. However, the phase-mask is designed to suppress the diffraction into the zero order

by controlling the depth of the corrugations. Thus, only the two +1 and -1 diffracted order beams interfere causing interference fringes of high visibility to produce a periodic grating pattern. The fiber is placed to stay inside this interference pattern. This interference pattern creates onto the fiber alternate bands of maximum and minimum intensity causing modulation of the refractive index of the photosensitive fiber core. These changes form a periodic structure which constitutes the Bragg grating. The period of the grating is approximately half of the phase-mask period (Λ_{pm}).

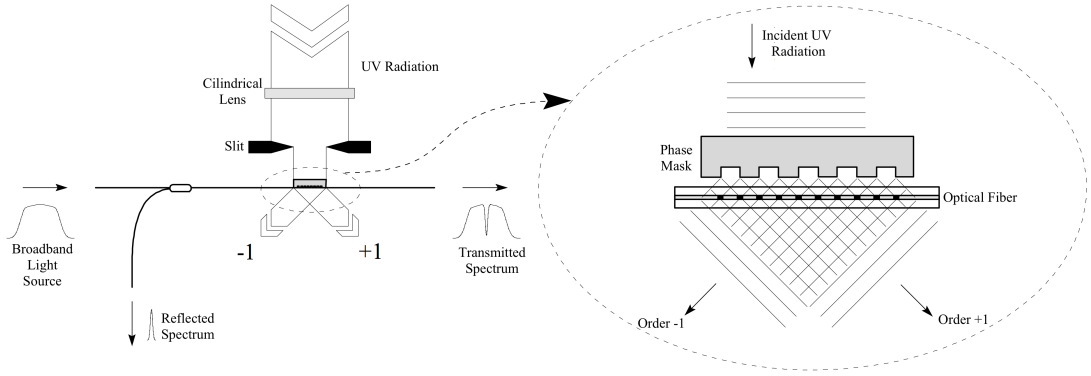

Figure 3.5: Operation principle of FBG and phase mask fabrication technique.

The possibility to manufacture these devices with high reproducibility, at a potentially low cost and without affecting the physical strength of the optical fiber, has increased the research and outputs applications in the fields of optical fiber communications [128] and optical fiber sensors [7] in the last years. Specially in optical fiber sensors, due to all the advantages normally attributed to fiber sensors, and additionally, to the fact that, typically, the information of measurands such as strain and temperature, are encoded in the resonant wavelength of the grating, which is an absolute parameter. Thus, these devices are inherently self-referenced. Moreover, there are several intrinsic advantages associated with FBG technology such as operation in reflection, narrowband spectral response, compatibility with standard telecom technology, and the intrinsic multiplexing capability, particularly important in the context of remote, distributed and multi-parameter sensing [8, 129, 130]. FBG has been widely used for strain and temperature sensing. In particular in the area of quasi-distributed embedded sensing in materials to create smart structures. In this case, fibers with sensor arrays can be embedded into the materials to allow measurement of parameters such as load, strain, temperature, from which the health of the structure can be monitored in real-time [131]. For all this reasons FBG technology have a strong impact on the field of optical fiber sensing, being an essential part of

fiber technology now available in the market. FBGs can be also useful as the optical sensing element in a range of other fiber sensor configurations: FBG based chemical sensors, pressure sensors, and accelerometers are some representative examples [7].

3.3.3 Sensitivity Characteristics of FBGs

The vast majority of the work on FBG sensors has focused on the use of these devices for providing quasi-distributed arrays of strain and/or temperature sensing [7]. As it was stated, an FBG acts as a selective mirror which reflects a narrow band of wavelengths around the Bragg wavelength (λ_B) that is dependent on the effective index of the guide mode ($n_{eff,co}$), i.e., on the index of the core and the cladding; and on the periodicity of the grating (Λ). Thus, λ_B will be also a function of any physical measurand which may alter these parameters interacting in optical fiber containing the Bragg grating. Therefore, it is possible to speak about FBG sensors. Like most of the optical fiber sensors, Bragg grating sensors are inherently sensitive to temperature, axial and transverse strain, pressure and, in particular situations, to the magnetic field. Through these sensitivities, mainly axial strain, Bragg grating sensors can be used to measure a variety of physical parameters. The sensitivity of the FBG to temperature and axial strain can be obtained by differentiating the equation 3.4 [7, 132, 133].

The thermal response of an FBG arises due to the inherent thermal expansion of the fiber material and the temperature dependence of the refractive index. The temperature sensitivity an FBG may be assessed by differentiating equation 3.4 [131];

$$\frac{\Delta\lambda_B}{\lambda_B} = \frac{\Delta\left(n_{eff,co}\Lambda\right)}{n_{eff,co}\Lambda} = \left(\frac{1}{\Lambda}\frac{\partial\Lambda}{\partial T} + \frac{1}{n_{eff,co}}\frac{\partial n_{eff,co}}{\partial T}\right)\Delta T = (\alpha \pm \varsigma)\Delta T = \beta_T \Delta T, \quad (3.10)$$

in the expression above, β_T is the thermal sensitivity coefficient of the FBG sensor, α the thermal expansion coefficient of the optical fiber and ς is the thermo-optic coefficient that establishes the dependence between the effective refractive index and temperature. Regarding the thermal expansion coefficient, it is essentially the contribution of the thermal expansion coefficient of pure silica, is about 12.55×10^{-6} °C. The thermo-optic coefficient, on the other hand, depends mostly on the temperature and is slightly wavelength dependent. For wavelengths in the infrared region and temperatures up to 200 °C, ς it is typically around 6.7×10^{-6} °C. It can be seen that the contribution of the thermal expansion coefficient to the thermal sensitivity of the FBG is around twelve times lower than the contribution of the thermo-optical coefficient, which is true for most of the fibers. According with equation 3.10, $\Delta\lambda_B$ varies

linearly with ΔT and increases with increasing values of temperature. Considering a Bragg wavelength of 1550 nm, the substitution of these values into equation 3.10 leads to $\frac{\Delta\lambda}{\Delta T}$ of 11.2 pm/°C, which is the typical value for the thermal sensitivity of the Bragg sensors operating in the third telecom window. In many applications, this sensitivity can be improved by coating the FBG with materials with higher thermal expansion coefficient than that of silica.

The axial strain response of an FBG arises due to both the physical elongation of the fiber (and the corresponding fractional change in grating pitch), and the change in the fiber refractive index due to the photo-elastic effects. Analogously to the previous case, the dependence on the strain can be expressed as a function of the relative change in length, i.e., as a function of strain $\Delta\varepsilon = \frac{\Delta L}{L} = \frac{\Delta\Lambda}{\Lambda}$, and can be obtained by differentiating equation 3.4 [131];

$$\frac{\Delta\lambda_B}{\lambda_B} = \frac{\Delta\left(n_{eff,co}\Lambda\right)}{n_{eff,co}\Lambda} = \left(1 + \frac{1}{n_{eff,co}}\frac{\partial n_{eff,co}}{\partial\varepsilon}\right)\Delta\varepsilon = (1 + p_e)\Delta\varepsilon = \beta_\epsilon\Delta\varepsilon, \qquad (3.11)$$

where p_e is the photo-elastic constant of the silica ($p_e = -0.22$) and β_ε is the strain sensitivity of the FBG. The relation between the photo-elastic constant with the wavelength is almost negligible, resulting in a linear relationship between the Bragg wavelength and the strain. For an FBG written at 1550nm, $\frac{\Delta\lambda_B}{\Delta\varepsilon}$ is about 1.2 pm/με. In the case of strain, the waveguide (physical elongation) represents the main contribution to the overall sensitivity.

The nature of the output of FBGs provide these sensors with a built-in self-referencing capability. The measurand information is encoded directly in the Bragg wavelength, which is an absolute parameter, that does not depend on the optical power. This is widely acknowledged as one of the most important advantages of these sensors. Moreover, the wavelength encoded nature of this technology also facilitates wavelength division multiplexing by allowing each sensor to be assigned to a different slice of the available source spectrum [130]. These features enable a quasi-distributed sensing of strain, temperature, or potentially other measurands by associating each spectral slice with a particular spatial location [7].

FBG sensors have been widely and successfully used for strain and temperature measurement [8]. However, in their standard configuration and as it was described, they cannot be used as a fiber refractometer since the radiation is strongly confined within the fiber core and only a small portion of the light travels in cladding, nearby the core/cladding interface, never reaching the external medium. Therefore, different strategies should be conceived to promote the interaction of the optical radiation with

the external environment. Typically, FBG based refractometers rely on the evanescent field of the core modes under fiber etching conditions, which enables interaction with the surrounding medium. In the next section, new configurations aiming to obtain refractive index sensors based on FBGs will be addressed.

3.3.4 FBG based Refractometers

The interaction of the optical radiation traveling along the fiber core with the external medium can be achieved by tailoring the FBG structure either by reducing the cladding diameter or using a different modulation pattern (blazed) or even employing in-fiber mechanisms to excite the cladding modes of a simple FBG.

The presence of a substantial evanescent field in the interface cladding/external medium guarantees the interaction of the optical radiation which travels along the fiber axis with the external environment. In a standard FBG it does not occurs, because the optical radiation is confined to the fiber core. Modifying the fiber geometry it is possible to expose the optical signal to the external medium. Refractive index measurements with an FBG can be achieved by etching the fiber cladding in the region of the grating to a diameter such that the evanescent field of the fundamental mode interacts with the surrounding environment. In this way, the core mode will become sensitive to the external index, through the effective refractive index of the fundamental mode, which is affected by the SRI. Thus, in this case the variation of the Bragg wavelength as a function of the SRI can be expressed as [21];

$$\Delta\lambda_B = 2\Lambda\Delta n_{eff,co}, \tag{3.12}$$

where $\Delta n_{eff,co} = \eta_p(n_{ext} - n_{cl})$, with n_{ext} and n_{cl} being the indices of the surrounding medium and the cladding, respectively. η_p is the fraction of the total power of the unperturbed fundamental mode that flows in the etched region, and is, therefore, lost to the surrounding medium. Clearly, the change of the effective index will be greater for greater η_p , thus, this factor affects the sensitivity to external index, that depends on the the effective index of the fundamental guided mode. η_p is directly proportional to the area of the cross section of the etched ring and, therefore, it will be higher for smaller fiber diameters [4]. On the other hand, it is also dependent on the contrast between the cladding and external index. For a smaller difference between them, the guided mode will be less confined to the core and η_p will be increased, as well as the sensor sensitivity [4]. It is worth to note that due to the power loss that occurs in the etched region of the fiber, the reflectivity of the FBG decreases when the fiber radius

becomes smaller. Additionally, after a certain stage, the decrease of the fiber radius due to etching will also have consequences on the value of the Bragg wavelength of the grating. This is so because the effective index of the fundamental mode starts to be affected [21]. Figure 3.6 shows the Bragg peak before and after the etching process, clearly illustrating the two effects described above [21].

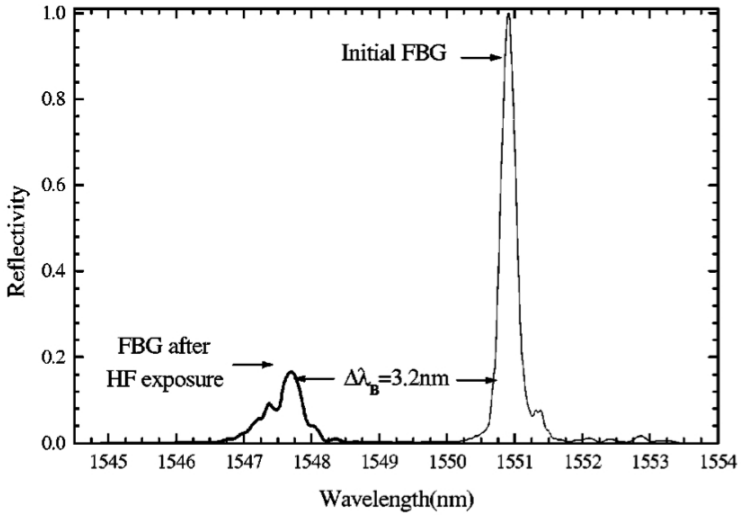

Figure 3.6: FBG spectrum before and after etching. The fiber diameter was reduced until approximately 7 μm [21].

Fiber Refractometers were reported in chemically etched FBG [4, 11, 21, 134] and side-polished FBG [9]. It is important to stress that due to the asymmetry induced by the side polishing process, the SRI sensitivity becomes polarization dependent. Refractometers based on Etched FGBs preserve all the benefits associated to FBG technology, however, it sacrifices the physical integrity of the sensing structure, which will be weaker, as higher sensitivity is needed. For a bench-top tool it can be suitable, but a special packaging will be necessary in case of *in-situ* sensing applications.

The transmission spectrum of a simple (uniform) FBG can exhibit discrete dips at shorter wavelengths than the Bragg wavelength. Usually it happens in gratings with strong modulation index, i.e. high reflectivity ($> 98\%$). These losses are due to coupling to cladding modes. Figure 3.7 shows a practical example of this phenomenon [27]. The main dip corresponds to the so-called Bragg resonance (coupling between the co-propagating and contra-propagating core modes). The remainder resonances at shorter wavelengths, are due to the coupling between the core mode and contra-propagating cladding modes of the fiber [27]. As higher is the order of the mode, shorter is the wavelength in the spectrum. These cladding modes attenuate rapidly

along the propagation axis due to the absorption coefficient of the buffer cladding. Therefore these peaks are observable in transmission, but not in reflection. Whereas such coupling phenomenon are undesirable for optical communications purposes, they can be very useful if enhanced with appropriate in-fiber gratings and turned into refractive index sensors.

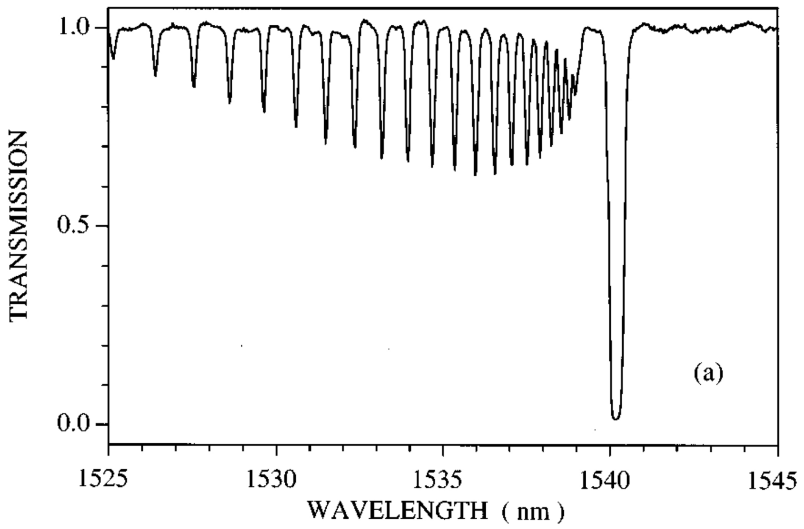

Figure 3.7: Experimentally measured transmission spectra of a standard FBG, demonstrating both core mode– core mode and core mode – cladding mode coupling [27].

Following the Bragg condition, the central wavelength for the m^{th} cladding mode (λ_{BR}^{m}) is given by;

$$\lambda_{BR}^{m} = \left(n_{eff,co} + n_{eff,cl}^{m}\right) \Lambda. \tag{3.13}$$

To the best of our knowledge, cladding modes of a common FBG written in a standard SMF-28 fiber were not reported for SRI sensing. Probably, because those modes normally appear spectrally closer to the Bragg resonance and therefore correspond to low order modes, with no appreciable interaction with the external medium. Gratings with common profiles in length and modulation usually do not excite high order cladding modes. However, in the last few years efforts were made in order to excite high order modes of a simple FBG by introducing an in-fiber core-cladding coupling/recoupling mechanism upstream of the FBG. Thus, in the reflected spectrum, the core and cladding modes appear as a result of cladding-mode-assisted couplings by the concatenated structure. Figure 3.8 shows a schematic of concatenated structure and two different types of mode recoupling mechanism. In type I recoupling (Figure

3.8 (a)), the guided light coupled to the counter-propagating cladding mode by the FBG is re-coupled to the guided mode by the in-fiber coupling mechanism. In type II recoupling (Figure 3.8 (b)), the guided light coupled from the core to the cladding mode by the in-fiber coupling mechanism is re-coupled to the counter-propagating guided mode by the FBG. It should be pointed that the light must propagate in the upstream direction of the FBG for these recoupling mechanisms to occur [135].

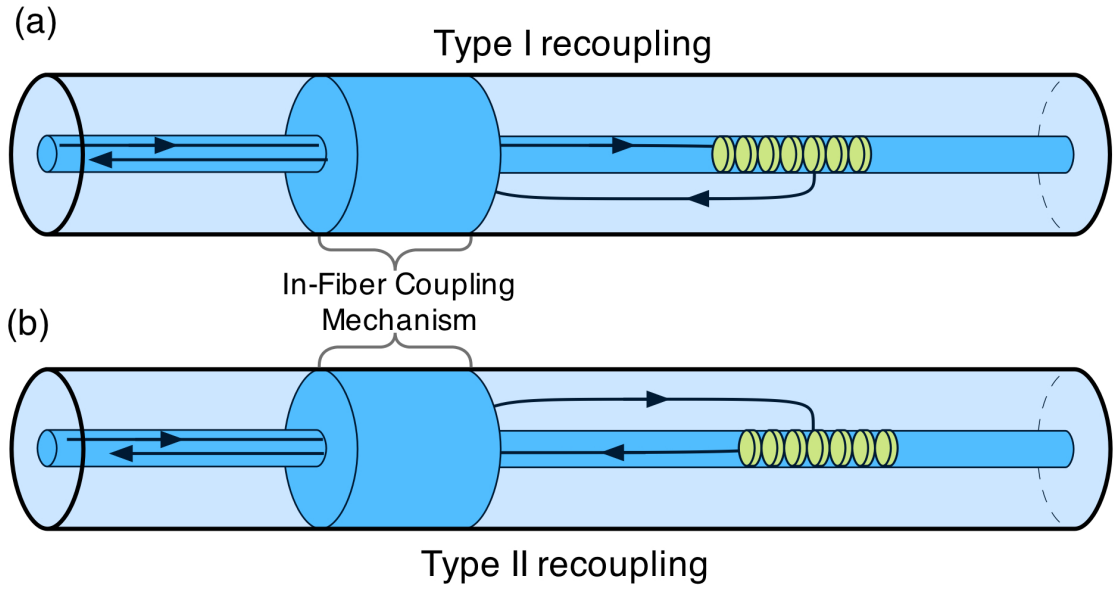

Figure 3.8: Recoupling of the coupled light to the backward guided mode in the concatenated in-fiber coupler and a FBG. (a) backward cladding-mode-assisted recoupling; (b) forward cladding-mode-assisted recoupling.

Few authors have explored the opportunity to measure the SRI by using the cladding modes of a simple FBG. This aim was achieved using different in-fiber coupling mechanisms such as LPGs [17, 136] and core diameter mismatches [18, 137]. The use of the LPGs is the most reliable one due to possibility of controlling with the fabrication parameters the excited mode and the transferred power, whilst with the other techniques it is a hard task to do, in a controllable fashion.

A TFBG is a special kind of Bragg grating in which the grating planes are blazed by an angle θ with respect to the fiber axis [138]. This asymmetry enhances the coupling to symmetric ($LP_{0,m}$) and asymmetric ($LP_{1,m}$) contra-propagating cladding modes. Contrarily, it decreases the coupled energy to the contra-propagating core mode (i.e. the Bragg peak). Therefore, in the transmission spectrum both a core-mode resonance and several cladding-mode resonances appear. Figure 3.9 shows the

experimental grating transmission spectrum measured in air (tilt angle of 6°) [16]. It is possible to observe the strong coupling to the symmetric and asymmetric cladding modes in detriment of the core mode.

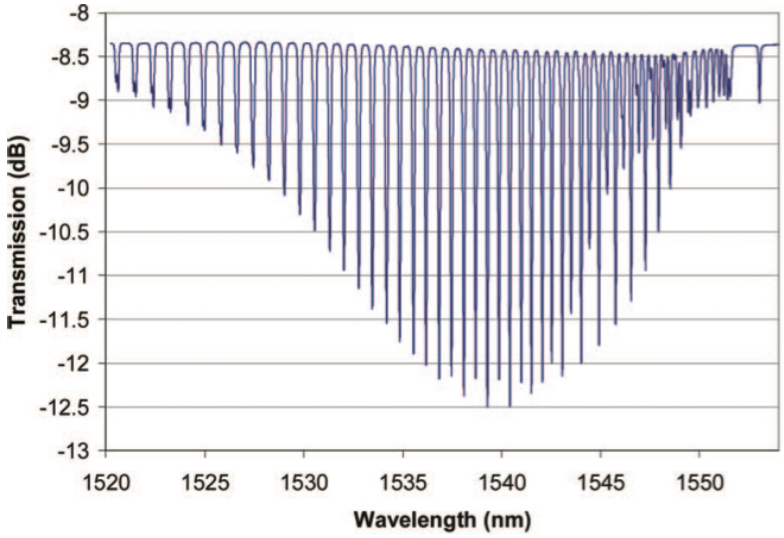

Figure 3.9: Experimental TFBG (Corning SMF-28 fiber, $\theta = 6°$) transmission spectrum measured in air [16].

In the case of the TFBG, following the Bragg condition, the central wavelength for the m^{th} cladding mode (λ_{BR}^{m}) is given by [15];

$$\lambda_{BR}^{m} = \left(n_{eff,co} + n_{eff,cl}^{m}\right) \frac{\Lambda}{\cos\theta}, \tag{3.14}$$

where $n_{eff,co}$ and $n_{eff,cl}^{m}$ are the effective indices of the core and m^{th} cladding mode, respectively. The cladding modes are guided by the cladding boundary, as a result, their effective index depends on the SRI. When the external index is increased, the center wavelength of the resonances experiences a shift to higher wavelengths. Moreover, the intensity of the resonant peaks drops progressively, to fit a smooth loss curve. Thus, by monitoring the wavelength shift or the optical power of the cladding modes resonances it is possible to measure the SRI. The sensitivity of the cladding-mode effective index to changes in the external index increases with mode order as well with the external index since, the penetration depth of the evanescent field increases in both conditions [16]. TFBG has been reported to measure refractive index [15, 16]. TFGBs based refractometers preserve the fiber integrity, presents very narrowband resonances and with a single grating it is possible to measure refractive index (cladding modes) and temperature (Bragg peak) independently. Nevertheless, the sensitivity of these devices is very low. It is possible to increase the sensitivity by

increasing the tilt angle. However, it implies to use a very broad spectrum (around 100 nm) with a large amount of resonances, which hinders its multiplexing capability.

LPGs on the other hand, due to its core to cladding coupling ability is the most popular device to RI sensing. The next section is devoted to the most important concepts regarding LPG theory, fabrication, and sensing characteristics.

3.4 Long Period Gratings

The popularity of long period gratings has increased steadily over the last years as a notable number of long period grating based devices and systems have been demonstrated for a multitude of applications in optical fiber communication and sensing. In this section, a thorough discussion of all the relevant topics regarding long period grating operation, manufacture and sensing characteristics is addressed. Special emphasis is given to its refractive index sensing capability that make them a good candidate to be used as a probe for biochemical sensing.

A LPG is a photonic device realized by inducing a periodic modulation of the optical properties of a singlemode optical fiber (mostly), generally the refractive index of the core, obtained by either a reversible method, inducing a physical deformation in the fiber [139], or by a permanent modulation of the fiber core by UV radiation exposure [28], femtosecond laser pulses [140], CO_2 laser irradiation [141], electric-arc discharges [142] or ion implantation [143]. This periodic perturbation satisfies the phase matching condition between the fundamental core mode and a forward propagating cladding mode of an optical fiber [28]. Thereby, in an LPG, the core mode couples into the cladding modes of the fiber, resulting in several attenuation bands centered at discrete wavelengths in the transmitted spectrum, each corresponding to coupling with a different cladding mode. They have periodicities ranging in hundreds of micrometers (typical values are 100-600 μm), refractive index modulation strength of the order of 10^{-4} and lengths of few centimeters (typically 2–4 cm). The bandwidth of the resonant dip varies from few nanometers up to tens of nanometers depending on its physical length.

3.4.1 Theory

Figure 3.10 illustrates the working principle of an LPG. It is possible to observe schematically the mode coupling mechanism, and the resulting attenuation bands corresponding to each excited cladding mode. Each of these attenuation (rejection) bands occurs at a specific wavelength range. Unlike FBGs, where mode coupling

is counter-propagating, for LPGs the core mode is coupled, at specific resonance wavelengths, to several cladding modes propagating in the same direction until it is completely attenuated by scattering in the air-cladding interface, by curvature losses, and in the fiber coating. Thus, LPG devices allow energy coupling between the fundamental guided mode ($LP_{0,1}$) propagating in the core and the forward propagating cladding modes ($LP_{0,m}$), which are then quickly attenuated/absorbed.

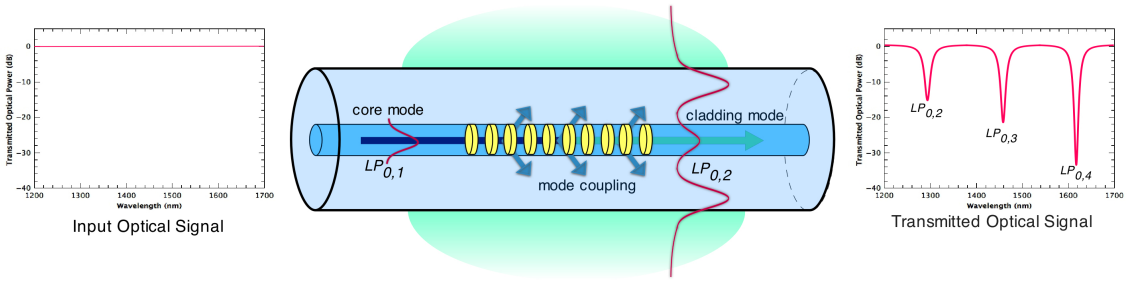

Figure 3.10: Schematic representation of the working principle of an LPG.

A SMF consists of a cylindrical structure, having a high-index core surrounded by a lower-index cladding, surrounded by air (or the external medium). The core (smaller radius a_{co}), supports only the fundamental mode, meanwhile, the cladding generally having a much larger radius a_{cl}, supports a large number of modes. Figure 3.11 shows the transmission spectrum of an LPG. Each attenuation feature that appears at a discrete resonant wavelength band corresponds to coupling from the core fundamental mode to a specific cladding mode. Detailed investigation of the interaction that takes place between the guided core mode, and the cladding modes supported by a SMF, can be done through the coupled-mode theory [144]. Theoretical analysis has shown that efficient coupling is possible only between core and cladding modes that have a large overlap integral, which is only possible for modes having similar electric field profiles [145]. Thus, coupling is observed between the core and circularly symmetric ($LP_{0,m}$) cladding modes of odd order. This is due to the fact that the electric field profile of the even order modes is such that the field amplitude is low within the core, whereas the electric field profiles of the odd modes have a peak located within the core [145]. This requirement explains why, over large wavelength ranges, coupling occurs only to a finite number of distinct cladding modes.

The fundamental core mode has a propagation constant β_{co}, and an effective refractive index of $n_{eff,co}$. These two parameters of the fundamental mode depend on the operation wavelength and on the fiber construction (geometry and constitution). The m^{th} cladding mode is characterized by a propagation constant β_{cl}^{m} and effective

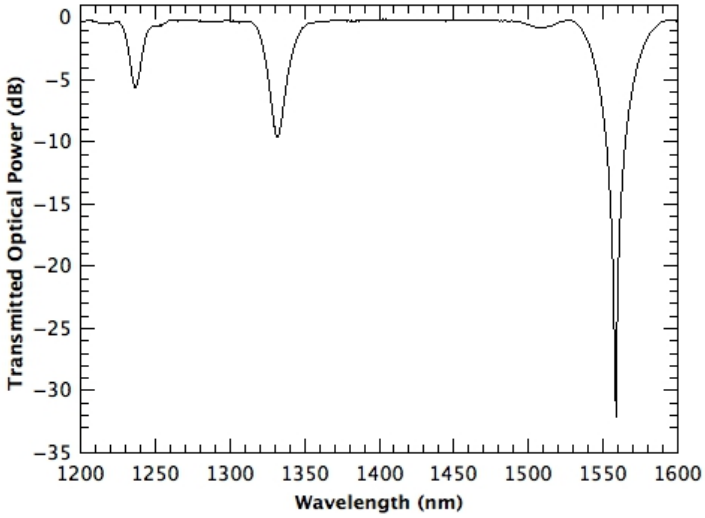

Figure 3.11: Transmitted spectrum of a LPG.

refractive index $n^m_{eff,cl}$ [29]. Thus, the propagation constants of the core and m^{th} cladding modes excited by a grating, can be expressed as;

$$\beta_{co} = \frac{2\pi}{\lambda} n_{eff,co} = k n_{co} \sin(\theta_1), \tag{3.15}$$

$$\beta^m_{cl} = \frac{2\pi}{\lambda} n^m_{eff,cl} = k n_{cl} \sin(\theta_2), \tag{3.16}$$

in above expressions the angles θ_1 and θ_2 are the propagation angles of the core and cladding mode, respectively and $k = \frac{2\pi}{\lambda}$. The phase matching between the fundamental mode propagating in the core of the fiber and a forward propagating cladding mode is achieved at the wavelength, λ, when the equation 3.5 $\left(\beta_{co} - \beta^m_{cl} = \frac{2\pi}{\Lambda}\right)$ is satisfied [28]. This relation was expressed as a function of the coupled cladding mode in the section 3.2 as $\lambda^m_R = \left(n_{eff,co} - n^m_{eff,cl}\right)\Lambda$ (equation 3.6).

λ^m_R present the resonant peak wavelength of the LPG corresponding to the m^{th} forward propagating cladding mode. Given some specific fiber parameters, it is the periodicity of the grating that determines which cladding modes can be excited by the fundamental core mode [28]. A graphical representation of the phase matching condition is shown in Figure 3.12, that illustrates the above mentioned concepts. For different order cladding modes, the propagation constants have different numerical values, as found in the continuous shaded region between 0 and $2\pi\frac{n_{cl}}{\lambda}$ for an infinite cladding region. Larger wavelength values ($\lambda_2 > \lambda_1$) imply a more condensed interval in which the propagation constants can occur. With the same grating period, it is possible to visualize coupling of the fundamental guided mode to the two first order

cladding modes at different resonant wavelengths (λ_2, λ_1). Continuing in this way, it is possible to visualize coupling of the fundamental guided mode to a continuum of cladding modes at different resonant wavelengths, resulting in several different loss bands in the LPG transmission spectrum [28].

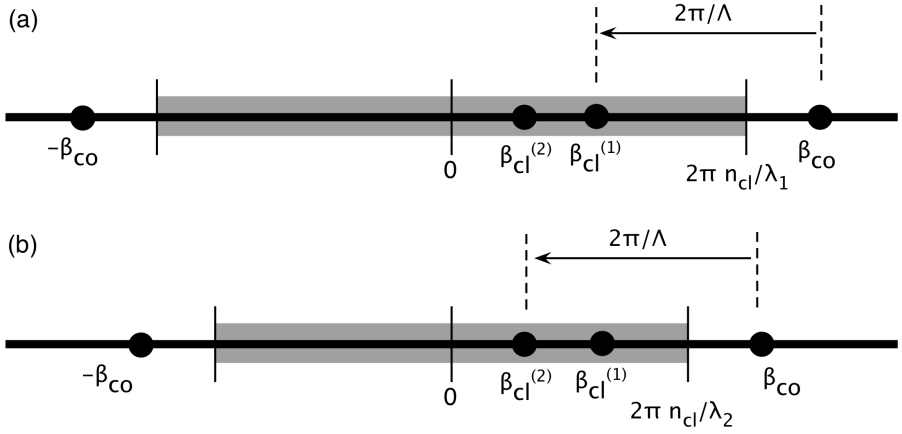

Figure 3.12: β axis showing the coupling conditions of LPGs for two different cladding modes.

The minimum transmission of the attenuation bands is given by the expression;

$$T_i = 1 - \sin^2(k_m L), \tag{3.17}$$

where L is the length of the LPG and k_m is the coupling coefficient for the m^{th} cladding mode, which is determined by the overlap integral of the core and cladding mode and by the amplitude of the periodic modulation of the core refractive index.

The theoretical modeling of LPGs requires the calculation of the effective indices of the core and cladding modes, enabling the determination of the central wavelengths of the attenuation bands, and the estimation of the mode field profiles, allowing the determination of the coupling strength and the shape of the spectral features. The effective index of the propagating core mode of the fiber can be determined, idealizing the fiber geometry, i.e., considering it a cylindrical waveguide with two layers [28]. A three layer waveguide model to determine the effective index of each cladding mode has been used, allowing an accurate determination of the coupling wavelengths [145]. In this model the effect of the core upon each effective index and respective mode profile of the different cladding modes was considered for accurate simulation of LPG characteristics. The modeling of the LPGs characteristics was performed using a modified software, originally made by Dario Baptista (INESC Porto, Universidade da Madeira) [146].

Figure 3.13(a) shows the dependence of the period of the LPG with the coupling wavelength for the first nine cladding modes. These plots were calculated following the three layer method described in the previous paragraph. The graphs indicate that coupling to low order modes is achieved using longer periods, while shorter periods facilitate coupling to the high order modes (Figure 3.13(a)). It can be seen that, the phase-matching curves for $LP_{0,2-9}$ show a positive slope throughout all the wavelength range. On the other hand, Figure 3.13(b) shows in more detail the cladding modes $LP_{0,7-9}$ in a wavelength range between 1400-2000 nm. In this case, it is possible to observe a sign change in the slope from positive to negative with increasing wavelength at the points denoted by open circles. The point at which the slope of the phase-matching curve changes its sign, is the so called turn-around-point [147]. Thus, for each mode that exhibits a turn-around-point in its dispersion curve, a given LPG period corresponds to two resonant wavelengths and results in coupling to a single cladding mode characterized by dual resonant peaks in its transmission spectrum. The turn-around-point occurs at longer wavelengths for lower order modes, and at shorter wavelengths as the mode order increases. Theoretically, each cladding mode exhibits a turning point, provided that the wavelength range observed is sufficiently large [148]. It should be stated that small changes in the coupling conditions could result in very large changes in the separation of the two resonant peaks, which is an interesting feature for sensing purposes. For LPGs fabricated to operate precisely at the turn-around-point in the RI of interest (open circles in Figure 3.13(b)), it has been observed that changes in the coupling conditions result in a change in the coupling efficiency (resonance depth), but not in the wavelength [148].

3.4.2 Fabrication

The fabrication of LPGs relies on the introduction of a periodic modulation of the optical properties of the fiber. This may be done by permanent modification of the refractive index of the core of the optical fiber or by physical deformation of the fiber. The most common fabrication technique is by UV irradiation, taking advantage of the photosensitivity of Ge-doped silica optical fibers, and due to the fact of UV-exposure is a well established technique, given its widespread use in the fabrication of Bragg gratings [149]. The UV-induced index modulation is typically achieved using wavelengths between 193-266 nm. The refractive index modulation can be achieved by exposure of the fiber through an amplitude mask [28] imprinting the mask pattern in to the fiber core, where the periodicity is determined by the mask period, or in a more flexible way, through a point by point technique [150]. The latter is induced by

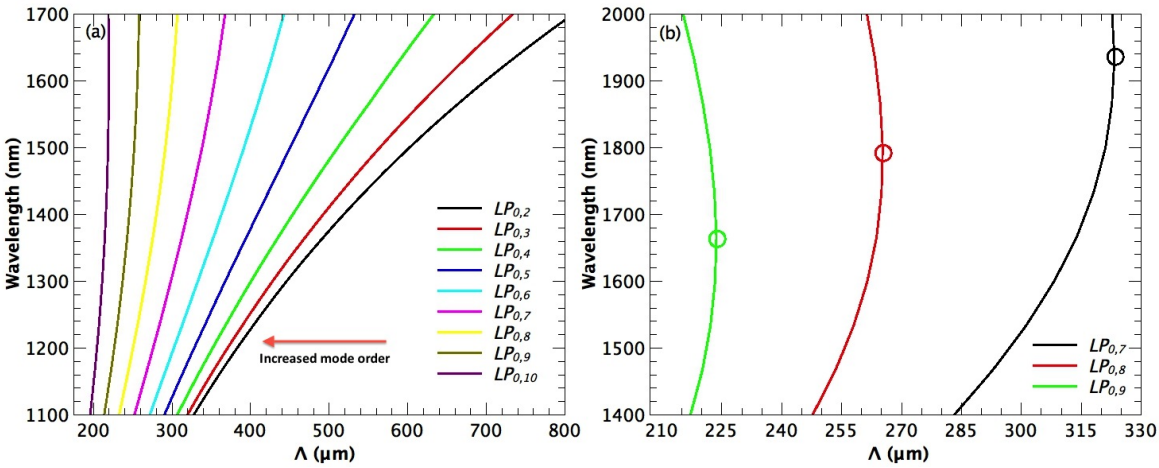

Figure 3.13: Resonant wavelength as a function of the LPG period for the first nine cladding modes (a). Similar as the previous one, by changing the wavelength range in order to note the turn-around-points (b). The following values were used in the analysis: n_{co}=1.4676, n_{cl}=1.4625, a_{co}=3.6 μm, a_{cl}=62.5 μm.

single spot illumination at different points along the fiber separated by the grating period, until the desired grating length is achieved. A great advantage of the point by point method is that it is an extremely flexible technique: the grating periodicity, length and blaze are all independent parameters, which can be individually adjusted to meet the desired LPG specifications and corresponding spectral characteristics.

The use of UV-exposure technique presents some constraints. Its use has implications for the spectral characteristics and stability of the LPG spectrum, especially to work at high temperatures. Gratings obtained by UV-exposure are known to contain an unstable component, which decays in time causing a significant change in the central wavelengths of the attenuation bands and in the coupling strength [28]. This unstable component may be removed by thermal annealing, but needs to be taken into consideration when designing an LPG for a particular application. The use of hydrogen loading of fibers to enhance their photosensitivity can result in further changes to the central wavelength and peak loss of the attenuation bands occurring after fabrication, as the hydrogen diffuses out of the fibers [151].

There are, however, several alternative techniques for gratings fabrication that do not require the fiber to be photosensitive. LPGs were written in Corning SMF-28 fiber using nanosecond pulses from a 157 nm femtosecond laser [152]. Femtosecond pulses in the near infrared (800 nm) were also employed [140]. The irradiation causes a densification of the glass, resulting in an index change. Compared with LPGs fabricated by UV light irradiation, those fabricated by focused irradiation of femtosecond

pulses have a high temperature resistance and a superior aging characteristic. Femtosecond manufactured LPGs are made by point by point method, taking advantage of the benefits associated to this technique.

CO_2 laser irradiation at 10.6 μm is another point by point writing method used to fabricate LPGs [141]. Also, does not require photosensitization and UV-irradiation. Hence, this technique could be, used to write LPGs in almost all types of fibers, including pure-silica photonic crystal fibers (PCF) [153]. The CO_2 laser exposure of the fiber was originally thought to result in the densification of the glass, and/or the relaxation of tensile stresses built into the cladding of fibers such, as Corning SMF-28, during fabrication [154]. However, there is evidence to suggest that the change in refractive index is a result of breakage of Si–O–Ge chains [155]. To write a single period of a grating, the laser light is focused to a spot on a section of optical fiber using a spherical or cylindrical lens and translating the fiber by the period of the grating and then by exposing the new section of fiber to laser light creating the index modulation at specific points. The refractive index modulation was obtained opening and closing a shutter positioned in front of the lens controlling the amount of time that the fiber is exposed to laser light at a specific pulse rate. The LPG period can then be controlled by translation of the fiber and the grating strength is determined by the pulse duration and laser output power. CO_2 laser irradiation has been shown to produce LPGs with high temperature stability [156].

The continued investigation of methods for LPG fabrication that do not require photosensitization and UV-irradiation has led to the use of electric-arcs from a commercial fiber fusion splice [157]. Electric-arc fabrication of an LPG relies upon a combination of up to four effects to generate the periodic modulation of the fiber properties. The mechanisms exploited include the induction of micro-bends on the fiber [158], periodic tapering of the waveguide [153], the diffusion of dopants [159] and the relaxation of internal fiber residual stress [157]. Typically, the electrodes of a fusion-splicing machine are used, exposing to the arc a region of fiber with a length of the order of 100 μm, limiting the minimum period of LPG that can be produced. Electric currents (on the order of a few milliampere) of short duration (0.5-2 s) are used whilst applying a lightweight tension. The modulation amplitude is controlled by the electric-arc parameters. There are several advantages associated to this technique, the simplicity and cost are the most relevant in comparison with the previously exposed. Also, its flexibility since it is a point by point writing process, is applicable to a wider variety of fibers, including PCF [160] and the gratings fabricated are very stable at high temperatures. The principal disadvantages of this technique is some

lack of reproducibility and the limitation for shorter period fabrication [157]. The shortest periods reported so far, to the best of our knowledge was 345 μm and 221 μm, respectively, for LPGs written on the SMF-28 and PS1250/1500 fibers [31].

LPGs fabrication has also been demonstrated using other techniques. For instance, ion implantation through a metal amplitude mask [143], and dopant diffusion into the core of an optical fiber [161]. Other techniques based on the deformation of the structure have been also reported, such as, corrugation of the cladding [162, 163] and micro-structuring of tapered fibers [164, 165]. Long period dynamic gratings with controllable transmission characteristics can be implemented. Hollow-core optical fiber filled with a liquid crystal solution can be periodically poled by applying voltage to electrodes to create an LPG structure [166], and pressing on an optical fiber with a grooved plate is another method by which an LPG can be temporarily created [139, 167, 168]. A temporary LPG can also be created using acoustical modulation of a length of an optical fiber [169].

3.4.3 Sensitivity Characteristics of Long Period Gratings

The shape of a LPG transmission spectrum in terms of attenuation bands central wavelength, depends on the grating period, the length of the LPG and few external parameters such as temperature, strain, bend radius and SRI. Changes in these parameters modify the period of the LPG and/or the differential refractive index of the core and the m^{th} cladding mode [29]. Thereby, the phase matching condition is modified, resulting in a change in the central wavelengths of the attenuation bands. In fact, any parameter that is able to affect the difference of the effective indices of the core and cladding modes and/or the grating period, is able at the same time to affect the phase matching condition and the coupling strength. The sensitivity to a specific measurand depends on the composition of the fiber, the geometry, the order of the cladding mode to which the guided optical power is coupled, and thus, is different for each attenuation band. The combination of this factors allows the fabrication of gratings that have a range of responses to a particular measurand. A single LPG may have attenuation bands that have a positive sensitivity to a particular measurand, others that are insensitive to the measurand and others with a negative sensitivity. This characteristic makes them particularly attractive for sensor applications, with the prospect for multi-parameter sensing using a single sensor element [170]. LPGs have been used for strain, temperature and refractive index sensing, among others [30].

3.4.3.1 Axial Strain

The axial strain sensitivity of LPGs may be assessed by differentiating equation 3.6 [171];

$$\frac{d\lambda_R^m}{d\epsilon} = \frac{d\lambda_R^m}{d(n_{eff,co} - n_{eff,cl}^m)} \left(\frac{dn_{eff,co}}{d\epsilon} - \frac{dn_{eff,cl}^m}{d\epsilon} \right) + \Lambda \frac{d\lambda_R^m}{d\Lambda}, \tag{3.18}$$

where ϵ is the applied axial strain. The sensitivity arises from two mechanism, the material and the waveguide effects. The material effects are induced by the change in the dimensions of the fiber and the elasto-optic effect $\left(\frac{dn}{d\varepsilon}\right)$, and the waveguide effects arise from the slope of the dispersion term $\left(\frac{d\lambda_R^m}{d\Lambda}\right)$. For LPGs with periodicity >100 μm, the material contribution is negative, while the waveguide contribution is positive. Appropriate choice of grating period and fiber composition will thus allow the generation of attenuation bands with positive, negative or zero sensitivity to strain [171].

3.4.3.2 Temperature

In the introduction of this section, the possibility of having a grating with positive, negative or zero sensitivity for a certain measurand was exposed. This particular characteristic is very important for telecommunication applications and also for sensing, specially to avoid undesirable cross-sensitivity effects. For instance, for the fabrication of an inherently temperature insensitive refractometer. The temperature sensitivity of LPGs may be obtained by differentiating equation 3.6 [171];

$$\frac{d\lambda_R^m}{dT} = \frac{d\lambda_R^m}{d(n_{eff,co} - n_{eff,cl}^m)} \left(\frac{dn_{eff,co}}{dT} - \frac{dn_{eff,cl}^m}{dT} \right) + \Lambda \frac{d\lambda_R^m}{d\Lambda} \frac{1}{L} \frac{dL}{dT}, \tag{3.19}$$

where T is the temperature. The first term is the material contribution, and is related with the change in the differential refractive index of the core and cladding arising from the thermo-optic effect $\left(\frac{dn}{dT}\right)$. This contribution is dependent upon the composition of the fiber and is highly dependent on the order of the cladding mode. When coupling to low-order cladding modes (periods above 100 μm), the material contribution is predominant. For coupling to higher order modes (periods below 100 μm), the material effect for standard germanosilicate fibers can be negligible [171]. The second term is the waveguide contribution as it results from changes in the grating period. The magnitude and sign of the term depend upon the order of the cladding mode. When coupling to low-order cladding modes $\frac{d\lambda_R^m}{d\Lambda}$ is positive, but for higher order modes this term is negative. Therefore, choosing an appropriate grating period, it

is possible to balance the two contributions to the temperature sensitivity, thus, producing a temperature-independent LPG and also producing attenuation bands with temperature sensitivities (positive or negative) appropriate to specific applications.

3.4.3.3 Refractive Index

One of the most interesting characteristic of an LPG is its intrinsic sensitivity to the SRI. This property arises from the phase matching condition (equation 3.6), due to the dependence of the effective index of the m^{th} cladding mode upon the difference of indices between de cladding and the surrounding medium. This way the effective index of the modes propagating in the cladding will be affected by environmental changes. This dependence of the cladding mode effective index and the external medium occurs due to the presence of the evanescent field of this mode beyond the cladding-surround medium interface.

If the refractive index of the surrounding medium does not exceed the refractive index of the cladding, the LPG sensitivity to refractive index manifests itself as a change in the resonant wavelengths and in the minimum transmission value of the attenuation bands [40]. The latter effect is caused by successively smaller coupling coefficients as a result of a decrease in the overlap integral between core and cladding modes. The dependence of the LPG spectrum can be explained by the material dispersion of the core, cladding and environment refractive indices, together with the waveguide dispersion of the propagation constants, which implies that the effective indices of the core and cladding are wavelength dependent. The reduction of the coupling strength with increasing refractive index for each of the LPG resonance is attributed to the increasing expansion of the cladding mode beyond the cladding boundary (as it becomes less confined to the cladding material), thus decreasing the coupling coefficient. Figure 3.14 illustrates the behavior of an LPG 7^{th} order resonance to changes in the SRI in terms of wavelength and depth of the attenuation band.

The refractive index sensitivity of LPGs can be assessed by differentiating equation 3.6 ;

$$\frac{d\lambda_R^m}{dn_{ext}} = \frac{d\lambda_R^m}{dn_{eff,cl}^m}\left(\frac{dn_{eff,cl}^m}{dn_{ext}}\right), \tag{3.20}$$

where n_{ext} is the SRI. The previous equation assumes that the fundamental core mode is well confined to the fiber core and is not affected by changes in the SRI; the period of the grating remains unaltered under the effect of the SRI. The situation described above (equation3.20) is for the case where the SRI is lower than the cladding index.

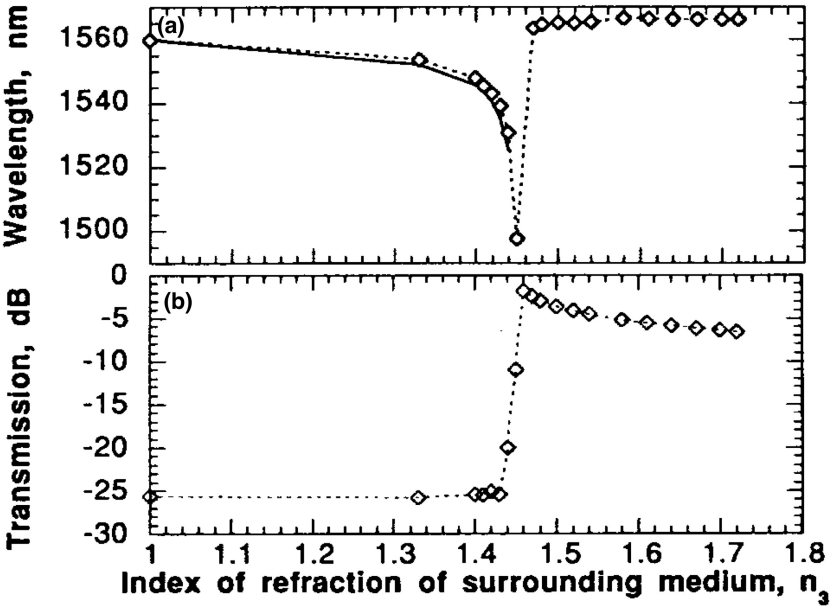

Figure 3.14: Measured wavelength for 7^{th} order resonance of an LPG with a period $\Lambda = 275$ as a function of SRI (open diamonds with dashed line) (a). Attenuation of the band (open diamonds with dashed line) as a function of SRI (b) [40].

However, there are two additional situations that may occur: SRI equal or higher than that of the cladding index. When the surrounding index is equal to that of the cladding, the cladding appears to be of infinite extent and thus supports no discrete modes, the cladding modes are converted into radiation modes as a result of the lack of total internal reflection at the cladding boundary. In such case, the attenuation bands are not observed [26, 40]. For surrounding refractive indices higher than that of the cladding, the resonant wavelengths show a considerably reduced sensitivity, but a change in the shape of the transmission spectrum is observed, in that the depth of the attenuation bands is reduced [49], as is illustrated in Figure 3.14. The presence of the attenuation bands in this situation, where the cladding is no longer acting as a waveguide, is due to the existence of attenuated cladding modes arising from Fresnel reflection, rather than total internal reflection from the cladding/external medium interface [26, 40, 49].

The sensitivity characteristic of a resonance of a LPG to the SRI changes has an increasing (in modulus) non-linear monotone trend. The result is that the maximum sensitivity is achieved when the external index is close to the cladding index while for lower refractive indices (around 1.33) the LPG is scarcely sensitive (this can be observed in Figure 3.14). This can be explained by the extension of the evanescent field which increases as the SRI approaches the cladding index. Therefore, the pen-

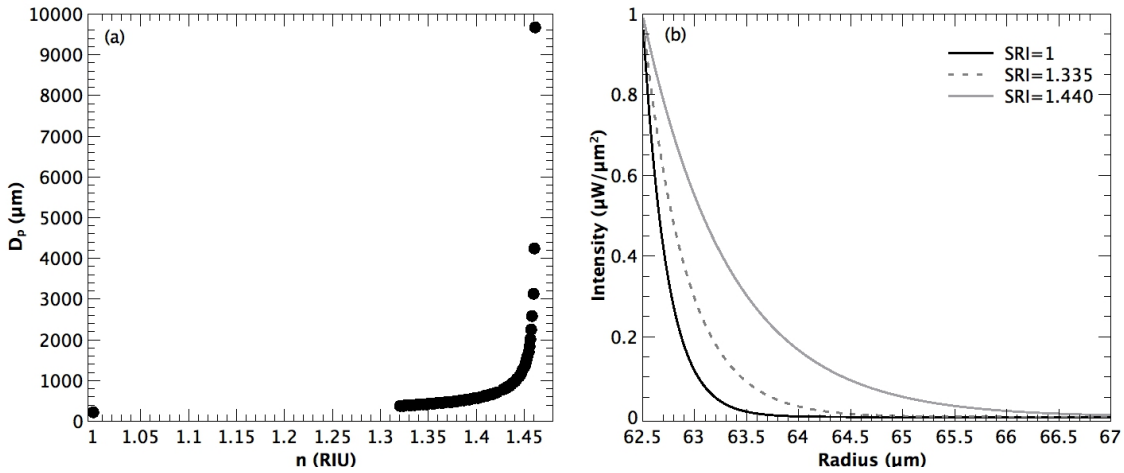

Figure 3.15: Calculated penetration depth (d_p) for a 7^{th} order mode resonance at 1550 nm as a function of the external index (a). Representation of the evanescent field (same parameters as before) for three different SRI (b). The following values were used in the analysis: n_{co}=1.4676, n_{cl}=1.4625, a_{co}=3.6 µm, a_{cl}=62.5 µm.

etration depth of the field also increases and, consequently, greater is the fraction of power of the mode in contact with the external environment. Figure 3.15 illustrates the previous reasoning. In (a) is shown the calculated penetration depth (d_p) for a 7^{th} order mode resonance at 1550 nm as a function of the SRI, and in (b) the plotted evanescent field for three different external indices. Appears evident that the higher the external index, more intense becomes the penetration of the evanescent field on the external medium.

As it was mentioned before, generally, in a LPG spectrum, a series of attenuation bands are observed. Each resonance, corresponds to a specific cladding mode, where longer wavelengths correspond to higher order modes. High order modes are less bound to the waveguide structure formed by the fiber itself, extending further into the external medium and, hence, they are more sensitive to the SRI, and obviously these are the most desirable for sensing purposes. An increase in the order of the coupled cladding mode can be attained by decreasing the grating period. It is worth to say, that, the evanescent field depends strongly on the wavelength, and longer resonance wavelengths result in a higher evanescent field interaction, yielding higher sensitivities. Figure 3.16 (a) shows the calculated center wavelength of the attenuation bands corresponding to the modes $LP_{0,6-9}$, resulting from four different grating periods. Λ was chosen in order to have a resonance (for $n_{ext} = 1$) around 1580 nm. In (b) $\frac{\Delta\lambda}{\Delta n}$ was obtained from the data of the previous plot. It can be seen that overall, sensitivity is much higher when the SRI approaches the cladding index. Considering

a particular case, theoretically, it can be seen that, for the $LP_{0,9}$ mode a sensitivity of 30000 nm/RIU can be achieved when the SRI is close to the cladding index. Also, it is apparent that higher order modes exhibit somewhat higher sensitivity than lower order modes.

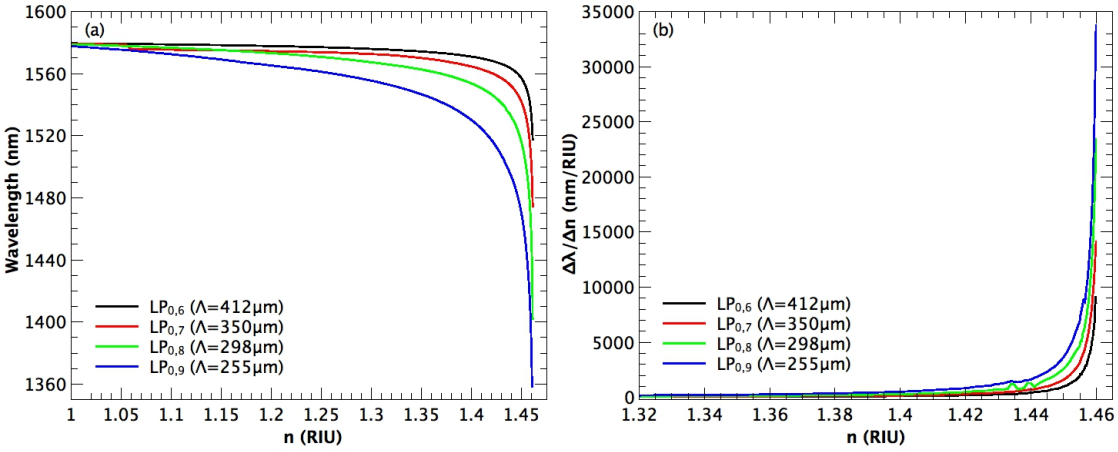

Figure 3.16: Calculated resonance wavelength shift for a variation o SRI from 1 to 1.46 for different modes orders ($LP_{0,6-9}$) (a). The Λ was chosen in order to have a resonance (for $n_{ext} = 1$) around 1580 nm, $\frac{\Delta\lambda}{\Delta n}$ obtained from the data of the previous plot (b). The following values were used in the analysis: n_{co}=1.4676, n_{cl}=1.4625, induced core index change=3×10^{-4}, a_{co}=3.6 μm, a_{cl}=62.5 μm.

The sensitivity for each mode depends on the slope of the phase matching curve, the larger the slope, the greater the sensitivity. Thus, small changes in the phase matching condition can imply huge changes in the resonant wavelength. It is for this reason that the higher order modes are more sensitive, because its slope is higher. Since the slope of each dispersion curve achieves its maximum in the turn-around-point $\left(\left|\frac{\Delta\lambda}{\Delta n}\right| \to \infty\right)$, the highest sensitivity for each mode is reached for the period that satisfies the phase condition at the wavelength where the turning point occurs. Figure 3.17 shows the phase matching curves for the cladding modes 1-10 (a) and 11-20 (b) for a B-Ge co-doped fiber. The small circles indicates the turn-around-point for each mode. The region bounded by the two dotted lines was defined by Shu *et al.* [30] as the greatest sensitivity region, which matches exactly with the region of maximum slope of each curve. It should be noted that, as exposed in the theory, the turn-around-point occurs at longer wavelengths for lower order modes, and at shorter wavelengths as the mode order increases. Generally, an LPG can be designed to exhibit very high sensitivity for a particular wavelength by selecting a cladding mode and period at, or very close to, a turn-around-point.

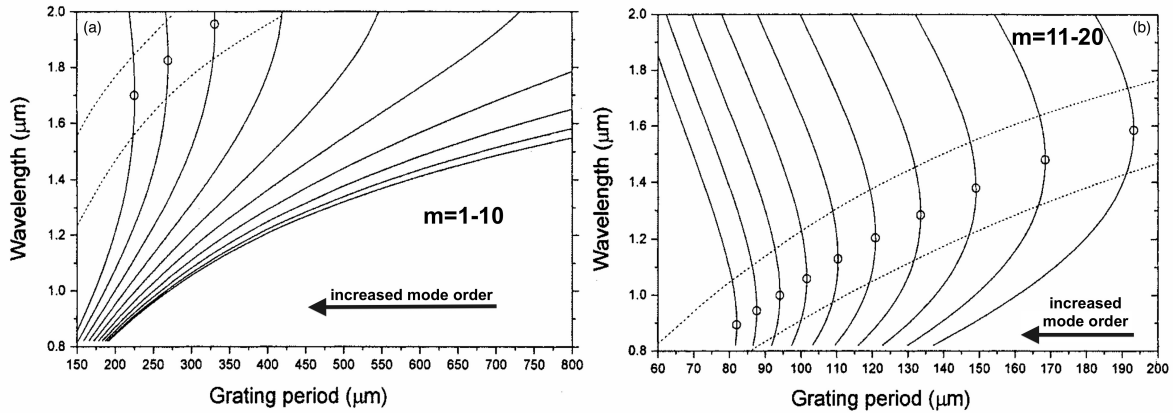

Figure 3.17: Calculated variation of the λ_R with the grating period (Λ) for a B-Ge co-doped fiber. Modes m=1-10 (a), modes m=11-20 (b). The small circles locates the turn-around-point for each mode. The region between the two dotted lines is defined by the author as the greatest sensitivity region [30].

Considering practical application, it is worth looking into a restricted wavelength range, around 1550 nm, which is the third telecom window and, hence, is easier to work with, due to the availability and lower cost of the light sources and other fiber optic devices. Additionally, working in this range, also allows easier integration within fiber optic networks, facilitating multiplexing and remote sensing applications. Shu *et al.* [30] experimentally evaluated the sensitivity to the SRI of a set of LPGs with small, medium, and large periods aimed to generate resonances at wavelengths in this range. The authors used B–Ge co-doped fiber and the range of RI evaluated was between 1-1.36 RIU. Figure 3.18 plots the sensitivity to the SRI as a function of the coupled mode order. As expected, resonances resulting from the coupling of high order modes ($m > 9$) present higher sensitivity, with a maximum value of ∼1481 nm/RIU, shown for $m = 11$, which, according with Figure 3.17(b) corresponds to a resonance near the turning point. It is noticeable, the switch from negative to positive of the sensitivity coefficient (for $m > 12$), meaning that, henceforward resonances coupled at 1550 nm occur above the turn-around-point.

Concerning the influence of the fiber geometry, Chiang *et al.* [172] have found that the sensitivity may be significantly enhanced by reducing the cladding radius (a_{cl}) since its is inversely proportional to the cladding radius cubed $\left(\frac{\Delta\lambda}{\Delta n} \propto a_{cl}^{-3}\right)$. This relation has been verified experimentally by measurement of the response of etched LPGs. Reducing the cladding radius of a LPG allows also to tune the spectral position of the attenuation bands toward higher wavelengths. However, both effects depend on the fact that thinning the fiber cladding reduces the effective refractive

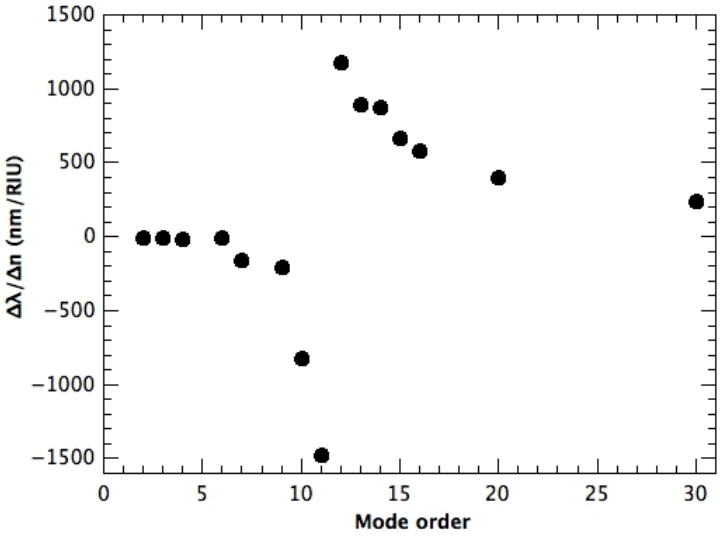

Figure 3.18: Experimentally measured values for $\frac{\Delta\lambda_R}{\Delta n}$ plotted against the mode order for resonances close to 1550 nm, in the range of refractive index between 1-1.36 RIU [30].

index of the cladding modes and consequently the resonance wavelengths increase as well as the cladding mode evanescent field interaction with the surrounding medium. Nevertheless, this technique physically weakens the fiber structure hindering its handling.

Until now, regarding the analysis of the refractive index sensitivity of an LPG, three situations were considered; when the external index is lower than the cladding index and when the external index is equal or higher than the cladding index. In all these cases, it is assumed that the bare fiber is surrounded by a medium of infinite thickness. However, if a thin overlay of higher refractive index than the cladding is deposited between the cladding and the surrounding medium of infinite thickness, the cladding modes are confined within the fiber structure, the cladding and coating included. Depending on the characteristics of the overlay and the SRI, this will lead to huge changes in the propagation conditions of the cladding modes, and therefore, in the phase matching condition and consequently, it will have a great impact in the sensitivity to the external index of the coated device. HRI Coated LPGs were firstly proposed by Rees *et al.* [32] and since then, several authors have explored its use for LPG RI sensitivity enhancement [33–37] and for chemical sensing applications [38, 39]. In the following section the principles of HRI coated gratings are exposed.

3.4.4 High Refractive Index coated Long Period Gratings

The use of HRI overlays in fiber optic refractometers based on evanescent wave was explored initially by Schroeder *et al.* [9] for a polished FBG. The deposition of a HRI layer onto an LPG leads to a decrease of the cladding mode power bounded within the core and cladding, while a small fraction of the optical power carried by the cladding mode moves towards the overlay, enhancing the evanescent field in the surrounding medium and increasing the cladding mode effective index. This important modification of the cladding mode distribution is determined by the optical thickness of the layer (nTh) and the SRI . Consequently, there is an increased sensitivity of the coated device, in terms of wavelength shift and amplitude variations of the resonances in response to changes of the above mentioned parameters [173, 174]. Figure 3.19(a) illustrates the increase of the field energy contained within the overlay as the overlay thickness is increased, as well the enhancement of the evanescent field reaching the outer medium. Also 3.19(b) shows in more detail for a overlay thickness of 250 nm, the field content within the overlay for two distinct order modes [175]. In summary, the presence of the HRI overlay increases the extension of the evanescent field of the modes in the surrounding medium making them more sensitive to the SRI changes compared with the bare device.

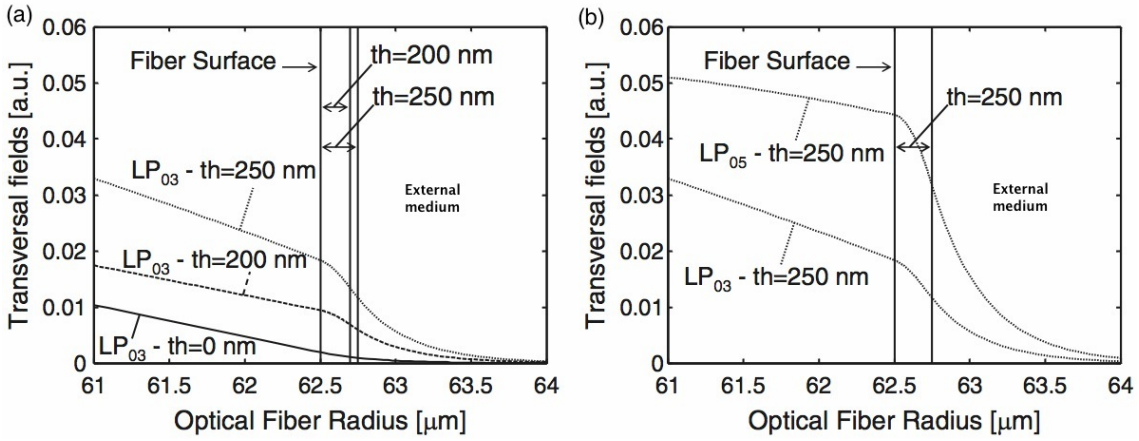

Figure 3.19: $LP_{0,3}$ cladding mode in the bare fiber and in coated fibers with overlays coatings of 200 nm and 250 nm (a). $LP_{0,3}$ and $LP_{0,5}$ cladding modes in a coated fiber with thicknesses of 250 nm (b). The following values were used in the analysis: n_{co}=1.5362, n_{cl}=1.5306, a_{co}=4.15 μm, a_{cl}=62.5 μm, n_{ext}=1.33, $n_{overlay}$=1.578, considering a wavelength of 1310 nm [175].

As the thickness of the layer is increased, the HRI overlay acquires the ability to guide one of the cladding modes and thus the coating acts itself as a waveguide.

When the coating thickness approaches this condition, the optical power in the overlay reaches its maximum and so does the evanescent wave, providing a stronger interaction with the surrounding environment. At this thickness, due to the maximized evanescent field, a higher sensitivity to SRI variations is achieved compared to other overlay thicknesses. In this situation, a reorganization of the effective indices of the cladding modes occurs, and the lowest order cladding mode (cladding mode with highest effective refractive index) becomes guided into the overlay. This phenomenon is the so called modal transition [174]. This technique allows to increase the sensitivity to the external index for a specific application (index range), by proper selection of the optical thickness of the overlay [173].

The resonance wavelength shift is maximum when the effective index of the mode is half way between its original effective refractive index (before deposition) and the original effective refractive index (before deposition) of the next lower cladding mode. Consequently, there is an optimum HRI overlay thickness which results in the highest sensitivity. This value strongly depends on the refractive index of the coating and on the external index. These parameters define the amount of material necessary and the sensitivity to the SRI. On the other hand, an optimum thickness value can be calculated for the middle value of the SRI range where the refractometer will operate [173]. In this way, it is possible to design highly sensitive refractometers for lower refractive index ranges, where bare LPGs are scarcely sensitive.

If a HRI overlay is deposited on the LPG, the effective refractive index of the cladding modes shifts to higher values if the thickness of the layer increases. The cladding mode is mostly guided by the layer when the thickness is above some threshold. It is exactly the lowest order cladding mode that jumps to the overlay, which means that the highest effective index mode becomes guided by the overlay. As a result, a reorganization of the effective index of the other modes occurs. Higher order cladding modes than the one that is guided by the layer will shift their effective index value towards the effective index of the immediate lower order cladding mode. As the thickness increases, the effective index distribution before deposition is recovered. The same occurs for the resonance wavelength values. The phenomenon repeats with the increment of the thickness. This means that if the thickness continues to be increased, the number of modes guided in the overlay also increases and new reorganizations of cladding modes take place. In Figure 3.20 , the effective index of the core mode and of the first ten cladding modes are represented as function of the overlay thickness, for a fixed wavelength of 1200 nm. It can be observed that $LP_{0,2}$, $LP_{0,3}$,

$LP_{0,4}$, $LP_{0,5}$, become guided by the layer for thicknesses of 300, 1200, 2100 and 3000 nm, respectively [173].

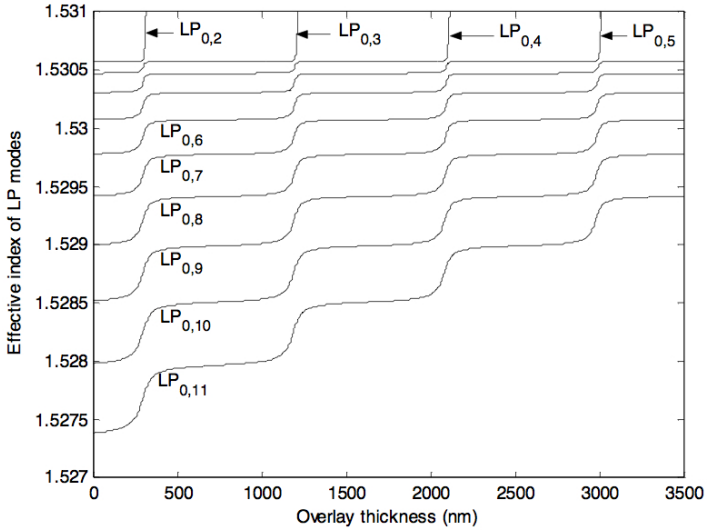

Figure 3.20: Effective index as a function of the overlay thickness for the first ten cladding modes considering a fixed wavelength (1200 nm). The following values were used in the analysis: n_{co}=1.5362, n_{cl}=1.5306, a_{co}=4.15 μm, a_{cl}=62.5 μm, $n_{overlay}$=1.67 [173].

Likewise, for a fixed overlay thickness, there is a value of the SRI that leads the lowest order cladding mode (higher effective index) to become guided by the overlay. This modal transition is characterized by an effective index of the involved mode higher than the cladding index. As the lowest order cladding mode moves to be guided within the overlay, a reorganization of the other cladding modes occurs. The immediate consequence is a simultaneous shift in the effective index of all the cladding modes to recover the original distribution. As a matter of fact, the effective index of the m^{th} mode shifts to match the initial index of the $(m-1)^{th}$ mode, and so forth. Furthermore, since the effective refractive index difference between consecutive cladding modes increases with the mode order, the higher the mode order, the greater the effective index change [36, 174]. Figures 3.21 (a) and (b) show the effective indices of the first seven cladding modes ($LP_{0,2-8}$) as a function of the SRI for coated LPG with $n_{overlay}$ of 1.578 and thicknesses of 150 nm and 250 nm, respectively [175]. For (a) it is clear that the effective indices increase along with the SRI until a critical point is reached. At this point, a significant shift in the effective indices of the cladding modes occurs. Looking to both results (Figure 3.21), it is notorious that the transition region moves to lower indices as the overlay thickness increases, approaching the refractive index of 1.33 where bare LPGs usually demonstrate a significant lower sensitivity.

As a collateral effect, the SRI sensitivity becomes smaller as the overlay thickness increases. However, even if the absolute sensitivity decreases, the relative sensitivity in comparison to the bare device is still higher. Again, a fundamental feature of this mechanism is the possibility to tune the transition region in the desired SRI range by acting on the overlay thickness.

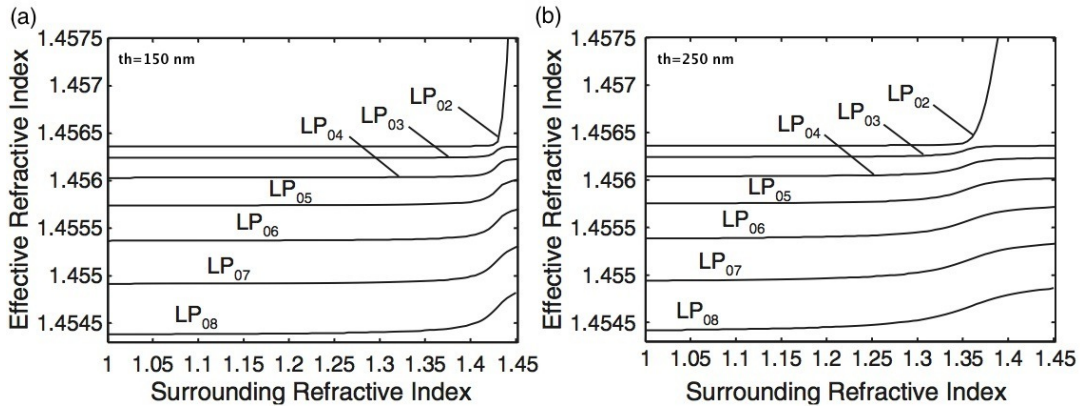

Figure 3.21: Effective index of the first seven cladding modes ($LP_{0,2-8}$) as a function of the SRI, considering a fixed wavelength (1310 nm) for a layer with $n_{overlay}$=1.578 and thicknesses of 150 nm (a) and 250 nm (b) . The following values were used in the analysis: n_{co}=1.5362, n_{cl}=1.5306, d_{co}=8.3 μm, d_{cl}=125 μm, n_{ext}=1.33, considering a wavelength of 1310 nm [175].

Another effect observed in the modal transition is the decreasing of the coupling coefficient, and thus, a decrease of the resonance depth (expected according with equation 3.17). It is due to the fact that during the modal transition the transverse field profile of the cladding modes is stretched towards the HRI overlay and this causes a reduction of the overlap integral between cladding and core modes. When the first cladding mode becomes guided into the overlay, in correspondence of the transition point, its coupling coefficient vanishes rapidly. At the same point, the coupling coefficients of the higher order cladding modes shift to quasi recover the original configuration of the coupling coefficients. This process is repeated for each transition. It is important to emphasize that, the lower the mode order, the bigger the coupling coefficient change. This is clearly expected since the lowest order cladding modes are the first to experience the modal transition.

The resonance wavelengths are strongly related to the HRI layer refractive index through the effective index. Figure 3.22 shows that the sensitivity of the mode effective index to changes in the overlay refractive index, varies as function of the layer thickness for the different modes, considering a fixed external index around the water

index. It can be concluded that for a fixed mode, a great sensitivity improvement can be achieved by increasing the coating thickness until the transition region is approached. At the transition, the sensitivity of the lowest order mode dramatically increases, because it becomes guided within the overlay. Nevertheless, this sensitivity cannot be exploited because the lowest order mode transition also leads to the vanishing of its related resonance, as it was referred in the above discussion about the coupling coefficients analysis. For other modes, the sensitivity increases with the increased overlay thickness, reaching a maximum value similar for each mode at the same layer thickness. For the example illustrated in Figure 3.22, the highest sensitivity to overlay refractive index changes occurs for an overlay thickness of 265 nm in match with the mode transition, likewise to what happens concerning to the sensitivity to SRI changes, where a strong field enhancement within the overlay occurs [175]. However, this is valid only because the analysis is done at a fixed wavelength. If each cladding mode is considered at a wavelength at which it is coupled, it would be concluded that, the higher the cladding mode order, the higher the sensitivity. Further, the thickness corresponding to the highest sensitivity would be slightly higher for higher order cladding modes. This is mainly a consequence of the fact that the higher order cladding modes are coupled at higher wavelengths.

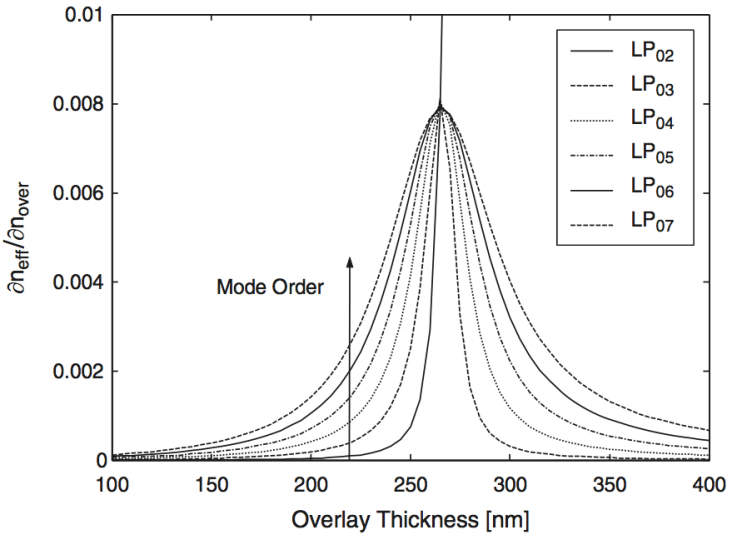

Figure 3.22: Sensitivity of the effective refractive index to changes in the overlay RI, for the first six cladding modes ($LP_{0,2-7}$) as a function of the overlay thickness for different cladding modes with water as a surrounding medium. The following values were used in the analysis: n_{co}=1.5362, n_{cl}=1.5306, a_{co}=4.15 μm, a_{cl}=62.5 μm, n_{ext}=1.33, $n_{overlay}$=1.578, considering a fixed wavelength of 1310 nm [175].

Experimentally, Cusano et al [35, 36, 69, 174, 176] have been studying the phe-

nomena of the mode transition, its impact in the external index sensitivity and its dependence on the thickness and SRI. LPGs coated with syndiotactic polystyrene (sPS), whose refractive index is 1.57, were analyzed. An analytical form was proposed to model the transition curves. The Lorentzian-Cumulative function was found to be the best fit of the experimentally determined transition curves [36, 176]. This model allowed to estimate a series of key parameters that play an important role in the final sensing properties of the coated devices, such as the maximum sensitivity, the transition index (SRI at maximum sensitivity) and the bandwidth (SRI range evaluated at half maximum sensitivity). All these parameters are strongly dependent on the overlay thickness and the mode order. Figure 3.23 shows the sensitivity characteristics of the $LP_{0,8}$ cladding mode for three different values of the coating thickness: 140, 180, and 215 nm [175]. It seems clear how the sensitivity characteristics can be tailored for refractive indices in different ranges by varying the coating thickness. Hence, by increasing the overlay thickness, the transition value of the SRI moves toward lower values, and thus the maximum sensitivity can be located in the desired SRI range. It is worth noting that, although the maximum sensitivity decreases for thicker overlays, the sensitivity gain with respect to the bare device increases.

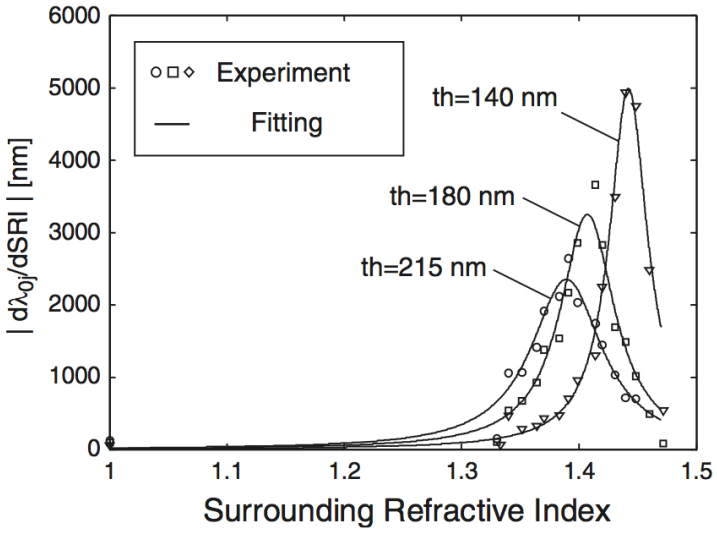

Figure 3.23: Sensitivity characteristics of the mode $LP_{0,8}$ for different overlay thickness values. The following values were used in the analysis: n_{co}=1.5362, n_{cl}=1.5306, a_{co}=4.15 μm, a_{cl}=62.5 μm, $n_{overlay}$=1.67 [175].

An important niche of possibilities for HRI coated LPGs is in the biological and chemical sensors fields, where the demand of a set of tools for real-time and remote measurement with high accuracy, are essential to proper operation of a diversity of

complex systems ranging from industrial processes, environment among others. If the optimal overlay design (nTh, SRI) is estimated for a material whose refractive index changes with some parameter, for instance a chemical or biological target, it is possible to have highly sensitive biosensing devices [36, 37, 39, 72, 177].

3.5 Conclusion

The discovery of photosensitivity of optical fibers, that brought the possibility of writing periodic structures on its core, signified an important advance in fiber optic technology for communications and later for sensing. From that moment on, the scientific research in this area shows a huge development, resulting in diversity of fabrication techniques and different grating structures. Fiber gratings were successfully fabricated in spectral regions of interest for fiber optic communications, for filtering and sensing, raising the general interest towards the practical applications of fiber periodic structures. Specially in the sensing field due to the intrinsically sensitivity of those devices to external parameters. This sensitivity comes from own dependency of the silica matrix and the waveguide itself to these parameters. Fiber gratings can be classified as FBGs and LPGs.

FBG sensors are a well-known case of success in optical fiber sensors, above all things due to their applications in structural health monitoring, based on their strain and temperature sensitivity. FBG based solutions are currently present in the market in areas such as structural engineering, energy, aerospace, among others. Bragg gratings have all the advantages associated to the fiber optic sensors, additionally FBG technology provide an absolute measurements without the need for referencing, reflection operation, narrowband spectral response and compatibility with standard telecom technology, all together reveals an inherent serial multiplexing capability, which is particularly important in the context of remote, multi-point and multi-parameter sensing.

Bragg gratings works mainly with radiation confined to the fiber core, this way strategies have to be devised in order for the radiation to interact with the external medium. Typically, FBG based refractometers rely on the evanescent field of the core mode under fiber etching conditions, where the sensitivity of the etched devices depends highly in the fiber diameter and highest sensitivities correspond to smallest fiber diameters. Nevertheless, the etching process introduces fragility in the fiber sensor, that is greater as high sensitivity is needed.

TFBG do not require etching, therefore, maintain the fiber integrity. A TFBG couples the core mode to a large number of cladding modes large spectral range. The most sensitive to the SRI are, obviously the high order modes, which appear at shorter wavelengths and far from the Bragg resonance. This issue implies the use of a broader spectral range, that renders difficulty for signal readout and multiplexing. Finally, the cladding modes of simple FBGs are still a field to explore. It enables the possibility of readout in reflection the core and the selected cladding mode, potentially enabling a temperature self-referenced SRI measurement. Work still have to be done in the field to improve mode engineering. Nowadays, all-grating devices are very promising in this area, since they provide control of the mode excitation and the power transferred. It should be pointed that probably the sensitivity is the drawback of FBG based refractometers. Nonetheless, narrower resonant bands presented by the FBGs, for instance, in comparison with LPG or SPR, provide a more accurate detection of the peak, thus, compensating and allowing for detection limits quite acceptable.

LPGs, on the other hand, are one of the most popular fiber optic devices that have been widely used for optical communications and sensing. Specially for chemical and biological sensing due its intrinsic sensitivity to the external index. It is a diffraction structure, where the refractive index of the fiber core is modulated. This periodic perturbation satisfies the phase matching condition between the fundamental core mode and a forward propagating cladding mode of an optical fiber. Thereby, in an LPG, the core mode couples into the cladding modes of the fiber, resulting in several attenuation bands centered at discrete wavelengths in the transmitted spectrum, where each attenuation band corresponds to the coupling to a different cladding mode. The period of modulation ranges between 100-600 μm, and it can be induced in the optical fiber using different techniques. One of the reasons for its popularity is that it can be fabricated by several ways, some of them relatively low cost. Point-to-point techniques are the most widespread and interesting due its flexibility permitting to fabricate gratings with specific characteristics.

Through the period, the modulation index and length it is possible to control a set of parameters with huge impact in the performance of this photonic device such as: the excited cladding mode, the amount of power transferred, the resonance wavelength and bandwidth. On the other hand, changes in external parameters such as temperature, strain and refractive index will imply variations of the transmitted spectrum. Hence, any parameter able to modify the period of the LPG and/or the differential refractive index of the core and the m^{th} cladding mode will lead a change

in the phase matching condition and consequently in the resonant wavelength/depth. The sensitivity to a specific measurand depends on the composition of the fiber, the geometry, the order of the excited cladding mode and thus, is different for each attenuation band.

Concerning the sensitivity of the LPGs to the SRI, it is higher for shorter periods, which excite high order cladding modes. The greatest sensitivity corresponds to resonances close to the turn-around-point. The maximum sensitivity of a certain resonance occurs at refractive indices approaching that of the cladding. This behavior changes when a thin layer of few hundreds of nanometers and with higher refractive index than the cladding is deposited on the LPG. The presence of HRI overlays allows to increase the sensitivity of the gratings, through enhancement of the evanescent field; and also to tune the maximum sensitivity to a desirable range of RI, by playing with the thickness and the refractive index of the material. This technique opens a niche opportunities within the biochemical sensors, where the HRI overlay itself can be functionalized in order to respond to a certain parameter of interest constituting a probe with very high sensitivity and specificity.

Chapter 4

Fiber Bragg Gratings Based Sensors

Summary

Fiber Bragg grating sensors have generated great interest in recent years because of their many industrial and structural health monitoring applications. Based on diffraction mechanism, the fiber grating can be used as fiber mirror or in-fiber filter for fiber optic sensing or communications. Bragg grating sensors have been widely used and commercialized for strain and temperature measurement. In this chapter, experimental work carried out during the PhD will be presented addressing topics such as: FBG based Fabry-Perot cavities for refractive index sensing and FBG cladding modes for multi-parameter sensing.

4.1 High-Birefringence FBG based Fabry-Perot Cavity for Refractive Index Sensing

The refractive index measurement in is an important issue for medical, chemical and biological applications. Fiber optic sensors are an interesting solution for this issue due to their high sensitivity, small size, and capability for on-site, real-time, remote, and distributed sensing. In this context, FBG sensors have generated great interests in recent years because of their many industrial and environmental applications. Several refractometers based in Bragg gratings have been studied, where the core was exposed by etching the fiber cladding [4, 21] or by side-polishing [9] in the grating region.

Alternative techniques using TFBGs were also presented [15, 16]. All these sensing schemes are based on evanescent interaction. Nevertheless, etched or polished FBGs introduces fragility in the fiber sensor. TFBGs, on the other hand, do not require etching, therefore, maintain the fiber integrity. However, it uses a broader spectral range, that renders difficulty for signal readout and multiplexing.

In this work, a fiber optic sensor for simultaneous measurement of refractive index and temperature is described. The refractive index measurement is based on the visibility variations of a Fabry-Perot interferometer. It is formed with the interfering waves generated from a low reflectivity Bragg grating inscribed on a Panda fiber and from the fiber end tip (Fresnel reflection) in contact with the liquid. The sensor is characterized by immersing the fiber tip in distilled water with different concentrations of ethylene glycol. A linear relation of the interferometer fringe visibility with refractive index variation is observed. The temperature is determined by the wavelength shift of the FBG peaks. Results show the feasibility of simultaneous measurement of refractive index and temperature and also the possibility of adjusting fringe visibility via polarization control.

4.1.1 High-Birefringence FBG

In axially symmetric SMF, there are two orthogonally polarized modes (HE_{11}^x, HE_{11}^y), according with their polarization directions. If the fiber structure is indeed axially symmetric, these orthogonally polarized modes have the same propagation constants ($\beta_x = \beta_y$). This is why the fiber is called singlemode. However, in practice, standard fibers presents an axial non-symmetry induced by the core deformation and/or core eccentricity to the outer diameter, and it causes a slight difference in the propagation constants between both polarization modes. In such fibers, the state of polarization of the output radiation randomly varies, since the mode coupling takes place between both modes, which are caused by fluctuations in core diameter along the z-direction, vibration and temperature variations. Hence, these fibers cannot be used in coherent optical communications [178].

High-Birefringence (HiBi) fibers are special fibers used in telecommunication networks to avoid uncontrolled changes in the polarization of the light. The difference of the propagation constants between HE_{11}^x and HE_{11}^y modes are intentionally made large in HiBi fibers. Birefringent fibers are also called polarization-maintaining fibers (PMF). The birefringence implies different values of the propagation constants (β_x,β_y) of the two orthogonally polarized modes HE_{11}^x and HE_{11}^y. These linear polarization modes are the slow and fast modes, associated with the main axis of the fiber. The

birefringence is introduced in the fabrication process through geometrical or stress induced effects. The geometrical effect is easily obtained when the core is non-circular, for example, the elliptical core fiber. The stress effect can be obtained by applying mechanical tension around the core, as occurs in the case of Panda or bow-tie fibers [178]. In Figure 4.1 the Panda fiber profile is shown, where two stress rods are observable around the core.

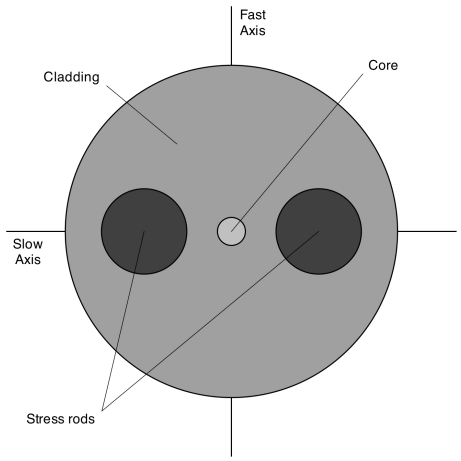

Figure 4.1: Schematic profile of a Panda HiBi fiber.

Due to their special characteristics some studies have been published in sensing area, mostly of interferometric nature based on the interfering waves of both polarization modes. The majority of these works aimed to measure physical parameters. [179]. Bragg gratings have been written in HiBi fibers [180]. Since a HiBi fiber has different propagation constants for the slow and fast axes, an FBG written in a PMF has two distinct Bragg reflection wavelengths corresponding to the fast and slow axis. Each reflected Bragg wavelength has also different response on temperature, strain and on others parameters depending on the geometry or composition of the stress rods [181]. By using this property it is possible to have multi-parameter sensing with a single HiBi FBG through the wavelengths of the reflected peaks. Figure 4.2 shows the spectrum of an FBG written on a Panda fiber. It is possible to observe the two reflected peaks corresponding to both orthogonal polarization modes. The separation between the peaks is given by the birefringence of the fiber. HiBi FBGs have been employed for simultaneous measurements of temperature and strain [180, 181], temperature and external index [182] and also for the determination of transverse strain [183, 184].

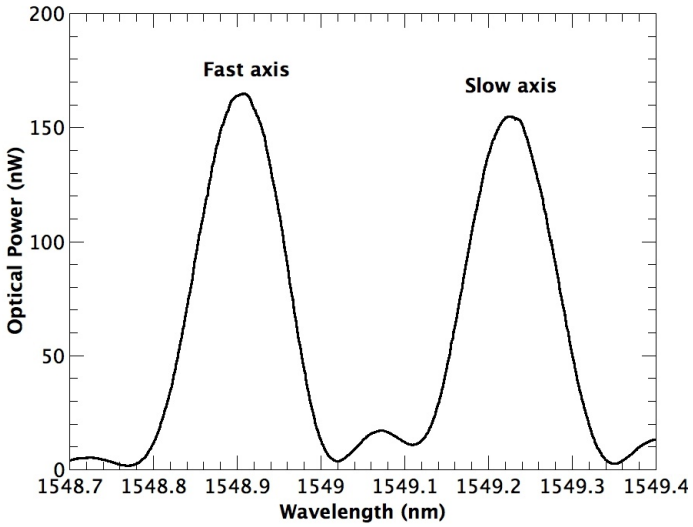

Figure 4.2: Spectrum of a FBG written on a Panda HiBi fiber.

4.1.2 Sensing Head

The scheme of the sensing head developed is shown in Figure 4.3(a). The sensitive system is formed by a low-reflectivity HiBi FBG structure (R $\approx$ 4%, 6 mm in length) located 40 mm away from the end tip of the fiber. The grating has been written in HiBi Panda fiber (PM1550-HP) by UV beam scanning phase mask technique. An FBG written on a Panda fiber originates two reflection peaks at slightly different wavelengths. These arise from the fact that the birefringence fiber presents a fast and slow axis, where the two orthogonal polarization modes experience slightly different refractive indices [181]. In order to obtain a 4% Fresnel reflection at the tip, the fiber was cleaved, perpendicular to the direction of light propagation using a standard fiber cleaver. In this situation, a low finesse Fabry–Perot cavity was formed between the fiber end and the low-reflectivity FBG.

With the proposed configuration, the refractive index surrounding the fiber tip changes the reflectivity at the fiber tip interface and can, therefore, be retrieved from the visibility of the channeled spectrum. The visibility (V) of the fringes can be obtained by calculating $V = \frac{P_P - P_V}{P_P + P_V}$, where P_P is the optical power of a peak and P_V is the optical power of a valley of the interferometric pattern. The visibility measurements are self-referenced intensity measurements and therefore independent of power fluctuations. On the other hand, the FBG peaks shift in wavelength according with temperature [7]. Therefore, tracking the envelope of the peaks it is possible to obtain the temperature value. Since the visibility depends only on the Fresnel reflection at the fiber - external medium interface, changes in this parameter are practically

independent from temperature. Additionally, the spectral shift of the envelope is independent of the external refractive index. In this way, the two parameters can be obtained from independent measurements.

Figure 4.3(b) shows the spectra of the HiBi FBG before and after the cavity is built (interference arises only after a good quality cleave is performed at the fiber tip). Analysis of the spectral output revealed two peaks, corresponding to the slow and fast axis, separated by 320 pm, each with a FWHM of 120 pm. In air, the fringes visibility was approximately 40% with a spectral periodicity of 20 pm.

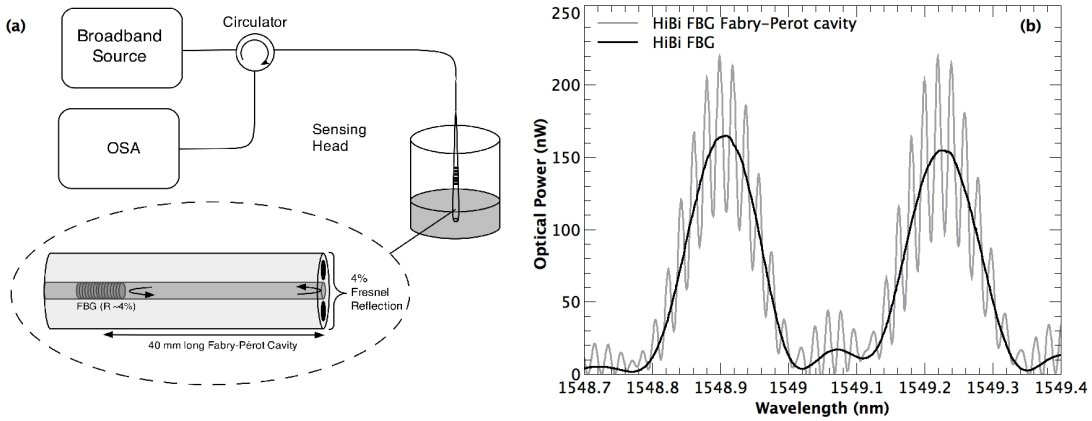

Figure 4.3: Experimental setup (a) and spectra of the HiBi FBG before and after the cavity is built (b).

Characterization of the sensing probe properties was done using a simple setup where an erbium-doped fiber source illuminated the sensor through an optical circulator which enabled the reflected Fabry–Pérot signal to be observed using an Advantest Q8384 optical spectrum analyzer with a maximum wavelength resolution of 10 pm. For calibration, the sensing head was immersed in samples of water mixed with different percentages of ethylene glycol at a constant temperature (20℃) to provide RI standards. The liquid samples were previously characterized by an Abbe refractometer using the sodium D line (589 nm). The necessary adjustments, considering the sensing head operation at 1550 nm, were made using the Cauchy equation with the respective coefficients [185, 186].

4.1.3 Results and Discussion

The polarization effect was studied before characterization of the sensing head. For this purpose, a fiber optic polarizer and a polarization controller were inserted between the optical source and the sensing head. Polarizing the light along the birefringence

axis of the fiber allows the control over the power input into each resonance being even possible to cancel one of them. This technique enables the optimization of the visibility of each peak and consequently may be used to tune the refractive index sensitivity. Figure 4.4(a) shows the channeled spectra for different polarization angles and the corresponding visibility changes can be observed in Figure 4.4(b). It is clear that it is possible to improve the visibility and even practically cancel the peak corresponding to each axis. It is observable that the fast axis peak is more sensitive to the polarization than the slow one. In this case the visibility can be improved by a 40% factor as compared to depolarized illumination.

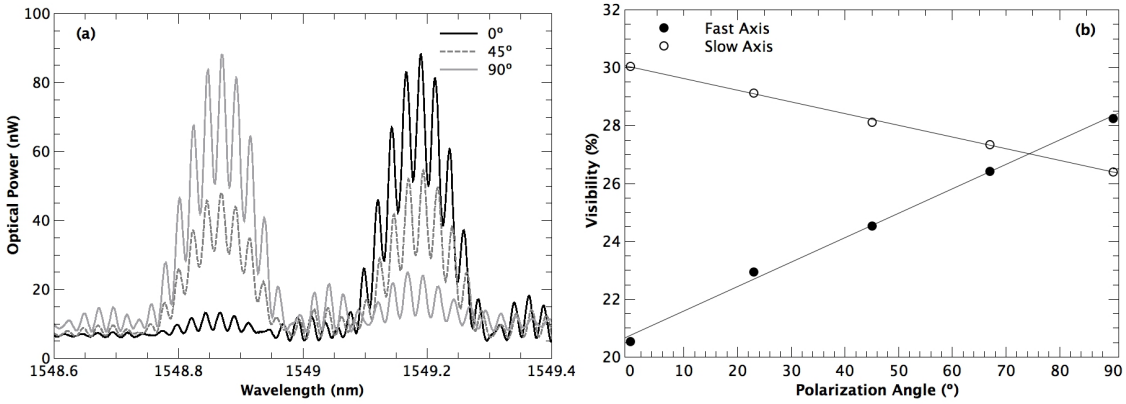

Figure 4.4: Polarization effects in the visibility of the cavity. (a) channeled spectra for three different polarization angles and (b) visibility as a function of the polarization angle.

Introducing the sensing head in the solution resulted in a big decrease in visibility due to the reduced index contrast at the fiber-liquid interface. This could be compensated with polarization control. Nevertheless, for practical purposes, the sensing head was characterized using depolarized light. In this case normalization algorithms were used to track the visibility changes with higher accuracy. Figure 4.5(a) shows the channeled spectra obtained with the sensing head inserted in solutions with two distinct refractive indices (1.3223 and 1.3497, respectively). It is observable the variation of the visibility of the interferometric fringes in the channeled spectrum, as consequence of the variation of Fresnel reflection in the fiber tip-liquid interface. As expected, the central wavelength of the channeled spectrum is nearly independent of refractive index changes, minor changes observed were related with temperature fluctuations (approximately 15 pm drift was observed in peak wavelength which can be accounted for by a variation of temperature of approximately 1.43 ℃) Nevertheless, the changes observed do not impact the visibility, or the measured refractive index.

The changes of the visibility of each peak due to immersion in solutions with different refractive indices are shown in Figure 4.5(b). The decrease of the visibility is due to increase of the surrounding refractive index in the fiber tip. For the fast axis peak, an approximately linear relation between the visibility and the refractive index was found (R^2=0.995) with a sensitivity of 210 ± 9 %/RIU. For the slow axis a linear relation was also found (R^2=0.996) with a sensitivity of 190 ± 7 %/RIU. Noteworthy is the difference in sensitivity for each of the peaks (∼20 %), a relevant fact when multi-parameter measurement is needed. Although reduced sensitivity was observed, some adjustments can be made to greatly improve the results such as using a grating with lower reflectivity and using polarization control to enhance visibility (by balancing the power reflected by the grating with the Fresnel reflection). In similar configuration proposed by Silva et al [20], using standard SMF-28 fiber, a resolution of ± 10^{-3} RIU was reported. In the present configuration similar figures should be easily attainable where in this case we have the added value of the multi-parameter capability.

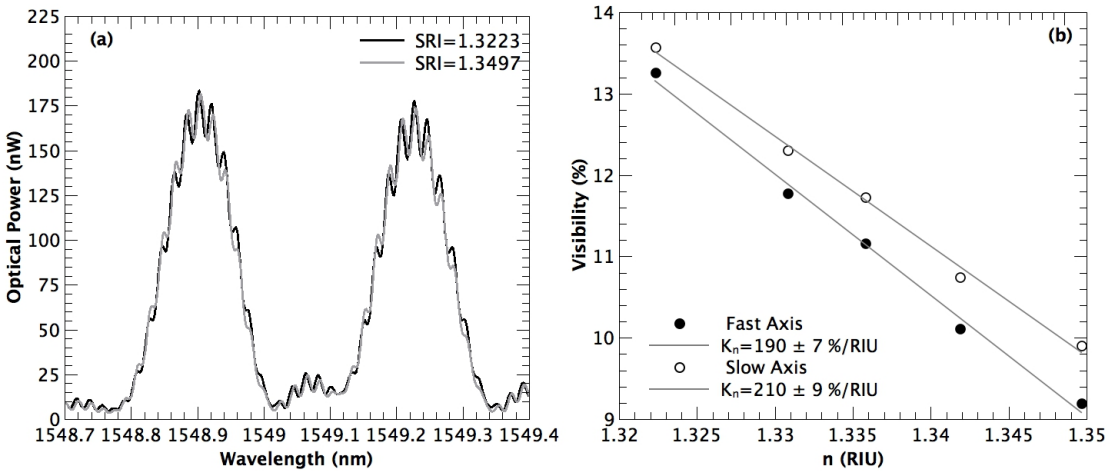

Figure 4.5: Channeled spectra for two different RI solutions (a) and sensing head response (two peaks) for SRI changes (b).

Also using a shorter FBG, and therefore, broader spectra FBG in this application can facilitate visibility analysis by reducing the effects of the fringe amplitude modulation. For temperature characterization, the sensing head was immersed in distilled water. Figure 4.6 shows the response of the sensing head to temperature in the 20 ℃ to 90 ℃ range. There is a linear relation between the temperature and peak wavelength of both peaks of FBG, both with R^2=0.999. Again the peaks show slightly different sensibilities (∼ 4%), the fast axis peak shifts in wavelength 10.52

± 0.06 pm/℃ and the slow axis 10.13 ± 0.06 pm/℃. No changes in visibility were observed as the impact of the refractive index dependence with the temperature is too small to be measurable by this configuration.

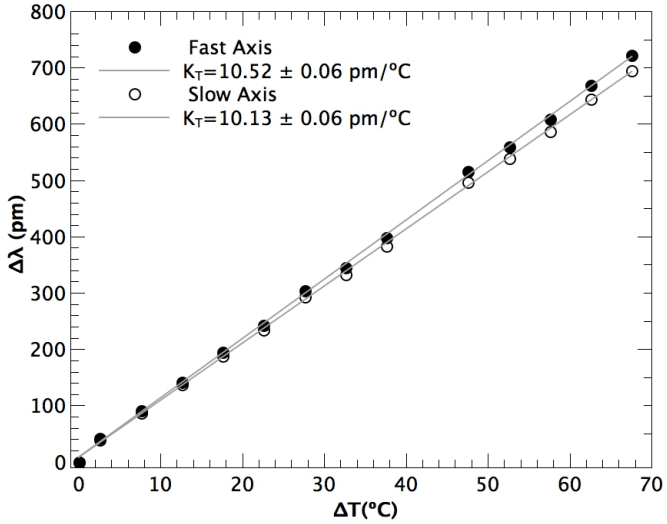

Figure 4.6: Sensing head response (two peaks) to temperature.

A compact Fabry-Perot cavity to measure liquid refractive index and temperature was studied. The structure is based on a low-finesse Fabry-Perot interferometer with interfering waves generated by a low reflectivity HiBi Bragg grating written in a Panda fiber and the fiber-end Fresnel reflection. The results show that each peak has different sensitivities for refractive index (visibility) and temperature (wavelength shift), allowing the possibility of simultaneous measurement of refractive index and temperature.

4.2 FBG Cladding Modes excited by a Core Misaligned Splice for Multi-Parameter Sensing

FBGs represents a great case of success in the field of fiber optic sensors, due to the sensitive nature of the silica matrix and its influence in the Bragg condition, these photonic devices are frequently used to the measurement of physical parameters [7]. Cladding modes are very interesting, since each mode responds to a particular measurand with a different sensitivity, enabling the possibility of simultaneous measurement of multi-parameters using a single sensor element [187–189]. Several authors have been exploring the possibility to readout in reflection the cladding modes of a TFBG using diverse methods, all of them based in a core-cladding coupling and recoupling

mechanism inserted upstream of the TFBG. An LPG [190], an abrupt tapered fiber [191], a misaligned splice [192–194] and a core mismatch section (short section with larger or shorter core diameter) [195]. These works were used to measure curvature [190, 195], acceleration [191], vibration [192, 193] and refractive index [194]. However, the spectral characteristics of this devices present a relatively large set of resonances, where is patent the absence of a predominant mode, thus, the cladding modes are spectrally not so clear, which hinder its interrogation.

On the other hand, as exposed in previous sections, usually, simple FBGs with strong modulation index present also cladding modes, manifested in the transmission spectra. The utilization of such modes in reflection has been also explored by few researchers. Once more an LPG was used with such purpose [17, 135, 136, 196]. It is worth to note, that, probably it is the best option, since it is possible to precisely control the excited mode, and the amount of power transferred [196]. In this work a different approach is proposed using a high reflectivity FBG combined with a large core-offset-splice in a SMF. This technique enables the possibility to readout simultaneously in reflection a dominant cladding mode and the core mode. Permits also, to change, in a simple manner the excited cladding mode (within a narrow range) and the amount of light that is going to the cladding.

Within the overall objective of the thesis, the goal of this work was to use both modes for simultaneous measurement of temperature and RI. Nonetheless, in the studied sensing devices, the cladding mode did not show sensitivity to the SRI. Different sensing structures, with lateral core offsets ranging from 5-9 μm, were subjected to changes in the SRI in a range between 1.321 and 1.382 RIU, with apparently no response by the cladding mode resonant peaks, probably for being a lower order mode, with very little contact between the radiation and the external medium. It is worth to say that subsequent works have reported the measurement of the SRI by using the reflected cladding modes of a simple FBG. These works were based in a different technique for core-cladding coupling, for instance, a core mismatch section [18, 137]. In these works, the coupling mechanism based on a CDM was capable to excite high order modes, and thus, the FBG cladding mode peak shows response to the external index.

Although the configuration was not able to measure RI, the main research focus of this PhD work, it has been exploited for other applications such as bent, strain and temperature. In the case of the curvature sensing, an intensity self-referenced system based in the normalized ratio of the reflected optical power of both modes is presented. Since the measurement parameter is wavelength independent, a simple power based

detection scheme was used. The signal detection was based on a wavelength division multiplexer (WDM) and two photodetectors. Once the reflected optical power do not depend on the temperature induced shifts in both peaks, the implemented curvature sensor was also temperature-independent.

Thereafter, the same sensing probe was used to measure simultaneously strain and temperature. Based on the principles described in the section 3.3.3 both modes are strain and temperature dependent, exhibiting slightly different sensitivities when subjected to strain and a reasonably higher difference for temperature changes. The effect of temperature on the sensing head is probably due to the different thermo-optic coefficient of the core and cladding which affects in a different manner both modes. This capability allows to measure both parameters without ambiguity. In this experiment, the wavelength of both peaks was monitored by using an optical spectrum analyzer.

4.2.1 Sensing Head

The sensitive system is formed by a high-reflectivity FBG (R $\approx$ 98%, 6 mm in length). The grating has been written in a hydrogen loaded SMF-28 fiber by UV beam scanning phase mask technique. The fiber segment containing the grating was cleaved at approximately 5 mm distance from the FBG. Another long piece of fiber previously connected to an optical circulator was cleaved. Both cleaved fibers were placed into a splice machine. To monitor the spectral behavior and optimize the cladding modes, the splice was real-time monitored in reflection using an Advantest Q8384 OSA. In order to obtain a dominant cladding mode, a lateral core-offset was induced. In the distal end of the sensing head, an index matching gel was used to avoid undesirable reflections. There are two different types of mode recoupling mechanisms. In the first one, the guided light coupled from core to the cladding modes by the misaligned section is re-coupled to the backward guided mode by the FBG. In the second mechanism, the guided light is coupled to the backward cladding modes by the FBG and is re-coupled to the guided mode by the lateral core off-set section [135]. In this sensing head, the first mechanism represents the major contribution to the overall reflected signal, whilst the second one has a residual contribution, due to the multiple reflections that occur in the diffractive structure. Figure 4.7(a) illustrates the sensing head schema and the dominant recoupling mechanism. Figure 4.7(b) shows the misaligned splice, where the lateral core off-set was approximately 9 μm.

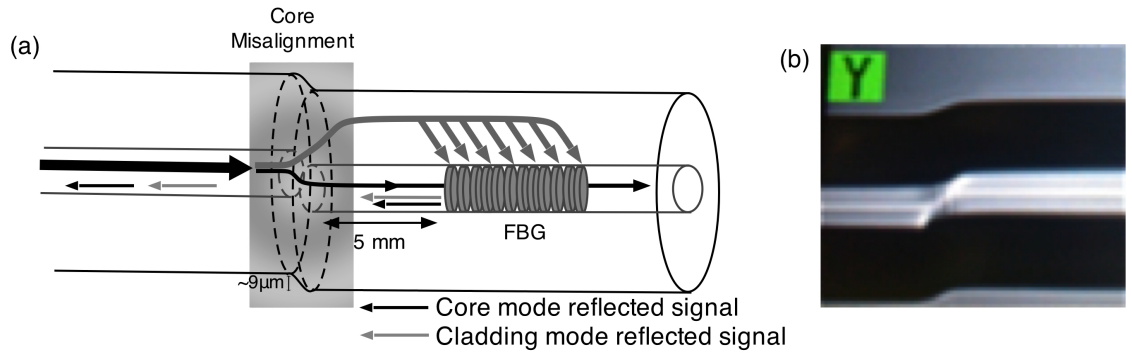

Figure 4.7: (a) Sensing head formed by a high reflectivity FBG and a misaligned core splice, where the dominant recoupling mechanism is described. (b) It is shown the splice with a lateral core off-set of ∼9 μm.

Figure 4.8 illustrates the reflection spectrum of the sensing head. The two main peaks are related to the dominant cladding mode and to the core mode, respectively, being separated by 3.75 nm. The cladding mode corresponds to the high effective index cladding mode, in resonance with the grating period, centered in 1547.84 nm and with a FWHM of 500 pm. The core mode peak, which satisfies the Bragg condition for the fundamental mode, is centered in 1551.58 nm, and presents a FWHM of 0.85 nm. The difference of power of the dominant cladding mode to the core mode is approximately of 5 dB.

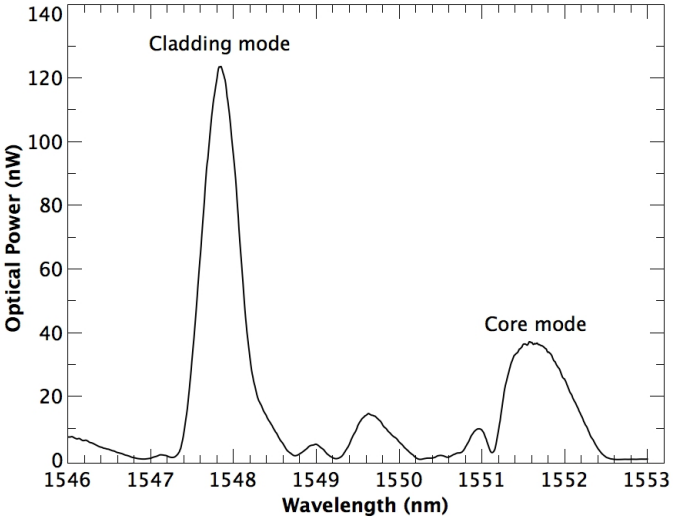

Figure 4.8: Reflection spectrum of the sensing head.

4.2.2 Curvature Sensing

Figure 4.9 shows the experimental setup for the curvature characterization of the sensing head. An erbium-doped fiber source illuminated the sensor through an optical circulator which enabled the Fiber Bragg reflected signal to be readout in reflection. Using a WDM to separate the core reflection from the cladding reflection enabled the corresponding optical powers to be readout by two simple photodetectors.

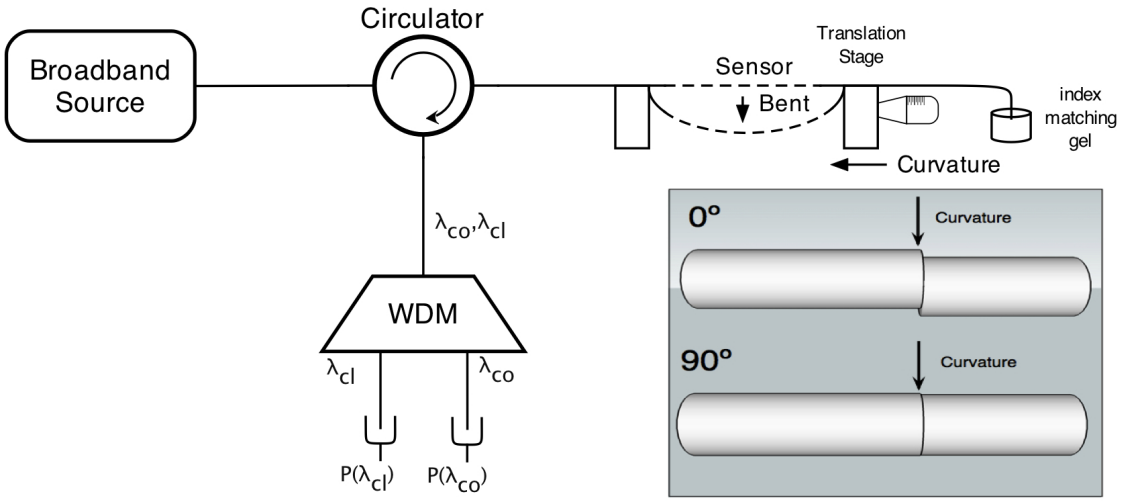

Figure 4.9: Experimental setup for curvature measurement.

The amount of light which is re-coupled from the backward guided mode by the FBG is highly dependent on the fiber curvature, enabling the possibility to measure the curvature as a function of the reflected optical power of the cladding mode. In order to avoid axial strain, the bending sensitivity measurements were performed by loosely fixing the two ends of the fiber containing the sensing probe on two blocks, being one mounted on a translation stage, in order to bend the fiber. The sensing head was placed in the middle of the two blocks (as shown in Figure 4.9). The resulting curvature $\frac{1}{R}$ is simply given by the following expression [189], $\frac{1}{R} = \frac{2h}{\left(h^2+\left(\frac{d}{2}\right)^2\right)}$ where d is the distance between the two blocks and h is the bending displacement. The curvature was applied in a range of 0 to 1.75 m^{-1}. When curvature was applied, the reflected optical power of the dominant mode decreased, at the same time the reflected optical power by the core mode remained constant. The measurements were obtained by computing the optical power difference between the cladding mode and the core mode. The dependence of the curvature with the sensing head fiber positioning was also studied. The inset of Figure 4.9 clarifies schematically the fiber position for

0° and 90°, respectively. The fiber was rotated from 0° to 90°. For 0°, maximum sensibility was observed. For 90°, no curvature sensitivity was observed. Prior to the characterization, the effect of curvature in the reflected peaks was observed using an optical spectrum analyzer. Figure 4.10(a) shows the effect of bending on the reflected spectrum for three different curvature values. It can be seen that no wavelength shift was observed. The normalized optical power as function of the curvature is shown in Figure 4.10(b), where a non-linear behavior was observed (fitted by second order polynomial). In a first order approximation, a variation in the cladding mode optical power of approximately 5 dB was observed when curvature was changed between 0 m^{-1} and 1.75 m^{-1}.

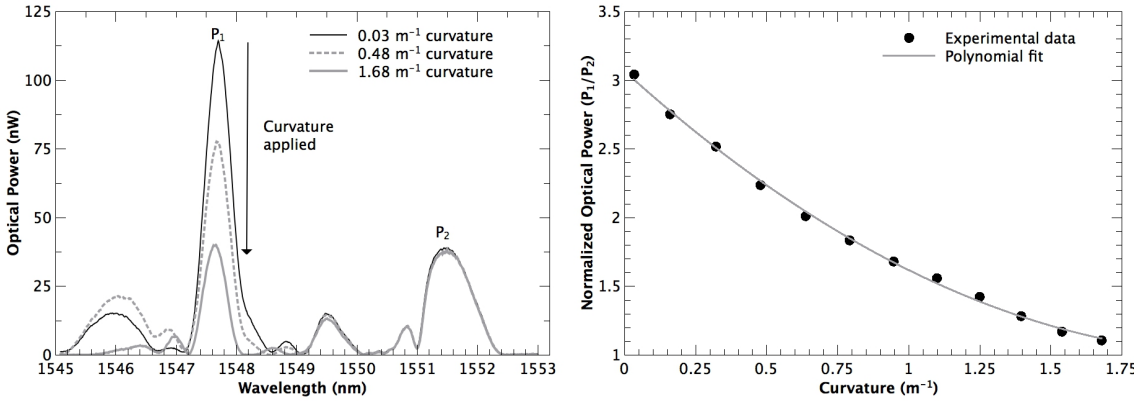

Figure 4.10: Reflection spectrum of the sensing head for three different curvatures (a) and the normalized optical power as a function of curvature (b).

The behavior of the optical power of both reflected peaks with temperature variation was also studied. For temperature measurement the sensing probe was fixed in a chamber filled with hot water. The sensing head was submitted to variation of the temperature from 25 °C to 70 °C. The observed changes in the reflected power of the cladding and core modes were minimal. Figure 4.11 illustrates the variation of the power difference as function of the temperature. The temperature changes did not affect the reflected optical power, which means that through this technique, it is possible to obtain curvature measurements quasi-independent of temperature. The variation of optical power due to temperature change is less than 1 %/°C, which corresponds to a variation of curvature of 0.15 m^{-1} for 50 °C of temperature variation. It is worth the explain that, this fact depends on the spectrum of the light source and the transfer function of the WDM, once both can modulate in amplitude the reflected power of both modes.

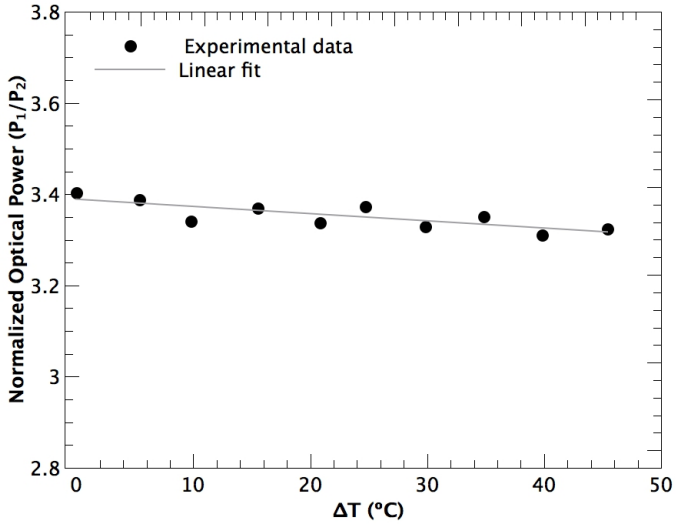

Figure 4.11: Normalized optical power as a function of temperature changes.

A compact and simple curvature sensor system was described. The sensor is based on a simple FBG spliced to a core off-set fiber. This configuration permits to read the cladding mode of the Bragg grating reflected spectrum. For curvature, the optical power of the cladding mode is sensitive to fiber bending, while the core mode is not sensitive. Dividing both reflected optical powers, it is possible to obtain a self-referenced measurement of curvature. This configuration is temperature insensitive for small variations of temperature. The sensing head presents important advantages when compared with TFBG based configurations. A standard FBG was used, which is easier to fabricate. Moreover, by varying the core off-set magnitude of the misaligned splice, it is possible to change, in a simple manner, the excited cladding modes and the amount of light that is going to the cladding. This process results in well-resolved spectral peaks simplifying the interrogation mechanism and enhancing the measurement accuracy.

4.2.3 Strain and Temperature Measurement

The strain measurements were made using the setup shown in the Figure 4.12. The two ends of the fiber containing the sensing element were fixed on two blocks, being one them mounted on a translation stage (with a resolution of 10 μm) in order to apply strain to the fiber. The sensor is characterized by applying strain to the fiber from 0-1500 με range.

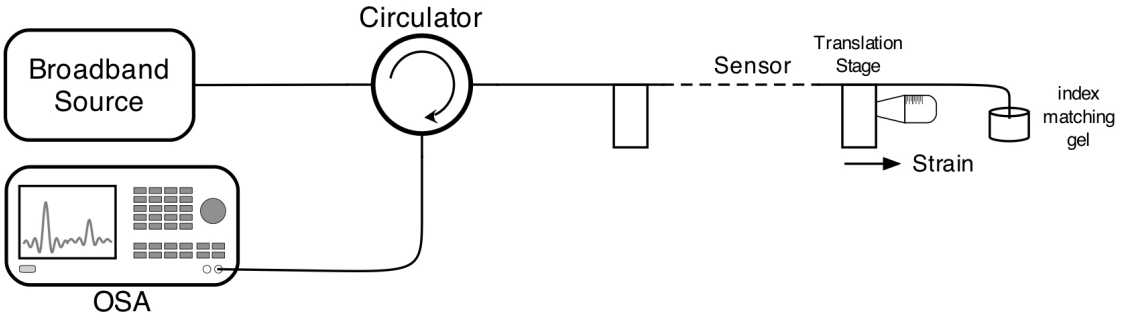

Figure 4.12: Experimental setup for strain characterization.

As expected the central wavelength of the core and the cladding mode increased when strain was applied. Figure 4.13(a) shows the effect of the strain in the sensing head. It is clear the wavelength shift of the cladding and core mode peaks. The strain change affect also the reflected optical power but this effect was not considered. Figure 4.13(b) shows the response of the sensing structure to strain where a linear behavior is observed. The cladding mode presented a sensitivity of 1.10 ± 0.02 pm/με, whilst for the core mode was 1.08 ± 0.02 pm/με.

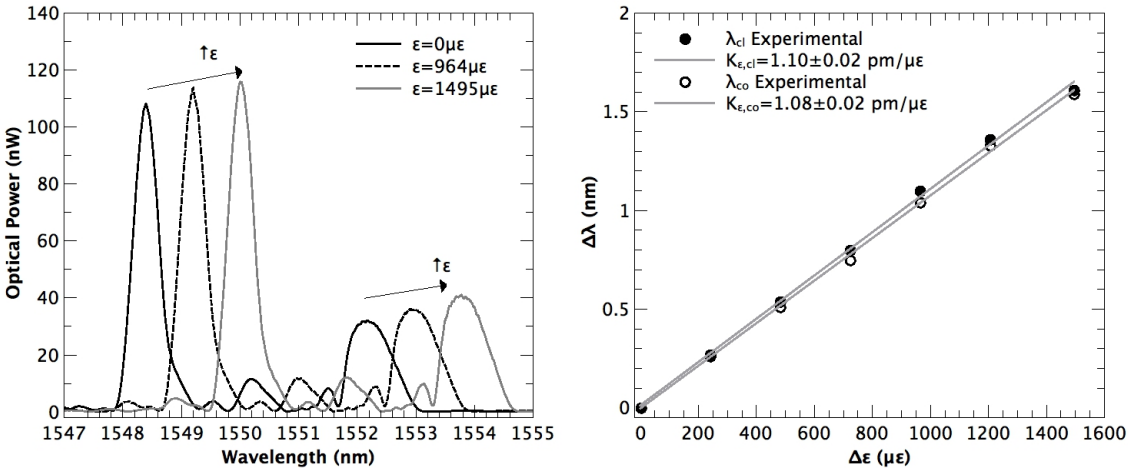

Figure 4.13: Effect of the strain in the reflected spectrum (a) and strain characterization of the sensing head (b).

The temperature sensitivity was also studied. For temperature measurement, the sensing probe was fixed in a chamber filled with water. The sensing head was submitted to a temperature variation of 30 ℃ to 75 ℃. As expected, an increment in temperature implies a shift to higher wavelengths. Figure 4.14(a) illustrates the effect of temperature in the reflected spectrum. The temperature changes, cause an small increment in the reflected optical power, but it was not considered. Figure 4.14(b)

shows the wavelength shift difference as function of the temperature. The sensitivity of the cladding mode was 9.5 ± 0.2 pm/℃ and 11.1 ± 0.3 pm/℃ for the core mode. The different sensitivities show the possibility of multi-parameter measurements.

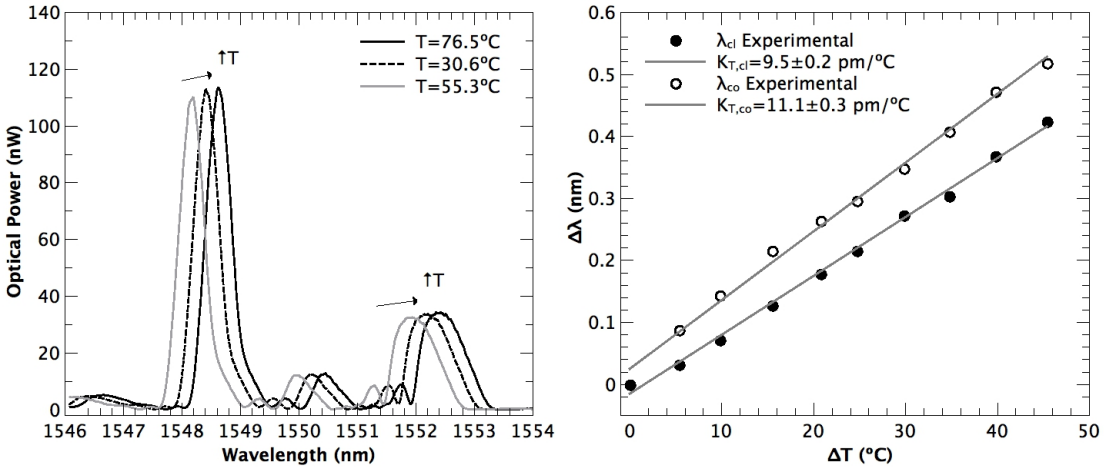

Figure 4.14: Effect of the temperature in the reflected spectrum (a) and temperature characterization of the sensing head (b).

The dual response of the FBG cladding and core mode wavelengths to strain and temperature allows for the writing of a conditioned system of two equations for $\Delta\varepsilon$ and ΔT, given in matrix form as [8];

$$\begin{pmatrix} \Delta T \\ \Delta\varepsilon \end{pmatrix} = \frac{1}{K_{\epsilon,cl}K_{T,co} - K_{T,cl}K_{\epsilon,co}} \begin{pmatrix} K_{\epsilon,cl} & -K_{\epsilon,co} \\ -K_{T,cl} & K_{T,co} \end{pmatrix} \begin{pmatrix} \Delta\lambda_{co} \\ \Delta\lambda_{cl} \end{pmatrix}, \tag{4.1}$$

where $K_{\varepsilon,cl}$, $K_{\varepsilon,co}$ and $K_{T,cl}$, $K_{T,co}$ matrix coefficients are the sensitivity coefficients represented in Figure 4.13(b) and Figure 4.14(b), respectively;

$$\begin{pmatrix} \Delta T \\ \Delta\varepsilon \end{pmatrix} = \frac{1}{1.95} \begin{pmatrix} 1.10\pm0.02 & -1.08\pm0.02 \\ -9.5 \pm 0.2 & 11.1\pm0.3 \end{pmatrix} \begin{pmatrix} \Delta\lambda_{co} \\ \Delta\lambda_{cl} \end{pmatrix}. \tag{4.2}$$

From the λ_{cl}, λ_{co} responses, this method allows recovering the strain and the temperature without ambiguity.

A fiber optic FBG cladding modes based sensor, for simultaneous measurement of strain and temperature was described. The FBG cladding modes are efficiently excited by the large core-offset in the upstream of the FBG written on a SMF. The core lateral offset allows a low order cladding mode to recouple back to core mode after passing through the mismatched interface. This technique enables the possibility to readout simultaneously in reflection the cladding mode (λ_{cl}) and the core mode

(λ_{co}). λ_{cl}, λ_{co} are strain and temperature dependent showing different sensibilities for each parameter, enabling their discrimination. The results show the feasibility of simultaneous measurement of strain and temperature through the matrix method. In this context, the proposed configuration due to its simplicity, low cost, small size, operation in reflection and multiplexing capability can potentially be used as a multi-parameter sensing head for strain and temperature measurements.

4.3 Conclusion

FBG sensors are a well-known case of success in optical fiber sensors, above all things due to their applications in structural health monitoring, based on their strain and temperature sensitivity. In this chapter, two works were presented: one related with a HiBi Fabry-Perot Cavity for refractive index and temperature measurement and; a second one based on cladding modes of a single FBG excited by a core-offset splice for multi-parameter sensing purposes.

A compact Fabry-Perot cavity to measure liquid refractive index and temperature was studied. The structure is based on a low-finesse Fabry-Perot interferometer with interfering waves generated by a low reflectivity HiBi FBG and the fiber-end Fresnel reflection. The results show that each peak has different sensitivities for refractive index (visibility) and temperature (wavelength shift), allowing the possibility of simultaneous measurement of refractive index and temperature. In this context, the proposed configuration due to its simplicity, low cost, small size, operation in reflection and multiplexing capability, can potentially be used as a multi-parameter sensing head for temperature and refractive index. Its application in the biochemical field can be also an interesting issue by depositing in the fiber tip, a chemically or biologically selective material [25].

Finally a simple and compact FBG cladding modes-based sensing structure for curvature, strain and temperature measurements. The FBG cladding modes are efficiently excited by the large core-offset in the upstream of the FBG written onto a SMF. The core lateral offset allows a low order cladding mode to recouple back to core mode after passing through the mismatched interface. This technique enables the possibility to readout simultaneously in reflection the cladding mode and the core mode. For curvature, the optical power of the cladding mode is sensitive to fiber bending, while the core mode is not sensitive. Dividing both reflected optical powers, it is possible to obtain a self-referenced measurement of curvature. The bent measurement is thermally insensitive for small variations of temperature. On the other

hand, the cladding mode and the core mode are strain and temperature dependent showing different sensibilities for each parameter, enabling their discrimination. The results show the feasibility of simultaneous measurement of strain and temperature through the matrix method. In this context, the proposed configuration due to its simplicity, low cost, small size, operation in reflection and multiplexing capability can potentially be used as a multi-parameter sensing head. Moreover, by varying the core off-set magnitude of the misaligned splice, it is possible to change, in a simple manner, the excited cladding modes (within a restricted range) and the amount of light that is going to the cladding.

Chapter 5

Long Period Gratings for Biochemical Sensing

Summary

The popularity of long period gratings in the sensing area has increased substantially over the last few years, as a notable number of long period grating based devices and systems have been reported for a multitude of applications. In particular, many LPG based refractive index sensing platforms have been explored in the implementation of different label-free sensors for chemical and biological parameters. In this chapter, a extensive study regarding long period grating devices for refractive index sensing is presented. Few structures fabricated mainly by electric-arc technique with different features and configurations were characterized and compared. Due to the high sensitivity of the LPGs to temperature, all the devices were also characterized in response to thermal changes. The impact of high refractive index overlays on the sensitivity to the external medium was also evaluated. Finally, two applications are described. An LPG coated with p-nitro-phenol based material is presented for CO_2 sensing, and a LPG biosensor for detection and quantification of *E. coli* is also reported.

5.1 Introduction

LPGs are probably the most popular fiber optic devices for chemical and biochemical sensing. There are several reasons that justify this fact. In an LPG the fundamental mode traveling in the core is coupled into cladding modes, resulting in several attenuation bands in the transmitted spectrum, each of them corresponding to a cladding mode. Due to the interaction between the cladding modes and the external medium, an LPG device is intrinsically sensitive to the external index, preserving the fiber integrity, unlike the majority of fiber refractometers that are based on etching, polishing and tapering processes that weaken the fiber structure. On the other hand, it is possible to control the performance of the device, by controlling the settings on the fabrication stage. The order of the mode, the FWHM and the wavelength of each resonance depend on the period of the diffraction structure, the number of periods and the modulation index. Also, LPGs can be manufactured by using different techniques and nowadays some of them are not very costly. Finally, in the last few years the use of HRI overlays has increased the sensitivity of coated LPGs to values exceeding those attained by SPR configurations. In the next sections, experimental work carried out during the PhD work is presented, starting by the description of electric-arc system for LPG fabrication at INESC Porto.

5.2 Electric-arc Setup at INESC Porto

Figure 5.1 shows in detail the setup for LPG fabrication by the electric-arc discharge technique at INESC Porto [197]. A stripped fiber is placed between the electrodes with a gap between 0.9-1.0 mm. The electrodes have 2 mm diameter and are made in tungsten rods with a small amount of thorium (2%). The apex angle is between 20º- 40º. The high voltage power supply is a BICC AFS3100 fusion splicer machine. The fiber alignment is performed with the help of two sets of v-grooves which help the fiber to remain in the same position relative to the electrodes. The electrodes are mounted on an x, y, z translation stage to properly position the fiber relatively to the electrodes in such way that the electric discharge engages the fiber homogeneously. This step is executed with the help of a microscope. After alignment the fiber is held in the same position with the help of a set of V-grooves with two clamp arms. One end of the fiber is clamped in a fiber holder on top of the translation stage, controlled with the precision of 0.1 μm. At the other end a mass is attached to keep the fiber under a constant axial tension (5-40 g). An arc discharge is then produced with an

electric current of 8.5-10.0 mA for 0.5–2.0 s. As a result, a short portion of the fiber length is exposed to the arc generated heat. Afterwards, the fiber is translated by the grating period, typically 300–600 μm. This sequence is repeated several times (15–180) until a required attenuation loss peak is obtained [198]. This process is controlled by a computer using a Labview program. During the fabrication, the fiber is illuminated with a white light source (WLS) and the spectrum is obtained with an optical spectrum analyzer (OSA).The electrodes degrade during the arc discharges due to oxidation or to contamination by dust or silica particles that adhere to their tips. Therefore, after some use they need to be replaced and polished [197]. It is worth to say that, due to the asymmetric nature of the arc-discharge [197], coupling mainly occurs between the $LP_{0,m}$ and $LP_{1,m}$ modes.

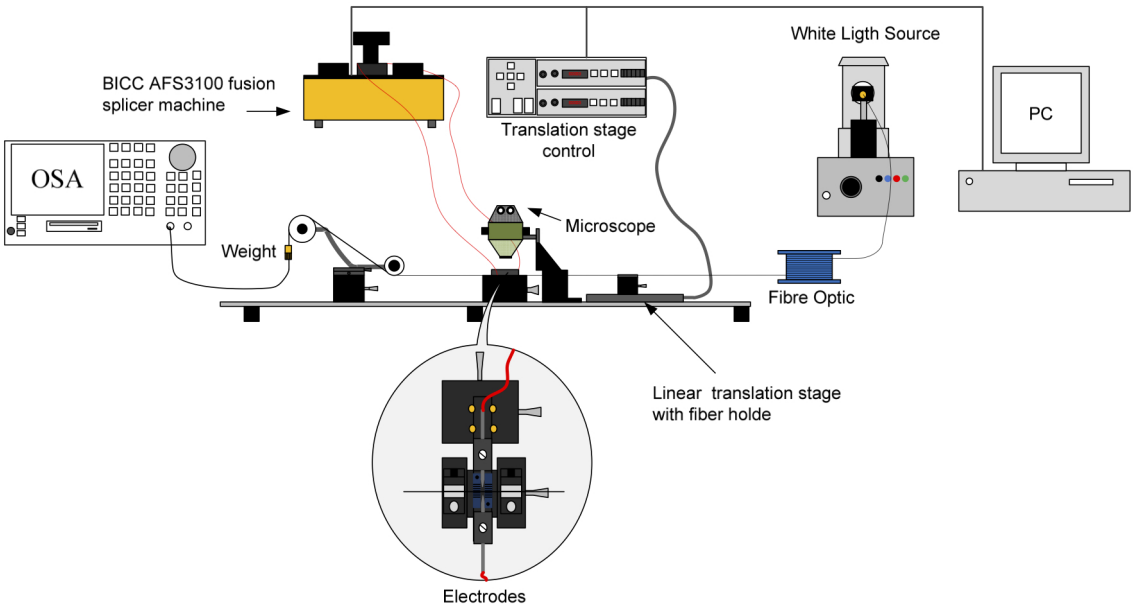

Figure 5.1: Electric-arc setup at INESC Porto [198].

5.3 Experimental Procedure

The sensitivity of LPG based devices to changes of the external refractive index and temperature was studied. The setup used for this purpose is shown in Figure 5.2. Each LPG was placed into the measurement chamber and properly fixed with fiber clamps in both sides, where a small fixed tension was applied with a translation stage to avoid strain/curvature cross sensitivity. The sensing elements were characterized using a FS2200SA from Fibersensing, SA (Portugal) working in the 1500-1600 nm

range, with 1 pm of resolution, and able to measure signals both in reflection and transmission modes in separate channels. The LPGs were connected to the unit in transmission mode. Labview control of the FS2200SA enabled real-time direct access and processing of the data sets, corresponding to the transmitted spectrum of the devices. The resonance wavelength peak was tracked by using a standard peak detection of Labview.

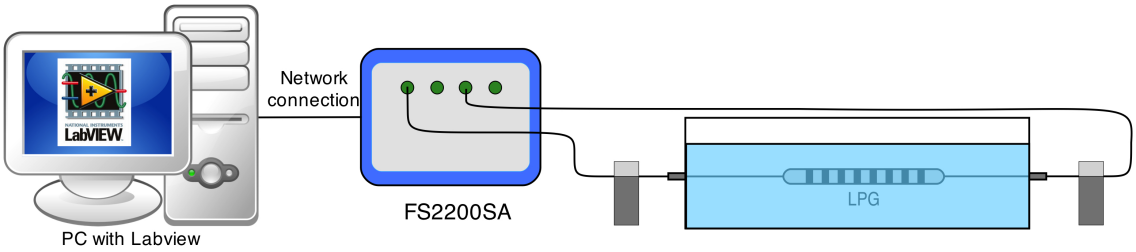

Figure 5.2: Experimental setup used for characterization of the LPG regarding refractive index and temperature sensitivity.

The response of the LPGs to the SRI was studied by exposing the sensing head to different solutions of distilled water mixed with different concentrations of ethylene glycol to provide the RI standards in a range approximately between 1.32 – 1.38 RIU. The refractive index was increased by continuously adding ethylene glycol (in order to keep the mixture homogeneous, the solution was stirred through a magnetic stirrer). The data was recorded after stabilization of the output signal and of the solution temperature. The liquid samples were characterized by an Abbe refractometer using the sodium D line (589 nm). The necessary adjustments, considering the sensing head operation at 1550 nm, were made using the Cauchy equation with the respective coefficients [185, 186]. Using this procedure, all the calibration curves presented here refer to the refractive index values at 1550 nm. Each calibration curve results from a series of measurements that incorporate a large time span and number of measures (100 s, 1 S/s), where each point corresponds to the average of each set of acquired data. The sensitivity of the sensor, in the range of RIs where its behavior was linear, is assessed through the slope of the calibration curve. The statistics of the measured values allows us to estimate the refractive index resolution of each sensing device. For this purpose, it is considered a minimum detectable signal of two times the average calculated standard deviation of each data set (2σ) divided by the sensitivity in the corresponding measurement interval.

For characterization of the sensing devices to variations in temperature, the arrangement is similar, the sensing element was placed into the chamber, with the

particularity that the grating was inside of a 260 μm diameter metallic capillary tube, thereby sensitive to temperature changes in the solution but insensitive to the refractive index variations in the solution. The chamber was filled with distilled water heated up until 90 ℃. The resonant wavelength was monitored continuously during the temperature drop. The temperature was measured using a thermocouple.

5.4 Electric-arc Bare Long Period Gratings

For this experiment an LPG fabricated using the setup described in the section 5.2 was used [157]. The grating was manufactured in a standard SMF-28 fiber using the following set of fabrication parameters: an axial tension of 5.1 g, arc discharges with an electric current of 9 mA and arc duration of 1 s, the grating period was 396 μm and the number of discharges 95 in order to produce a resonant wavelength at approximately 1560 nm, corresponding to the $LP_{1,6}$ cladding mode. The resulting resonance depth and FWHM were around 32 dB and 26 nm, respectively. To monitor this process, the fiber was illuminated with a WLS and the transmission spectrum was acquired with an OSA. The spectrum of the LPG used in this experiment is shown in Figure 5.3. It is observable three resonant peaks corresponding to the $LP_{1,4}$, $LP_{1,5}$ and $LP_{1,6}$. It was the sensitivity of the last one (larger wavelength) that was investigated.

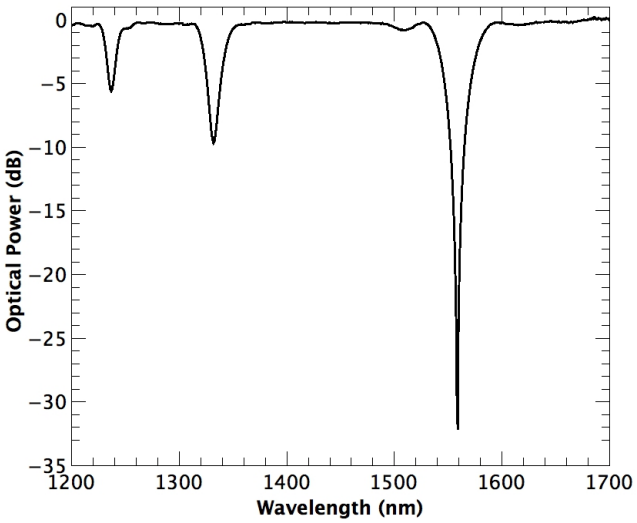

Figure 5.3: Transmission spectrum of a LPG with period of 396 μm and 95 discharges.

Figure 5.4(a) shows the response of the resonant wavelength of the LPG to variations in the SRI. It is noticeable that for an increasing SRI the wavelength decreases as expected. A non-linear behavior is observed, which can be fitted to a second order

polynomial function. The sensitivity of the LPG to the SRI can be splitted in two regions: one for lower indices (close to water index) and another for higher indices (closer than cladding refractive index). Figure 5.4(b) and (c) show these two regions in more detail. Sensitivities up to 147 ± 3 nm/RIU were obtained for the range between 1.321-1.345, whilst sensitivities around 358 ± 14 nm/RIU resulted when operating for SRI between 1.345-1.38. As might be expected the sensitivity was more than two times higher in the larger RI range. This happens because when the SRI approaches the cladding index, the confinement of the cladding modes becomes weaker and the sensitivity to refractive index changes becomes much stronger. Noteworthy, that for biological applications usually, sensing probes should operate on the lower RI range. Therefore, this is the region of interest for such applications.

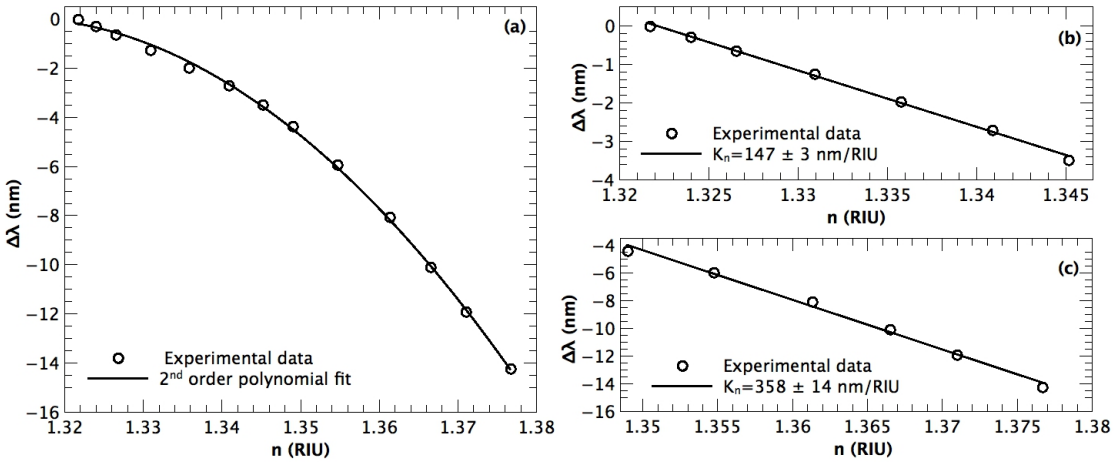

Figure 5.4: Response of the resonant wavelength to the changes in the SRI for the full range evaluated (a). For the range 1.32-1.345 RIU (b) and for the range 1.345-1.38 RIU (c).

An average refractive index resolution of ± 4.1×10^{-5} RIU for the lower RI range and ± 2.1×10^{-5} RIU for the higher RI range were calculated. The resonance wavelength as a function of temperature is shown in Figure 5.5. An increment in the temperature results in a shift to higher wavelengths. A linear behavior is noticeable and a sensitivity of 113 ± 1 pm/℃ is assessed from the slope of the calibration curve. Regarding the reproducibility of the sensing characteristic, it is possible to state that, during the experiments several LPGs with similar features (period, length, resonance wavelength and depth) were characterized, it was revealed that they all have very similar sensitivities, within the error presented.

In order to achieve higher sensitivity, using the same fabrication parameters as before an LPG with a shorter period of 338 μm and 160 discharges was fabricated.

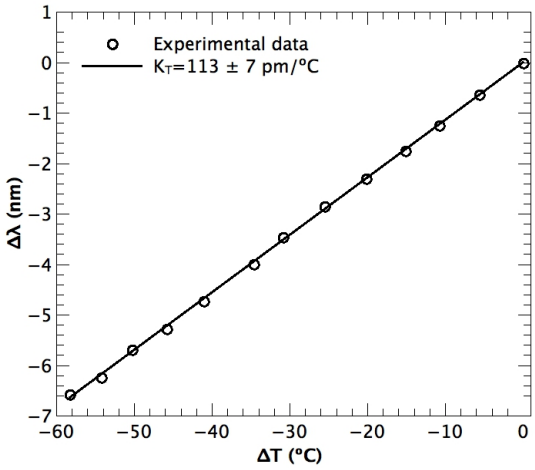

Figure 5.5: Resonant wavelength change as a function of temperature.

The resulting grating presents a resonant wavelength at approximately 1547.50 nm, corresponding to the $LP_{1,7}$ cladding mode. The resonance depth and FWHM were around 27.6 dB and 24.5 nm, respectively. The spectrum of the LPG used is shown in Figure 5.6. Two resonant peaks can be observed corresponding to the $LP_{1,6}$ and $LP_{1,7}$. The sensitivity of the latter was evaluated.

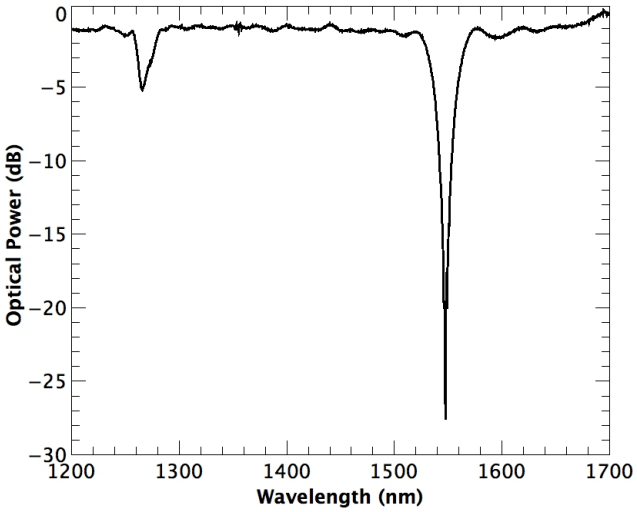

Figure 5.6: Transmission spectrum of an electric-arc LPG with a period of 338 μm and 160 discharges.

The response of the resonant wavelength of the LPG to the SRI is presented in Figure 5.7(a). The behavior is similar to the observed with $LP_{1,6}$, but with higher sensitivity. Figure 5.7(b) and (c) illustrate the two regions evaluated. Sensitivities of up to 290 ± 6 nm/RIU were obtained for the range between 1.321-1.345 RIU, whilst a

sensitivity around 708 ± 28 nm/RIU resulted when operating for SRI between 1.388-1.42. As expected, the sensitivity was higher for the higher index range. Average refractive index resolutions were estimated with ± 2.6×10^{-5} RIU for the lower RI range and ± 1.5×10^{-5} RIU for the higher RI range.

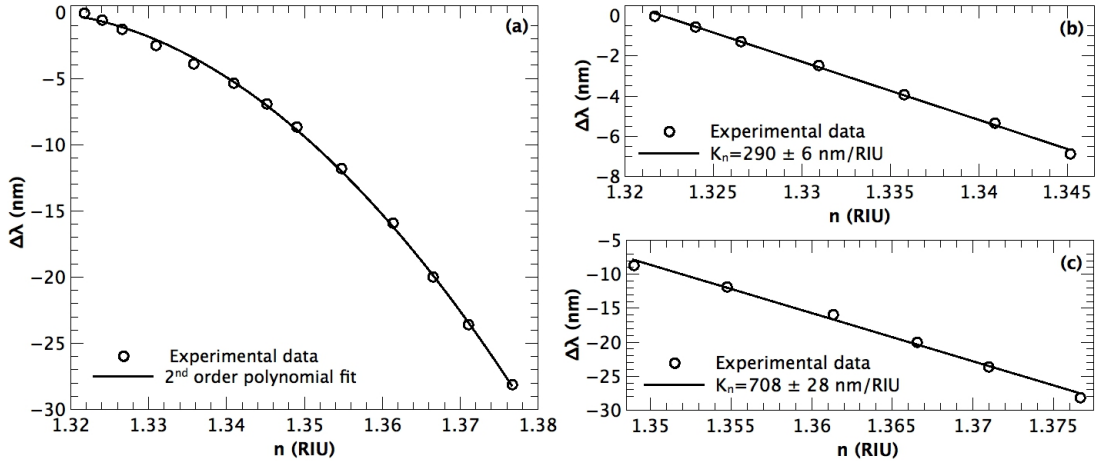

Figure 5.7: Response of the resonant wavelength to changes in the SRI for the full range studied (a), for the range 1.32-1.345 RIU (b) and for the range 1.35-1.38 RIU (c).

The resonance wavelength as a function of temperature is shown in Figure 5.8. An increment in the temperature results in a shift to higher wavelengths. A linear behavior is noticeable and a sensitivity of 165 ± 16 pm/°C is assessed from the slope of the calibration curve. Concerning the reproducibility of the sensing characteristic, it is possible to assert that, during the experiments few LPGs with similar features (period, length, resonance wavelength and depth) were characterized, it was noticeable that within the error presented, they all exhibited an analogous behavior.

Considering the two LPGs tested, in terms of the response to the temperature, the higher sensitivity observed for the shorter grating period is due to the higher number of refractive index perturbations per unit length. Concerning their response to SRI, the shorter period higher order $LP_{1,7}$ grating, offers a an improved resolution and a two times higher sensitivity in the region of interest, when compared to the longer period (lower order) $LP_{1,6}$ grating. As expected, higher order modes offer higher sensitivity, and higher sensitivities can be achieved by using shorter periods, nevertheless, one of the constrains of electric-arc induced LPGs, is the limitation of the minimum modulation period that can be induced. It is extremely difficult to fabricate gratings below 330 μm on SMF-28 fiber, making it tough to excite higher

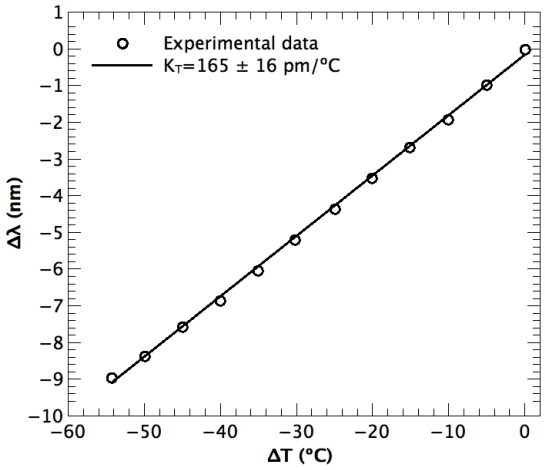

Figure 5.8: Shift in the resonant wavelength change as a function of temperature

order cladding modes around 1550 nm. Contrarily, UV LPGs can be written with shorter periods, exciting higher order modes. In the next section, an UV written LPG close to the turn-around-point will be studied.

5.5 Ultra-violet Bare Long Period Gratings

The LPG used in this work was provided by the Central Glass and Ceramic Research Institute (CGCRI), India, in the context of a bi-national cooperation project. It was fabricated in standard singlemode fiber SMF-28e, the stripped fiber was illuminated with light from a 248 nm KrF excimer laser and the grating was written using point-by-point technique. The period of 165 μm was chosen in order to have a resonance around 1500 nm, corresponding to the 12^{th} order cladding mode. Following the fabrication, the LPGs were annealed at 500 ℃ for 12 hr before being ready for use in the subsequent experiments. The 12^{th} cladding mode exhibits a turn-around-point in its dispersion curve in the wavelength range between 1200-1600 nm. Thus, this grating couples the $LP_{0,12}$ cladding mode in two resonant wavelengths at approximately 1200 nm and 1500 nm, respectively. The resonance depth and FWHM measured were around 16 dB and 70 nm, respectively. It is worth to say that, the sensitivity behavior of dual-peak LPGs is different from the previous gratings studied in this work. For the increment in the SRI (with $n_{sur} < n_{cl}$) the spectral distance between them will increase, thus, each peak will have opposite behavior. Concerning the temperature response, it was observed that, with the temperature rising, decreased the separation between the two peaks. Figure 5.9 shows the transmission spectrum of the grating used. Two resonant peaks corresponding to the $LP_{0,12}$ near to the turn-around-point

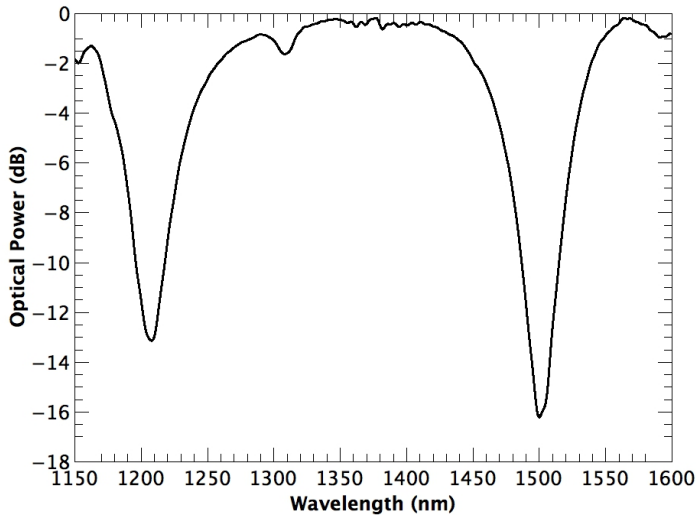

Figure 5.9: Transmission spectrum of a UV written LPG with period of 165 μm.

are observed. For the present experiment the peak corresponding to larger wavelength resonance will be studied.

The response of the resonant wavelength of the LPG to the SRI is presented in Figure 5.10(a). The resonance shifts to larger wavelengths with the increment of the SRI. Figure 5.10(b) and (c) show the two regions of RI evaluated. Sensitivities of up to 636 ± 21 nm/RIU were obtained for the range between 1.321-1.35, whilst a sensitivity around 1618 ± 57 nm/RIU resulted when operating for SRI between 1.35-1.375. It was estimated a refractive index resolution of ± 2.6×10^{-5} RIU and ± 1.4×10^{-5} RIU for the lower and higher RI range, respectively. Compared with the electric-arc $LP_{1,7}$ previously characterized, this one offers a slightly better resolution and a sensitivity approximately two times higher in the region of interest.

The resolution is closely related with the accuracy by which λ_R^m is measured, which in turn is inversely proportional to the resonance bandwidth [199]. For this grating, the FWHM is around twice as high as the previous studied grating (electric-arc - $LP_{1,7}$), thereby limiting the accurate detection of the resonant peak. On the other hand, it is important to emphasize that, considering two gratings manufactured with the same period and length, one by electric-arc and the second by UV-exposure; the one written by the arc-technique presents higher sensitivity to the SRI. This occurs, due to the physical modulation in the surface of the optical fiber, induced by the arc, that enhances the evanescent field.

The resonance wavelength as a function of temperature is shown in Figure 5.11. An increment in the temperature results in a shift of the resonant peak to shorter

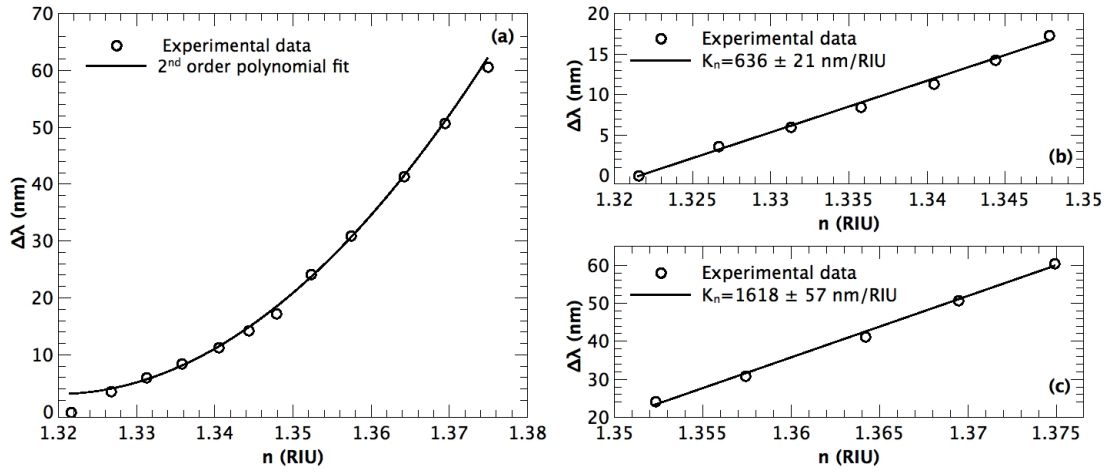

Figure 5.10: Response of the resonant wavelength to the changes in the SRI for the full range studied (a) for the range 1.32-1.35 RIU (b) and for the range 1.35-1.38 RIU (c).

wavelengths. A linear behavior is noticeable and a sensitivity of 177 ± 2 pm/°C is assessed from the slope of the calibration curve. The reproducibility of the measurements was not studied, due to the absence of a second grating with similar features.

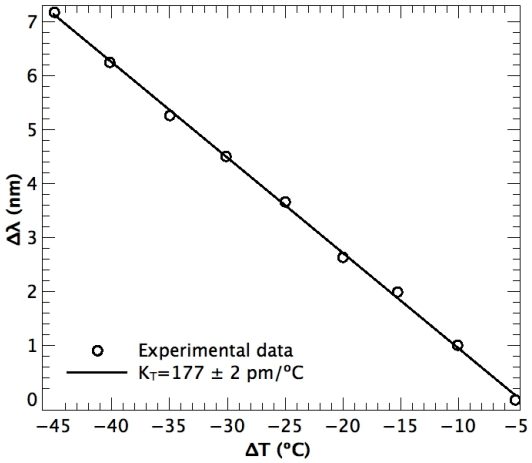

Figure 5.11: Resonant wavelength variation as a function of temperature.

LPGs show a high sensitivity to the SRI, nevertheless, they are also sensitive to temperature. The influence of temperature must be accounted for when high resolution RI measurements are carried out for high sensitivity detection of biological or chemical parameters. Therefore, the desirable situation is to have a system capable of measuring simultaneously the temperature and the SRI or of measuring the SRI independent from temperature. In the next section, a PS-LPG is evaluated to serve

as a device for simultaneous measurement of both parameters.

5.6 Phase Shifted Long Period Gratings

The measurement of RI independent from temperature is a crucial issue for high resolution refractometric sensing. A number of techniques have been proposed in order to get rid of the temperature cross-sensitivity mainly based on the use of a second grating sensitive only to temperature or with different sensitivities for both parameters [42–45]. In this context, Huang *et al.* [47] presented a reflection based PS-LPG for simultaneous measurement of temperature and refractive index, arising from the different sensitivities of each peak to both measurands. One advantage of using point-to-point (such as the electric-arc discharge) writing technique is the versatility for device fabrication. This technique allows to change the writing parameters, after each point, producing a complex pattern of modulation in refractive index along the fiber. In particular, it is possible to introduce a phase-shift ($\Delta\varphi$) in the LPG. In this case, the PS-LPG is obtained by introducing a separation Lp between two gratings sections, with the same grating period (Λ), for $Lp < \Lambda$ [200]. The relationship between the phase-shift and the distance Lp is given by [48];

$$\Delta\varphi = 2\pi\frac{L_p}{\Lambda}. \tag{5.1}$$

In this context, and exploiting the possibility of the measurement of the SRI and temperature without ambiguity with a single device, a PS-LPG was produced with the same set of fabrication parameters used for the previous gratings. The period of the LPG was 396 μm. The first LPG section was fabricated up to the point where the transmission loss at the resonance wavelength around 1555 nm was approximately 6.9 dB. When this point was reached, the fiber was translated by $Lp \approx$198 μm to introduce the phase shift and, afterwards, the writing process was repeated for the second LPG section until the desired transmission spectrum was achieved. In this case the phase shift is π, originating two peaks symmetrically located around a central wavelength. Figure 5.12 shows the final transmitted spectrum of the obtained device, where two peaks are observed corresponding to the $LP_{1,6}$. The first one centered at 1539.29 nm, with 23.75 dB depth and FWHM of 17.11 nm. The second one centered at 1574.76 nm, with 26.52 dB depth and FWHM of 18.95 nm. Finally, a small advantage associated with these gratings is the FWHM, they present narrower peaks, allowing more accurate tracking of λ_R, and consequently an improvement in the resolution [199].

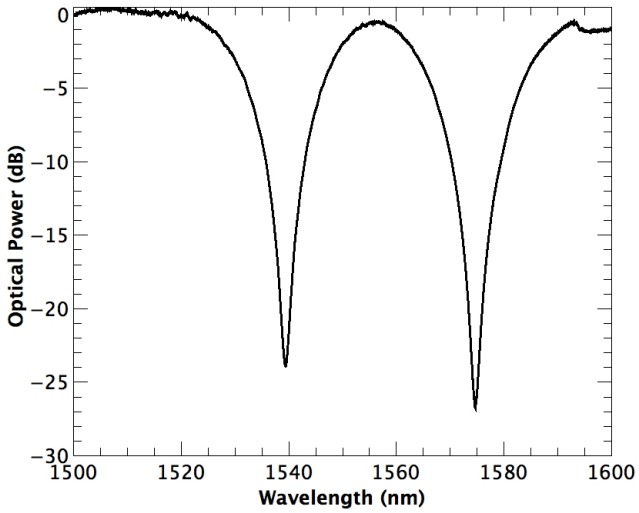

Figure 5.12: Transmission spectrum of a PS-LPG with period of 396 μm, and a $Lp \approx$198 μm.

Figure 5.13(a) illustrates the wavelength shift of the two resonant peaks. As expected a second order polynomial response is observed. Note that the second peak, which correspond to the larger wavelength, shows slightly higher sensitivity than the first one (shorter wavelength), probably due to enhanced evanescent interaction which is proportional to the wavelength. Figure 5.13(b) and (c) present two regions of lower and higher range of RI. Sensitivities of 125 ± 3 nm/RIU and 144 ± 4 nm/RIU were obtained for the first and second peak, respectively, in the range between 1.321-1.345, whilst a sensitivities up to 257 ± 8 nm/RIU and 301 ± 9 nm/RIU were estimated for the first and second peak, respectively, when operating for a SRI between 1.35-1.375. Average refractive index resolutions of ± 5.1×10^{-5} RIU and ± 4.4×10^{-5} RIU were calculated for the first and second peak, respectively, in the lower RI range and ± 2.8×10^{-5} RIU and ± 2.3×10^{-5} RIU were estimated for the first and second peak, respectively, for the higher RI range.

The resonance wavelength as a function of temperature is shown in Figure 5.14. A sensitivity of 114 ± 1 pm/℃ and 122 ± 1 pm/℃ is assessed from the data. Concerning the reproducibility of the sensing characteristic, it is possible to affirm that, during the experiments few PS-LPGs with similar features (period, length, resonance wavelength and depth) were studied, it was noticeable that within the error presented, they all exhibited an similar sensitivities.

For the possibility of simultaneous measurement, the matrix method is used. The principle behind the measurement of N number of parameters relies in the identifica-

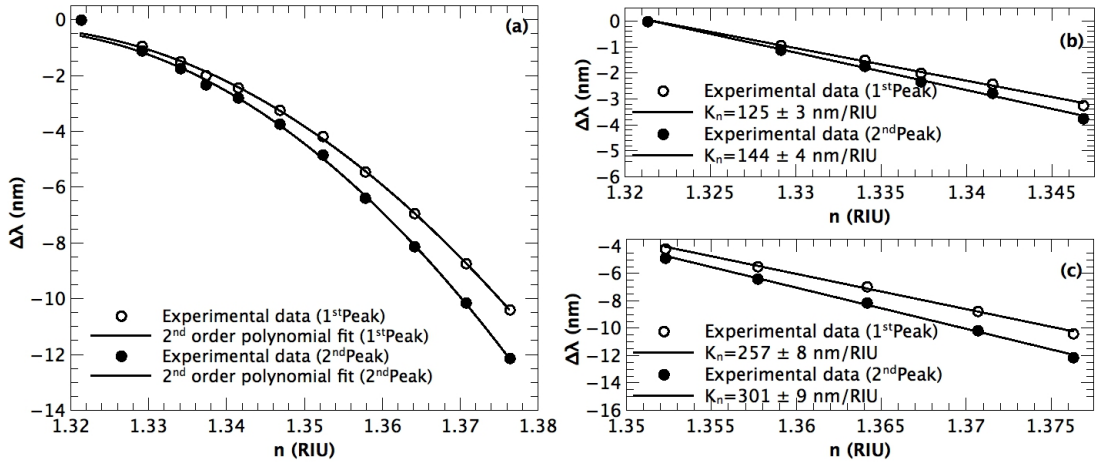

Figure 5.13: Response of the resonant wavelength to the changes in the SRI for the full range studied (a), for the range 1.32-1.345 RIU (b) and for the range 1.35-1.375 RIU (c) .

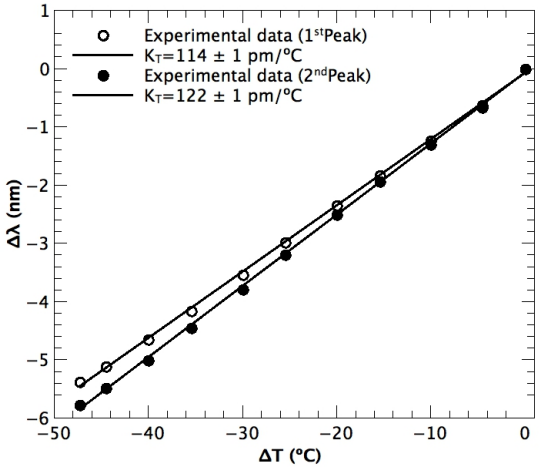

Figure 5.14: Resonant peak wavelength change as a function of temperature.

tion of N characteristics of the sensing probe that change differently under the action of the measurands of interest. If this happens, and in the particular but important case of linear dependences, it is always possible to write N independent equations that allows explicit solutions for the value of each measurand, even in the situation where all of them are changing [8]. The latter corresponds to the characteristics of the PS-LPG studied above, where two peaks respond differently and simultaneously to temperature and SRI changes, which enable the writing of a system of two equations for Δn (low SRI range) and ΔT, given in matrix form as;

$$\begin{pmatrix} \Delta\lambda_{P1} \\ \Delta\lambda_{P2} \end{pmatrix} = \begin{pmatrix} 0.114 \pm 0.001 & 125 \pm 3 \\ 0.122 \pm 0.001 & 144 \pm 4 \end{pmatrix} \begin{pmatrix} \Delta T \\ \Delta n \end{pmatrix}. \tag{5.2}$$

However, within the presented errors, the equations for both peaks are linearly dependent, and consequently, is not possible to have the measurement of both parameters without ambiguity. Contrarily to the work presented by Huang *et al.* [47], this transmission PS-LPG is not suitable to perform the simultaneous measurement. The main difference between both works is the reflection nature of the first one, in that case, the LPG is located a $\frac{\Lambda}{4}$ away from the silver mirrored tip. In such a case, the phase of the light traveling into the cladding should suffer a deviation at the silica-silver interface, consequently affecting the response of the signal of both peaks for the different parameters.

As explained in the section 3.4.3.3, the response of a bare LPG to the SRI is scarcely sensitive for the lower range of RI, close to water index, where usually the bioassays are performed. This behavior can be changed by depositing a HRI layer onto the grating. In the next section, the enhancement of electric-arc written LPGs by using HRI layers will be investigated.

5.7 High Refractive Index coated Long Period Gratings

In this section the increment of sensitivity of arc-induced LPGs coated with HRI overlays will be studied. Initially PS dissolved in chloroform was used as a HRI layer and finally a sol-gel co-doped with zirconium oxide (ZrO) and zinc oxide (ZO) was evaluated. The response of the coated devices to the external index and temperature was studied. The bare devices were coated by drag-coating process, where the stretched fiber passes through a drop of the coating solution (with few tens of μl) at a controlled and constant withdrawal speed (this control was done by a motorized

translation stage). The thickness of the layers was controlled by adjusting the viscosity and withdrawal velocity. By using a slow withdrawal speed, the solution has more time to drain from the fiber and a thinner coating layer will be deposited, whereas if a high withdrawal speed is used the solution has less time to drain and more particles will be deposited on the surface, leading to thicker films. The particle concentration of the solution affects its viscosity and has an effect on the film thickness. If the particle and aggregate concentration in the solution are low, thinner films are deposited compared to films which have been deposited from a solution with a high particle concentration [201]. The procedure and experimental setup for RI and temperature measurement was the same employed earlier, with a slight difference, the aim of this experiment is to increase the sensitivity of the LPG for lower RI range, thus, the gratings were characterized only in the SRI range between 1.32-1.35 RIU.

5.7.1 Polystyrene coated Long Period Gratings

PS is a common plastic present in every day life. Thin films of PS can be deposited in optical fibers by conventional coating techniques such as dip-coating or drag-coating. In addition, due to its good optical properties, thin films of PS represent a good choice from the point of view of the device optical design. PS was previously used as a HRI overlay to enhance the sensitivity of LPGs [41, 69, 176, 202] and, at the same time, it is largely used for biomolecules immobilization [36, 203–205].

For this experiment an LPG fabricated by electric-arc technique was employed. The grating was fabricated in a standard SMF-28 fiber using the same set of parameters described in the section 5.4. The grating period was 397 μm and the number of discharges 86 in order to produce a resonant wavelength at approximately 1586 nm, corresponding to the $LP_{1,6}$ cladding mode. The resonance depth and FWHM were around 22 dB and 39 nm, respectively. As exposed previously, a drag-coating technique was employed to deposit the thin films of PS (M.W. 280.000, Sigma Aldrich) whose refractive index is around 1.59. The deposition process onto the grating consists on passing the stretched fiber through a drop (75 μl) of the chloroform solution of the polymer at a velocity of 2 mm/s. Different overlay thicknesses were obtained for different experiments by changing the solution concentration, namely 5.5, 6 and 6.5 % by weight of PS. In all the experiments, the same LPG was used, before each deposition the LPG was cleaned with chloroform, to ensure that the PS had been completely removed. After solvent evaporation (few seconds), the coated device was ready for characterization. Previously, samples in bare fibers were deposited with the same parameters and characterized through scanning electron microscopy (SEM). Figure

5.15 illustrates this study. It is noticeable the homogeneity of the thin films, and from this information an approximate thickness can be inferred. The resulting overlay thicknesses after coating from the 5.5, 6 and 6.5 % solutions were approximately 385 nm, 420 nm and 515 nm, respectively.

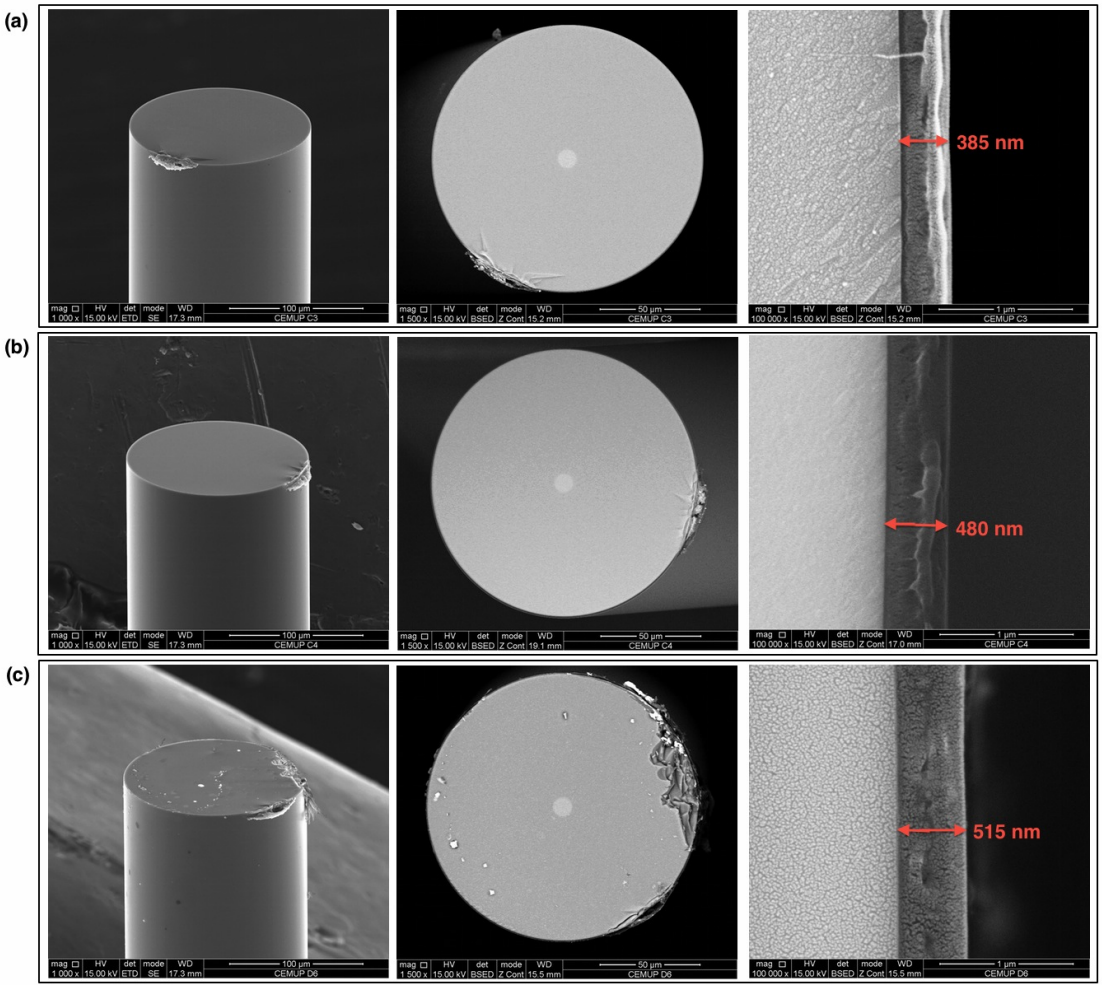

Figure 5.15: SEM images for the different coated fibers with 5.5 (a), 6 (b) and 6.5 % (c) of PS.

Figure 5.16 shows the spectral position of the resonance related to the 6^{th} cladding mode for the bare device and for the coated grating for three different films. It was measured a wavelength shift around 18 nm, 22 nm and 28 nm for the coated gratings with 385 nm, 480 nm and 515 nm thicknesses, respectively.

Figure 5.17(a) illustrates the response of the 385 nm PS coated LPG to the SRI. The behavior is linear and a sensitivity of 360 ± 7 nm/RIU was estimated for the range between 1.321-1.345. A resolution of ± 1.5×10^{-5} RIU can be calculated. The

temperature behavior is shown in Figure 5.17(b). From the curve slope, a sensitivity of 144 ± 1 pm/°C was measured.

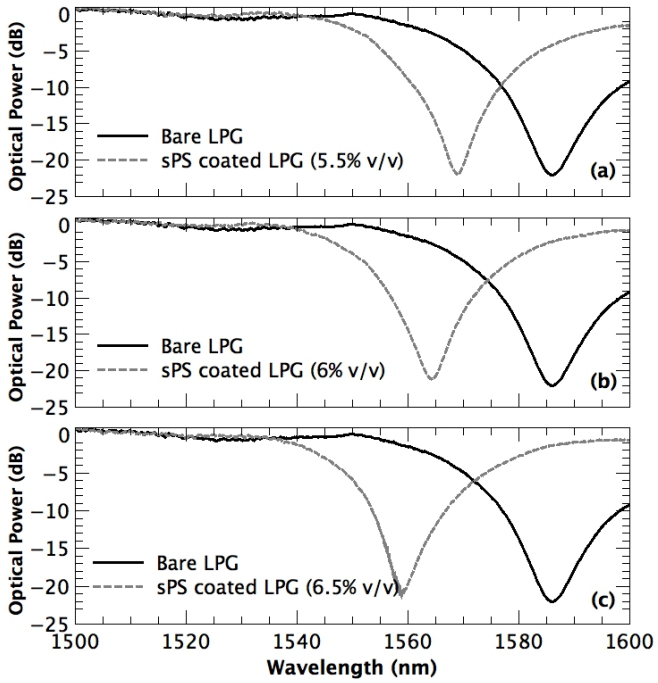

Figure 5.16: LPG resonance spectrum before and after deposition for PS coatings with a thickness of 385 nm (a), 480 nm (b) and 515 nm (c).

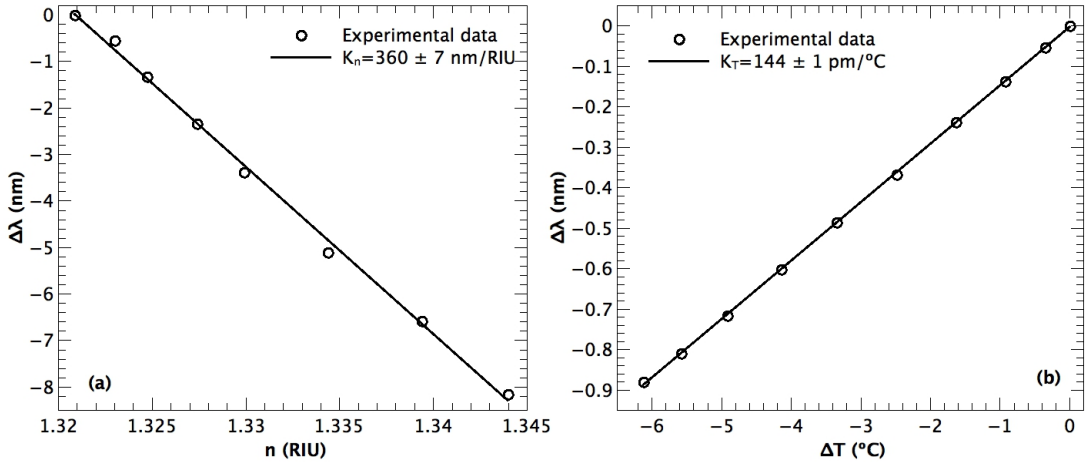

Figure 5.17: Resonant wavelength change as a function of SRI (a) and temperature (b) for a 385 nm PS coated LPG.

The response to the external index obtained from the 480 nm PS coated grating is shown in Figure 5.18(a). A linear behavior is observed and from the slope of the

curve a sensitivity of 770 ± 7 nm/RIU was calculated for the range between 1.321-1.345. From the statistics of acquired data a resolution of ± 1.03 $\times 10^{-5}$ RIU can be estimated. The temperature behavior is shown in Figure 5.18(b). From the curve slope, a sensitivity of 255 ± 4 pm/°C was measured.

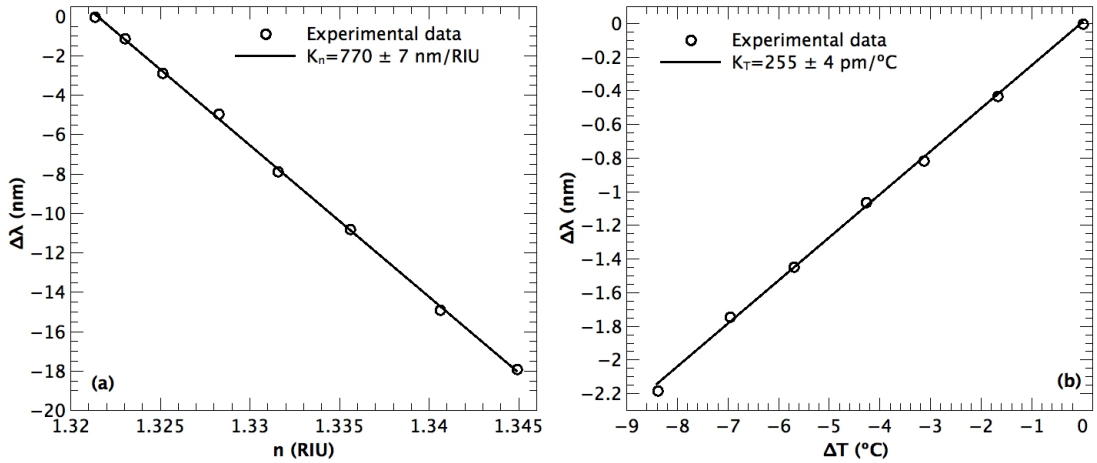

Figure 5.18: Resonant wavelength change as a function of SRI (a) and temperature (b) for the 480 nm PS coated LPG.

Finally, the sensitivity characteristic of the 515 nm PS coated LPG to SRI changes is shown in Figure 5.19(a). It appears to have a decreasing non-linear monotone trend, with a maximum sensitivity achieved when the external index is close to the water index. Considering just the first four points of the calibration (Figure 5.19(b)), for the range of RI between 1.321-1.322, a linear behavior is observed and a sensitivity of 2729 ± 92 nm/°C can be estimated.

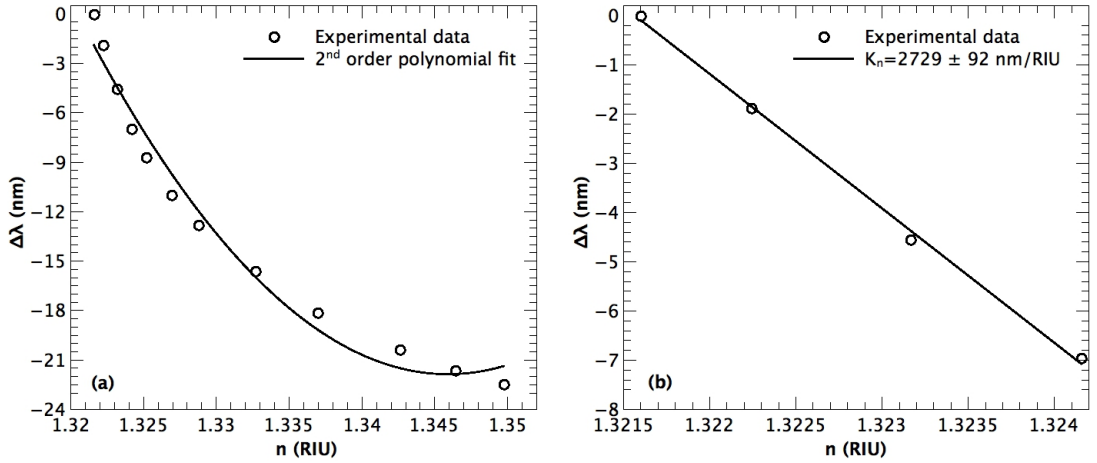

Figure 5.19: Resonant wavelength change as a function of external index for the full range studied (a) and for the range 1.3215-1.3224 RIU (b).

A resolution of ± 1.85 $\times 10^{-5}$ RIU can be inferred from the statistics of the acquired values. The temperature behavior is shown in Figure 5.20. From the curve slope a sensitivity of 303 ± 5 pm/°C was estimated.

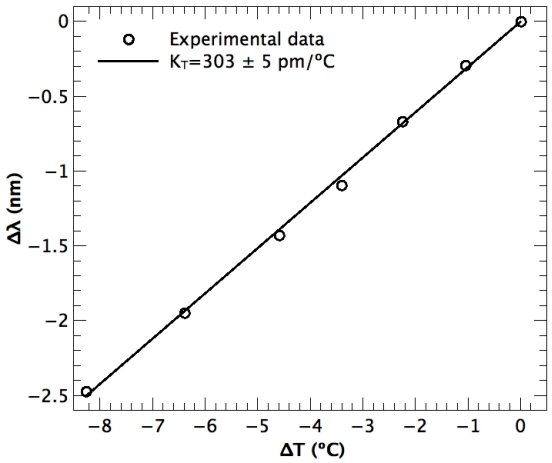

Figure 5.20: Resonant wavelength change of the 515 nm coated PS LPG as a function of temperature.

The goal of this work to increase the LPG sensitivity was successfully achieved by depositing PS onto the fiber grating. In Table 5.1, the summary of the results obtained is presented. It is clear, that by increasing the thickness of the PS layer, the evanescent field becomes stronger, increasing also the sensitivity to the SRI. Additionally, it is also noticeable the capability of tailoring the sensitivity to the external index, in order to have a maximum, at certain range of RI. For instance, with the film thickness of 515 nm, apparently the peak of sensitivity is close to water RI, which is ideal for biological applications. Nevertheless, and despite the capabilities of these coatings to enhance the sensitivity of the grating to the SRI and its widespread use for biomolecules immobilization, the sensitivity to temperature also increases considerably (due to the high thermal expansion coefficient, which is roughly 21 times higher than the silica), which is an undesirable side effect. In the next sub-section, HRI overlays based on sol-gel coatings will be presented.

Film Thickness	K_n (nm/RIU)	K_T (pm/°C)
Bare LPG	147 ± 3	114 ± 1
385 nm	360 ± 7	144 ± 1
480 nm	770 ± 7	255 ± 4
515 nm	2729 ± 92	303 ± 5

Table 5.1: PS coated LPGs: a comparison.

5.7.2 Sol-gel coated Long Period Gratings

Sol–gel technique is considered one of the fastest growing fields of contemporary chemistry. It offers a low temperature alternative to conventional glass production, enabling final products with high homogeneity and purity. The sol–gel dip-coating method is a versatile technique that enables the preparation of coatings for optical fibers [206, 207]. This technique has been widely used in fiber optics biochemical sensing, for entrapping chemical or biological active agents on the surface of the optical fiber [25, 38, 106, 206, 208].

In sol–gel synthesis, typical precursors solutions have metal alkoxides (like titanium and silicon alkoxides), water, an acid or a base and also an alcoholic solvent. In an aqueous environment, together with an acid or base catalyst, alkoxides start to hydrolyze and condensate, which leads to particle formation in the sol. Sols are colloidal suspensions of solid particles (about 1–1000 nm) in a liquid. In the alkoxide based sols, the size of the particles and particle aggregation depend on the pH and sol concentration used. Typically, the particle size in an alkoxide based sol is between 2 and 10 nm. If the sol is very dilute, the gelation of the sol can be a very slow process or the sol can become stable. A gel is considered to be formed when a continuous solid skeleton encloses a continuous liquid phase. During the drag-coating process, the fiber passes through the sol and withdraws from the sol at a constant speed. During the film deposition, particles from the sol are deposited on the fiber surface and the solvent is evaporated. The deposited gel can be further heat-treated in order to densify the coating. The coating process can take place at room temperature. Typically, sol–gel produced materials are nano-porous because of the nature of the sol: a sol contains nano-particles, and, after gel formation and drying, these particles are very close to each other and the pores are formed in between these particles. The refractive index of the film mainly depends on the coating material and the resulting porosity; for example, titanium and zirconium (Zn) coatings have a higher refractive index than silica (SiO_2) coatings [209]. Thin coatings with different refractive indices can be prepared with by sol–gel method. The refractive index and the thickness of sol–gel derived thin coatings can be controlled , in theory, gives the opportunity to increase the sensitivity of the LPGs.

For this experiment LPGs fabricated by electric-arc technique were used. The gratings were fabricated in a standard SMF-28 fiber using the same set of parameters as before. The grating period was 396 μm and the number of discharges between 85-90 in order to produce a resonant wavelength at approximately 1555 nm, corresponding

to the $LP_{1,6}$ cladding mode. The resonance depth and FWHM were around 22-25 dB and 28-30 nm, respectively.

The HRI coating was prepared by sol-gel method, using a solution provided by CGCRI, India. The solution of zinc oxide-zirconium dioxide (ZnO-ZrO_2) in a proportion (1:4) was prepared by sol–gel method from zinc acetate and zirconium oxychloride octahydrate (ZOO) as source of ZnO and ZrO_2, respectively, in ethanol-2-butanol solvent medium. Acetyl-acetone (AcA) (molar ratio, AcA:ZA= 1: 1.5) was used as a stabilizer. In order to increase the viscosity, the solution was heated up to 60 ℃, to have two solutions with different viscosities, part of the resultant solution was kept in heating for 3 h, whilst the remainder for 5 h. The resulting solutions were used to prepare overlays on the fibers by drag-coating technique; different withdrawal speeds in the range 1-4 mm/s were used. Before each deposition the LPG was cleaned with ethanol. The coated fibers were initially cured at room temperature for 8h, followed by 2 h in air oven at 400 ℃ to get oxide coatings. The refractive index of the coating is expected to be around 1.78 RIU.

After curing, the coated device is ready for characterization. Previously, samples in bare fibers were deposited with the same parameters and characterized through SEM. Nevertheless, due to the low electrical contrast between the silica of the fiber and the sol-gel of the coating, it was difficult to infer the thickness of the films. Figure 5.21 shows the top the the coated fiber, where it is possible to verify that indeed, the presence of the film is almost not perceptible.

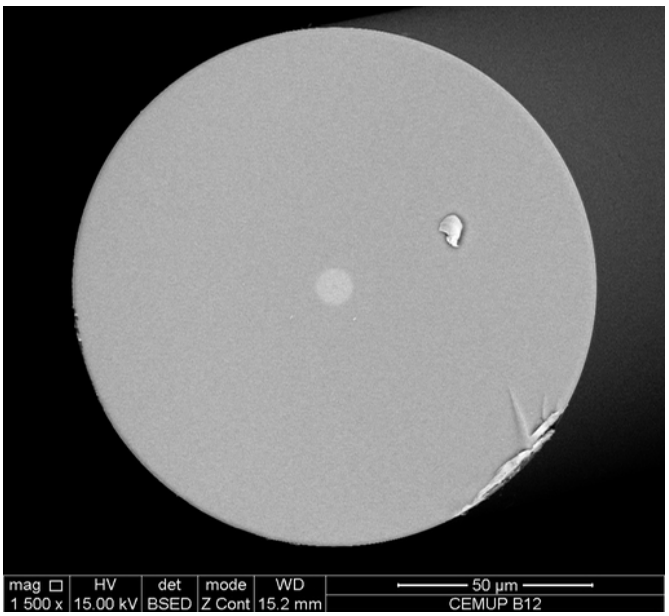

Figure 5.21: SEM image for a coated fiber (top view).

However, after coating, the fiber samples are cleaved and after cut, in a few regions the film cracks. As a result, few of the resulting fragments were used to evaluate/estimate the film thickness. Figure 5.22 shows the SEM images of the coated samples. It is noticeable the homogeneity of the thin films, and the approximate thickness was inferred. The resulting overlay thicknesses after coating were approximately 65 nm, 90 nm and 136 nm, respectively.

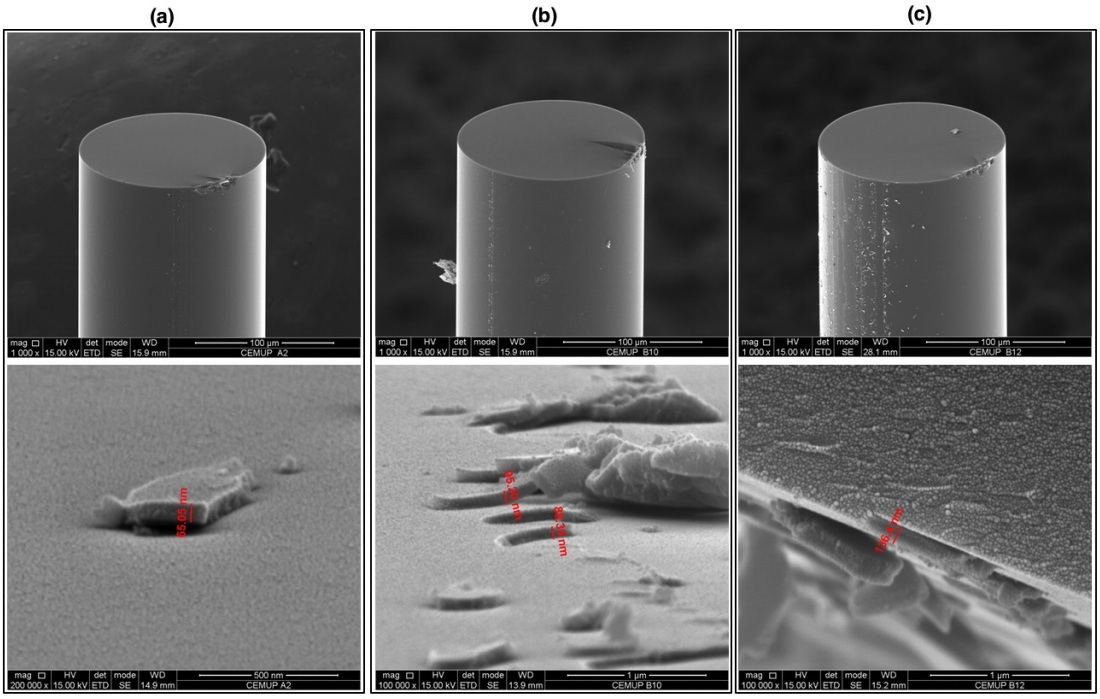

Figure 5.22: SEM images for the different coated fibers: 65 nm (a), 90 nm (b) and 136 nm (c).

Figure 5.23 shows the spectral position of the resonance related to the 6^{th} cladding mode for the bare device and for the coated grating for three different films. A wavelength shift of approximately 3.75 nm, 4.75 nm and 6.35 nm for the coated devices with 65 nm, 90 nm and 136 nm thicknesses, respectively, was measured. To evaluate the sensitivity enhancement produced by the nano-coating, both coated and bare LPGs were characterized for refractive index and temperature response.

Figure 5.24(a) shows the response of the 65 nm sol-gel coated grating to the SRI. The behavior is linear, and from the slope of the curve, a sensitivity of 234 ± 5 nm/RIU was estimated for the range between 1.321-1.35. A resolution of ± 4.2×10^{-5} RIU was calculated. The temperature behavior is shown in Figure 5.24(b), from the curve slope, a sensitivity of 128 ± 2 pm/℃ was estimated.

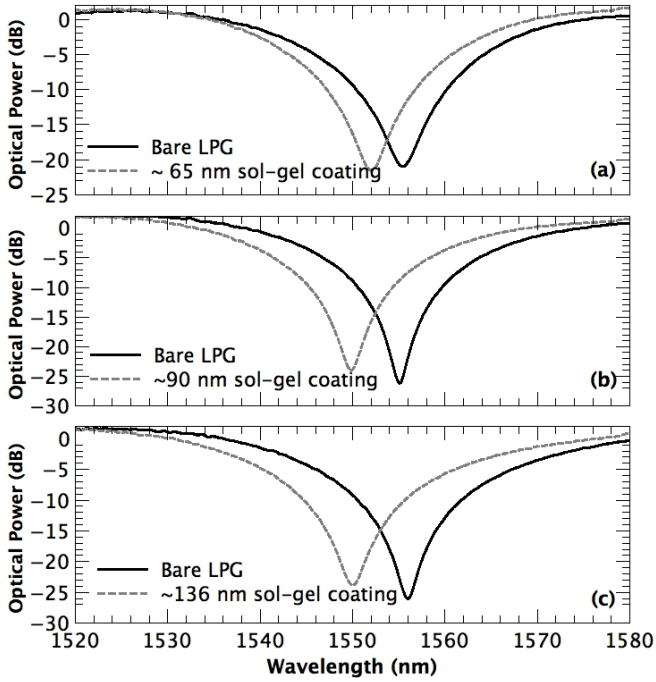

Figure 5.23: LPG resonance spectrum before and after deposition of thin silane films of 65 nm (a), 90 nm (b) and 136 nm (c).

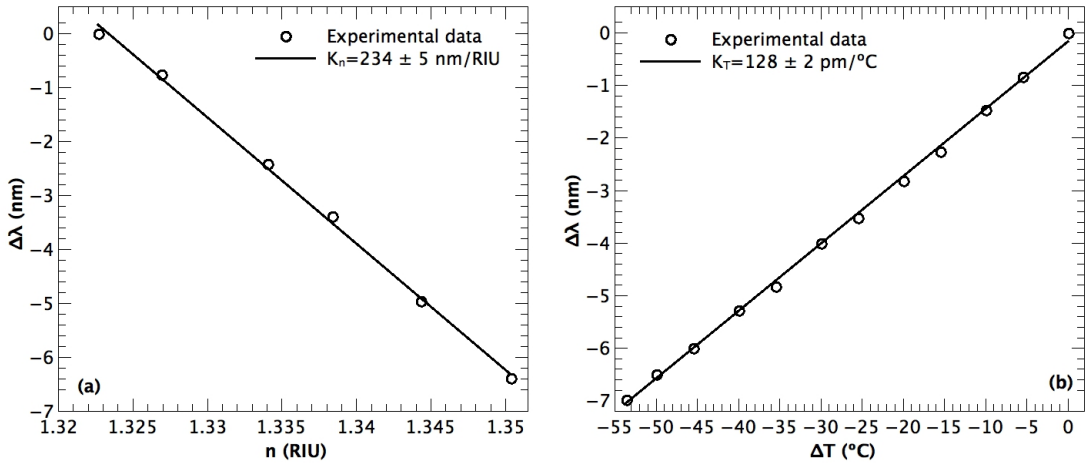

Figure 5.24: Resonant wavelength change as a function of SRI (a) and temperature (b) for a 65 nm sol-gel coated device.

The response to the external index from the 90 nm sol-gel coated grating is shown in Figure 5.25(a). A linear behavior is observed and from the slope of the curve, a sensitivity of 279 ± 9 nm/RIU was calculated for the range between 1.321-1.35. It was estimated a resolution of ± 3.8×10^{-5} RIU. The temperature behavior is shown in Figure 5.25(b). From the slope of the curve, a sensitivity of 132 ± 2 pm/°C was

measured.

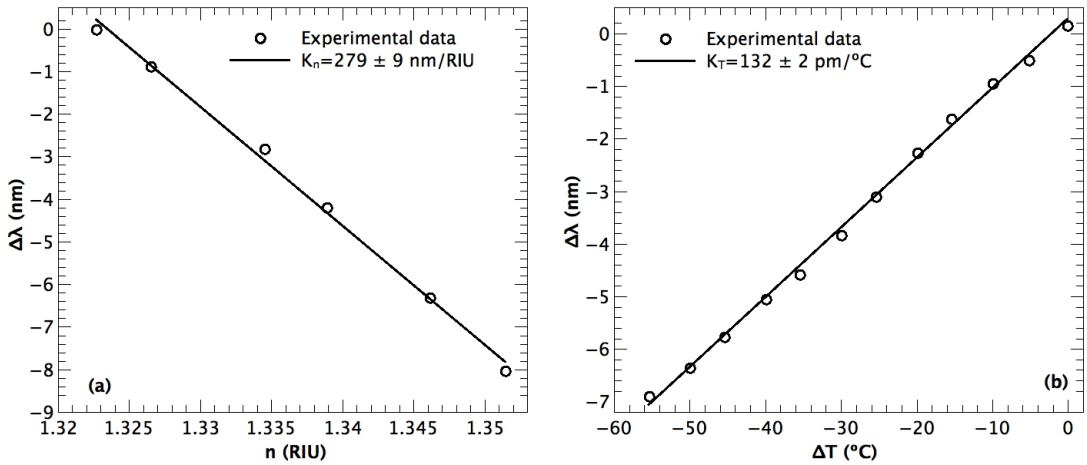

Figure 5.25: Resonant wavelength as a function of SRI (a) and temperature (b) for a 90 nm sol-gel coated LPG.

The behavior of the 136 nm sol-gel coated grating to SRI changes is shown in Figure 5.26(a). A linear behavior is observed and from the slope of the curve a sensitivity of 362 ± 8 nm/RIU was calculated for the range between 1.321-1.35. A resolution of ± 3.2×10^{-5} RIU can be inferred, from the statistics of the acquired data. The temperature behavior is shown in Figure 5.26(b). From the curve slope, a sensitivity of 153 ± 2 pm/℃ was estimated.

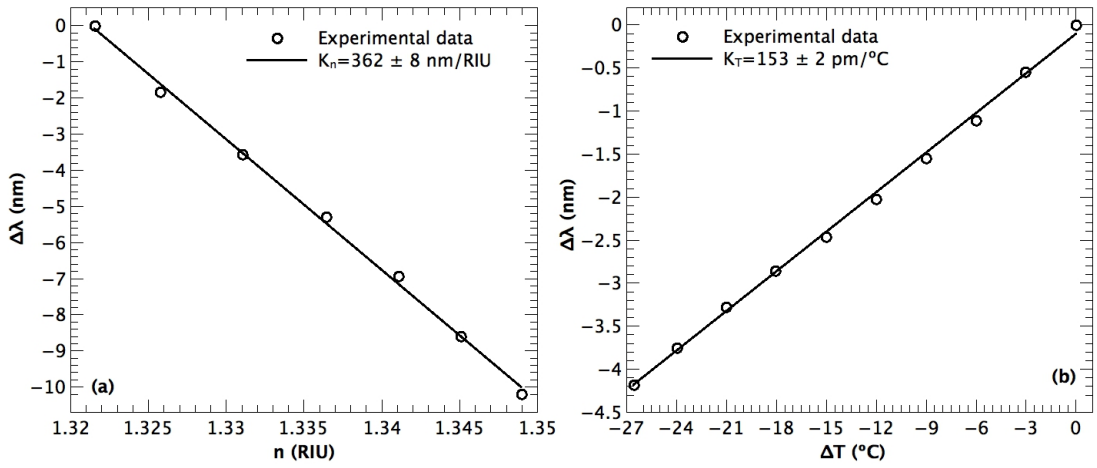

Figure 5.26: Resonant wavelength as a function of SRI (a) and temperature (b) for a 136 nm sol-gel coated device.

Finally, the sol-gel coating was also tested with an arc-induced LPG with a period of 339 μm. The set of parameters used was the same as before, the number of

discharges was 162. The resulting grating presents a resonant wavelength at approximately 1589.50 nm, corresponding to the $LP_{1,7}$ cladding mode. The resonance depth and FWHM were around 17 dB and 22 nm, respectively. The grating was cleaned with ethanol and coated with a silane layer of approximately 136 nm. The spectrum of the LPG after and before deposition is shown in Figure 5.27. It is observable a wavelength shift of 13.1 nm due to the HRI coating.

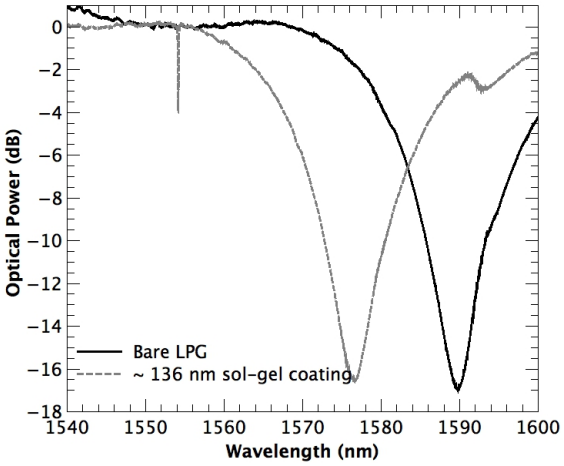

Figure 5.27: LPG resonance spectrum before and after deposition of thin silane coating of 136 nm.

Figure 5.28(a) illustrates the response of the last coated device to the SRI. A linear behavior is observed, from the slope of the curve a sensitivity of 717 ± 21 nm/RIU was calculated for the range between 1.321-1.355. From the statistics of acquired data a resolution of ± 1.5×10^{-5} RIU can be estimated. The temperature behavior is shown in Figure 5.28(b). From the curve slope, a sensitivity of 243 ± 4 pm/°C was measured.

As already detailed in the theory, with the four layer model, it is possible to determine the optimal thickness for a certain material (known RI) to tune the sensitivity peak of the response of the grating to a desirable range of RI (which in the present work is the water index). In the absence of such a model, and using the data obtained in the previous section, considering nTh, it is possible to estimate that to achieve similar results in terms of sensitivity for the 6^{th} order mode (Λ = 396 μm), a layer with a thickness of approximately 460 nm would be necessary, a thicknesses value far from the obtained in the performed experiments, but that can be achieved using more viscous solutions.

Concerning, the 7^{th} order cladding mode, we do not have a term of comparison (with PS coated), however, comparatively with lower order mode, the sensitivity

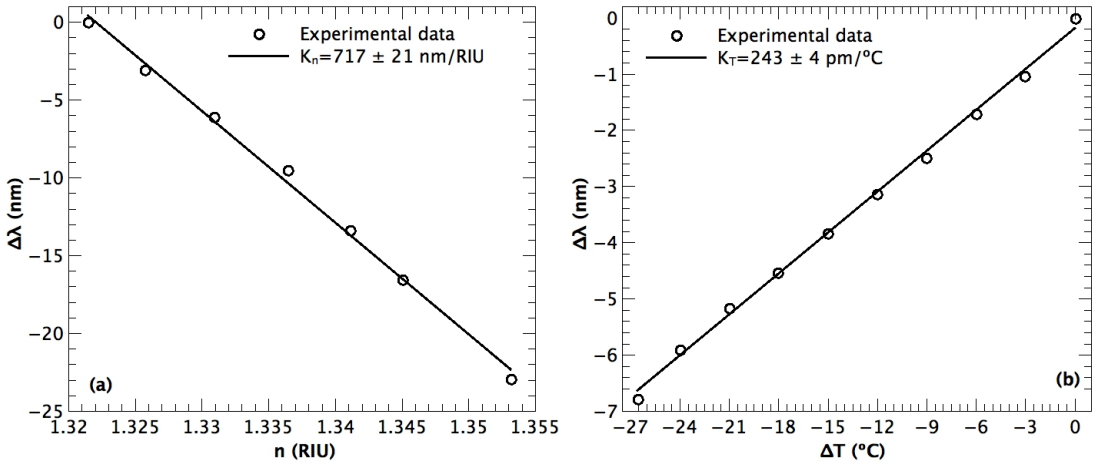

Figure 5.28: Resonant wavelength as function of SRI (a) and temperature (b) for a 136 nm sol-gel coated device

was improved as expected. In this work the potential and feasibility of the use of silane based HRI layers to increase the sensitivity of LPGs was demonstrated as an alternative to the PS coated devices previously studied. Table 5.2 summarizes the results obtained in this section.

Film Thickness	K_n (nm/RIU)	K_T (pm/°C)
Bare LPG (6^{th} order)	147 ± 3	114 ± 1
65 nm	234 ± 5	128 ± 2
90 nm	279 ± 9	132 ± 2
136 nm	362 ± 8	153 ± 2
Bare LPG (7^{th} order)	290 ± 6	165 ± 16
136 nm	717 ± 21	243 ± 4

Table 5.2: Silane coated LPG: a comparison.

Comparing PS and co-doped silane coated LPGs, it is possible to affirm that, PS is an easier material to work with. Due to the nature of the solution (PS dissolved in chloroform), it is simple to control the concentration and consequently the thickness of the layer. Moreover, the cure is practically instantaneous, and it is also easy to remove the layer using the solvent. As a disadvantage, it is not possible to work at high temperatures and it drastically increases the thermal sensitivity of the device.

On the other hand, the silane coated devices, are capable to work at high temperatures, and chemically more resistant. However, it involves complex process for the solution preparation, control of the viscosity, as well as for the curing. Additionally, the layer is difficult to remove. Nevertheless, this increased complexity in the prepa-

ration, can further allow to dope the coating material with a chemically sensitive substance, opening the possibility of having a high sensitive chemical sensor.

Optical interferometry is a well established technique and it is associated with high RI accurate measurements. LPG based interferometers have shown that, it is possible to achieve higher resolution in the RI measurement when used instead of a single LPG. In the next section, a Mach-Zehnder LPG based configuration is studied.

5.8 Mach-Zehnder LPG

An optical interferometer is an instrument in which two or more optical path lengths are compared and the resultant intensity varies with the relative optical path difference, with a period equal to the optical wavelength. Thus, optical path lengths can be measured on the scale of the wavelength of light [2]. The emergence of SMF and related components made possible to construct in-fiber interferometers, equivalent to bulk-optic interferometers that are robust enough to be used in practical applications, outside the laboratory environment.

In this context, modal interferometers are very attractive, particularly the ones with the reference path along the optical fiber core and the sensing path associated to a specific cladding mode excited by an LPG. These interferometric devices are appealing to SRI sensing because it is possible to tune the device sensitivity by selecting the order of the excited cladding mode, the length of the device, but also due to the reduced thermal sensitivity of the interferometer (depending on the fiber, the thermo-optic coefficients of the core and cladding modes are not substantially different). The most common structure of this type is based on the Mach-Zehnder configuration: a pair of LPGs are written into the fiber, separated by a distance L, to induce interference between the core and a selected cladding mode [49]. It is also possible to have an LPG based interferometer in a Michelson layout if the light crosses a single LPG twice by mirroring the fiber tip at a distance L from the grating [51].

The Mach-Zehnder LPG (MZ-LPG) interferometer is obtained by writing in series two identical LPGs, with around 3 dB of resonance depth (half of the power), separated by a distance L, where an interferometer cavity is formed between the two gratings. The typical configuration is shown in Figure 5.29. In this situation, the first LPG couples a fraction of light to a specific cladding mode, whereas the remaining light keeps propagating in the fiber core. Due to the presence of a second identical LPG, light propagating in the cladding is coupled back to the fiber core where interference with the core mode occurs.

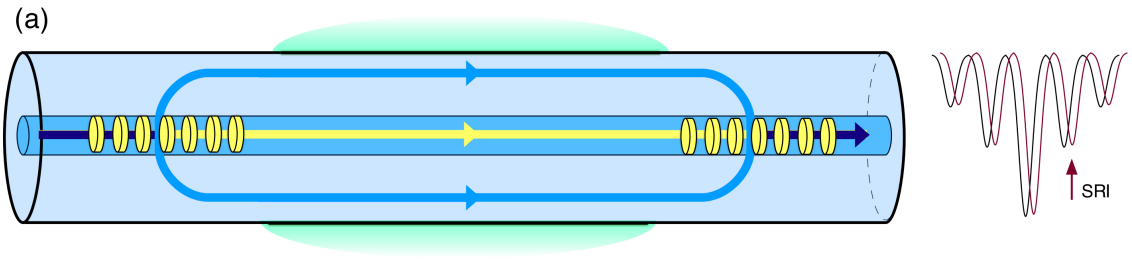

Figure 5.29: Schematic of an in-fiber LPG based Mach-Zehnder interferometer.

The intensity of a Mach-Zehnder interferometer at certain wavelength is given by the equation of a two wave interferometer;

$$I = I_1 + I_2 + 2\sqrt{I_1 I_2}\cos\left(\frac{4\pi\Delta n L}{\lambda} + \phi_0\right), \tag{5.3}$$

where I_1, I_2 are the optical powers traveling in the core and the cladding and depend on the grating coupling coefficients, Δn is the difference of refractive index between the m^{th} cladding mode and the core mode (in the range of 10^{-3} RIU, depending on the order of the mode), L is the distance between the center of both devices and ϕ_0 the initial phase of the interferometer. The characterization was made following the procedure described in section 5.3. The experimental setup is shown in Figure 5.30, it is also similar with the difference that both of gratings were out the measurement chamber, and just the region between them was in contact with the solution.

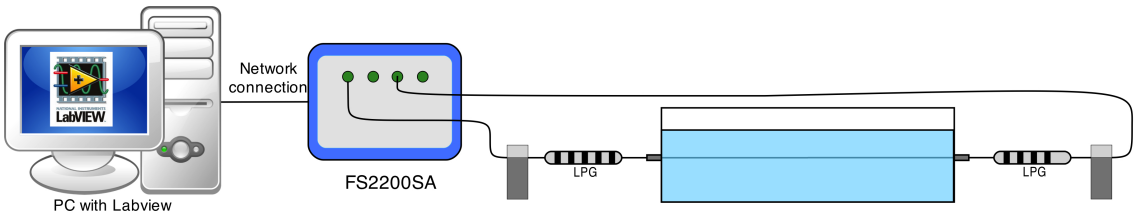

Figure 5.30: Experimental setup for the characterization of a MZ-LPG for RI and temperature.

The MZ-LPG used in this experiment was produced by electric-arc technique, with the same set of fabrication parameters used for the previous gratings. The period of the LPGs were 396 μm. The first LPG was fabricated up to the point where the transmission loss at the resonance wavelength around 1560 nm was approximately 3 dB. When this point was reached, the fiber was translated by a distance of 100 mm and, afterwards, the writing process was repeated for the second LPG until the maximum visibility of the interference fringes was achieved. The spectrum of the

LPG used is show in Figure 5.31. It is observable the channelled spectrum, resulting from the interference between the excited cladding mode ($LP_{1,6}$) and fundamental core mode ($LP_{0,1}$). The fringe period is around 5.30 nm.

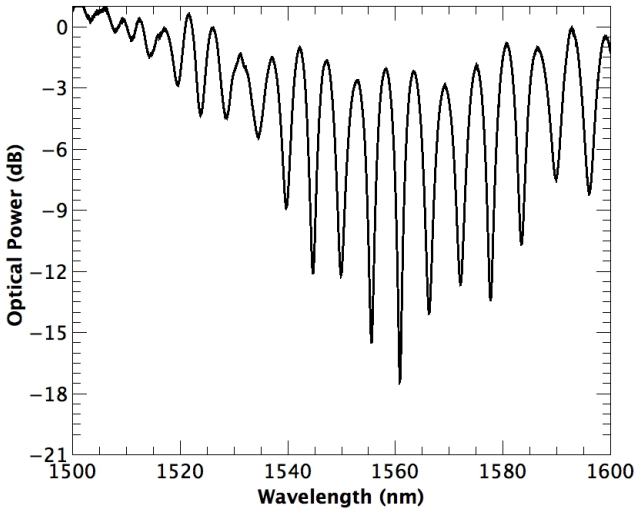

Figure 5.31: Transmission spectrum of the MZ-LPG used in the experiment.

The wavelength shift of the the fringe pattern of the MZ-LPG in function of the SRI is presented in Figure 5.32(a). A non-linear behavior is observed, with approximately two linear regions. Figure 5.32(b) and (c) illustrates the two regions evaluated. Sensitivities up to 56 ± 4 nm/RIU were obtained for the range between 1.321-1.35, and a sensitivity around 177 ± 8 nm/RIU resulted when operating for SRI between 1.355-1.38.

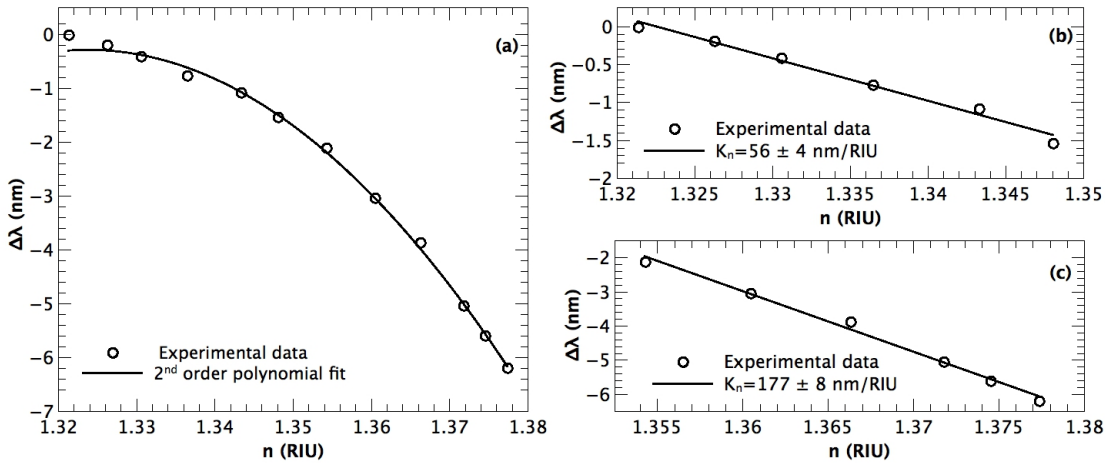

Figure 5.32: The wavelength shift of the the fringe pattern of the MZ-LPG to the changes in the SRI for the full range studied (a), for the range 1.32-1.35 RIU (b) and for the range 1.35 - 1.38 (c).

A resolution of ± 1×10^{-4} RIU for the lower RI range and ± 4.4×10^{-5} RIU for the higher RI range was achieved. The resonance wavelength as a function of temperature is shown in Figure 5.33. An increment in the temperature results in a shift to higher wavelengths. A linear behavior is noticeable and a sensitivity of 70 ± 1 pm/℃ is assessed from the slope of the calibration curve. Regarding the reproducibility of the sensing characteristic, it is possible to assert that, during the experiments, few MZ-LPGs with similar features (mode, length) were studied, it was observed that within the error presented, they all exhibited an analogous behavior.

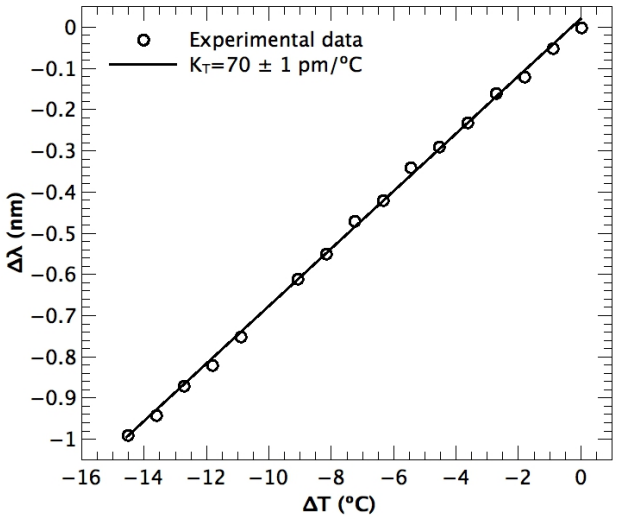

Figure 5.33: Resonant wavelength as a function of temperature.

In the same way as done above, the vast majority of LPG based interferometers (and other probes from the same nature) reported in the literature, the sensing response was recorded by monitoring the wavelength shift of the resultant fringe pattern with a spectrometer, OSA or another spectrum analyzer device [56, 64, 210–215]. However, this interrogation method does not show the real potential in terms of sensitivity of the sensing device. However, the wavelength shift of the fringe pattern is proportional to the interferometric phase and the latter parameter is inherently related with the periodicity of the fringes. Thus, an identical wavelength shift for instance of 5 nm for cavities with periodicities of 5 nm and 10 nm respectively, will lead different phase changes. Assuming that a period represents 2π, the phase change will be 2π and π respectively. It means, as expected, for the same wavelength shift, the fringe pattern with shorter period, i.e. bigger cavity and with greatest interaction region shows two times higher sensitivity. It was shown by Swart *et al.*, a Fourier analysis to convert the wavelength shift of fringe pattern into a phase shift [51, 216].

Nevertheless, it is more attractive the detection of the phase variation caused by the measurand with an interferometric readout system [217]. The interferometric readout system has several advantages. It takes full advantage of the interferometric nature of the sensing interferometers with increased sensitivity and resolution, using electrical modulation at high frequencies (kHz range) that permit to attenuate the effect of the $\frac{1}{f}$ noise of the electronics devices. High-performance interferometric demodulation techniques have achieved phase resolutions as small as $\pm$ 10^{-6} rad. Moreover, it is potentially low cost, when compared with spectral interrogation systems; the phase detection can be implemented with relatively low cost optoelectronics using coherence addressing and optical demodulation. Additionally, coherence addressing also enables coherence multiplexing on interferometric devices [218–221]. LPG based interferometers have been interrogated by using phase readout systems showing its potential as high resolution platform for refractometric sensing [222, 223]. For instance, considering the period of the interferometer used in this experiment (5.3 nm) and departing from the calibration shown in Figure 5.32(b), the sensitivity in radians would approximately 66 rad / RIU. Using a readout interferometer with a resolution of 10^{-5} will led a the detection limit of 10^{-6}, about two orders of magnitude better. In the Chapter 7 a interferometric readout device system is described to measure RI with high accuracy.

5.9 Applications

In this section, two LPG based probes for biochemical applications are presented and described. Initially, a coated LPG with a p-nitro-phenol polymeric film is used for CO_2 measurement. Following, a DNA aptamer electrostatically immobilized onto an LPG surface, is used for *E. coli* detection and quantification in water samples.

5.9.1 Long Period Grating based Carbon Dioxide Sensor

The real-time determination of CO_2 concentration is an important issue in diverse fields, such as chemical and clinical analysis, food industry and environmental monitoring [224–226]. Specifically in aquaculture systems, the level of CO_2 is an important issue for fish health and development. Elevated dissolved carbon dioxide concentration (dCO_2) in the water will induce stress responses in fish causing significant physiological disturbances that can result in reduced growth and poor feed conversion. In spite of its critical nature in fish farms, presently existing systems for CO_2 determination, still do not satisfy the industry needs [227, 228].

Several fiber optic based configurations have been proposed for carbon dioxide detection mostly relaying in either colorimetric or fluorescence based methods. Segawa *et al.* [229] presented a CO_2 fiber sensor based on the pH indicator dye thymol blue, immobilized in a sol-gel matrix. The optical attenuation varied according with the CO_2 concentration due to absorption changes of an indicator dye caused by the carbon dioxide induced acidification. Amao and Nakamura [230], on the other hand, demonstrated a CO_2 sensor based in luminescence intensity changes of tetraphenylporphyrin (TPP) due to absorption changes of a co-immobilized pH indicator dye. Nevertheless, configurations using indicator dyes are prone to suffer from leaching and photobleaching effects. In addition, working in the visible range imposes some limitations in applications where remote and multipoint detection are a priority. Using direct absorption spectroscopy of the gas absorption lines in the mid infrared is also a reliable sensing mechanism. Nevertheless for remote multipoint sensing at these wavelengths ($\sim$ 4,6 μm) special chalcogenide glass optical fibers are needed, also, costly light sources and detectors are necessary [231]. Using higher vibrational harmonics it is possible to detect CO_2 also at 1.57 μm. Orghici *et al.* [232], showed that CO_2 concentration could be measured using an evanescent field sensor based on a quartz multimode fiber in this wavelength range. However, this approach required DFB laser sources, relatively long interaction lengths and was very sensitive to contamination of the fiber surface.

In this work, a CO_2 optical fiber sensor is proposed using standard optical fiber technology. In particular a polymer layer sensitive to CO_2 is deposited onto an LPG. The sensing layer is based on the acid-base equilibrium of phenol and of its derivative p-nitro-phenol, which, in the presence of CO_2, are protonated introducing changes in the optical signal. The initial idea was to have a membrane, that changes its own RI in presence of the gas, a preliminary characterization of the material, have shown variations also in absorption in the wavelength range around 410 nm. Thus, the sensing material was characterized in absorption and refractive index changes. The dual effect observed, demonstrates the possibility of CO_2 determination using either mechanism. Therefore, it is possible to use this sensitive layer with fiber optics in visible range using standard colorimetric arrangements or in refractometric configurations based in standard telecom optoelectronic components. The latter approach is quite promising in terms of multiplexing and remote monitoring capabilities. This work was framed within the project AQUAMONITOR PTDC/AAC-AMB/112424/2009, whose goal was to develop a CO_2 sensor for application in intensive aquaculture systems.

5.9.1.1 Principle and Experiment

The CO_2 sensitive layer is based on the acid-basic equilibrium of phenol and of its derivative p-nitro-phenol. They are kept in their deprotonated form in the sensing membrane. In the presence of carbon dioxide, hydrogen carbonate is formed that partially protonates the phenols. The hydroxyl group is involved in protolitic reactions that modifies the charge distribution in the molecule. As result of the interaction with carbon dioxide, a change in absorption and in refractive index is expected due to the delocalization of the electrons in the aromatic ring of these compounds. A quaternary ammonium compound, didodecyl-dimethyl-ammonium hydroxide (DDMA) was used to deprotonate the phenols, preparing them for being protonated by the analyte.

The sensing polymer layers were prepared from a 5% (m/m) polyurethane hydrogel (D4) dissolved in ethanol. Then 50 µl of 0.1 M ethanolic p-nitro-phenol and 100 µl of 0.1 M ethanolic DDMA solution were added to 500 µl of polymer solution. The response of the new sensitive material to CO_2 was characterized by absorption spectroscopy and its refractive index was also monitored using a fiber optic long period grating scheme.

For absorption spectroscopy characterization, the setup showed in Figure 5.34(a) was used. Several glass slides were coated by a casting method. The coated samples, which presented a yellow color, were homogeneous, and were placed in a test chamber and illuminated by a violet LED (λ_c at 410 nm) through a 4 mm diameter fiber bundle. The transmitted signal was collected through an identical fiber bundle and carried for detection. An Ocean Optics USB4000 spectrometer, connected to a PC, was used for the absorption measurements. The membrane thickness was approximately 1 µm. It is worth to note, that due to the rubbery characteristic of the deposited material, it was not possible to measure precisely the thickness of the layer.

Prior to the thin film deposition onto the LPG, a test was made with the sensing layer precursor cocktail, in order to determine the RI difference of the solution in its protonated (when submitted to CO_2 bubbling) and deprotonated states (bubbling with N_2), an FBG based FFPI was used [20]. The tip of the optical fiber sensor was immersed into the cocktail. Changes in the RI of the solution were retrieved through the visibility in the channeled spectrum, that was proportional to the index contrast in the fiber/cocktail interface. The visibility of its interferometric output was monitored using a scanning laser unit FS4200 from Fibersensing (Portugal), working in the wavelength range from 1520 to 1590 nm, with 1 pm max. resolution. Also, few silicon oxide slides were spin-coated with thicknesses around 400 nm and the RI of the

layer was estimated by ellipsometry at Instituto de Engenharia Biomédica (INEB). Then, the LPG was coated and subsequently characterized.

Figure 5.34(b) shows the schematic setup used to evaluate the CO_2 induced refractive index changes in the polymer layer using a LPG as the sensing probe. Coating the grating with the CO_2 sensitive membrane, it is possible to quantify the gas concentration as function of the resonance wavelength. For the experiment, a 40 mm long LPG with period Λ=396 μm (fabricated by the electric-arc technique) and center wavelength λ=1572 nm was used. This resonance wavelength corresponds to the 6^{th}order cladding mode. Prior to coating, the fiber was cleaned with 5 M HCl solution and silanized using fresh 10% 3-aminopropyl-triethoxysilane (APTS). This procedure allows a better attachment of the sensing material to the silica surface. After drying, the fiber was coated using drag-coating technique (withdraw velocity ∼0.5 mm/s). The sensing element was evaluated using a FS2200SA from Fibersensing, SA (Portugal), with 1 pm resolution, working in the 1500-1600 nm range, operating in transmission mode.

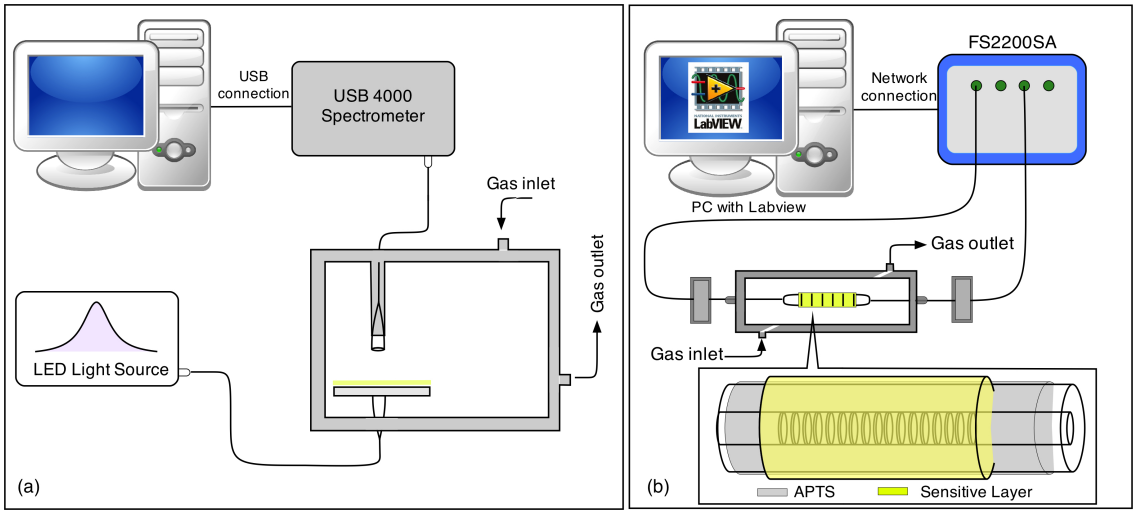

Figure 5.34: Experimental setup for the colorimetric measurements (a) and for refractometric measurements (b)

Using the schemes described above, the sensors were tested in the concentrations range from 0% to 100% CO_2. This was achieved by using a flow control system fed with CO_2 and N_2 inlets. At this stage, measurements were made in saturated moisture environment, to avoid cross sensitivity with humidity level. All the measurements were made at room temperature (23 ℃). The pressure and the flow rate were kept constant.

5.9.1.2 Material Characterization

In Figure 5.35(a) the response of the sensor to dynamic changes in CO_2 concentration can be observed. The inset shows the transmitted spectrum after crossing the test chamber for three different CO_2 concentrations, it is noticeable the dependence of the transmittance with the gas concentration. From the dynamic behavior a calibration curve for the lower range of CO_2 levels, <15%, could be obtained and is shown in Figure 5.35(b). The results present a clear increase of transmittance with the increment of the CO_2 concentration showing that, indeed, the presence of the gas in the membrane is causing changes in the electronic distribution of the sensitive membranes through protonation induced by the presence of carbonic acid. Observing the calibration curve in Figure 5.35(b), it can be seen that the sensor is more sensitive in the lower concentration range and that a saturation effect occurs at higher concentrations. The transmittance variation for the range between 0 % and 15.25 % was approximately 60 %. In this range, the highest sensitivity was observed between 0% and 8%, where a transmittance variation of ∼52 % was noticeable. A full range response was also evaluated. From 0 % to 100 %, the transmittance increased by a factor of 3.4, confirming the saturation effect of the membrane. From the dynamic behavior displayed in Figure 5.35(a), a response time of 30 s for lower concentrations could be estimated. Also from this data, a resolution of ± 0.15 % was calculated considering a minimum detectable signal of two times the standard deviation. In Figure 5.35(a) is also noticeable the reversibility of the response from 15.25 % to 0 % and from 100 % to 0 %. The repeatability of the response was evaluated by performing the same experiment three times, the results agreed within the measured standard deviation.

Relatively to the measurements of variations of RI in the cocktail, the results showed a consistent visibility difference of 1% between the two states, meaning that there was a refractive index decrease of ∼ 0.005 RIU induced by the increase in CO_2 concentration. While it is expected that these refractive index changes will be different after film deposition and membrane solidification, this result demonstrate, nevertheless, although small, an effective response to CO_2. Regarding the ellipsometry tests, the RI of the layer was between 1.38-1.39 RIU. The high uncertainty of this measurement is due to the low optical quality of the coated layers..

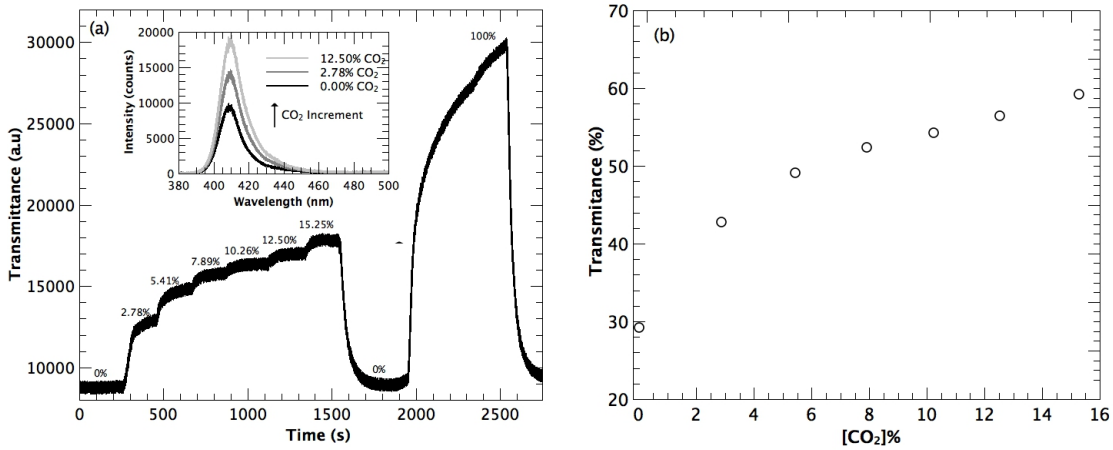

Figure 5.35: Colorimetric results: (a) the time response, the inset shows the spectral changes arising with the increment of the CO_2. (b) the resulting calibration.

5.9.1.3 Long Period Grating based CO_2 Sensing Probe

Figure 5.36(a) shows the sensing probe transmission spectrum during the different stages of the fabrication. It is possible to appreciate a wavelength shift of 1.5 nm and 6.4 nm after the silanization and coating, respectively. In Figure 5.36(b) the response of the sensing probe to dynamic changes in CO_2 levels can be seen. From this data a calibration curve can be obtained that is showed in Figure 5.36(c). The results show that the presence of CO_2 increases the refractive index of the layer, shifting the LPG resonance to shorter wavelengths. Observing the calibration curve in Figure 5.36(c) it is appreciable that similarly to what was seen in the colorimetric measurements, the sensor is more sensitive in the lower concentration range. The wavelength shift for the range between 0 % and 30 % was approximately 180 pm. On the other hand, in the full 0% to 100% concentration range, the wavelength shift observed was around 300 pm. From the dynamic behavior, a response time of 12 s for a concentration change from 0-57 % can be estimated. Also from this data, a resolution of $\pm$ 0.50% was calculated considering a minimum detectable signal of two times the standard deviation. In Figure 5.36(b) it is also noticeable the reversibility of the response. The repeatability of the response was also observed by performing the same experiment three times, the results obtained agreed within the measured standard deviation. The difference between the response time between colorimetric and the refractometric experiments are related with the thickness of the layers and difference in the volumes of the chambers used.

The results shown that, with the colorimetric setup, the sensor is able to distinguish a variation of CO_2 of $\pm$ 0.15 %, which is roughly 1.33 times better that the

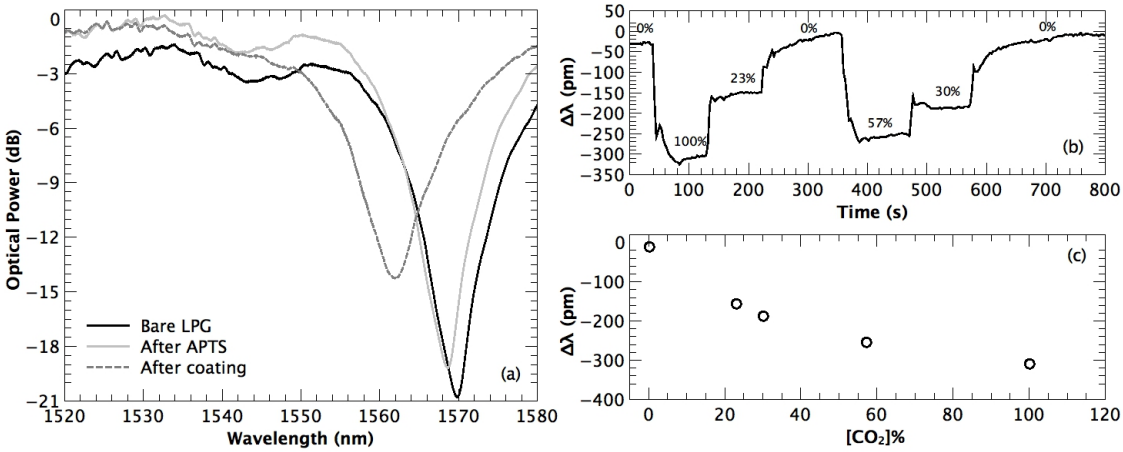

Figure 5.36: The evolution of the LPG spectrum obtained during the different stages of the fabrication process (a), the time response of the resonant peak of the LPG as a function of the CO_2 concentration (b) and the resulting calibration curve (c).

result achieved with the LPG based probe. Although it is not possible to compare directly both measurements, it seems clear, that the sensitivity of the sensing layer to colorimetric changes at 410 nm is much higher than the sensitivity for the refractometric changes at 1550 nm. One of the reasons for the small RI variations at 1550 nm is directly related with strong absorption at 410 nm, that implies also a high index change at the same wavelength. This high sensitivity decreases as the wavelength moves away from 410 nm [2, 124]. Several attempts were made in order to increase the sensitivity of the LPG based probe without success. The use of intermediate PS overlays (already studied in this chapter) with a thicknesses of around 480 nm, between the LPG surface and the sensitive layer were used, but the resonance vanishes after the deposition of the sensing layer.

This alternative requires very accurate control of the layers parameters. It is extremely important to know the precise refractive index of the sensitive layer. On the other hand, it is well known , that the deposition of a HRI overlay, depending on its characteristics, can shift the maximum SRI sensitivity to a certain index, it is desirable that the sensitive layer has an index slightly below, to ensure that the resonance will not disappear. The resonance vanishes, when the effective index of cladding mode traveling within the waveguide structure comprising the core, the cladding and the HRI overlay approaches to the sensitive layer index. It causes the decrease of the overlap between the core and cladding modes, and consequently, the guiding is almost non-existent [40].

Another solution explored, was to increase the sensing chemistry (p-nitro-phenol)

in detriment of the support polymer (D4). It was done through the sintetization of a polymer, the poly-p-nitro-phenol. This attempt, was not successful due to problems in the attachment of the layer to the fiber and also bleaching was observed.

5.9.2 Long Period Grating based DNA-Aptamer Biosensor for the Specific Recognition of *E. coli*

E. coli bacteria is of major concern due to its potential for serious impact on human health. This pathogen produces toxins that may cause skin irritation, stomach cramps, vomiting, nausea, diarrhea, fever, blisters of the mouth, urinary tract infections, respiratory illness and liver damage. There are multiple routes for the transmission of such pathogens including direct ingestion of contaminated water or food, transmission through the faecal–oral or oral–oral route, through aerosols and also through dermal contact [233].

In this section, the use of an *E. coli* DNA aptamer (ECA) for the determination of the E. coli outer membrane protein (EcOMP), using a LPG as a refractometric sensor is described. The aptamer raised against EcOMPs was immobilized through an electrostatic immobilization method, using poly-L-lysine as cationic polymer. The functionalized bare LPGs were characterized and tested against EcOMPs and applied to spiked environmental water samples.

5.9.2.1 Principle and Experiment

The measurement setup is shown in Figure 5.37 with an inset of the sensing head scheme. The LPG was manufactured in a standard SMF-28 fiber by electric-arc discharge technique. The grating period was 396 μm and the number of discharges was 95, which gives a length of approximately 40 mm. With this period, a resonant wavelength at approximately 1550 nm, corresponding to the $LP_{1,6}$ cladding mode is excited. The LPG was properly fixed with fiber clamps in both sides, outside the measurement chamber, and a small tension was applied with a translation stage to avoid strain/curvature cross sensitivity. The sensing element was characterized using a FS2200SA from Fibersensing, S.A. (Portugal) working in the 1500-1600 nm range, with 1 pm of resolution, and modified to measure signals both in reflection and transmission modes in separate channels. The sensing probe was connected to the unit in transmission mode.

The sensing principle of the LPG based biosensor relies on monitoring the resonant wavelength (λ_R) shift due to the changes in the SRI. The changes in λ_R are tracked in

real-time by the unit and from step to step the spectrum is also recorded. The amine-functionalized ECA was bind to the LPG surface which was modified by means of a non-covalent approach, using a cationic polymer poly-L-lysine (electrostatic interaction). The polycationic nature of the poly-L-lysine leads to its electrostatic attraction onto a negatively charged surface in an aqueous environment at neutral pH. The sensing probe was then incubated with 200 nM of ECA. Afterward, the sensing probe was incubated with several varying concentrations of EcOMP. Between all these steps, the wavelength shift of the resonance was measured.

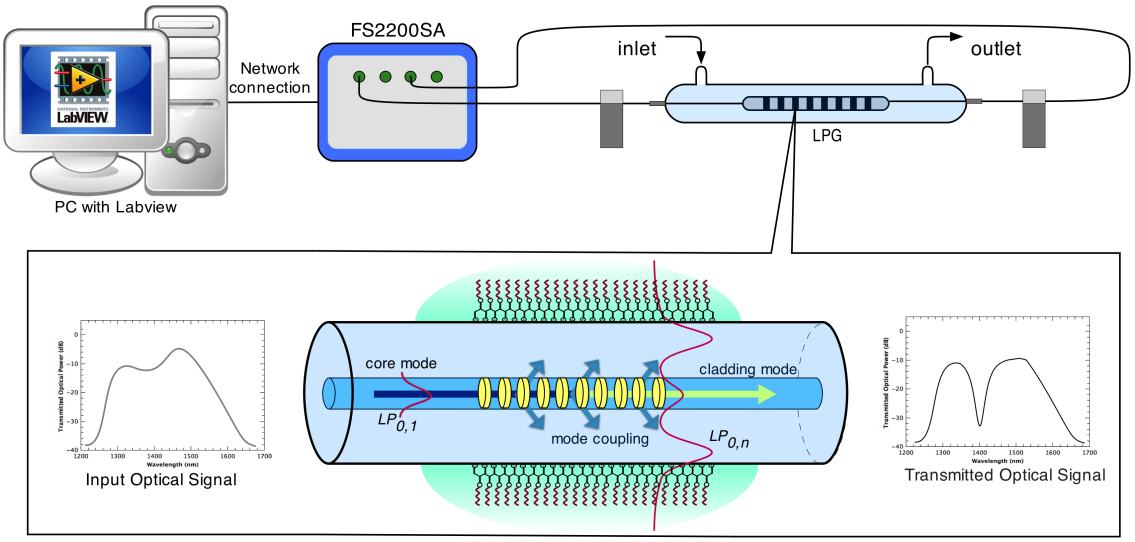

Figure 5.37: Experimental setup for the functionalization and characterization. The inset shows the scheme of LPG based sensing probe

5.9.2.2 Results and Discussion

Figure 5.38(a) shows the spectrum of the LPG during the different stages of the immobilization procedure of poly-L-lysine and following the affinity-assay between ECA and EcOMPs. It is noticeable, the wavelength shift of the resonance for each step. The self-assembly of the ECA and consecutively the binding of EcOMPs, onto the LPG surface, increases the effective index cladding mode resulting in a shift of the resonance as a function of the surface mass, that is also increasing. In the presence of EcOMPs, the ECA folds around the proteins and forms an EcOMP-ECA complex. The formation of this complex also causes an increase in the effective refractive index of the cladding and consequently a decrease of the wavelength of the resonance. The wavelength shift observed is of about 1.8 nm from the bare LPG to the affinity-assay between ECA and EcOMP. The sensor performance was tested

by the evaluation of the sensing probe against increasing concentrations of EcOMPs ranging from 0.1 nM to 10 nM. Measurements were conducted at room temperature in a buffer solution. Figure 5.38(b) presents the calibration curve resulting from the affinity-assay of the complex ECA-EcOMPs for the concentration range tested, where a non linear behavior is observable. Figure 5.38(c) shows the linearization of the calibration. A sensitivity of 0.156 nm per logarithmic EcOMP concentration unit is inferred.

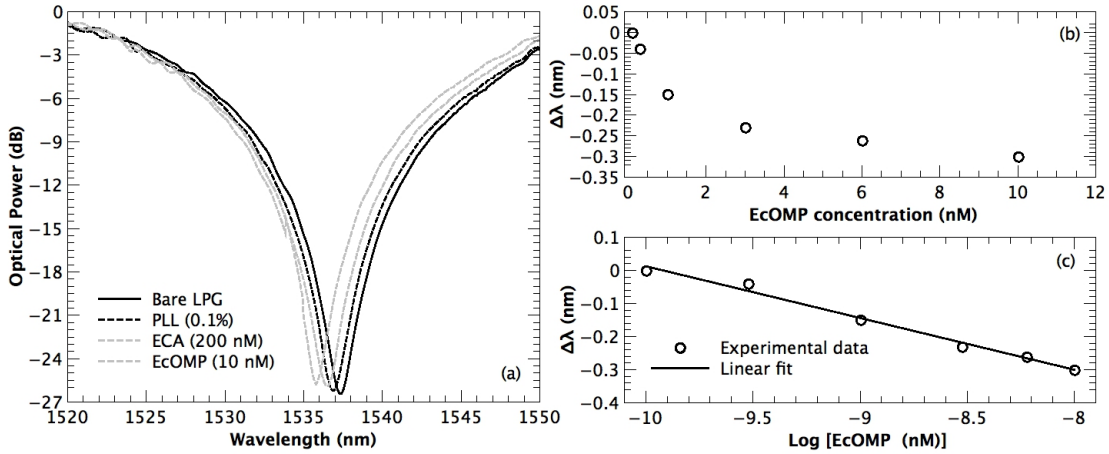

Figure 5.38: The LPG spectrum during the different stages of the functionalization and thereafter the affinity-assay between ECA and EcOMPs (a). The resulting calibration curve and linearization is shown in (b) and (c), respectively

The regeneration of the sensing probe was tested by carrying out consecutive binding and washing steps. The shift of the resonance was measured before and after the functionalization of the sensing heads, after the immobilization of the ECA and after the incubation of 200 nM ECA with 0.1 nM EcOMPs. Then, sensing heads were washed with a 2 M HCl solution for 30 min, to regenerate the probe for re-use and re-incubate with 0.1 nM EcOMPs. Figure 5.39(a) shows this result. As can be seen the wavelength increases with the removal of the EcOMPs and decreases again after the immobilization of the EcOMPs, which demonstrates the surface is entirely regenerated after 20 min and capable of detecting EcOMPs again with the same sensitivity. The sensing probes shows good stability and regeneration due to their ability of detect EcOMPs in successive binding and washing events.

In order to investigate the application of the present method to the analysis of environmental waters (pH 6.5), spiked waters were tested and the corresponding relative errors calculated. Environmental water samples were collected in a well and stored in amber glass bottles previously rinsed with double-deionized water. The pH

and ionic strength of the water samples were adjusted by addition of affinity buffer (50:50), and they were stored at 4 ℃ until analysis. These assays were carried out with sensors calibrated within 1 nM to 10 nM of EcOMPs. The average recoveries of three spiked solutions was 106%. The sensor showed an error of about 6%, thus requiring more studies and optimization in order to be used in real samples.

To assess the non-specific binding of other molecules that could be present in water systems the sensing probe was incubated with 1 nM EcOMPs and with 1 nM of Microcystin-Leucine (MCYST-LR) and with a mixture of both for 60 minutes in the affinity buffer. The wavelength shift of λ_R induced by the complex ECA-EcOMP for both types of sensing heads was shown to be much higher than the shift obtained when incubating in MCYST-LR solution alone (Figure5.39(b)). In the case of the mixture EcOMP/MCYST-LR, the wavelength shift of the λ_R presented a similar value to the complexes ECA-EcOMP. These results show the specificity of EcOMP binding to the ECA on the LPG even in the presence of potential interference molecules.

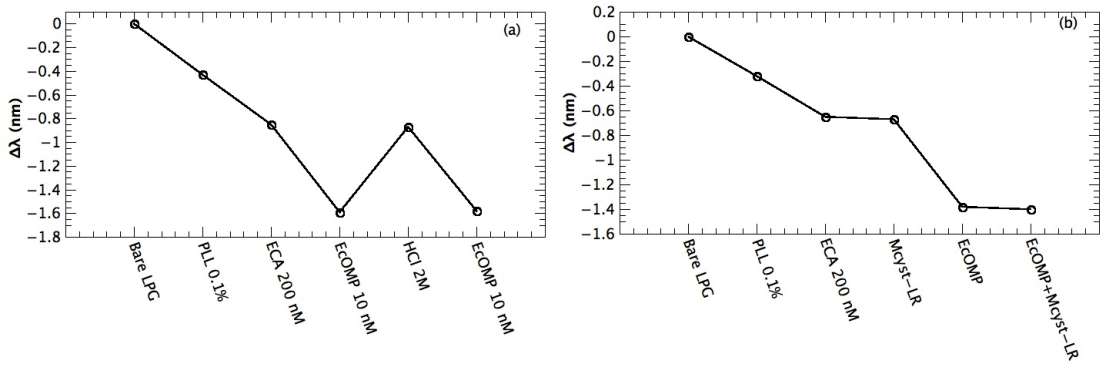

Figure 5.39: The regeneration of the sensing probe is shown in (a) and the selectivity test is illustrated in (b)

Regarding the reproducibility of the sensing probe, it is possible to state that, during the experiments several LPGs with similar features were functionalized and characterized, it was revealed that, following the same experimental protocol, a wavelength shift of 1.6 ± 0.4 nm for the full procedure was observed.

5.10 Conclusion

LPGs are one of the most popular fiber optic devices that have been widely used for optical communications and sensing. Specially for chemical and biological sensing due its intrinsic sensitivity to the external index. Several LPGs were characterized in refractive index and temperature, all of them with resonances in the third telecom

window (1550 nm). It is important to stress that the aim of this study was geared towards chemical and biological applications. Thereby, the range of RI of interest was between 1.32-1.35 RIU. The temperature characterization was done due its importance as cross-sensitivity issue. With an in-house electric-arc setup, LPGs were manufactured with periods of 396 μm and 338 μm which excite the $LP_{1,6}$ and $LP_{1,7}$ mode respectively. As expected the LPGs with shorter period show a sensitivity roughly two times higher. Due to the physical limitation to fabricate arc-induced LPGs with even shorter periods, and with the need to increase further the sensitivity, a UV written LPG close to the turn-around-point provided by the CGCRI (India) was also studied. The LPG with a period of 165 μm that excites the $LP_{0,12}$ cladding mode was studied showing a sensitivity of approximately 635 nm/RIU.

Generally, LPGs show a high sensitivity to the external index, nevertheless, they are also highly sensitive to temperature. A wide variety of solutions to measure simultaneously both parameters can be found in the literature, mainly based in the use of a pair of gratings. Assuming that would be interesting to have a solution with a single grating and following a work from another group, arc-induced PS-LPGs were written and characterized, but unfortunately the RI and temperature response of both resulting peaks did not show an independent response, disabling the possibility of simultaneous measurement.

HRI overlays based on PS and ZnO/ZrO doped silane and deposited by drag-coating were studied. PS is a very common plastic with an RI of 1.59, with excellent optical properties and its easy to deposit, and even to biofunctionalize. Arc-induced LPG coated with different thicknesses were tested, showing sensitivities close to the water index of up to 2700 nm/RIU, with a 515 nm layer. However, due to its high thermo-optic coefficient, the sensitivity to temperature also increases dramatically, additionally, PS presents constraint to work at relatively high temperatures or in chemically hazardous environments. In contrast, ZnO/ZrO doped silane, shows high potential due its thermal behavior. Sol-gel is a well established process for fabrication of photonics devices, its more complex and time consuming but, at the same time, very versatile, allowing a number of possibilities in the final product by varying certain parameters during the fabrication and curing. The ZnO/ZrO doped silane has an RI around 1.78 RIU. Arc-induced LPG coated with different thicknesses were studied, showing sensitivities up to 700 nm/RIU, with an overlay with 136 nm. Considering nTh, it is possible to estimate that, to achieve a sensitivity to the SRI as high as with PS, for the 6^{th} cladding mode, a layer with a thickness of approximately 460 nm would be necessary. Sol-gel is very promising technique for HRI coated LPGs since

the final product is a glass and thereby is fiber friendly. It is a very flexible process, that permits to change the composition in order to include in the matrix chemical or biological agents with specificity to fabricate high sensitivity biochemical sensors. Furthermore, by controlling nTh, it is possible to have high sensitivity RI sensors for lower range of RI, for instance close to water or air index. Future work will allow to improve this results by employing thicker layers. Table 5.3 shows a summary of the sensitivities achieved for the RI in the lower index range and for the temperature with the single LPG devices.

LPG	K_n (nm/RIU)	K_T (pm/°C)
Arc-induced bare LPG (6^{th} order)	147 ± 3	114 ± 1
Arc-induced bare LPG (7^{th} order)	290 ± 6	165 ± 16
UV-induced bare LPG (12^{th} order)	636 ± 21	177 ± 2
Arc-induced LPG (6^{th} order) Silane 136 nm	362 ± 8	153 ± 2
Arc-induced LPG (7^{th} order) Silane 136 nm	717± 21	243 ± 4
Arc-induced LPG (6^{th} order) PS 515 nm	2729 ± 92	303 ± 5

Table 5.3: Single LPGs: a comparison between different orders, bare gratings and HRI coated devices.

A MZ-LPG was also studied. Optical interferometry is well-known technique and it is associated with high accuracy measurements. The MZ-LPG interferometer was obtained by writing in series two identical LPGs, with around 3 dB of resonance depth, separated by a distance L , where an interferometer cavity was formed between the two gratings. In the experiment, arc-induced LPGs were used separated by a distance of 100 mm. As a result, a sensitivity of about 56 nm/RIU (or $\sim$ 66 rad/RIU) was achieved. Coupling this sensing probe with a readout interferometer with pseudo-heterodyne detection a very-high resolution can be achieved (around ± 10^{-6} RIU).

Two applications were presented, an LPG coated with p-nitro-phenol based material was studied for CO_2 sensing, and a LPG biosensor for detection and quantification of *E. coli* was investigated. The CO_2 sensitive layer was based on the acid-base equilibrium of phenol and of its derivative p-nitro-phenol which, in the presence of CO_2, are prone to protonation introducing absorption and refractive index changes. Thin films casted on glass slides were characterized in absorption spectroscopy. The layers were tested in the full concentrations range, showing an increase on the transmittance with the increment of the CO_2 level. The membrane presents a non-linear response. The transmittance variation for the range between 0% and 15.25% was approximately 60%. The dynamic behavior was also analyzed in this range. The determined response

time was 30 s and a resolution of ± 0.15% was estimated. For refractometric measurements an LPG coated with the new sensing layer was used. The resonance of the LPG varies according with the CO_2 concentration indicating a refractive index change in the layer. A wavelength shift of 180 pm for a variation in the range between 0% and 30% was noticeable. A resolution of ± 0.50% was calculated and a response time of 12 s was determined. These results show the viability of a carbon dioxide optical measurement using the phenol-based membrane with the application of colorimetric or refractometric based configurations. The colorimetric configuration showed better performance than the LPG refractometric probe, nevertheless, the latter approach is more promising in terms of multiplexing and remote monitoring capabilities. Therefore, strategies for the improvement of sensitivity should be studied. One possibility to improve the results obtained, is introducing the sensing chemistry in a HRI layer.

Finally, a biosensor based on a LPG as a refractometric platform for the detection of EcOMPs based on the specific recognition between an aptamer capture probe and bacteria proteins is proposed. The behavior of the LPG resonant wavelength showed a dependence on the concentration of the protein and a shift of ∼2 nm was measured. The sensing probe was regenerated (under low pH conditions) and the deviation of the subsequent detection was less than 0.1 %. The sensors displayed high selectivity to Mcyst-LR (a common toxin in environmental waters) and offered simplicity in designing and analysis as well as low limit of detection (0.1 nM EcOMPs). These analytical features, as well as its fabrication easiness and operational convenience, make it a promising method for the detection of *E. coli*.

Chapter 6

Multimode Interference in a Fiber Loop Mirror

Summary

A fiber optic sensor for simultaneous measurement of refractive index and temperature is presented. The sensing structure is realized by introducing a multimode interference device inside a high-birefringence fiber loop mirror resulting in a configuration capable of refractive index and temperature discrimination. The multimode interference peak is sensitive to the surrounding refractive index (90 nm/RIU) and slightly responsive to the temperature (0.01 nm/℃). On the other hand, the birefringent fiber loop mirror is highly sensitive to temperature (2.36 nm/℃) and it has almost no response to refractive index. Using a power ratiometric peak detection scheme, a temperature independent refractive index measurement can be achieved with a resolution of $\pm$ 2.25$\times$10^{-5} RIU.

6.1 Introduction

Refractometric sensors based on optical fiber technology are promising and interesting for chemical and biological measurands due to their advantages, such as high sensitivity, immunity to electromagnetic interferences, compact size and because they are made from silica, which is, chemically and biologically inert. Chapter 2 gives an overview of the most important technologies used in refractometric fiber sensors.

Including, surface plasmon resonance [234], long period gratings [29], fiber Bragg gratings [4, 15], tapered fibers [81] and multimode interferometers [90].

Multimode interference (MMI) based refractometers are an interesting solutions that rely on the concept of re-imaging effects of MMI patterns present in multimode waveguides. In these devices, the transmitted spectral power distribution is highly sensitive to the optical path length of the multimode fiber and its SRI. Different MMI based refractometers have been proposed, showing robustness and sensitivities in the biological range between 90-150 nm/RIU, depending on the MMF diameter [90, 92, 235, 236]. All those presented technologies have strengths and weaknesses that were already described in Chapter 2. However, all of these configurations are also sensitive to temperature. Furthermore, some of these sensors are more sensitive to temperature than to refractive index.

Temperature cross-sensitivity is a characteristic which affects in greater or lesser degree all optical fiber sensors, this arises from the intrinsic sensitivity of the silica matrix to temperature, through the thermo-optic and photo-elastic coefficients, which induce changes in the effective refractive index and in the effective length of the fiber, respectively, thus, varying the optical signal as a function of the thermal conditions. These changes may be higher or lower, depending on the type of optical device used and on the evaluated optical parameter. Typically, the thermo-optical coefficient of silica is 8.0×10^{-6} K^{-1} and its thermal expansion coefficient has the value of 0.55×10^{-6} K^{-1}, these figures may change according with the fiber composition[7]. Frequently, dopants used for tuning the refractive index of these waveguides introduce stronger temperature dependences. Therefore, the influence of temperature must be accounted when high resolution RI measurements are carried out for high sensitivity detection of biological or chemical parameters. Presently, in most of practical applications authors deal with temperature dependence working with temperature stabilized systems. Nevertheless, even when temperature is stabilized to $\pm$ 0.1 ℃, such fluctuations can still be significant in face of the need to measure variation of refractive index in the order of 10^{-5} or less.

Therefore, the desirable situation is to have a system that can either compensate or simultaneously measure temperature. During the last few years, several fiber optic refractometric configurations for simultaneous measurement of temperature and RI were presented. In the case of fiber gratings based configurations, the use of a second diffractive structure, sensitive only to temperature or with different sensitivities for both measurands [42–45] has been recurrently addressed.

On the other hand, high birefringence fiber loop mirrors (HiBi FLM), are interesting devices that usually consist on a section of HiBi fiber that is spliced between the output ports of a directional optical coupler to obtain an optical path difference between the fast and the slow axis. Independence of input polarization and insensitivity to perturbations in the lead in fibers are some of its most attractive features. HiBi FLM has been widely explored for the measurement of physical parameters [179] and due to its high temperature sensitivity, this structure was also presented for temperature discrimination [237]. Nonetheless, just a few works were reported to measure RI with FLM. Generally this is accomplished by introducing a RI sensitive element inside the loop. For instance, a D-type fiber [238] an LPG written in a polarization maintaining fiber [239], or non-adiabatic fiber taper [83]. Recently, using two sections of HiBi fiber with different lengths into a FLM, where one of the sections was partially etched, a differential index measurement configuration was demonstrated [240].

In the present work, a sensing structure capable of simultaneous measurement of refractive index and temperature is demonstrated by combining the strengths of two well-known fiber sensing devices. The sensing probe consists in a coreless multimode fiber segment inserted into a HiBi FLM. The multimode interference device introduces advantages such as low cost, ease fabrication and good RI sensitivity while keeping the fiber structure integrity, unlike other types of FLM based refractometers. When the MMI is inserted into HiBi FLM, on the other hand, the ability to measure temperature with high sensitivity is added. Thus, simultaneous measurement of refractive index and temperature is achieved with high resolution, paving the way for temperature independent label-free bio-chemical sensors.

6.2 HiBi Fiber Loop Mirror

One of the most used devices in optical fiber sensors and communications is the fiber loop mirror based on a ring configuration [241]. The fiber loop is formed when both output ports of a directional coupler are spliced. In this arrangement, the two waves at the coupler outputs travel in opposite directions following identical optical paths in the fiber ring, which assures constructive and destructive interference when the waves are recombined at the coupler, for the reflection and transmission output, respectively. Thereby, all light is reflected back to the input port limited just by losses essentially in the fiber, the splice region and the coupler [179]. Due to this "mirror" feature, the device is frequently used in optical fiber lasers for the formation of resonant cavities [242]. A FLM containing a section of HiBi fiber, results in an interference pattern.

It has several advantages compared with a more traditional interferometer. One of them is that the interferometric output is independent of the input polarization of light. Another one is the periodicity of the formed spectral filter, which depends only on the length of the HiBi fiber and not on the total length of the fiber loop mirror [243].

The HiBi FLM consists in a coupler and a HiBi fiber section, that in the right condition transforms it into an interferometric device that can be used as a filter or as a sensing probe. The obtained fringe pattern depends on the fiber characteristics. The birefringence is guaranteed during the fiber fabrication process through the geometrical or stress effects. The geometrical effect is easily obtained when the core is non-circular, for example, the elliptical core fiber. The stress effect can be obtained by applying mechanical tension around the core, as occurs in the case of the Panda or bow-tie fibers where stress rods are introduced parallel to the core, rendering it anisotropic [178].

The birefringence effect in optical fibers is regulated by the difference in refractive indices along the core eigen axes, the fast axis (n_y) and the slow axis (n_x). The birefringence B is defined as;

$$B = n_x - n_y = \frac{\lambda}{2\pi} \left(\beta_x - \beta_y \right), \tag{6.1}$$

where $\beta_{x,y}$ are the propagation constant associated to each fundamental mode of polarization and λ is the operation wavelength. This birefringence determines the beat length, L_B, which is the length over which the phase difference between the fields propagating along the fast and the slow axis light changes by 2π. L_B is given by the relation;

$$L_B = \frac{\lambda}{B}. \tag{6.2}$$

A typical HiBi FLM is shown in Figure 6.1. The HiBi FLM integrates a 3 dB coupler which splits the input light into two counter propagating beams, which transverse the loop. When properly arranged, using the polarization controller (PC), they propagate through the HiBi fiber with different velocities, and the beams will interfere at the output port.

Thus, the fiber loop filter characteristic is similar to an unbalanced Mach-Zehnder interferometer. The differential phase ϕ between the two polarization modes after propagating through an extension L of HiBi fiber is given by;

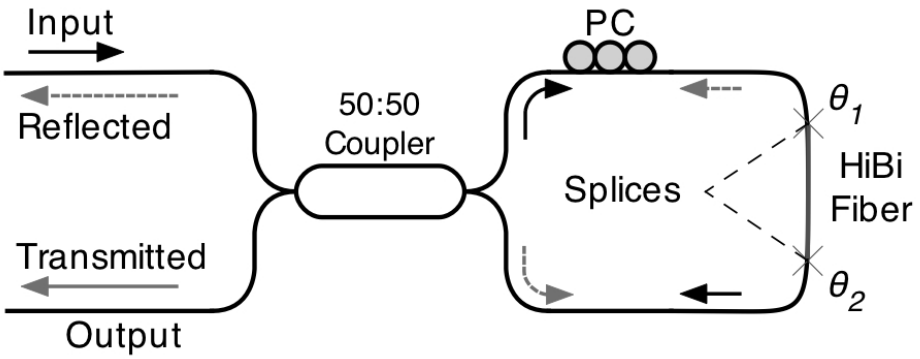

Figure 6.1: Schematic of a HiBi fiber loop mirror.

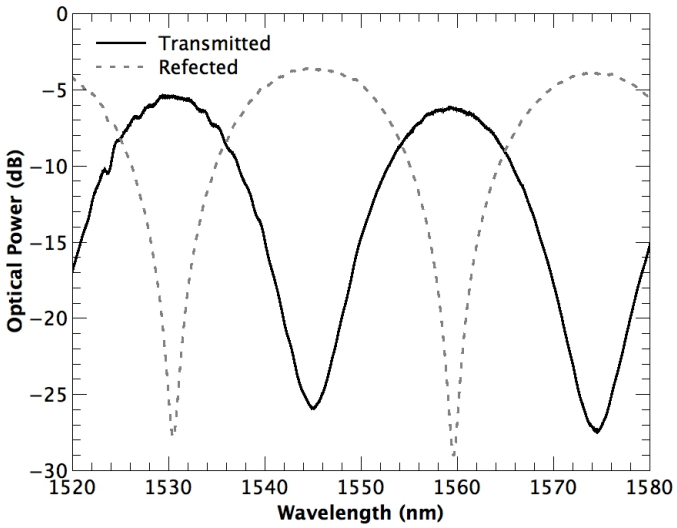

Figure 6.2: Transmitted and reflected spectra of a HiBi fiber loop mirror.

$$\phi = \frac{2\pi BL}{\lambda}. \tag{6.3}$$

In such case, the transmission spectrum (T) of the HiBi FLM is described by a periodic function of the wavelength, that follows the expression;

$$T(\lambda) = \left[\sin\left(\frac{BL}{\lambda}\right)\cos\left(\theta_1 + \theta_2\right)\right]^2, \tag{6.4}$$

where θ_1 and θ_2 are the angles between the polarization of light at both ends of the HiBi fiber and the fast or slow axis of the HiBi fiber, respectively, as shown in Figure 6.1. The reflected spectrum (R) of the HiBi FLM is given by, $R = 1 - T$. Figure 6.2 shows the transmitted and reflected spectrum of a typical HiBi FLM (Figure 6.1). It is possible to verify that they complement each other.

The periodicity of the fringe pattern ($\Delta\lambda$) is inversely proportional to the length and the birefringence of the HiBi fiber as follows [244];

$$\Delta\lambda = \frac{\lambda^2}{BL}. \tag{6.5}$$

In this way, for smaller fringe period, a larger birefringence or a longer length of the Hi-Bi fiber is required. Also, this spectral characteristic is independent of the polarization state of the input light [243]. Due to the ease of implementing interferometers based on this scheme and also because of the intrinsic sensitivity of the HiBi fiber to certain physical parameters, HiBi FLM has been widely applied in optical sensing, mostly in polarimetric sensors [244]. One of the most remarkable example is its use as an optical fiber gyroscope within the context of navigation instrumentation [245]. Besides the gyroscope application, it has been applied in strain [246] and temperature [247] measurement, in liquid level [248] and displacement [249]. Moreover, the HiBi FLM combined with a Bragg grating [250] or with a long period grating [237] was also demonstrated for simultaneous measurement of strain and temperature. Despite its extensive use in the measurement of physical parameters, however, only a few works were presented to measure the SRI with an HiBi FLM. Usually this is achieved by introducing a RI sensitive structure inside the loop such as D-type fiber [238] an LPG written in a polarization maintaining fiber [239], or non-adiabatic fiber taper [83]. More recently using two sections of HiBi fiber with different lengths were inserted into a FLM, being one of the sections partially etched and were used for differential RI measurement. [240]. In the present work a multimode interference device capable of measuring the SRI is inserted into the HiBi FLM enabling the simultaneous measurement of temperature and RI. In the next section the most relevant concepts about MMI are addressed.

6.3 Multimode Interference

Multimode interference is the basis of the implementation of a number of optical waveguide devices. Initially proposed for planar waveguides, MMI based devices rely in the the phenomenon of self-imaging. Self-imaging can be defined as a property of multimode waveguides by which an input field profile is reproduced due to constructive interference in single or multiple images at periodic intervals along the propagation direction of the guide [89]. Since the theory of the self-imaging in multimode waveguides was demonstrated, several MMI devices for optical applications

were successfully proposed; couplers, modulators and sensors are examples among others [89].

In an optical waveguide as shown in Figure 6.3(a), a MMI structure consisting of a multimode waveguide placed between input and output singlemode waveguides is schematically represented. Considering W_s and W_m the width of the singlemode and multimode planar waveguide, respectively, and L the length of the of multimode section. The input field at $Z = 0$ will be decomposed into the modal distribution of all possible modes in the multimode waveguides. The field profile at a distance $Z = L$ may be expressed as a superposition of the modal distribution of all possible modes. Under certain circumstances, the field at $Z = L$ will be a self-image (or reproduction) of the input field [89]. Figure 6.3(b) shows the simulated field profile within the multimode section and it is clear that self-imaging of the input field takes place so that at periodic intervals, a single image of the input field is reproduced. This occurs at distance Z of 2708, 5415, and 8122 μm, respectively. Multi-fold images of the input field can also be found, for example, two-fold images can be found at distance Z of 1354, 4062, 6770, and 9478 μm, respectively [251]. Self-imaging occurs at specific lengths only for certain wavelengths. The spectral response of a MMI-based device is, therefore, not flat and, in fact, has a bandpass type response, where the bandpass peak wavelength corresponds to the wavelength value where the self-imaging distance is exactly equal to the multimode section length [89].

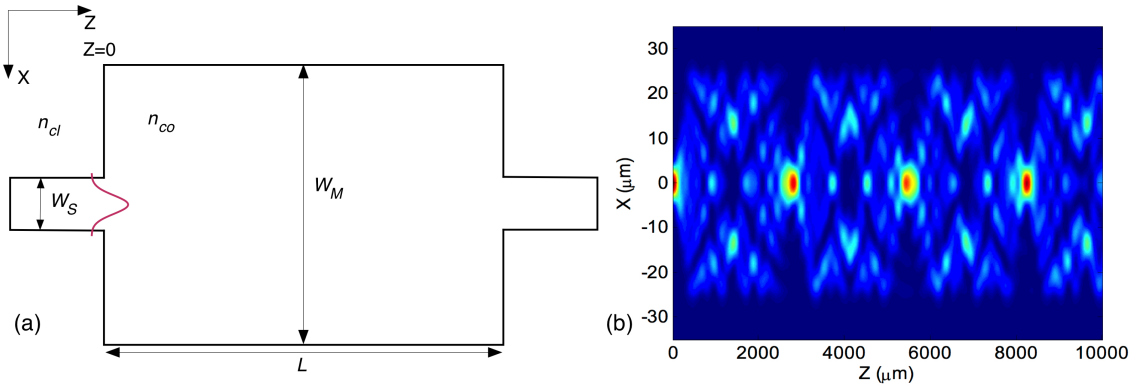

Figure 6.3: MMI Planar waveguide device scheme (a) and field distribution along the propagation axis for the multimode waveguide (b), for a kind of structure like (a). The parameters are: $\lambda = 1550$ nm $W_s = 5$ μm, $W_M = 50$ μm, $n_{co} = 1.454$ and $n_{cl} = 1.445$ [251].

Optical fiber MMI devices are generally implemented by splicing a section of step-index multimode fiber with a precise length between two sections of singlemode fiber, forming a singlemode-multimode-singlemode (SMS) structure (Figure 6.4). Thus, the

light field propagating along the input SMF is launched in to MMF section and several modes of MMF are excited. Therefore, differential phases between all the modes will accumulate, while the optical radiation propagates along the MMF section. Albeit the global field profile along the MMF section varies, it stays symmetrically distributed along the direction of propagation [252]. Thus, different field profiles are formed at the end of the MMF, depending on the particular propagation distance, of the multimode section. As well as in planar waveguides, there are several periodic planes along the direction of propagation where light field at the input of the MMF section is replicated, in both amplitude and phase, on the output of the MMF for a specific wavelength. Due its spectral characteristics MMI based SMS devices have been used as band-pass filters [253] and edge filters for wavelength demodulation [254]. In the sensing field, these structures have been used for strain [255], displacement [256], temperature [257] and curvature [258] measurement. If instead using a conventional MMF with core and cladding, a coreless fiber is used or if the cladding of the MMF is etched till the core, the excited modes propagating along the MMF are affected by the SRI and the field profile at the end of the MMF section becomes sensitive to the external index. In the following paragraphs, a brief theoretical approach is presented, giving emphasis to the refractive index sensitivity of the spectral characteristic of the SMS multimodal interferometer.

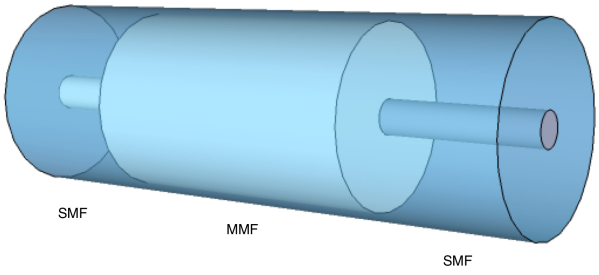

Figure 6.4: SMS based multimode interference device.

Considering the structure shown in Figure 6.4 and assuming that the SMF and MMF are perfectly aligned, due to the circular symmetry of the input field, just $LP_{0,m}$ modes can be excited in the multimode section. If the light at the entrance of the MMF has a mode field distribution $E(r,0)$, which is equal to the fundamental mode of the SMF, then the input field may be decomposed into the eigenmodes $LP_{0,m}$ in the MMF [89, 252]. Defining the field profile $LP_{0,m}$ as $\psi_m(r)$, $m = 0, 1, 2, ..., m-1$, where m is the number of modes in the MMF. The number of excited $LP_{0,m}$ modes can be calculated using $m \approx \frac{V}{\pi}$, where $V = \frac{2\pi}{\lambda} r_{co} \sqrt{n_{co}^2 - n_{cl}^2}$ is the normalized frequency. λ

is the operating wavelength, r_{co} is the core diameter of the MMF and n_{co}, n_{cl} are the indices for the core and cladding, respectively. Hence, the input field at the MMF section may be expressed as;

$$E(r,0) = \sum_{m=1}^{M} b_m \psi_m(r), \tag{6.6}$$

where $\psi_m(r)$ are the eigenmodes of the MMF determined by the core diameter, cladding and core refractive indices. b_m is the excitation coefficient of each mode that can be expressed as;

$$b_m = \frac{\int_0^\infty E(r,0)\,\psi_m(r)\,rdr}{\int_0^\infty \psi_m(r)\,\psi_m(r)\,rdr}. \tag{6.7}$$

Thereby, the field in the MMF section at the distance z can be calculated by;

$$E(r,z) = \sum_{m=1}^{M} b_m \psi_m(r) \exp(j\beta_m z), \tag{6.8}$$

where β_m is the propagation constant of each eigenmodes of the MMF. The fraction of the transmitted power in dB may be calculated by using the overlap integral method between the fundamental mode $E(r,z)$ and the fundamental mode of the output SMF $E_0(r)$ as;

$$L_s(z) = 10\log_{10}\left(\frac{\left|\int_0^\infty E(r,z)\,E_0(r)\,rdr\right|^2}{\int_0^\infty |E(r,z)|^2\,rdr\int_0^\infty |E_0(r)|^2\,rdr}\right). \tag{6.9}$$

The self-image occurs at the so called self-imaging distance L_z. $L_z = 10\frac{\pi}{\beta_0-\beta_1}$, where β_0, β_1 are the two first propagation constants of the MMF [252]. As the RI of the surrounding liquid changes, the effective index of the cladding varies, and thus, the eigenmodes $\psi_m(r)$ exited in the MMF will also vary, resulting in changes in the excitation coefficient for each mode b_m (equation 6.7), in the interference within the MMF (equation 6.8) and consequently in the field at the output SMF (equation 6.9). It is important to emphasize that the length and diameter of the MMF will determine the final output to the SMF, as shown in equation 6.9. Studies presented by Wu *et al.* [91] prove that, as expected, the sensitivity of the SMS structure to the SRI is highly dependent on the diameter of the MMF section. Several fiber refractometers based on SMS devices have been presented based on coreless fibers [235], etched [91] and tapered [92, 236] multimode fibers. In the next section a MMI based refractometer

inside of a HiBi FLM is used for the measurement of refractive index and temperature without ambiguity.

6.4 MMI in a HiBi FLM for Simultaneous Measurement of Refractive index and Temperature

A fiber optic sensor for simultaneous measurement of refractive index and temperature is described. The sensing probe is realized by introducing a multimode interference device inside a high-birefringence fiber loop mirror, resulting in a configuration capable of refractive index and temperature discrimination. The multimode interference peak is sensitive to the surrounding refractive index and slightly responsive to the temperature. On the other hand, the birefringent fiber loop mirror is highly sensitive to temperature and it has almost no response to refractive index.

6.4.1 Sensing Head

Figure 6.5 shows the experimental setup for simultaneous measurement of refractive index and temperature. The sensing head consists in a fiber loop mirror, containing a section of HiBi Panda fiber and a MMI structure. The sensing element was characterized using a FS2200SA Spectrum Analyzer (Fibersensing, SA) working in the 1500-1600 nm range, with 1 pm resolution. The HiBi FLM is formed by a 50:50 (2x2) optical coupler with low insertion loss, an optical PC and the HiBi singlemode fiber section. The Panda optical fiber PM1550-HP (Thorlabs, GmbH) is a polarization maintaining fiber for a wavelength of 1550 nm with a beat length of < 5.0 mm and an attenuation of < 1 dB/km. The HiBi FLM acts as periodic bandpass filter for the input signal. The input optical signal is splitted into two counter-propagating beams, which undergo the loop crossing the PC before or after propagating the Panda fiber. This asymmetry swaps the polarization components of both clockwise and counter-clockwise beams in such a way that, at the outputs, the two waves have an accumulated phase difference that is proportional to the difference in optical paths of the fast and slow axis of the HiBi section, resulting in constructive or destructive interference, depending on the relative phase at recombination after crossing the coupler ports. The result is a fringe pattern whose periodicity is proportional to the HiBi fiber length and its birefringence. Due to the dependence of the Birefringence of this Panda fiber with the temperature, the fringe pattern will be highly sensitive to temperature. The length used for the HiBi fiber was approximately 180 mm, resulting in a fringe pattern with a 30 nm periodicity.

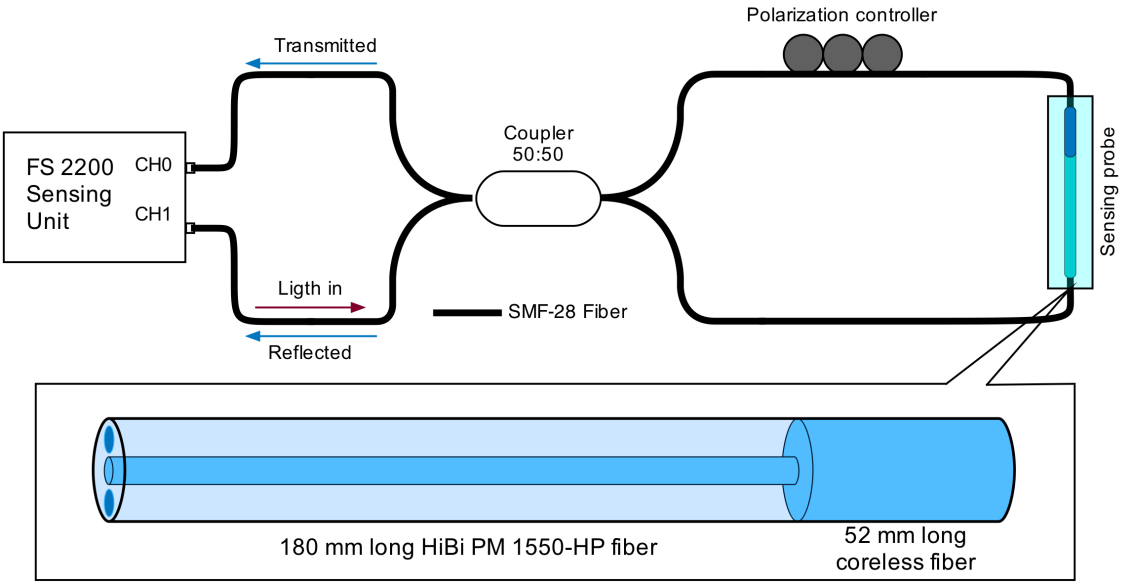

Figure 6.5: Experimental setup and sensing probe scheme.

The sensing probe for refractive index and temperature discrimination is based on a combination of the HiBi FLM and a MMI device. The MMI was formed by splicing a section of pure silica coreless multimode fiber (CMF) to the Panda fiber. The CMF was fabricated by drawing a silica rod down to the appropriate dimensions in a standard optical fiber drawing tower. Singlemode fibers, SMF-28, with core and cladding diameters of 8.2 and 125 μm, respectively, were used for both light input and output of the Panda-CMF section. In this situation, the CMF section behaves like a standard MMI device. At the input of the CMF several high order modes are excited generating a periodic interference pattern along the coreless section. Depending on the wavelength and on the geometrical length, the light into the CMF can interfere constructively or destructively resulting, at the end, in a device with different spectral characteristics. Therefore, the length of the CMF determines the spectral features of the MMI device. Depending where the interference pattern is 'intersected', constructive or destructive interference results at different wavelengths, yielding the transmission of resonant peaks or resonant losses, respectively. Independently of its shape, each of these spectral features will shift according to the surrounding RI with a similar sensitivity [90]. In the present work, a CMF with a diameter of 125 μm and a length of 52 mm was used to form the MMI structure. This length was chosen, based on previous experience on the group [235], to obtain a resonance dip centered at a wavelength of 1525 nm with a maximum loss of 25 dB and a FWHM of approximately 20 nm.

Prior to insertion of the sensing device into the FLM, its transmission spectra was observed by injecting light from either side, to make sure no asymmetry was introduced by the splicing process. The device spectral output was shown to be independent of the direction of observation demonstrating a good symmetry. Further preliminary tests were made to evaluate the degree of cross interference between the sensing properties of the two devices combined in this work. The MMI device was first inserted into a FLM, with no HiBi fiber. In this case no interference effects were observed, showing that the device had no birefringent properties. A resonant loss was observed with identical characteristics to what was observed outside the loop. On the other hand, it was verified that the HiBi interference pattern of the combined sensing device was not sensitive to refractive index, within the measurement error. This way, for the present experiment it was assumed that the working principles of each of the devices were operating in an independent way.

Figure 6.6 shows the transmitted (a) and reflected (b) spectra of the sensing element, when inserted into the FLM. It is possible to appreciate the periodic bandpass filter created by the loop superimposed with the MMI resonances. The MMI peak is sensitive to the SRI and slightly responsive to temperature. Conversely, the wavelength fringes formed by the loop mirror are highly sensitive to temperature and practically do not respond to SRI. The MMI interference pattern, being non birefringent is common to both polarization modes and it is therefore equally observable both in the transmitted and reflected signals. Its spectral characteristics are identical to what was observed prior to insertion into the loop, confirming no cross interference between the two sensitive elements. The HiBi segment, on the other hand, generates a fringe pattern whose visibility depends on the amount of radiation propagating in each birefringence axis. This way, using the PC it was possible to control the amount of light traveling in each polarization mode, and therefore control the relative visibility of the reflected and transmitted signals.

In the transmitted signal (Figure 6.6(a)), it is observable the superposition of the HiBi interference pattern and the MMI interference pattern. On the reflected signal (Figure 6.6(b)), on the other hand, since the visibility of the HiBi pattern was reduced to zero, by further adjusting the PC, only the MMI interference pattern is visible. In order to enhance the tracking resolution of the RI induced wavelength shifts, a ratiometric detection scheme was implemented. Labview control of the FS2200SA enabled real-time direct access and processing of the data sets, corresponding to both reflection and transmission signals. Two narrow spectral intervals (about 125 pm) were chosen at the each side of the resonant dip (shown in Figure 6.6(a)). The integrated

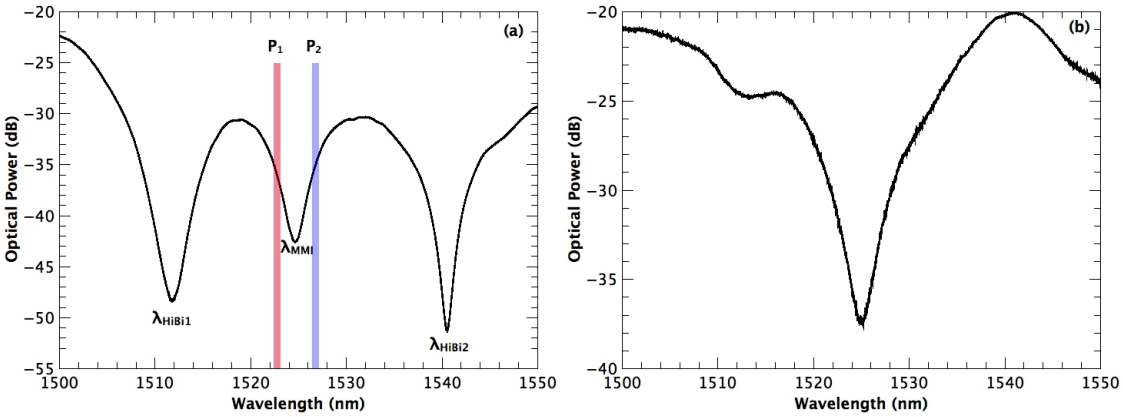

Figure 6.6: Transmitted (a) and reflected (b) spectra of the HiBi FLM–MMI device.

optical power of each wavelength slit resulted in signals P_1 and P_2. The subsequent computation of $R = \frac{(P_1-P_2)}{(P_1+P_2)}$ yields a signal that is proportional to the wavelength shift and is independent of any optical power fluctuation, providing higher accuracy than standard peak tracking schemes [43, 208]. It should be taken into consideration that the wavelength shift range of this algorithm is limited by the spectral position of the selected intervals. In fact this operation is suitable and intended to measure very small variation of a resonant peak with high accuracy. In such measurement ranges, changes in the resonance FWHM, which could otherwise cause measurement errors, are practically negligible. For the present experiment only the transmitted spectrum was considered, the R parameter was used to monitor with high resolution the MMI peak (λ_{MMI}). The wavelength of the second peak of the HiBi (λ_{HiBi2}), presenting much larger wavelength shifts, was recorded using a standard peak tracking algorithm.

6.4.2 Result and Discussion

Refractive index and temperature sensitivities were characterized separately. To avoid strain/curvature cross sensitivity, in both experiments, the sensing head was properly fixed and in the first case, placed inside a test chamber. The RI response was characterized by exposing the sensor head to different solutions of distilled water with different percentages of salt at constant temperature (25 ℃). The RI of each liquid sample was previously characterized with an Abbe refractometer using the sodium D line (589 nm). The studied solutions were in the RI range from 1.3216 (pure distilled water) to 1.3281 RIU. The necessary adjustments, considering the sensing head operation at 1550 nm, were made using the Cauchy equation with the respective co-

efficients [21]. The transmitted spectra for two different solutions of salty water are shown in Figure 6.7. As expected the MMI resonance shifts towards longer wavelengths as the RI, i.e. the salt percentage is increased. Meanwhile, the HiBi FLM peaks remain practically unaltered (only a small fluctuation with standard deviation of 15 pm was appreciable in the studied range).

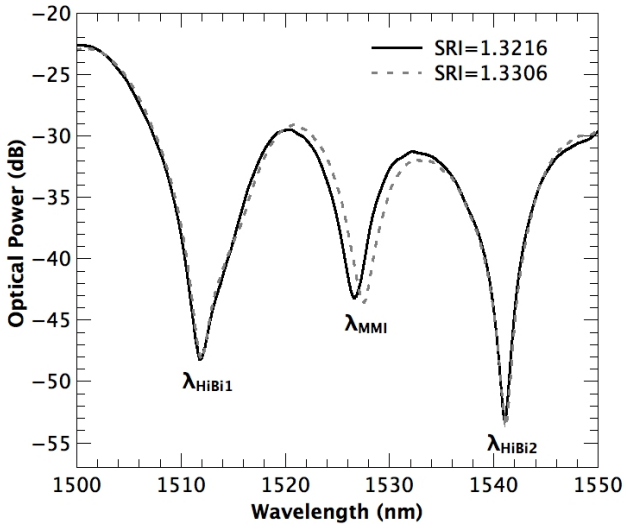

Figure 6.7: Transmitted spectra of the sensing probe for two different surrounding refractive indices.

Figure 6.8(a) illustrates the response λ_{MMI} to the SRI. Using a standard Labview peak detection algorithm it was possible to track the wavelength peak for the different values of refractive index and estimate a sensitivity of 90.5 ± 0.9 nm/RIU from the slope of the collected data. This calibration curve results from a series of measurements that incorporate a large time span and number of measured data points (150 s, 1 S/s), where each point corresponds to the average of each set of acquired data. The inset in Figure 6.8(a) illustrates the real-time response of λ_{MMI}, induced by a RI step change of 1.5×10^{-3} RIU. From the statistics of the measured values the standard deviation was calculated for each step. It was then considered a minimum detectable signal of two times the largest calculated standard deviation (2σ) in the measurement interval. From this procedure a refractive index resolution of ± 2.8×10^{-4} RIU could be estimated. As discussed earlier, to enhance the tracking resolution, a ratiometric power algorithm was implemented. Figure 6.8(b) shows the behavior of the R parameter as a function of the solution RI in the studied range. A sensitivity of 60.4 ± 0.3 RIU^{-1} can be estimated from the slope of the acquired data. The calibration results from a series of measurements that incorporate a large time span and number

of measured data points (150 s, 1 S/s), where each point corresponds to the average of each set of acquired data. The inset in Figure 6.8(b) illustrates the dynamic behavior of R, induced by a step change of 1×10^{-3} in the RI. From the statistics of the real-time retrieved data, the standard deviation was calculated for each step. It was then considered a minimum detectable signal of two times the largest calculated standard deviation (2σ) in the measurement interval. From this procedure a refractive index resolution of $\pm$ 2.25×10^{-5} RIU was estimated.

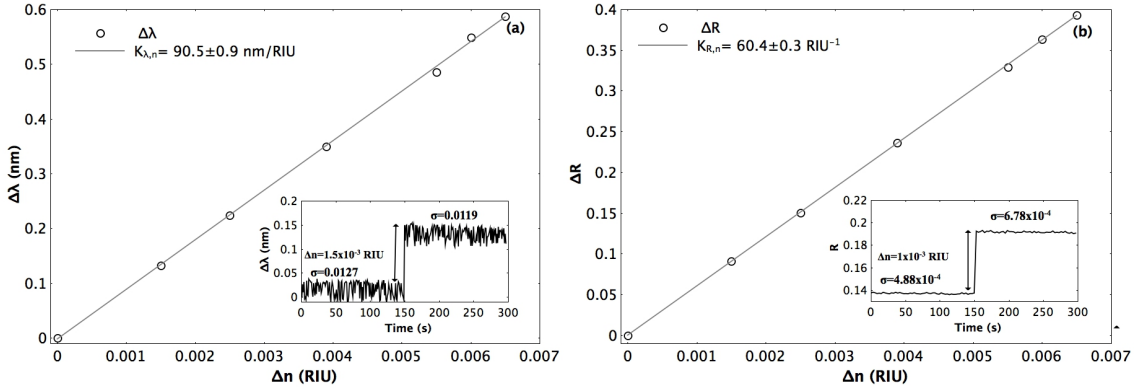

Figure 6.8: λ_{MMI} (a) and R parameter (b) as a function of the variation of the refractive index. The insets of (a) and (b), show a variation of λ_{MMI} and R respectively, induced by a step change of the SRI.

For temperature characterization, the sensing head was placed over a hot plate. The temperature was measured using a thermocouple. The temperature was changed between 28.75 ℃ and 30 ℃. Figure 6.9 shows the transmitted spectra for a variation of temperature of 1.25 ℃. As expected, with the increment of the temperature the HiBi peaks shift to shorter wavelengths. Simultaneously, it is noticeable a very small change in the MMI resonance towards longer wavelengths (inset of Figure 6.9).

Figure 6.10 shows the calibration curves resulting from the thermal studies. For λ_{HiBi2} a sensitivity of 2.36 $\pm$ 0.06 nm/℃ was measured. The R parameter of the MMI peak, on the other hand, varies 0.078 $\pm$ 0.001 /℃. This means that even for a temperature fluctuation of $\pm$ 0.1 ℃ an error of at least $\pm$ 10^{-4} RIU will be introduced. This way, for biosensing application, where high refractive index resolution is mandatory, and considering the resolution of this MMI sensor, simultaneous measurement of temperature must be performed in order to determine the refractive index without ambiguity.

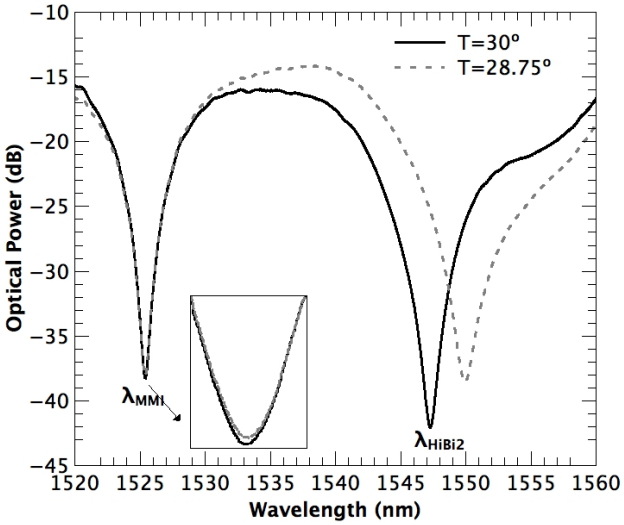

Figure 6.9: Transmitted spectra of the sensing probe for two different temperatures.

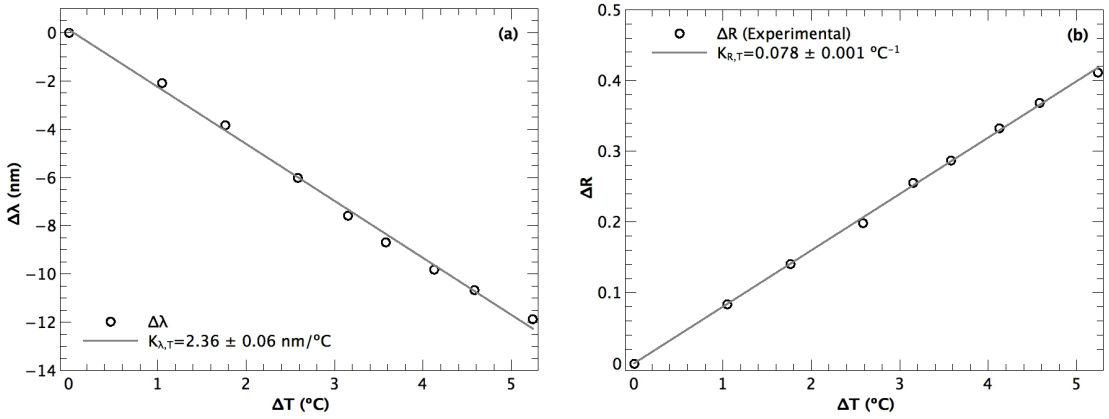

Figure 6.10: λ_{HiBi2} (a) and R parameter (b) as a function of the variation of the temperature.

In Table 6.1, it is summarized the sensitivity coefficients of the HiBi FLM - MMI sensor system for refractive index (K_n) and temperature (K_T) taken from the slopes of the linear fits represented in Figure 6.8(b) and Figure 6.10, respectively.

	K_n	K_T
ΔR	60.4 ± 0.3 RIU^{-1}	0.078 ± 0.001 /°C
$\Delta\lambda_{HiBi2}$	-	2.36 ± 0.06 nm/°C

Table 6.1: Sensitivity coefficients of the sensing probe for refractive index and temperature.

The dual response of the MMI R parameter and the wavelength shift, λ_{HiBi2}, of the FLM, allows writing a conditioned system of two equations for Δn and ΔT, given in matrix form as;

$$\begin{pmatrix} \Delta T \\ \Delta n \end{pmatrix} = \frac{1}{-K_{n,R}K_{T,\lambda}} \begin{pmatrix} 0 & K_{n,R} \\ K_{T,\lambda} & K_{T,R} \end{pmatrix} \begin{pmatrix} \Delta R \\ \Delta\lambda_{HiBi2} \end{pmatrix}, \tag{6.10}$$

where $K_{n,R}$, $K_{T,R}$ and $K_{T,\lambda}$, the matrix elements, are the sensitivity coefficients of the sensing probe represented in Table 6.1;

$$\begin{pmatrix} \Delta T \\ \Delta n \end{pmatrix} = -\frac{1}{142.544} \begin{pmatrix} 0 & 60.4\pm0.3 \\ 2.36\pm0.06 & 0.078\pm0.001 \end{pmatrix} \begin{pmatrix} \Delta R \\ \Delta\lambda_{HiBi2} \end{pmatrix}. \tag{6.11}$$

With these tools, temperature and refractive index can be determined unequivocally by processing the signals retrieved from the HiBi FLM and MMI sensing head. The system performance was evaluated when the sensing probe was simultaneously subjected to RI and temperature changes. In order to change both measurands a solution of ethylene glycol was used. When added to distilled water, ethylene glycol produces an exothermic reaction and consequently the increment of the solution temperature. Simultaneously, a variation of RI comes from the different concentrations of ethylene glycol. The measured raw signals and those processed through the resulting equations from the matrix are shown in Figure 6.11. Traces (a) and (b) correspond, respectively, to the raw signals given by the $\Delta\lambda_{HiBi2}$ and the ΔR parameter of the MMI peak. Traces (c) and (d), on the other hand, represent, respectively, the temperature and refractive index information retrieved through the matrix operations.

In Figure 6.11 trace (a) shows a wavelength shift that mimics the gradual increment in temperature as the glycol is added. Since the HiBi FLM signal just depends on temperature, the temperature retrieved by the matrix operation (trace (c)) exactly matches the wavelength behavior. It is clearly visible a sharp increment in temperature when the solution is spiked, followed by a slower cooling to an equilibrium temperature, as the solution is homogenized. The final temperature, nevertheless, is always higher than the original value, resulting in step increments of the average temperature. Trace (b), given by the R parameter of the MMI peak, depends both on temperature and refractive index. This way, the observed behavior results from the mixed response to these two parameters. However, applying the matrix operations the refractive index behavior, alone, can be retrieved and is represented in trace (d). It can be seen that right after the solution spiking sharp peaks are also observed in the refractive index trace. At this stage of the process, the solution is not homogeneous, so there is the chance the temperature and refractive index sensors are not

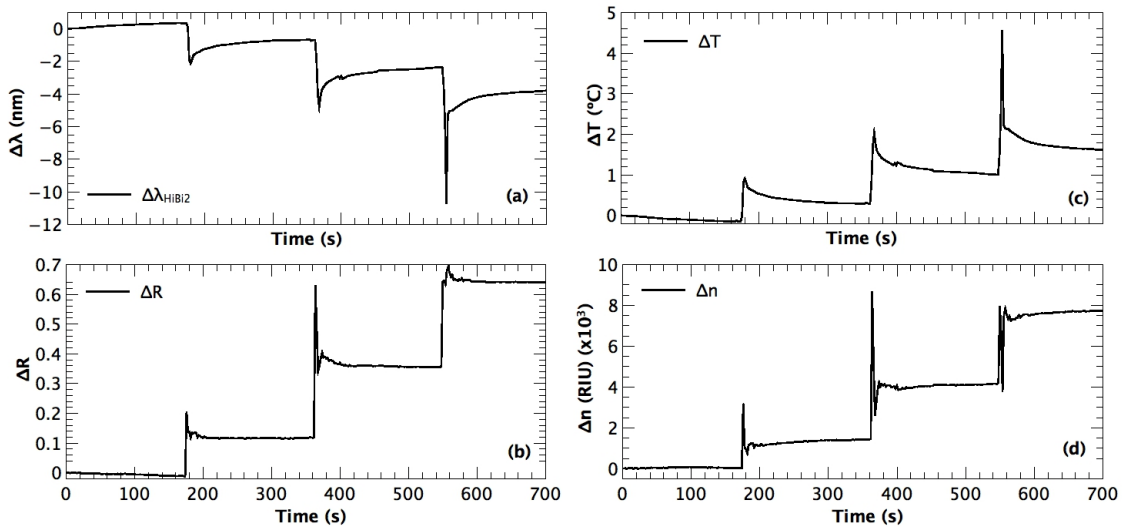

Figure 6.11: Sensor output for a simultaneous variation of refractive index and temperature. (a) Wavelength shift of λ_{HiBi2}, proportional only to temperature, (b) evolution of the R parameter, proportional both to temperature and refractive index, (c) temperature measurement retrieved using data from (a) and (b) and the matrix operations and (d) refractive index measurement retrieved using data from (a) and (b) and the matrix operations.

submitted exactly to the same conditions. In addition, refractive index of the solution is also dependent on its temperature via its thermo optic coefficient. This way, while refractive index spikes may indeed occur, prior to the solution homogenization, the temperature compensation performed by the matrix operation may not be totally effective. Nevertheless, at the equilibrium stage, where the solution has a more homogenous temperature and refractive index distribution, the compensation is indeed effective. This can be verified in Figure 6.12 that shows the recovered temperature and refractive index at different times, considering the average values or the "steady state" value of each incremental step.

Independent temperature and RI measurements of the solution using a thermocouple and Abbe refractometer are also shown. The adjustments considering the sensing head operation at 1550 nm, were made using the Cauchy equation with the respective coefficients [185, 186]. The maximum errors for temperature and RI measurements were found to be ± 0.02 ℃ and ± 2.25×10^{-5} RIU, respectively. This way, the proposed sensing system demonstrates to be suitable for high sensitivity refractometric measurement without temperature ambiguity. The RI sensitivity can be further increased (doubled) by using a smaller diameter coreless multimode fiber as it was recently demonstrated in a previous work [92, 235]. Also, the sensing probe

length can be reduced using a smaller section of HiBi fiber, in order to have just one peak in the 1500-1600 nm window or by using a different polarization maintaining fiber with higher birefringence. The smaller sensing head will be less prone to be affected by non-homogeneous distributions in the probed solutions.

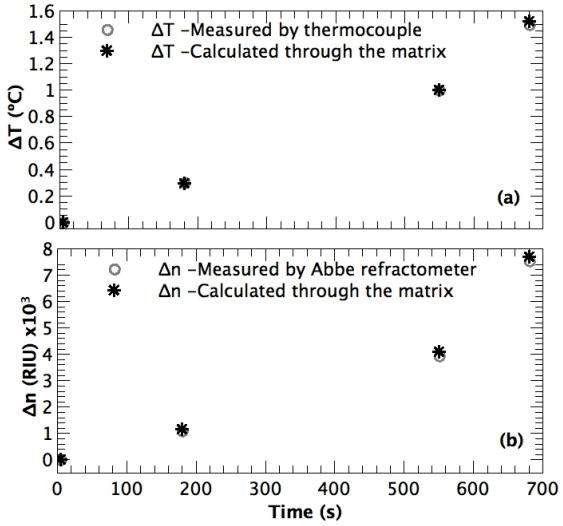

Figure 6.12: Data measured with the thermocouple and the Abbe refractometer and recovered by using the matrix method for the temperature (a) and refractive index (b).

The system presented, based in a refractive index and temperature fiber optic sensor is a platform for both chemical and biological sensing applications. For instance, direct measurements of refractive index were shown to provide valuable information on drug/DNA interaction, or cell growth [5, 82]. On the other hand, a variety of silica surface functionalization is described in the literature that will render a refractometer a powerful biosensor [6]. The present configuration eliminates the need for very stringent temperature control in such applications allowing for more reliable refractive index based chemical and biochemical monitoring.

6.5 Conclusion

The measurement of chemical and biological parameters is extremely important for a variety of applications ranging from the environment to the industry. In this context, label-free fiber optic refractometers represent a very promising alternative to the conventional techniques. One of the biggest challenges of fiber optic refractometers is how to deal with the temperature cross-sensitivity.

In this work, a sensing structure capable of measuring RI and temperature without ambiguity was demonstrated. The probe is achieved by combining a multimode interference based refractometer inside a high-birefringence loop mirror. The MMI refractometer relies on the concept of re-imaging effects of MMI patterns present in multimode waveguides. In these devices, the transmitted spectral power distribution is highly sensitive to the optical path length of the multimode fiber and to its SRI. On the other hand, the HiBi FLM consists on a section of HiBi fiber spliced between the output ports of a directional optical coupler arranged in a manner suitable to obtain an optical path difference between the fast and the slow axis, being very sensitive to temperature and fairly insensitive to RI.

In the presented configuration, a section of 180 mm of Panda fiber was spliced to a section of 52 mm of pure silica coreless multimode fiber. The Panda-CMF section was consequently spliced to the output ports of a directional optical coupler to form the MMI/FLM based probe. Spectrally, it was possible to observe the periodic bandpass filter created by the loop superimposed with the MMI resonance. The MMI peak is sensitive to the RI solution (90 nm/RIU) and slightly responsive to temperature (0.01 nm/℃). Conversely the external wavelength fringes formed by the loop mirror are highly sensitive to temperature (2.36 nm/℃) and practically do not respond to RI. The sensor system is capable to detect variation of refractive index in the order of ± 2.25×10^{-5} RIU. The system performance was evaluated when the refractometer was simultaneously subjected to refractive index and temperature changes over ranges of ∼ 0.008 RIU and 1.5 ℃, respectively. The maximum error was found to be ± 2.25×10^{-5} RIU and ± 0.02 ℃, respectively.

Chapter 7

Temperature Independent Refractive Index System using Differential White Light Interferometry

Summary

A fiber optic interferometric system for differential refractive index measurement is described. The system is based on a white light Mach–Zehnder configuration, with serrodyne phase modulation, used to interrogate two similar non-adiabatic tapered optical fiber sensors in a differential scheme. In this situation the system is able to measure the refractive index independent of temperature. Signal processing with low cost digital instrumentation developed in Labview environment allows a detectable change in refractive index of $\Delta n \approx 1.46\times10^{-6}$, which is, from the best of our knowledge the highest resolution achieved using a bare fiber taper device for a range of refractive index close to the water index. The results demonstrate the potential of the proposed scheme to operate as a self-referenced chemical and biological sensing platform.

7.1 Introduction

In the previous chapter, fiber optic refractometric sensors were described as viable and promising alternative for label-free biochemical sensing. The temperature cross-

sensitive issue was also exposed. A solution, consisting of the simultaneous measurement of both parameters (index and temperature) based on a multimode interference device in a HiBi loop mirror was reported.

If the aim of the sensing scheme is to measure the index of a solution, quantify the amount of an analyte present in a solution or measure index variations induced by certain reactions in a controlled environment, the temperature measurement may be enough to get an unambiguous measure of index that allows to conclude about the parameter of interest. However, sometimes it is necessary to work on real and complex uncontrolled environment, where the presence of a sensitive layer containing biomolecules with affinity to the target or chemical species having analyte specific ligands is needed, in such cases, the existence of many potentially interfering factors, molecules or elements is a critical issue for the reliability of the measurement. Thus, there is a need for a more robust system that enables not only to compensate the temperature, but also, the bulk refractive index of the solution and the target (analyte) among other interfering molecules present in such environment.

In this context, a differential system, where two sensing elements are used, one as a sensor, and another as a reference, could be an interesting concept of a truly self-referenced biosensing platform. Where the sensing device can be functionalized with the sensitive layer and the reference could be coated with a passive layer. Anyway, it should be clear that, the design of the sensitive membrane plays a key role for the definition of the sensitivity and the selectivity of the sensing probe, and the differential scheme serves as a mechanism to further provide a more reliable measurement and enhance the limit of detection of the sensing system.

In the previous chapter, a sensing probe capable of simultaneous measurement of the refractive index and temperature was presented, in this work, as in many other reported in literature, the sensors were interrogated in the spectral domain using devices such as an OSA. However, the use of interferometric methods can further increase the measurement resolution. White Light Interferometry (WLI) is one of the most attractive interferometric interrogation methods used for such purpose and it has been applied for remote measurement of diverse parameters such as strain, temperature, pressure and refractive index [222, 259–261]. This technique uses low coherence optical sources providing absolute measurement at high resolution and the ability of multiplexing sensors onto a single optical fiber using coherence multiplexing [217, 219, 220]. An issue associated with this readout technique, however, is the sensitivity of the readout interferometer to external and internal perturbations such as vibrations, temperature, among others. These perturbations can induce significant

phase drifts, limiting the resolution of the measurements. It is possible to decrease those phase deviations by properly isolating the readout interferometer. Nevertheless, due to its high sensitivity, this solution is not entirely effective.

In this context, using a Mach–Zehnder configuration it is possible to set up a differential measurement scheme through the comparison of the phase of two output signals of the interferometer. In such case the environmentally induced phase drifts will be canceled out (common phase noise rejection) allowing a very stable and accurate phase measurement. Such system is then a powerful tool to track the wavelength changes of external interferometric sensors. In particular, it can be used to interrogate two similar interferometric sensing devices simultaneously, one as the measurement sensor and a second one as a reference sensor. Using appropriate setting of the path imbalances of each of the interferometers, the phase difference between the two signals depends only on the modulation imposed by the parameter of interest, thereby reducing also the effects of cross-sensitivity, indissociable of these systems. Differential WLI systems have been employed to measure temperature [262, 263], liquid refractive index [264, 265], air refractive index [266] and for fuel conformity analysis [223].

In this work an interferometric readout system, controlled with virtual instrumentation, is described where a Mach–Zehnder white light system is used to interrogate two similar non-adiabatic fiber tapers in a differential arrangement. In this configuration it is possible to measure the RI with high resolution and independent of temperature. The results demonstrate the potential of the proposed scheme to operate as a high-resolution label-free biochemical sensing platform avoiding the need for temperature control.

7.2 Readout Interferometer

In this section the white light interferometry and the pseudo-heterodyne technique will be presented. The concept and the theory behind the readout interferometer used on the experiments are presented. The description of the developed white light interferometry system is also given.

7.2.1 White Light Interferometry

Fiber optic white light interferometry, also called low coherence interferometry, as its name suggest, uses broadband sources (low coherence) such as light emitting diode (LED) or super luminescent diode (SLD) instead of using monochromatic laser sources. WLI has drawn significant interest in the last years, due to its inherent

advantages; the measurement accuracy is virtually insensitive to optical power fluctuations and, since the WLI system can operate with LED or SLD devices, and avoids spectral interrogation, these systems can be cheap options. Thus, WLI has become widely used and an important technique for the absolute remote measurement of quasi-static parameters, such as displacement, temperature, pressure, strain and refractive index [217].

WLI was firstly described in 1975 by Delisle and Cielo [267] and then demonstrated in 1976, as a possible transmission scheme to be used in optical communications [268]. This technique was firstly reported for use in fiber optic sensing by Al Chalabi *et al.* in 1983 [269]. The first fully developed displacement sensor system based on the WLI technique was reported in 1984 [270].

A possible configuration for a WLI system is represented in Figure 7.1. Light from a broadband source is launched into one arm of a bidirectional fiber coupler, the output optical signal from the first interferometer, called sensing interferometer, is coupled via a fiber link into the second interferometer, named the local readout interferometer. The sensing interferometer is usually located in the measurand field, whilst the readout interferometer is normally placed away, in a controlled environment. The optical path difference (OPD) of the interferometers should be few times higher than the coherence length of the source, such that no interference will be observed in the time domain at the output of each individual interferometer. As long as the OPD of the readout interferometer (ΔL_R) is adjusted to match the OPD of the sensing interferometer (ΔL_S) within the coherence length of the source, interference occurs at the output of the readout interferometer. The phase and fringe visibility of the resulting interferometric signal will be a function of the difference between the OPD of both interferometers [217].

Analyzing the transfer function of this tandem interferometer system, it is possible to express the electric field at the output of a two-beam readout interferometer by [217];

$$E = E_{11} + E_{12} + E_{21} + E_{12}, \tag{7.1}$$

where E_{ij} is the component of the electric field at the output arising from propagation via the j^{th} arm of the sensing interferometer and the i^{th} arm of the readout interferometer, given by;

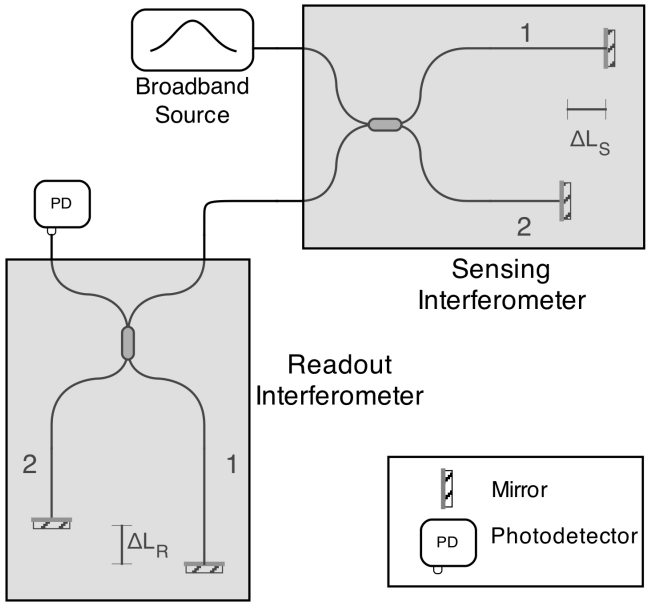

Figure 7.1: Basic low coherence interferometry system using Michelson interferometers.

$$\begin{aligned} E_{11} &= A_{11}e^{j\phi}, \\ E_{12} &= A_{12}e^{j(\phi+k\Delta L_S)}, \\ E_{21} &= A_{21}e^{j(\phi+k\Delta L_R)}, \\ E_{22} &= A_{22}e^{j[\phi+k(\Delta L_S+\Delta L_R)]}, \end{aligned} \tag{7.2}$$

where A_{ij} is the amplitude of each E_{ij}, k and ϕ are the wavenumber and the optical phase of E_{11}, respectively. The output optical intensity, I, can be obtained by taking the time averaging of equation (7.1), which is the product of the overall output electric field E and its complex conjugate;

$$I = \left\langle E^2 \right\rangle = \left\langle \left(E_{11}+E_{12}+E_{21}+E_{12}\right)\left(E_{11}+E_{12}+E_{21}+E_{12}\right)^* \right\rangle . \tag{7.3}$$

Assuming that the directional coupler is 50:50 and neglecting all the optical losses in the system, the output optical intensity is given by;

$$\begin{aligned} I = I_0 \{ 1 &+ I_1 \left|\gamma\left(\Delta L_S\right)\right| \cos\left(k\Delta L_S\right) + I_2 \left|\gamma\left(\Delta L_R\right)\right| \cos\left(k\Delta L_R\right) \\ &+ I_3 \left|\gamma\left(\Delta L_S+\Delta L_R\right)\right| \cos\left(k\left(\Delta L_S+\Delta L_R\right)\right) \\ &+ I_4 \left|\gamma\left(\Delta L_S-\Delta L_R\right)\right| \cos\left(k\left(\Delta L_S-\Delta L_R\right)\right) \} , \end{aligned} \tag{7.4}$$

where I_0 is the average optical power received by the detector, I_i are the normalized intensities of each term in equation (7.4) and $|\gamma(\Delta L)|$ is the absolute value of the normalized source autocorrelation function. When $\Delta L_S, \Delta L_R >> L_c$ (L_c is the coherence length of the source) and $\Delta L_S - \Delta L_R < Lc$, which is the necessary condition

for a remote WLI system, the second, third and fourth term in equation (7.4) are zero. Therefore, the interferogram obtained at the photodetector is given by [217];

$$I = I_0 \left\{1 + I_4 \left|\gamma \left(\Delta L_S - \Delta L_R\right)\right| \cos\left(k \left(\Delta L_S - \Delta L_R\right)\right)\right\}. \tag{7.5}$$

For a low-coherence source, the autocorrelation function usually has a Gaussian profile given by [271];

$$|\gamma(\Delta L)| = e^{-\frac{\pi}{2}\left(\frac{\Delta L}{L_c}\right)^2}. \tag{7.6}$$

Since the system is illuminated with a broadband source, with its coherence length shorter than the OPD of the sensing interferometer, the interference effects will only be observed at the output of the readout interferometer when the $\Delta L_R = 0$ or $\Delta L_R = \pm\Delta L_S$ [272]. Figure 7.2 shows the output of the readout interferometer as a function of its OPD when illuminated by a low coherence source.

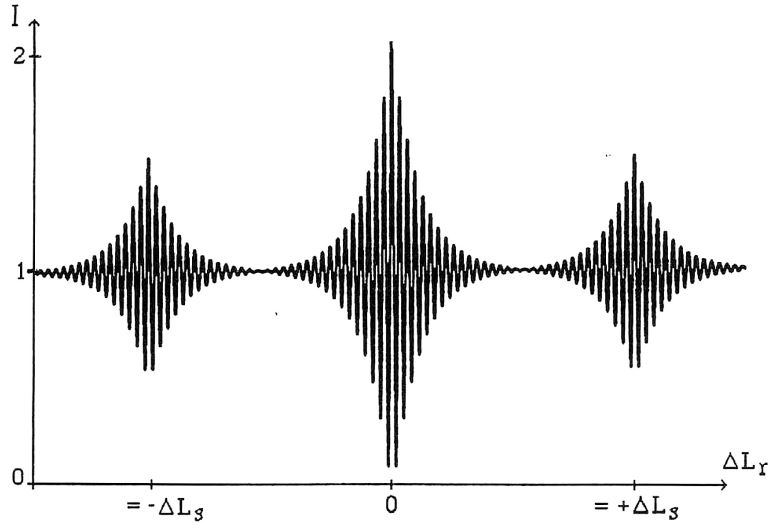

Figure 7.2: Interference fringes produced by the WLI system shown in Figure 7.1, as a function of ΔL_R in the readout interferometer [272].

An advantage for this technique is that the measurement accuracy is independent of the source stability, or such that the wavelength instability of the source are greatly reduced [272]. Also the signals of many sensors can be multiplexed by using coherence multiplexing [217, 219, 220, 273]. Unfortunately, it also has a disadvantage, the readout interferometer needs to be very stable for precision measurements [272]. On the other hand, as exposed in the first section of this chapter, the use of a differential scheme can mitigate fluctuations arising from the instability of the readout interferometer, building up a more robust device. Hence, in the readout interferometer

developed for this PhD work, a Mach-Zehnder configuration was selected, in order to use the two outputs to implement a differential scheme.

In WLI, changes in the OPD of the sensing interferometer are translated to the OPD of the readout interferometer. The effect of the measurand can be obtained by varying the optical path difference in the receiving interferometer, or by reading the phase of the interferometric system. The reading of the phase change allows a more precise measurement. To retrieve the phase, it is necessary to implement a dedicated phase readout scheme. Next section a brief summary of some of these techniques will be presented.

7.2.2 Detection Techniques

The main function of the detection scheme, using an interferometer as a sensor, is to convert the phase information of the interferometer to an electrical signal suitable for further processing. The detection of the phase of an optical signal, is a process that requires accuracy, stability and to have a reasonable operational range. Most of the detection techniques, in terms of operation may be classified as passive or active [274].

In the passive operation, the scheme does not have feedback or an active biasing element. Conversely, in the active operation, the scheme requires feedback loop controlling the optical source or other active element of the system, or employs an electrically active optical biasing element involving tracking, scanning or modulating mechanisms. Generally, the active detection schemes are more complex systems when compared to the passive ones but show better performance.

Additionally, the detection and signal processing techniques for interferometric sensors can be grouped into three categories [275];

1. Homodyne - the signal and the reference signal have the same frequency when interfering with each other. Thereby, the information signal remains in the original frequency band;

2. Heterodyne - the optical frequency of one arm (sometimes in both) of the interferometer is shifted in order to produce a beat frequency at the output of the interferometer. In this case, the information of interest appears as the phase (static or dynamic) of this beat frequency.

3. Pseudo–heterodyne – it creates a phase modulated carrier signal by modulating the wavelength of the optical source or the optical path length of one of the

interferometer arms. Thus, the signal information is transposed to the frequency of the carrier.

Table 7.1 are summarizes the principal techniques of interferometric phase detection [198].

Homodyne	Active	Active homodyne uses a quadrature phase feedback technique and compares the output optical signal arriving from the photodetector with a reference level, which is defined at the quadrature point of the interferometer. The error signal is amplified to drive a linear phase actuator within the interferometer to maintain the interferometer at this quadrature point. The feedback signal is the demodulated phase signal.
	Passive	The signals are retrieved by acting outside of the interferometer or by analysis of the interferometer outputs in quadrature.
Heterodyne		In this technique, the frequency is modulated in one arm of the interferometer. Typically, an acousto-optic or a PZT modulator is used to shift the frequency of one arm of the interferometer with respect to the other.
Pseudo-Heterodyne	Synthetic	This demodulation technique uses phase modulation in the form of a periodic sinusoidal function in one of the arms of the interferometer to obtain in the output a modulated carrier signal.
	True	This demodulation technique uses phase modulation in the form of a periodic ramp function in one of the arms of the interferometer to obtain in the output a modulated carrier signal.

Table 7.1: Phase detection signal processing techniques for interferometric sensors.

In the readout interferometer implemented for this PhD work, the pseudo-heterodyne technique was employed. The choice was based on a previous work conducted in our labs, where several schemes were studied, the results showed that the best technique was pseudo-heterodyne [276]. Between the synthetic and true heterodyne system, we select the latter, because the sawtooth modulation of one of the arms of the interferometer results in a sinusoidal modulation signal at the output, making easier its post-processing. In the following paragraphs this technique will be detailed.

The pseudo-heterodyne technique is implemented, by generating a carrier signal, with a frequency ω_c, produced by modulation of the OPD in one of the arms of the readout interferometer. This carrier signal is obtained by introducing a phase modulator in one arm of that interferometer, to which a sawtooth (or ramp) waveform electrical signal is applied. Thus, the OPD is periodically changed, introducing in the interferometer a periodic modulation.

The resulting signals at the output have complex spectrum, consisting of components at the fundamental and harmonics of the sawtooth frequency. The distribution of energy in each of these frequency components depends on the total phase excursion of the fringe pattern during the modulation period T. Experimentally, it was found to be possible to concentrate most of the power in the fundamental of the ramp frequency, by adjusting the amplitude of the modulation signal in order to produce a sinusoidal waveform at the output signal during each sawtooth period, i.e., $\left(\frac{d\phi}{dt}\right) T = 2\pi$. In this situation the period of the generated carrier signal (sinusoidal) is equal to the sawtooth signal.

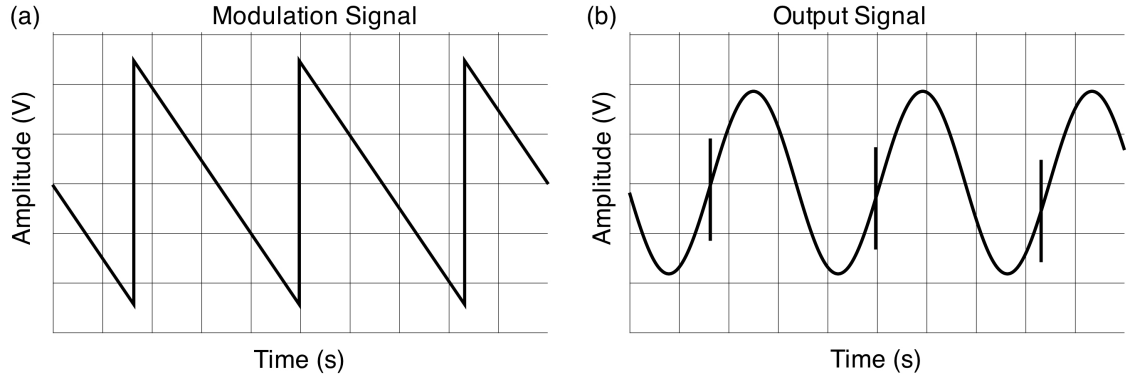

Figure 7.3: (a) sawtooth modulation signal and (b) sinusoidal output when the condition $\left(\frac{d\phi}{dt}\right) T = 2\pi$ is satisfied.

In Figure 7.3 it is possible to see a periodic perturbation in the sinusoidal signal. This perturbation arises from the discontinuity of the sawtooth signal that introduces a fast flyback period. This flyback can be eliminated using bandpass filtering around the modulation frequency. With the scheme shown in Figure 7.1, and using the true pseudo-heterodyne detection, the induced changes in the OPD of the sensing interferometer, derived from variations in the measurement field, can be retrieved through the phase of carrier signal. The signal detected at photodetector is then given by [274];

$$I = I_0 \left\{1 + I_4 \left|\gamma \left(\Delta L_S - \Delta L_R\right)\right| \cos\left(\omega_c t + k \left(\Delta L_S - \Delta L_R\right)\right)\right\}. \tag{7.7}$$

The signal reading can be made by using a physical lock-in amplifier or by using virtual instrumentation. In this work, the phase retrieving was made with virtual instrumentation developed in a Labview environment, based on the Fourier transform of the acquired signals [263]. Details regarding the implemented interferometer are given in the next section.

7.2.3 Implemented Readout Interferometer

Figure 7.4 shows the setup of the readout interferometer which is in a standard fiber optic Mach–Zehnder configuration, where the sensing and reference interferometers are connected to each of the output arms. As stated before, for operation, the path imbalance of the reading interferometer should match that of the sensor interferometers so that the overall path is nearly zero. For this purpose, in one of the arms of the Mach–Zehnder, an open air path is implemented through a circulator using a graded-index (GRIN) lens and a mirror mounted in a translation stage. With this arrangement the reading interferometer path imbalance can be tuned to match the optical path difference of the sensing interferometers. On the other arm, an electro-optical phase modulator (APE from JSDU) was inserted for carrier generation, where a sawtooth modulation with its amplitude adjusted to obtain a 2π phase excursion was used, yielding a sinusoidal carrier generation at the interferometer output.

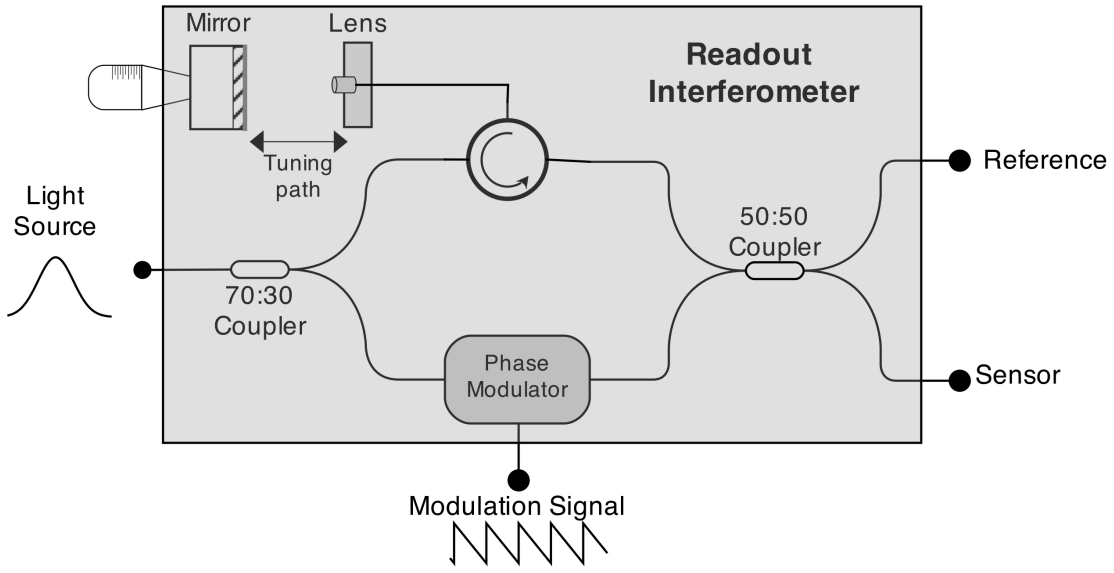

Figure 7.4: Implemented readout interferometer in a Mach-Zehnder layout.

The coupling ratio of the first coupler was chosen in order to maximize the fringe visibility of the interferometer. Due to high insertion loses of the phase modulator (4 dB) compared with the open air path (2 dB), a coupling ratio of 70:30 is used. Figure 7.5 shows the channeled spectrum of the readout interferometer. The spectrum was obtained by illuminating the interferometer (without modulation) with a SLD light source, meanwhile one of the outputs of the Mach-Zehnder was plugged to an Advantest Q8384 OSA, where the spectrum was recorded. A path imbalance of 0.4 mm was set and a visibility of $\sim 50\%$ can be estimated. In order to keep the readout device isolated from external environmental perturbation such as temperature and vibration, a proper packaging was carefully done using insulating materials.

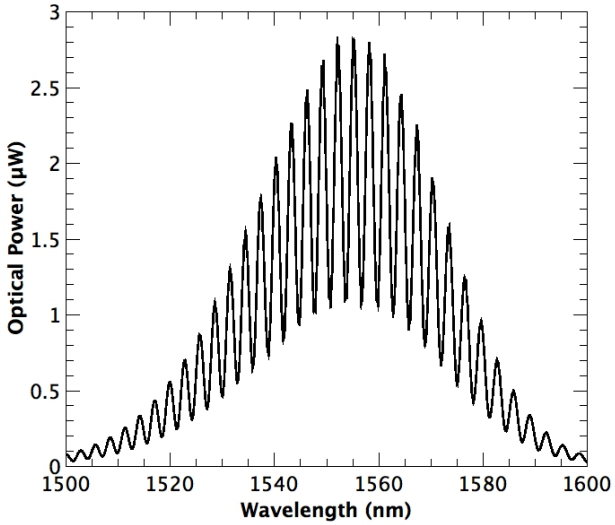

Figure 7.5: Channeled spectrum of the readout interferometer.

The coherence length of the SLD source used above was measured. For this purpose, the modulation signal was applied and one of the outputs of the reading device was plugged into a photodetector. The signal was acquired with a DAQ and the amplitude of the carrier was recorded as a function of the path imbalance. Figure 7.6 shows the resulting graph, from which it is possible to estimate that the coherence length of the light source is around 20 μm.

The two output ports of the readout interferometer are used to interrogate two similar interferometric sensors, which are subsequently connected to two photodetectors. In this arrangement, the readout interferometer acts as a modulator for the two sensing interferometers conditioning the signal received by the photodetectors. When the optical path difference of the sensors is matched to the readout interferometer within the coherence length of the source, it is possible to get the phase information

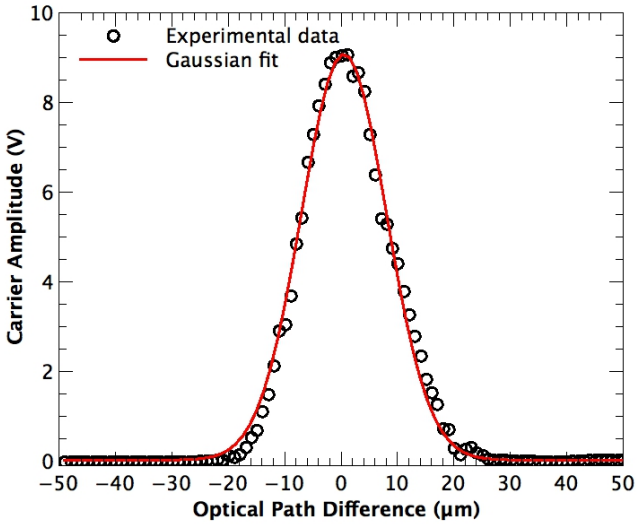

Figure 7.6: Peak-to-peak amplitude of the carrier signal as a function of the path imbalance of the readout device.

of the sensing probes at the frequency of the carrier. Using one of the interferometers as reference and the other as sensor, and since the Mach–Zehnder outputs are in phase opposition, most environmentally induce phase drifts can be canceled out, and the phase difference between both signals depends only on the modulation inferred by the parameter of interest, allowing a very stable and accurate phase measurement, retrieved using phase comparison software.

The software for the phase recovery is based on the Fourier transform of the two output signals [277]. Figure 7.7 shows a diagram with all the steps in the signal processing stage. The signals are acquired using a DAQ, sampled with a rate proportional to the frequency of the modulation signal. This condition guarantees the acquisition of a quasi-sinusoidal signal in the output. After acquisition, the DC component is removed. Subsequently, a band-pass filter, centered at the frequency of the carrier is applied. Both signals are then amplified and the Fourier transform is calculated. Once the Fourier transform is calculated, the phase difference between reference and sensor signals is easily retrieved. A standard unwrap algorithm allowed to eliminate the 2π phase ambiguity, enabling the extension of the dynamic range to thousands of degrees.

In the experiment, for the differential measurement of refractive index, the interferometers used as sensing devices were non-adiabatic tapered optical fibers (NATOF). In the next section, a brief description of such devices is given.

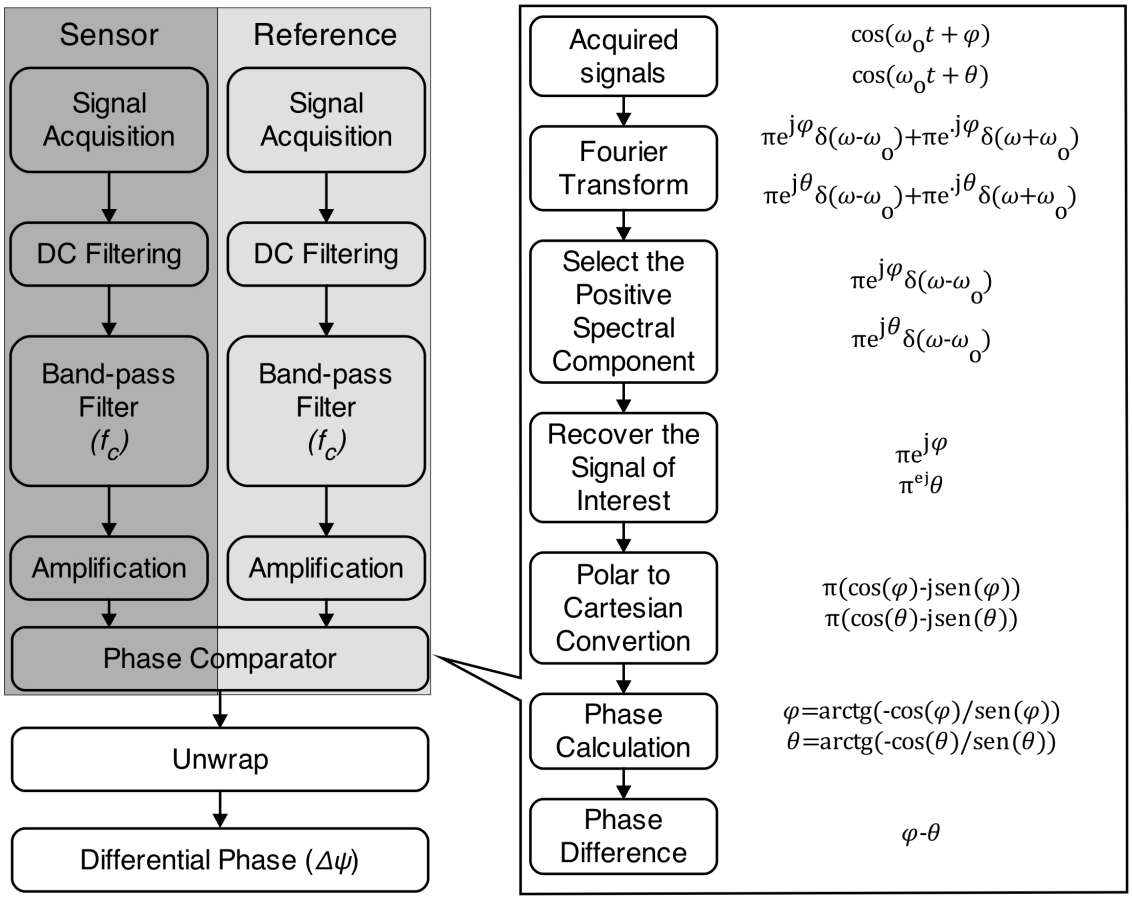

Figure 7.7: Schematic of the signal processing employed in the experiment.

7.3 Tapered Optical Fibers

Tapered singlemode fibers are the basis of many optical fiber devices and have attracted much interest over the last years. These devices are probably the most common alternative to the etched or polished fibers to promote evanescent field interaction for sensing applications. Generally, fiber optic tapers based sensors present higher sensitivity than those in which the cladding is removed [278]. Many applications have been developed, including their use as filters for fiber WDM devices [279], SPR based biosensors [115], fiber dye lasers [280], and for nonlinear research and communications [281].

A taper on a SMF essentially consists in reducing the cladding diameter to few micrometers along with the core, and it is usually made by heating a section of the fiber until its softening temperature, and pulling on both ends of the fiber in the opposite directions, either under a constant speed, force or tension. The heat source can be a gas burner flame [282], a focused CO_2 laser beam [5] or an electric-arc

formed between a pair of electrodes [283]. As a result, the tapered fiber consists of three contiguous sections. A taper waist segment with small and uniform diameter and two conical transition regions with gradually reduced diameter. At the ends of conical transition regions are untapered fibers. The material of the fiber core in the waist and transition regions do not have clear boundaries with the cladding material, because it get mixed together, after the tapering. A schematic of a tapered fiber is shown in Figure 7.8. The taper waist diameter, length, and transition shape, are critical for a specially required interference spectrum. By controlling the fabrication parameters such as pulling speed, heating length and temperature, tapered fibers with different shapes and properties can be fabricated [84].

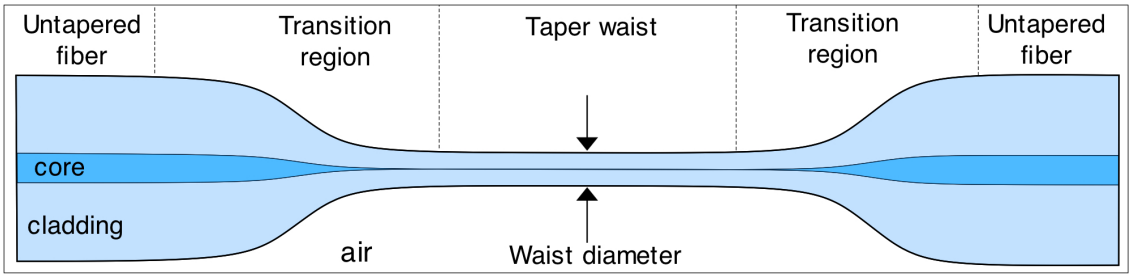

Figure 7.8: Schematic of a singlemode tapered fiber, showing the three contiguous parts.

In an untapered SMF, the thin core is surrounded by the cladding. The light is confined within the core and its propagation through an optical fiber may be described by wave theory. The V number determines the properties of the light traveling into the core. It defines the number of modes which can be supported by the core, and is given by;

$$V = \frac{2\pi}{\lambda} r_{co} \sqrt{n_{co}^2 - n_{cl}^2}, \tag{7.8}$$

where r_{co} is the radius of the core. In the untapered region, only the fundamental mode ($LP_{0,1}$) is propagating. However, in the transition region, due to the decreased diameter, the fiber core gets mixed together with the cladding to form a medium whose refractive index is very close to that of the cladding. This medium can be considered as an air/cladding waveguide, which has a larger radius than the original SMF core in the most part of the transition region, and a higher numerical aperture due to the large difference of indices between the air and the fiber cladding. Following equation 7.8, this region acts as a multimode waveguide that supports more than one mode. Depending on the transition region tapers are normally divided into two

distinct categories; adiabatic and non-adiabatic, in the adiabatic tapers the transition is smooth, whilst in the non-adiabatic tapers the transition is abrupt. For adiabatic transitions, the fundamental core mode $LP_{0,1}$ is efficiently transmitted (99.5 %) and the contribution of higher order modes is insignificant and can be neglected [284]. In the condition of non-adiabatic transition, some high-order modes can be excited, but just the first two modes $LP_{0,1}$ and $LP_{0,2}$ are relevant, if the fabrication is properly controlled.

In the taper waist region, part of the light energy is not confined by the thin waist, around which a high evanescent field is created, and mainly the first two modes $LP_{0,1}$ and $LP_{0,2}$ are coupled from one end of the non-adiabatic transition region and propagate at the air-cladding interface. $LP_{0,1}$ and $LP_{0,2}$ modes are coupled back into the fundamental mode at the end of the second non-adiabatic transition region, were they interfere. The efficiency of this last coupling depends on the relative phase of the participating modes $\Delta\phi = \Delta kL$, where Δk is the relative propagation constant and L the is length along the taper. Δk can be adjusted by changing the environment medium, and L can be changed by adjusting the taper waist length. The interference effect between $LP_{0,1}$ and $LP_{0,2}$ produces fringes in the transmission spectrum, typically with a sinusoidal behavior. Thus, a non-adiabatic tapered optical fiber behaves as a Mach-Zehnder modal interferometer [80, 285]. In order to ensure the interference, the taper waist diameter has to be well control. For instance, if it is less than 1 μm the interference effect does not exist for 1550 nm, because at such size the waist has similar properties as the core in the singlemode fiber and the $LP_{0,2}$ mode is no longer supported by the waveguide [84]. This diameter cut-off can be calculated by using equation 7.8.

Figure 7.9 (a) shows a conceptual scheme of the NATOF (a) and its behavior as a two waves interferometer (b). When there are only two modes, the relative phase, as a function of the effective indices of both modes, at the output can be expressed as;

$$\Delta\phi = \left(n_{eff,co} - n^{m}_{eff,cl}\right) L, \tag{7.9}$$

where $n_{eff,co}$ and $n^{m}_{eff,cl}$ are the effective indices of the core and the m^{th} cladding mode, respectively, and L, as stated above is the interaction length along the taper. Therefore, the spectral response of the taper will shift correspondingly by changing the above terms. For example, if the RI of the surrounding environment of the taper changes, the difference in effective index of the cladding and core modes and, consequently, the relative phase would be modified, leading to a shift of the spectral

response. NATOF based fiber refractometers have been used recently as refractometers in the biochemical field due to its high sensitivity and compact size [5, 82, 84].

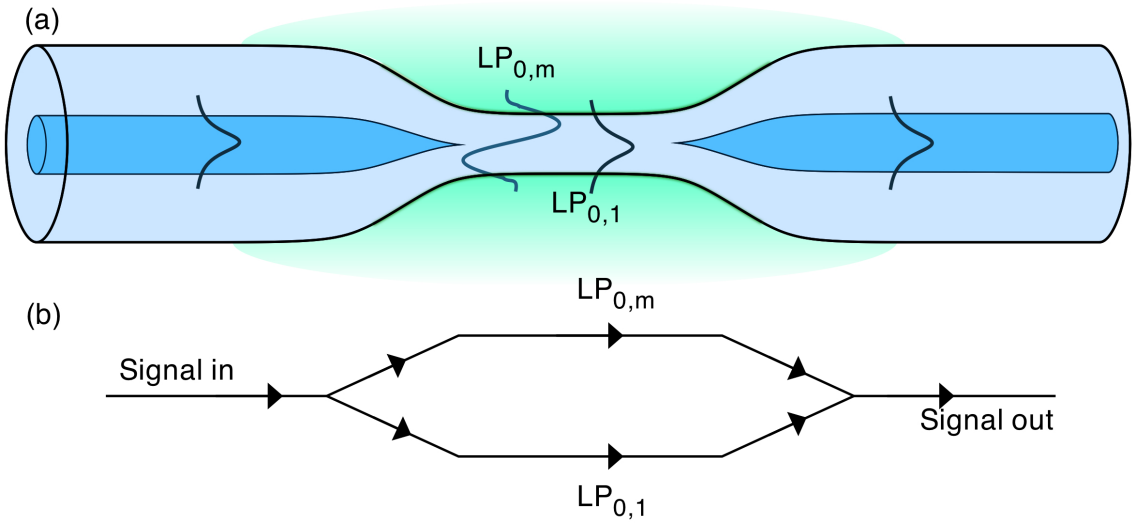

Figure 7.9: Schematic representation of non-adiabatic taper (a). Conceptual representation as a modal Mach–Zehnder interferometer (b).

In the next section a differential system based on WLI interrogation system and two quasi-identical NATOF sensing devices will be presented as a potential and powerful platform for biochemical sensing.

7.4 Differential Measurement of Refractive Index

A fiber optic interferometric system for differential refractive index measurement is reported. The system is based on a white light Mach–Zehnder configuration, with serrodyne phase modulation, used to interrogate two similar non-adiabatic tapered optical fiber sensors in a differential scheme. In this situation the system is able to measure the refractive index, independent of temperature. The promising results show the potential of the proposed scheme to operate as a self-referenced chemical and biological sensing platform.

7.4.1 Experimental

Figure 7.10 shows the experimental setup for differential measurement of refractive index. The readout interferometer was illuminated by a super-luminescent diode (SLD) source ($\Delta\lambda_{FWHM} \approx 40$ nm and $L_{coherence} \approx 18$ μm). A sawtooth modulation signal (1 kHz) with amplitude 7.2 V generated by a signal acquisition board (DAQ NI 6259

USB) was applied, to the phase modulator in one of the arms of the interrogator interferometer, in order to scan its sinusoidal transfer function by a full period. Two similar NATOFs connected to its output ports were used. The sensing devices were fabricated with heat pulling method using a CO_2 laser. The experiment was performed using NATOFs with a taper length around 20 mm, with a transition region of about 2 mm and a uniform waist length approximately of 16 mm, with an average taper waist diameter in the range of 6–8 μm. The optical power loss of the tapers was approximately 9%.

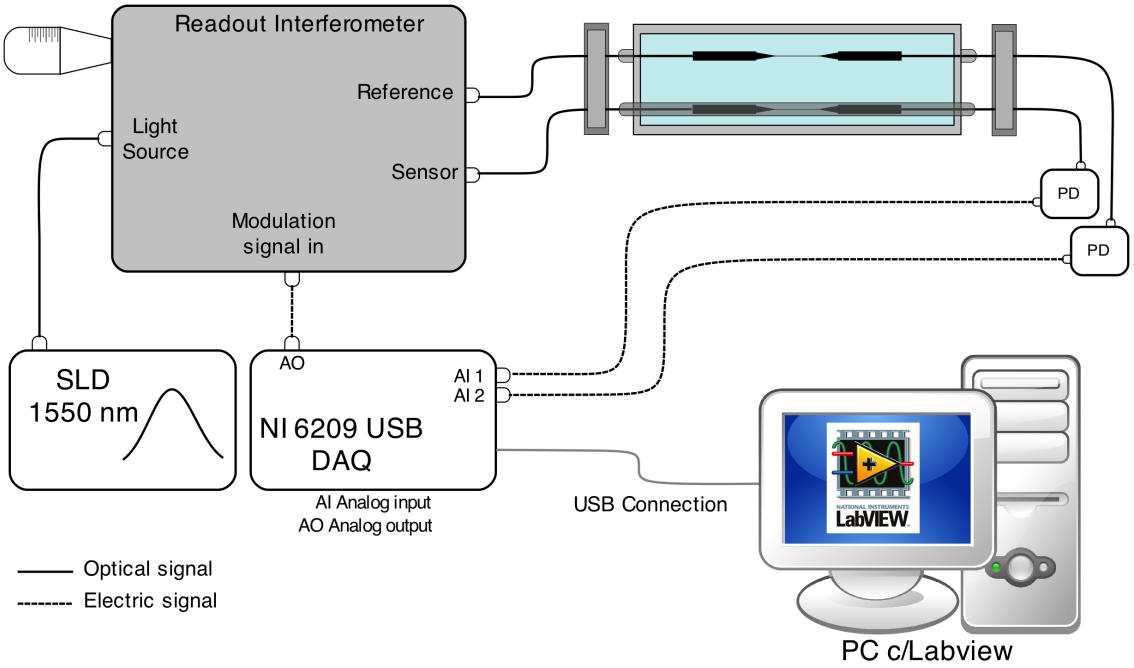

Figure 7.10: Experimental setup for the WLI based differential measurement of refractive index.

Before characterization, the spectra of both tapers were obtained by using a simple setup, which consisted in a SLD light source (the same used in the experiment) to illuminate the sensors, and an Advantest Q8384 OSA with 10 pm maximum resolution, where the sensors output spectra were recorded. Figure 7.11 shows the spectra of the two sensing probes. A very smooth fringe pattern is observed in both cases, modulated by the envelope of the optical source. Similar fringe periods and fringe visibility are observed in both cases, indicating that the sensors are almost identical interferometers making this set suitable to be used as a sensor/reference pair.

The sensing elements were placed into a test chamber with both fiber ends properly fixed to avoid strain/curvature cross-sensitivity. The reference element was fixed

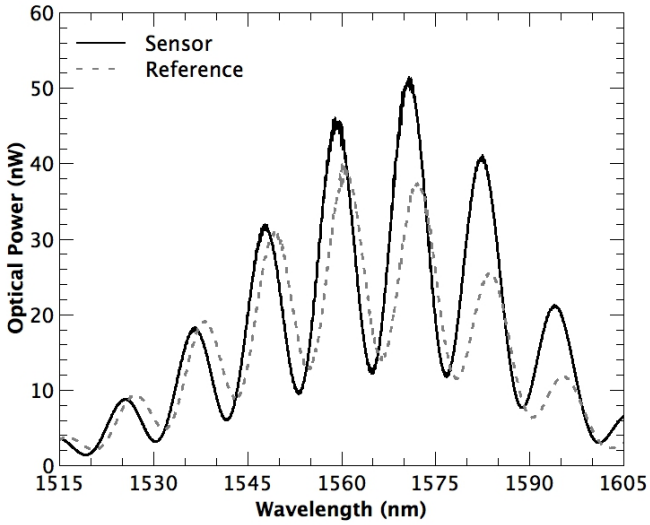

Figure 7.11: Transmitted spectra of the two NATOFs used in the experiment.

inside of a 260 μm diameter metallic capillary tube, protected from direct contact with the solution. Therefore, in this situation, the reference was sensitive to temperature changes in the solution but insensitive to the refractive index variations in the solution. The transmitted signals were guided toward two photodetectors plugged into an acquisition board. Then, at the signal processing stage, the output of the detectors was filtered through a band-pass filter centered at modulation frequency, thereby eliminating the remaining higher harmonic components (created by discontinuities induced by sawtooth modulation signal). The filter introduces a fixed bias on the phase of both signals. Therefore, the differential phase measurement was not affected by the constant phase deviation introduced by the filtering. In this situation, after filtering, the changes in the surrounding refractive index output arises as a phase shift on the sinusoidal carrier signal, which was retrieved using the relative phase comparison software. The differential phase signal was, therefore, sensitive only to the refractive index of the solution.

7.4.2 Results and Discussion

Prior to the refractive index characterization, the intrinsic stability of the readout interferometer was investigated by measuring the differential phase ($\Delta\psi$) between the two output ports, with no sensor plugged in. The two arms relative phase was monitored for a period of time of approximately thousand seconds. Figure 7.12 shows the recorded phase response during the tested time interval. From the statistics of the recorded values the standard deviation was calculated. This data shows the residual

random drift of the interrogation system, which is very small ($\sigma \sim 0.0047$) proving the effectiveness of common noise rejection of the differential scheme. This result shows that the system is able to resolve a minimum phase change of $\pm$ 0.009º (considering the resolution is given by 2σ).

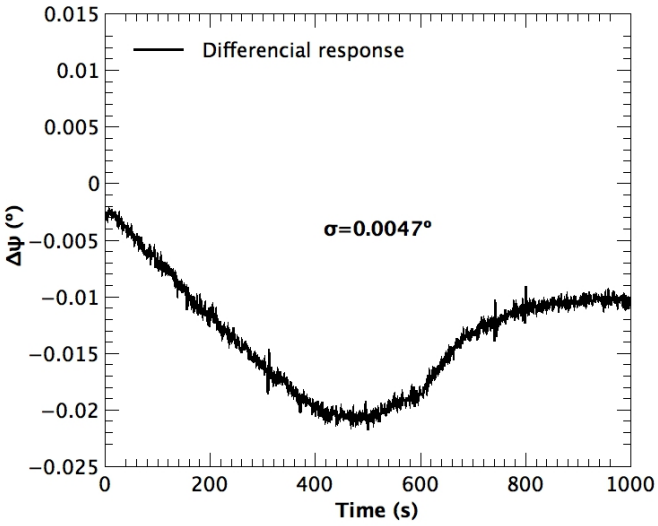

Figure 7.12: Stability of the differential phase between the two output ports of the readout device.

Following this initial test, the NATOF sensors were plugged into the readout interferometer outputs and tested for refractive index measurements. The response of the sensor to the SRI was studied by exposing the sensing head to different solutions of distilled water mixed with different concentrations of ethylene glycol to provide the RI standards in a range between 1.3216 – 1.3312. The refractive index was changed by successively adding different ratios of ethylene glycol /deionized water. In order to homogenize the mixture, the solution was stirred through a magnetic stirrer. After mixing, the stirring was stopped and the data was recorded, the process was repeated continuously for each of the steps. The liquid samples were characterized by an Abbe refractometer using the sodium D line (589 nm). The necessary adjustments, considering the sensing head operation at 1550 nm, were made using the Cauchy equation with the respective coefficients [185, 186]. The time response of the differential sensing platform to SRI step changes is shown in Figure 7.13. When acquiring this data, the recording was paused during the changing of the solutions, being resumed after 100 s. This way, all the mechanical perturbation introduced by the changing of the solutions was avoided. In a real application the sensors are bound to be inserted in flow system where this is not a problem.

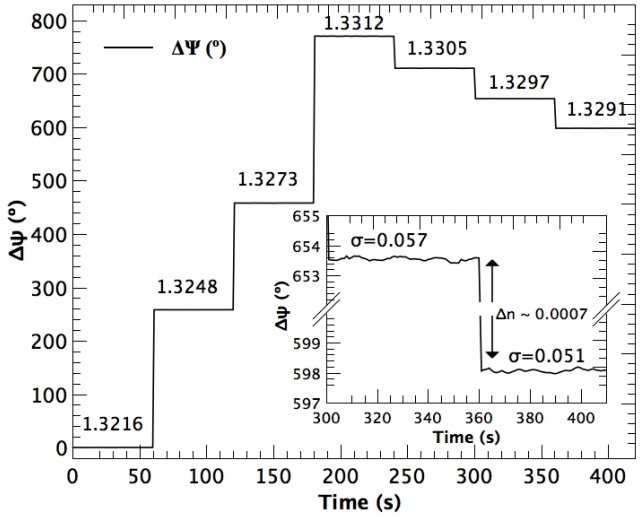

Figure 7.13: Time response of the sensing system to external refractive index changes. The inset shows with more detail the phase difference fluctuation for a change in SRI from 1.3305 and 1.3312.

The results show, as expected, an increment in the phase difference with the increase of the SRI. From this data, a calibration curve can be obtained that is shown in Figure 7.14. A sensitivity of 80084 ± 190°/RIU can be estimated from the slope of the acquired data. The inset in Figure 7.13 shows with more detail the phase difference fluctuation for a change in SRI from 1.3312 to 1.3305. From the statistics of the measured values, the standard deviation was calculated for each step. It was then considered a minimum detectable signal of two times the average calculated standard deviation (2σ) divided by the sensitivity in the measurement interval. From this procedure an average refractive index resolution of ± 1.46×10^{-6} RIU was calculated. This value is, from the best of our knowledge the highest resolution achieved using a bare fiber taper device for a range of refractive index close to the water index. In addition, in the best measurement obtained, a resolution of ± 6×10^{-7} RIU was achieved indicating the potential of this configuration to attain very high resolution. In a practical application more stringent statistics can be applied. In such case, for instance a 3σ standard would yield an average resolution of ± 2.16×10^{-6} RIU. Although a resolution of ± 7×10^{-7} RIU was reported by D. Monzon-Hernandez *et al.* (2006) [112] in this case the authors used an additional metal coating to obtain an SPR sensor over a fiber taper. In addition the measurements were performed for a range of RI close to the cladding index where sensitivity is higher. Also, the resolution was estimated, considering the resolution of the OSA and the accurate measurement of the SPR peak, which, neglects several factors namely; the resonance bandwidth and

signal fluctuations inherent to the measurement itself, due to temperature variation, low optical power, among others, all concurring to decrease the final system resolution.

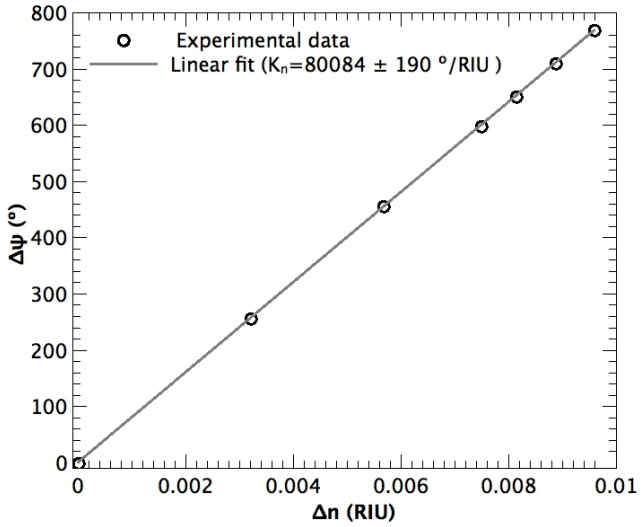

Figure 7.14: Calibration curve of the system for refractive index variations.

The small variations observed in the resolution, calculated in different intervals of refractive index, are probably due to actual refractive index fluctuations arising from heterogeneity in the dissolution of ethylene glycol in water. This is partially confirmed by the fact that highest resolution values were obtained for the solutions where the concentration of ethylene glycol was smaller. Also further improvements are possible by enhancing the interrogation interferometer stability. Having a birefringent element inside the interferometer (the phase modulator) introduces some polarization dependent noise. Therefore, the use of an active polarization control, or using an alternative way to modulate the interferometer phase, can potentially improve the results obtained.

It is important to emphasize that in the present configuration and for the achieved resolution, there is a limitation for the temperature independent measurement, which arises from the fact that the reference sensor was in air, although encapsulated. Assuming that the intrinsic sensitivity characteristics of both tapers are very close to each other, still, the fact that they are in different media limits the extent of compensation. The reference element is sensitive to variations in the thermo-optic coefficient of the air, which is around 10^{-6} [286], i.e. two orders of magnitude smaller than water thermo-optic coefficient. On the other hand, it is well-known that the sensitivity to the SRI of the evanescent field based sensors, shows a nonlinear monotonic behavior with increasing sensitivity as the SRI approaches the cladding RI. It means that the

sensitivity of the taper for a refractive index around 1 will be lower than for a RI close to 1.32. Some simple calculations performed to evaluate this difference revealed that, the sensitivity of the device for a SRI near to 1 is 6.6 times lower, than for SRI close to 1.32. Thus, it is possible to assert that, in the current configuration, it is possible to have an independent temperature measurement within the estimated resolution, for a variation lower than 10 ℃. For higher temperature changes, and since all the coefficients involved are known, it is possible to extend the compensation range by appropriate calibration and software correction.

In the cases where the thermo-optic coefficient needs to be compensated, the reference sensor has to be in contact with the solution. In the present configuration, this can be easily done by filling the capillary tube with deionized water. In such a case the sensing platform will be able to measure the refractive index variations in the sample. Such platform will enable to implement self-referenced biosensors where the measurement can be made independent of temperature, bulk refractive index changes and non-specific binding events at the surface.

Considering all the described features, the proposed sensing system demonstrates to be suitable for very high sensitivity refractometric measurement without temperature ambiguity, for both chemical and biological sensing applications. For instance, direct measurements of refractive index were shown to provide valuable information on drug/DNA interaction, or cell growth [5, 82]. On the other hand, a variety of silica surface functionalization strategies are described in the literature that can render a refractometer a powerful biosensor [6]. In such case, both sensing devices may be in contact with the solution, the reference can be functionalized with a passive layer enabling, therefore, to compensate for temperature, bulk refractive index and even non-specific binding events enabling a truly self-referenced biosensor.

7.5 Conclusion

In this work, a white light interferometric readout system, controlled with virtual instrumentation, was implemented where a standard Mach Zehnder fiber interferometer was used to interrogate two similar sensing interferometers in a differential arrangement. The developed readout system has several advantages. It takes full advantage of the interferometric nature of the sensing interferometers (NATOF, MZ-LPG, etc.) with increased sensitivity and resolution, also, using electrical modulation at frequencies in the KHz range permits to attenuate the effect of the 1/f noise of the electronics devices.

Differential measurements of refractive index were carried out using two similar NATOFs. One of the tapers was used as sensor and was exposed to variations of SRI and temperature and a second taper was used as a reference and exposed only to the thermal variations in the sample chamber. In this arrangement, changes in the surrounding refractive index arise as a phase shift on the sinusoidal carrier signal, which is retrieved using the relative phase comparison software. The differential phase signal is therefore sensitive only to the refractive index of the solution, including those induced by temperature.

The sensing system was characterized in the range between 1.3216 and 1.3312 RIU. A sensitivity of 84084 ± 190 $^{o}RIU^{-1}$ was estimated and an average resolution of ± 1.46×10^{-6} RIU was achieved (± 6×10^{-7} RIU in the best case). It was demonstrated, by the sensitivity and resolutions obtained that the proposed configuration is a sensing system with very high performance for label-free sensing applications. In biosensing applications, the reference can be functionalized with a passive layer, enabling, therefore, to compensate for temperature, bulk refractive index and even non-specific binding events enabling a truly self-referenced biosensor.

Chapter 8

Conclusions and Future Work

Summary

The work presented in this thesis is in the area of fiber optic sensors, particularly in the research and development of new sensing platforms for label-free biochemical sensing. The conclusions regarding the specific subjects covered in every chapter were already presented therein. Therefore, the aim of this chapter, is to present a global overview of the work done along the PhD, the major achievements of the research and point out some topics that are to be addressed in future research.

8.1 Final Remarks

The development of refractometric fiber optic platforms for label-free biochemical sensing is important, within the context of the demand for novel sensing tools capable of multiplexing, real-time and remote operation in electromagnetic or chemically hazardous environments. Fiber optic sensors, fulfill the requirements described above, and additionally, they are also compact, lightweight, and usually present high sensitivities.

The measurement of the external refractive index with optical fibers is frequently done through the evanescent field at the fiber/external medium interface. In a standard singlemode fiber, the light is confined into the core, and there is almost no interaction between the optical signal and the external medium. Therefore, strategies

must be devised to provide interaction between the optical signal and the surrounding medium. Typically, the evanescent field is exposed by drastically reducing the fiber diameter. It is done by etching, polishing or tapering processes, that normally introduces fragility on the sensing structure. In alternative, it is possible to use specific tools capable of coupling energy traveling in the core to the cladding. Some of these tools were described in this document, in this kind of devices the fiber integrity is preserved. Fiber gratings in particular are the most interesting devices to transfer energy between modes, specially the LPGs, that allow to control the excited mode and amount of power transferred by adjusting the fabrication parameters.

In addition to the underlaying platform, fiber optic biochemical sensors rely in the presence of a selective layer deposited on the fiber refractometer, to capture the analyte or that experience a refractive index change in its presence. This is achieved by using biomolecules with a natural affinity to the target, or chemical species having analyte specific ligands. When exposed to the analyte, a chemical/biochemical interaction takes place within this layer or on its surface. In this situation, only a portion of the optical radiation which reaches out of the sensor, the evanescent field, is modulated, depending on the thickness of the interaction region.

An important parameter that must be taken into account, in fiber optic biochemical sensors, is the penetration depth (d_p) of the evanescent field into the surrounding medium. Depending on the order of the mode, d_p can vary between few tens of nanometers up to few hundreds of nanometers. Thus, high order modes, penetrate into the external medium further away, being characterized by a greater value of d_p, showing higher sensitivity to the external index. This is valid to measure bulk refractive index of a solution. Nevertheless, this high sensitivity is not directly translated to a better performance of the biochemical device. Specially, in the case of a biological sensor, where the interaction occurs in a layer as thick as a few tens of nanometers. On the other hand, for chemical sensors, it depends on the thickness of the selective layer, of course, the thicker the layer, the higher will be the sensitivity, but also, higher will be the response time. A trade-off must be made between this two parameters.

The majority of the works reported in the literature present the sensitivity as the preponderant indicator of the performance of the device. However, the magnitude of the signal change (the sensitivity) does not wholly articulate the capability of the device to detect and quantify the properties of the analyte. It is equally important the ability to precisely and accurately detect the signal variations resulting from changes

in the sample. It is the resolution that defines the smaller change in the sample that can be detected by the system.

Besides the limitations of the interrogation hardware, there are two crucial aspects that can introduce noise in the signal, decreasing the resolution of the system. The spectral shape of the sensor and the absence of an effective mechanical and thermal stabilization. Regarding the first aspect, it is important to note that, for all the evanescent field based sensors, the maximum sensitivity is approached when the external index is close to the cladding index. On the other hand, the closer is the external index to the cladding index, the less defined is the spectral shape of the sensor. In this situation, it is difficult to accurately measure signal variations related with the sample. This statement suggests that, a situation of maximum sensitivity does necessarily not result in the higher resolution point.

Concerning the thermal and mechanical stability, it is a critical issue. Mechanical stability can be achieved by using a proper sensor packaging. On the other hand, the thermal stability is more complex. For the situation of in-situ measurements, it is extremely difficult to control the temperature. Although, in the case of a bench-top instrument the temperature can be controlled with a precision of $\pm$ 0.1 ℃, this is not enough, when high resolution measurement is being carried out. Therefore, to reach an optimal resolution, the development of a system capable of measuring the changes related with the analyte, independent from other parameters, has received highest relevance in this PhD work. Specially regarding the temperature cross-sensitivity issue, which impacts in greater or lesser degree all optical fiber sensors. Sensors for multi-parameter sensing purposes and the development of a differential readout interferometer were demonstrated. In the next section, the major achievements of the PhD work will be presented.

8.2 Major achievements

A review of the most important fiber optic refractometric sensing platforms for label-free biochemical sensing was presented, including the high sensitive SPRs, the well-known FBGs, the popular LPGs, a variety of modal interferometers ranging from tapers, mismatched fiber sections to MMI structures and also FFPI devices. Advantages and disadvantages were presented, and a comparison of performance of each sensing device in terms of sensitivity and detection limit. In this perspective, one of the aspects considered more carefully in this section, was to provide a list of references as current as possible with the most relevant works. Naturally, due to the speed

with which new developments occur in this area, should always be safeguarded either potential omissions of references that may be relevant in specific situations.

Two novel FBG based sensing configurations were described. An FBG based Fabry-Perot cavity formed between a low reflectivity HiBi FBG and the fiber tip was used for refractive index and temperature sensing. Although, the measurement of the SRI presents a quite low resolution, based on the fringe visibility, this configuration can be potentially explored for chemical sensing by coating the fiber tip with sensitive material [25]. In this case, the phase of the interfering fringes can be related with the analyte concentration.

A cladding mode of a simple FBG was excited for the very first time by a misaligned splice. Although, this configuration was initially designed for RI sensing, the excited cladding mode did not show sensitivity to the SRI. However, as a collateral benefit of this work a multi-parameter sensor was presented for the measurement of curvature independent form temperature and for the simultaneous measurement of strain and temperature.

LPGs are the most popular devices for biochemical sensing. An extensive characterization of several LPG based sensing probes was made along the PhD work. Regarding the fabrication with the INESC Porto electric-arc setup, in comparison with previous works, an LPG with a shorter period (Λ = 338 μm) using standard SMF-28 fiber was successfully fabricated, exciting a higher order mode, and increasing the sensitivity by a factor of 2. Due to the high sensitivity of this structures to temperature, the use of PS-LPGs for simultaneous measurement of RI and temperature was also explored. This particular work was motivated from interesting result presented in previous studies [47], but the results obtained in our work, did not allow to measure both parameters without ambiguity.

The study of the impact of HRI overlays in the sensitivity of the LPGs was done, by depositing PS (n =1.59) and ZnO/ZrO doped silane (n =1.78) with different thicknesses into the surface of several LPGs. The results show a huge increment in the sensitivity, and also the possibility of tuning the region of highest sensitivity of the sensing device to a certain range of RI. These studies on LPGs are extensible to other evanescent field based refractometers, such as FBG, MMI, among others.

Two LPG based sensing probes for the measurement of chemical and biological parameters, respectively, were also presented. An LPG coated with p-nitro-phenol based layer was used for CO_2 sensing. The results show that there is still so much work to do to improve the sensitivity of the sensor. An LPG functionalized with aptamer was described for the detection and quantification of *E. coli* bacteria proteins.

Regarding the temperature cross-sensitive issue, that affect fiber optic sensors in general, and the need a for precise measurement or control of the temperature, when high resolution measurement of RI is carried out, has led to design a novel configuration based on the combination of MMI structure inside of a HiBi FLM. The results show the possibility of measuring the refractive index and the temperature without ambiguity. One of the constraints of this sensing probe is its length, that can be reduced, by reducing the length of the Panda fiber, in order to have just one peak in the wavelength range between 1500-1600 nm. Also, a different refractometric structure can be used, for instance an LPG or using extra HiBi devices with specially designed fibers.

A WLI readout system, controlled with virtual instrumentation, was implemented where a standard Mach-Zehnder fiber interferometer was used to interrogate two similar sensing interferometers in a differential arrangement. The system shows the possibility of measuring the SRI independent from temperature, by using two quasi-identical tapers, used as a sensor and reference, respectively. It is worth to note, that this system is able to interrogate different kind of sensing interferometers, FBGs, among other sensing structures. This concept can be explored for a truly self-referenced biochemical sensor, in such a case, the sensor can be functionalized with an active layer and the reference with a passive layer enabling, therefore, to compensate for temperature, bulk refractive index and even non-specific binding events.

Different possibilities and combinations were studied during this PhD work, the choice of appropriate sensing platform will naturally depend on the application, and its specific characteristics that will determine the requirements of the sensing system. For instance, for biological application it is important to know in which range of refractive index the system will operate. For a chemical sensor, from the side of the refractometric platform, is crucial to know the optical properties of the sensing layer, would be prized to have a high-refractive index sensing membrane. The desirable response time is also necessary, in order to properly choose the mode order and the thickness of the sensing layer to maximize its performance. The possibility to control and choose the excited mode, is important, not just regarding reproducibility of sensing probe, but also to control the performance of the probe. In this case, the mode engineering that fiber gratings technology permits is valuable. For almost, all the situations, the possibility of use a differential system, would add robustness and reliability, allowing higher resolutions, by removing signal fluctuations arising from factors unrelated to the analyte.

It is worth to refer that, there are a few works carried out along the PhD programme, from which the results were not presented in this document. For instance, an LPG was used to remotely measure the refractive index using an OTDR system as interrogation equipment. The readout interferometer developed in Chapter 7 was used for the differential measurement of the magnetic field, using two FBGs, with one of them coated with Terfenol-D thin film. A similar interferometric readout system, was developed during the stay at UNICAMP. The system was used to real-time fuel conformity analysis. Also in a cooperation with UNICAMP, a Fabry-Perot cavity humidity sensor based on a Nafion film deposited in the tip of the fiber was investigated. Finally, based on a previous prototype unit, measurements of methane were carried out in the Department of Biotechnology of University of Lund with anaerobic digesters. Some of these results can be consulted through the publications listed in section 1.4.

8.3 Further Work

The research summarized above gives indications of topics requiring further investigation. In this PhD programme a large number of topics were studied and therefore, some might require, in fact, major improvements. A list of research topics that emerged within this work and require further investigation follows;

- The use of mode engineering based on fiber grating to efficiently excite high order modes of simple FBGs, to use in refractometry. The narrow peaks of FBGs ease its multiplexing and allow accurate detection of the resonant peaks permitting higher resolutions;
- The use of chemically sensitive and selective membranes to coat the FBG based FPPI developed and its integration with the readout interferometer to enhance the phase tracking;
- The acquisition of a CO_2 laser by the Optoelectronics Unit of INESC Porto, will allow the fabrication of LPGs with shorter periods, more sensitive LPG based interferometers and other devices;
- Proceed with experimental work with LPGs coated with ZnO/ZrO doped silane, in order to maximize its sensitivity, as it was done with the PS;
- Improvements in the performance of the CO_2 sensor by properly adjusting the refractive index of the sensing layer;

- Use the differential readout system to implement a truly self-referenced biosensor, using two quasi-identical LPG based interferometers, where one interferometer is functionalized with two different aptamers, one specific to the bacteria and the other one a non-specific.

References

[1] A. B. L. Ribeiro, J. L. Santos, J. M. Baptista, *et al.*, "Optical fiber sensor technology in portugal," *Fiber and Integrated Optics*, vol. 24, no. 3-4, pp. 171–199, 2005.

[2] E. Hecht, *Optics*, 4th ed. Addison-Wesley, 2001, vol. 1.

[3] F. Baldini, M. Brenci, F. Chiavaioli, *et al.*, "Optical fibre gratings as tools for chemical and biochemical sensing," *Anal Bioanal Chem*, vol. 402, no. 1, pp. 109–16, 2012.

[4] A. Asseh, S. Sandgren, H. Ahlfeldt, *et al.*, "Fiber optical bragg grating refractometer," *Fiber and Integrated Optics*, vol. 17, no. 1, pp. 51–62, 1998.

[5] M. I. Zibaii, H. Latifi, M. Karami, *et al.*, "Non-adiabatic tapered optical fiber sensor for measuring the interaction between alfa-amino acids in aqueous carbohydrate solution," *Measurement Science and Technology*, vol. 21, no. 10, p. 105801, 2010.

[6] X. Fan, I. M. White, S. I. Shopova, *et al.*, "Sensitive optical biosensors for unlabeled targets: a review," *Anal Chim Acta*, vol. 620, no. 1-2, pp. 8–26, 2008.

[7] A. D. Kersey, M. A. Davis, H. J. Patrick, *et al.*, "Fiber grating sensors," *Lightwave Technology, Journal of*, vol. 15, no. 8, pp. 1442–1463, 1997.

[8] O. Frazao, L. A. Ferreira, F. M. Araujo, *et al.*, "Applications of fiber optic grating technology to multi-parameter measurement," *Fiber and Integrated Optics*, vol. 24, no. 3-4, pp. 227–244, 2005.

[9] K. Schroeder, W. Ecke, R. Mueller, *et al.*, "A fibre bragg grating refractometer," *Measurement Science and Technology Technology*, vol. 12, no. 7, pp. 757–764, 2001.

[10] A. Iadicicco, S. Campopiano, A. Cutolo, *et al.*, "Nonuniform thinned fiber bragg gratings for simultaneous refractive index and temperature measurements," *Ieee Photonics Technology Letters*, vol. 17, no. 7, pp. 1495–1497, 2005.

[11] A. N. Chryssis, S. M. Lee, S. B. Lee, *et al.*, "High sensitivity evanescent field fiber bragg grating sensor," *Ieee Photonics Technology Letters*, vol. 17, no. 6, pp. 1253–1255, 2005.

[12] T. A. Birks and Y. W. Li, "The shape of fiber tapers," *Journal of Lightwave Technology*, vol. 10, no. 4, pp. 432–438, 1992.

[13] X. Fang, C. R. Liao, and D. N. Wang, "Femtosecond laser fabricated fiber bragg grating in microfiber for refractive index sensing," *Opt Lett*, vol. 35, no. 7, pp. 1007–9, 2010.

[14] Y. Zhang, B. Lin, S. C. Tjin, *et al.*, "Refractive index sensing based on higher-order mode reflection of a microfiber bragg grating," *Opt Express*, vol. 18, no. 25, pp. 26 345–50, 2010.

[15] G. Laffont and P. Ferdinand, "Tilted short-period fibre-bragg-grating-induced coupling to cladding modes for accurate refractometry," *Measurement Science and Technology*, vol. 12, no. 7, pp. 765–770, 2001.

[16] C. F. Chan, C. Chen, A. Jafari, *et al.*, "Optical fiber refractometer using narrowband cladding-mode resonance shifts," *Applied Optics*, vol. 46, no. 7, pp. 1142–1149, 2007.

[17] M. Han, F. Guo, and Y. Lu, "Optical fiber refractometer based on cladding-mode bragg grating," *Opt Lett*, vol. 35, no. 3, pp. 399–401, 2010.

[18] Q. Wu, Y. Semenova, B. Yan, *et al.*, "Fiber refractometer based on a fiber bragg grating and single-mode-multimode-single-mode fiber structure," *Opt Lett*, vol. 36, no. 12, pp. 2197–9, 2011.

[19] W. Liang, Y. Huang, Y. Xu, *et al.*, "Highly sensitive fiber bragg grating refractive index sensors," *Applied Physics Letters*, vol. 86, no. 15, pp. 151 122–151 122, 2005.

[20] S. F. O. Silva, O. Frazao, P. Caldas, *et al.*, "Optical fiber refractometer based on a fabry-perot interferometer," *Optical Engineering*, vol. 47, no. 5, pp. –, 2008.

[21] D. A. Pereira, O. Frazao, and J. L. Santos, "Fiber bragg grating sensing system for simultaneous measurement of salinity and temperature," *Optical Engineering*, vol. 43, no. 2, pp. 299–304, 2004.

[22] A. Cusano, A. Iadicicco, S. Campopiano, *et al.*, "Thinned and micro-structured fibre bragg gratings: towards new all-fibre high-sensitivity chemical sensors," *Journal of Optics a-Pure and Applied Optics*, vol. 7, no. 12, pp. 734–741, 2005.

[23] A. N. Chryssis, S. S. Saini, S. M. Lee, *et al.*, "Detecting hybridization of dna by highly sensitive evanescent field etched core fiber bragg grating sensors," *Ieee Journal of Selected Topics in Quantum Electronics*, vol. 11, no. 4, pp. 864–872, 2005.

[24] S. Maguis, G. Laffont, P. Ferdinand, *et al.*, "Biofunctionalized tilted fiber bragg gratings for label-free immunosensing," *Opt Express*, vol. 16, no. 23, pp. 19 049–62, 2008.

[25] C. Jesus, S. F. O. Silva, M. Castanheira, *et al.*, "Measurement of acetic acid using a fibre bragg grating interferometer," *Measurement Science and Technology*, vol. 20, no. 12, p. 125201, 2009.

[26] S. W. James and R. P. Tatam, "Optical fibre long-period grating sensors: Characteristics and application," *Measurement Science and Technology*, vol. 14, no. 5, pp. R49–R61, 2003.

[27] T. Erdogan, "Cladding-mode resonances in short- and long-period fiber grating filters," *Journal of the Optical Society of America a-Optics Image Science and Vision*, vol. 14, no. 8, pp. 1760–1773, 1997.

[28] A. M. Vengsarkar, P. J. Lemaire, J. B. Judkins, *et al.*, "Long-period fiber gratings as band-rejection filters," *Journal of Lightwave Technology*, vol. 14, no. 1, pp. 58–65, 1996.

[29] V. Bhatia and A. M. Vengsarkar, "Optical fiber long-period grating sensors," *Opt Lett*, vol. 21, no. 9, pp. 692–4, 1996.

[30] X. Shu, L. Zhang, and I. Bennion, "Sensitivity characteristics of long-period fiber gratings," *Lightwave Technology, Journal of*, vol. 20, no. 2, pp. 255–266, 2002.

[31] M. Smietana, W. J. Bock, P. Mikulic, *et al.*, "Increasing sensitivity of arc-induced long-period gratings—pushing the fabrication technique toward its limits," *Measurement Science and Technology*, vol. 22, no. 1, p. 015201, 2011.

[32] N. D. Rees, S. W. James, R. P. Tatam, *et al.*, "Optical fiber long-period gratings with langmuir-blodgett thin-film overlays," *Opt Lett*, vol. 27, no. 9, pp. 686–8, 2002.

[33] I. M. Ishaq, A. Quintela, S. W. James, *et al.*, "Modification of the refractive index response of long period gratings using thin film overlays," *Sensors and Actuators B: Chemical*, vol. 107, no. 2, pp. 738–741, 2005.

[34] I. Del Villar, M. Achaerandio, I. R. Matias, *et al.*, "Deposition of overlays by electrostatic self-assembly in long-period fiber gratings," *Opt Lett*, vol. 30, no. 7, pp. 720–2, 2005.

[35] A. Cusano, A. Iadicicco, P. Pilla, *et al.*, "Mode transition in high refractive index coated long period gratings," *Opt Express*, vol. 14, no. 1, pp. 19–34, 2006.

[36] P. Pilla, P. F. Manzillo, V. Malachovska, *et al.*, "Long period grating working in transition mode as promising technological platform for label-free biosensing," *Optics Express*, vol. 17, no. 22, pp. 20 039–20 050, 2009.

[37] L. Alwis, K. Bremer, T. Sun, *et al.*, "Analysis of the characteristics of pva-coated lpg-based sensors to coating thickness and changes in the external refractive index," *Sensors Journal, IEEE*, vol. 13, no. 3, pp. 1117–1124, 2013.

[38] Z. T. Gu and Y. P. Xu, "Design optimization of a long-period fiber grating with sol-gel coating for a gas sensor," *Measurement Science and Technology*, vol. 18, no. 11, pp. 3530–3536, 2007.

[39] J. M. Corres, I. R. Matias, I. Del Villar, *et al.*, "Design of ph sensors in long-period fiber gratings using polymeric nanocoatings," *Sensors Journal, IEEE*, vol. 7, no. 3, pp. 455–463, 2007.

[40] H. J. Patrick, A. D. Kersey, and F. Bucholtz, "Analysis of the response of long period fiber gratings to external index of refraction," *Journal of Lightwave Technology*, vol. 16, no. 9, p. 1606, 1998.

[41] P. Pilla, C. Trono, F. Baldini, *et al.*, "Giant sensitivity of long period gratings in transition mode near the dispersion turning point: an integrated design approach," *Opt Lett*, vol. 37, no. 19, pp. 4152–4, 2012.

[42] C. Trono, F. Baldini, M. Brenci, *et al.*, "Flow cell for strain- and temperature-compensated refractive index measurements by means of cascaded optical fibre long period and bragg gratings," *Measurement Science and Technology*, vol. 22, no. 7, p. 5204, 2011.

[43] C. Jesus, P. Caldas, O. Frazao, *et al.*, "Simultaneous measurement of refractive index and temperature using a hybrid fiber bragg grating/long-period fiber grating configuration," *Fiber and Integrated Optics*, vol. 28, no. 6, pp. 440–449, 2009.

[44] Y. Zhang, S. Gao, and A. Zhang, "Optically heated long-period grating as temperature-insensitive fiber-optic refractive-index sensor," *Photonics Journal, IEEE*, vol. 4, no. 6, pp. 2340–2345, 2012.

[45] J. Yan, A. Zhang, L.-Y. Shao, *et al.*, "Simultaneous measurement of refractive index and temperature by using dual long-period gratings with an etching process," *Sensors Journal, IEEE*, vol. 7, no. 9, pp. 1360–1361, 2007.

[46] Q. Han, X. Lan, J. Huang, *et al.*, "Long-period grating inscribed on concatenated double-clad and single-clad fiber for simultaneous measurement of temperature and refractive index," *Photonics Technology Letters, IEEE*, vol. 24, no. 13, pp. 1130–1132, 2012.

[47] J. Huang, X. Lan, A. Kaur, *et al.*, "Reflection-based phase-shifted long period fiber grating for simultaneous measurement of temperature and refractive index," *Optical Engineering*, vol. 52, no. 1, pp. 014 404–014 404, 2013.

[48] H. Ke, K. Chiang, and J. Peng, "Analysis of phase-shifted long-period fiber gratings," *Photonics Technology Letters, IEEE*, vol. 10, no. 11, pp. 1596–1598, 1998.

[49] O. Duhem, J. F. Henninot, and M. Douay, "Study of in fiber mach-zehnder interferometer based on two spaced 3-db long period gratings surrounded by a refractive index higher than that of silica," *Optics Communications*, vol. 180, no. 4-6, pp. 255–262, 2000.

[50] T. Allsop, R. Reeves, D. J. Webb, *et al.*, "A high sensitivity refractometer based upon a long period grating mach-zehnder interferometer," *Review of Scientific Instruments*, vol. 73, no. 4, pp. 1702–1705, 2002.

[51] P. Swart, "Long-period grating michelson refractometric sensor," *Measurement Science and Technology*, vol. 15, no. 8, pp. 1576–1580, 2004.

[52] L. Mosquera, D. Saez-Rodriguez, J. L. Cruz, *et al.*, "In-fiber fabry-perot refractometer assisted by a long-period grating," *Opt Lett*, vol. 35, no. 4, pp. 613–5, 2010.

[53] R. Falciai, A. G. Mignani, and A. Vannini, "Long period gratings as solution concentration sensors," *Sensors and Actuators B: Chemical*, vol. 74, no. 1-3, pp. 74–77, 2001.

[54] T. Allsop, L. Zhang, and I. Bennion, "Detection of organic aromatic compounds in paraffin by a long-period fiber grating optical sensor with optimized sensitivity," *Optics Communications*, vol. 191, no. 3-6, pp. 181–190, 2001.

[55] J. L. Tang, S. F. Cheng, W. T. Hsu, *et al.*, "Fiber-optic biochemical sensing with a colloidal gold-modified long period fiber grating," *Sensors and Actuators B-Chemical*, vol. 119, no. 1, pp. 105–109, 2006.

[56] G. R. C. Possetti, R. C. Kamikawachi, C. L. Prevedello, *et al.*, "Salinity measurement in water environment with a long period grating based interferometer," *Measurement Science and Technology*, vol. 20, no. 3, p. 4003, 2009.

[57] P. F. Manzillo, P. Pilla, A. Buosciolo, *et al.*, "Self assembling and coordination of water nano-layers on polymer coated long period gratings: Toward new perspectives for cation detection," *Soft Materials*, vol. 9, no. 2-3, pp. 238–263, 2011.

[58] Q. Li, X.-l. Zhang, Y.-S. Yu, *et al.*, "Enhanced sucrose sensing sensitivity of long period fiber grating by self-assembled polyelectrolyte multilayers," *Reactive and Functional Polymers*, vol. 71, no. 3, pp. 335–339, 2011.

[59] J. Barnes, M. Dreher, K. Plett, *et al.*, "Chemical sensor based on a long-period fibre grating modified by a functionalized polydimethylsiloxane coating," *Analyst*, vol. 133, no. 11, pp. 1541–9, 2008.

[60] J. A. Barnes, R. S. Brown, A. H. Cheung, *et al.*, "Chemical sensing using a polymer coated long-period fiber grating interrogated by ring-down spectroscopy," *Sensors and Actuators B-Chemical*, vol. 148, no. 1, pp. 221–226, 2010.

[61] J. Zhang, X. Tang, J. Dong, *et al.*, "Zeolite thin film-coated long period fiber grating sensor for measuring trace chemical," *Opt Express*, vol. 16, no. 11, pp. 8317–23, 2008.

[62] S. Korposh, S.-W. Lee, S. W. James, *et al.*, "Refractive index sensitivity of fibre-optic long period gratings coated with sio2 nanoparticle mesoporous thin films," *Measurement Science and Technology*, vol. 22, no. 7, p. 075208, 2011.

[63] M. P. DeLisa, Z. Zhang, M. Shiloach, *et al.*, "Evanescent wave long period fiber bragg grating as an immobilized antibody biosensor," *Analytical Chemistry*, vol. 72, no. 13, pp. 2895–2900, 2000.

[64] D. W. Kim, Y. Zhang, K. L. Cooper, *et al.*, "Fibre-optic interferometric immuno-sensor using long period grating," *Electronics Letters*, vol. 42, no. 6, pp. 324–325, 2006.

[65] J. Yang, P. Sandhu, W. G. Liang, *et al.*, "Label-free fiber optic biosensors with enhanced sensitivity," *Ieee Journal of Selected Topics in Quantum Electronics*, vol. 13, no. 6, pp. 1691–1696, 2007.

[66] Z. Y. Wang, J. R. Heflin, K. Van Cott, *et al.*, "Biosensors employing ionic self-assembled multilayers adsorbed on long-period fiber gratings," *Sensors and Actuators B-Chemical*, vol. 139, no. 2, pp. 618–623, 2009.

[67] Z. Wang and H. Xiao, "Optical intensity-based long-period fiber grating biosensors and biomedical applications [life sciences]," *Signal Processing Magazine, IEEE*, vol. 26, no. 2, pp. 121–122, 124–127, 2009.

[68] D. Y. Wang, Y. Wang, M. Han, *et al.*, "Fully distributed fiber-optic biological sensing," *IEEE Photonics Technology Letters*, vol. 22, no. 21, pp. 1553–1555, 2010.

[69] P. Pilla, V. Malachovska, A. Borriello, *et al.*, "Transition mode long period grating biosensor with functional multilayer coatings," *Opt Express*, vol. 19, no. 2, pp. 512–26, 2011.

[70] H. Shibru, Y. Zhang, K. L. Cooper, *et al.*, "Optimization of layer-by-layer electrostatic self-assembly processing parameters for optical biosensing," *Optical Engineering*, vol. 45, no. 2, pp. 024 401–024 401–6, 2006.

[71] P. Pilla, V. Malachovska, A. Borriello, *et al.*, "Functional multilayer coated long period grating tuned in transition region for life science applications," 2010.

[72] P. Pilla, A. Sandomenico, V. Malachovska, *et al.*, "A protein-based biointerfacing route toward label-free immunoassays with long period gratings in transition mode," *Biosens Bioelectron*, vol. 31, no. 1, pp. 486–91, 2012.

[73] K. L. Cooper, A. B. Bandara, Y. Wang, *et al.*, "Photonic biosensor assays to detect and distinguish subspecies of francisella tularensis," *Sensors (Basel)*, vol. 11, no. 3, pp. 3004–19, 2011.

[74] X. Chen, L. Zhang, K. Zhou, *et al.*, "Real-time detection of dna interactions with long-period fiber-grating-based biosensor," *Opt Lett*, vol. 32, no. 17, pp. 2541–3, 2007.

[75] H. S. Jang, K. N. Park, J. P. Kim, *et al.*, "Sensitive dna biosensor based on a long-period grating formed on the side-polished fiber surface," *Opt Express*, vol. 17, no. 5, pp. 3855–60, 2009.

[76] A. V. Hine, X. Chen, M. D. Hughes, *et al.*, "Optical fibre-based detection of dna hybridization," *Biochem Soc Trans*, vol. 37, no. Pt 2, pp. 445–9, 2009.

[77] M. Smietana, W. J. Bock, P. Mikulic, *et al.*, "Detection of bacteria using bacteriophages as recognition elements immobilized on long-period fiber gratings," *Optics Express*, vol. 19, no. 9, pp. 7971–7978, 2011.

[78] S. M. Tripathi, W. J. Bock, P. Mikulic, *et al.*, "Long period grating based biosensor for the detection of escherichia coli bacteria," *Biosens Bioelectron*, vol. 35, no. 1, pp. 308–12, 2012.

[79] A. Deep, U. Tiwari, P. Kumar, *et al.*, "Immobilization of enzyme on long period grating fibers for sensitive glucose detection," *Biosens Bioelectron*, vol. 33, no. 1, pp. 190–5, 2012.

[80] G. Salceda-Delgado, D. Monzon-Hernandez, A. Martinez-Rios, *et al.*, "Optical microfiber mode interferometer for temperature-independent refractometric sensing," *Opt Lett*, vol. 37, no. 11, pp. 1974–6, 2012.

[81] A. Kumar, T. Subrahmanyam, A. Sharma, *et al.*, "Novel refractometer using a tapered optical fibre," *Electronics Letters*, vol. 20, no. 13, pp. 534–535, 1984.

[82] M. I. Zibaii, A. Kazemi, H. Latifi, *et al.*, "Measuring bacterial growth by refractive index tapered fiber optic biosensor," *J Photochem Photobiol B*, vol. 101, no. 3, pp. 313–20, 2010.

[83] M. I. Zibaii, O. Frazao, H. Latifi, *et al.*, "Controlling the sensitivity of refractive index measurement using a tapered fiber loop mirror," *Photonics Technology Letters, IEEE*, vol. 23, no. 17, pp. 1219–1221, 2011.

[84] Y. Tian, W. Wang, N. Wu, *et al.*, "Tapered optical fiber sensor for label-free detection of biomolecules," *Sensors (Basel)*, vol. 11, no. 4, pp. 3780–90, 2011.

[85] Z. B. Tian, S. S. H. Yam, and H. P. Loock, "Single-mode fiber refractive index sensor based on core-offset attenuators," *Ieee Photonics Technology Letters*, vol. 20, no. 13-16, pp. 1387–1389, 2008.

[86] F. Pang, H. Liu, H. Guo, *et al.*, "In-fiber mach-zehnder interferometer based on double cladding fibers for refractive index sensor," *Sensors Journal, IEEE*, no. 99, pp. 1–1, 2011.

[87] Q. Rong, X. Qiao, R. Wang, *et al.*, "High-sensitive fiber-optic refractometer based on a core-diameter-mismatch mach–zehnder interferometer," *Sensors Journal, IEEE*, vol. 12, no. 7, pp. 2501–2505, 2012.

[88] Y. Ma, X. Qiao, T. Guo, *et al.*, "Mach–zehnder interferometer based on a sandwich fiber structure for refractive index measurement," *Sensors Journal, IEEE*, vol. 12, no. 6, pp. 2081–2085, 2012.

[89] L. B. Soldano and E. C. M. Pennings, "Optical multi-mode interference devices based on self-imaging: principles and applications," *Lightwave Technology, Journal of*, vol. 13, no. 4, pp. 615–627, 1995.

[90] Y. Jung, S. Kim, D. Lee, *et al.*, "Compact three segmented multimode fibre modal interferometer for high sensitivity refractive-index measurement," *Measurement Science and Technology*, vol. 17, no. 5, pp. 1129–1133, 2006.

[91] Q. Wu, Y. Semenova, P. Wang, *et al.*, "High sensitivity sms fiber structure based refractometer–analysis and experiment," *Opt Express*, vol. 19, no. 9, pp. 7937–44, 2011.

[92] C. R. Biazoli, S. Silva, M. A. Franco, *et al.*, "Multimode interference tapered fiber refractive index sensors," *Appl Opt*, vol. 51, no. 24, pp. 5941–5, 2012.

[93] X. Lan, J. Huang, Q. Han, *et al.*, "Fiber ring laser interrogated zeolite-coated singlemode-multimode-singlemode structure for trace chemical detection," *Opt Lett*, vol. 37, no. 11, pp. 1998–2000, 2012.

[94] T. H. Xia, A. P. Zhang, B. B. Gu, *et al.*, "Fiber-optic refractive-index sensors based on transmissive and reflective thin-core fiber modal interferometers," *Optics Communications*, vol. 283, no. 10, pp. 2136–2139, 2010.

[95] B. Gu, M. J. Yin, A. P. Zhang, *et al.*, "Low-cost high-performance fiber-optic ph sensor based on thin-core fiber modal interferometer," *Opt Express*, vol. 17, no. 25, pp. 22 296–302, 2009.

[96] Z. L. Ran, Y. J. Rao, W. J. Liu, *et al.*, "Laser-micromachined fabry-perot optical fiber tip sensor for high-resolution temperature-independent measurement of refractive index," *Optics Express*, vol. 16, no. 3, pp. 2252–2263, 2008.

[97] T. Wei, Y. Han, Y. Li, *et al.*, "Temperature-insensitive miniaturized fiber inline fabry-perot interferometer for highly sensitive refractive index measurement," *Opt Express*, vol. 16, no. 8, pp. 5764–9, 2008.

[98] F. J. Arregui, I. R. Matias, Y. Liu, *et al.*, "Optical fiber nanometer-scale fabry-perot interferometer formed by the ionic self-assembly monolayer process," *Optics Letters*, vol. 24, no. 9, pp. pp. 596–598, 1999.

[99] D. Galbarra, F. J. Arregui, I. R. Matias, *et al.*, "Ammonia optical fiber sensor based on self-assembled zirconia thin films," *Smart Materials and Structures*, vol. 14, no. 4, pp. 739–744, 2005.

[100] I. Del Villar, I. R. Matias, F. J. Arregui, *et al.*, "Fiber-optic hydrogen peroxide nanosensor," *IEEE Sensors Journal*, vol. 5, no. 3, pp. 365–371, 2005.

[101] C. Elosua, I. R. Matias, C. Bariain, *et al.*, "Development of an in-fiber nanocavity towards detection of volatile organic gases," *Sensors*, vol. 6, no. 6, pp. 578–592, 2006.

[102] N. Liu, J. Hui, C. Q. Sun, *et al.*, "Nanoporous zeolite thin film-based fiber intrinsic fabry-perot interferometric sensor for detection of dissolved organics in water," *Sensors*, vol. 6, no. 8, pp. 835–847, 2006.

[103] Y. Zhang, H. Shibru, K. L. Cooper, *et al.*, "Miniature fiber-optic multicavity fabry-perot interferometric biosensor," *Opt Lett*, vol. 30, no. 9, pp. 1021–3, 2005.

[104] Y. M. Wang, K. L. Cooper, and A. B. Wang, "Microgap structured optical sensor for fast label-free dna detection," *Journal of Lightwave Technology*, vol. 26, no. 17-20, pp. 3181–3185, 2008.

[105] X. W. Wang, K. L. Cooper, A. B. Wang, *et al.*, "Label-free dna sequence detection using oligonucleotide functionalized optical fiber," *Applied Physics Letters*, vol. 89, no. 16, p. 163901, 2006.

[106] R. B. Queiros, S. O. Silva, J. P. Noronha, *et al.*, "Microcystin-lr detection in water by the fabry-perot interferometer using an optical fibre coated with a sol-gel imprinted sensing membrane," *Biosens Bioelectron*, vol. 26, no. 9, pp. 3932–3937, 2011.

[107] J. Homola, S. S. Yee, and G. Gauglitz, "Surface plasmon resonance sensors: review," *Sensors and Actuators B-Chemical*, vol. 54, no. 1-2, pp. 3–15, 1999.

[108] R. C. Jorgenson and S. Yee, "A fiber-optic chemical sensor based on surface plasmon resonance," *Sensors And Actuators B-Chemical*, vol. 12, no. 3, pp. 213–220, 1993.

[109] J. Homola, R. Slavik, and J. Ctyroky, "Interaction between fiber modes and surface plasmon waves: spectral properties," *Optics Letters*, vol. 22, no. 18, pp. 1403–1405, 1997.

[110] O. Esteban, M. Cruz-Navarrete, A. Gonzalez-Cano, *et al.*, "Measurement of the degree of salinity of water with a fiber-optic sensor," *Appl Opt*, vol. 38, no. 25, pp. 5267–71, 1999.

[111] A. Diez, M. Andres, and J. Cruz, "In-line fiber-optic sensors based on the excitation of surface plasma modes in metal-coated tapered fibers," *Sensors And Actuators B-Chemical*, vol. 73, no. 2-3, pp. 95–99, 2001.

[112] D. Monzon-Hernandez, J. Villatoro, D. Talavera, *et al.*, "Optical-fiber surface-plasmon resonance sensor with multiple resonance peaks," *Applied Optics*, vol. 43, no. 6, p. 1216, 2004.

[113] M.-H. Chiu, S.-F. Wang, and R.-S. Chang, "D-type fiber biosensor based on surface-plasmon resonance technologyand heterodyne interferometry," *Opt. Lett.*, vol. 30, no. 3, pp. 233–235, Feb 2005.

[114] A. K. Sharma, R. Jha, and B. D. Gupta, "Fiber-optic sensors based on surface plasmon resonance: A comprehensive review," *Ieee Sensors Journal*, vol. 7, no. 7-8, pp. 1118–1129, 2007.

[115] N. Díaz-Herrera, A. Gonzalez-Cano, D. Viegas, *et al.*, "Refractive index sensing of aqueous media based on plasmonic resonance in tapered optical fibres operating in the 1.5 [mu] m region," *Sensors And Actuators B-Chemical*, vol. 146, no. 1, pp. 195–198, 2010.

[116] J. Pollet, F. Delport, K. P. Janssen, *et al.*, "Fiber optic spr biosensing of dna hybridization and dna-protein interactions," *Biosens Bioelectron*, vol. 25, no. 4, pp. 864–9, 2009.

[117] F. Delport, J. Pollet, K. Janssen, *et al.*, "Real-time monitoring of dna hybridization and melting processes using a fiber optic sensor," *Nanotechnology*, vol. 23, no. 6, p. 065503, 2012.

[118] T. Schuster, R. Herschel, N. Neumann, *et al.*, "Miniaturized long-period fiber grating assisted surface plasmon resonance sensor," *Journal of Lightwave Technology*, vol. 30, no. 8, pp. 1003–1008, 2012.

[119] Y. Shevchenko, T. J. Francis, D. A. Blair, *et al.*, "In situ biosensing with a surface plasmon resonance fiber grating aptasensor," *Anal Chem*, vol. 83, no. 18, pp. 7027–34, 2011.

[120] K. Hill, Y. Fujii, D. Johnson, *et al.*, "Photosensitivity in optical fiber waveguides: Application to reflection filter fabrication," *Appl. Phys. Lett.*, vol. 32, no. 10, pp. 647–649, 1978.

[121] D. Williams, B. J. Ainslie, J. R. Armitage, *et al.*, "Enhanced uv photosensitivity in boron codoped germanosilicate fibers," *Electronics Letters*, vol. 29, pp. 45–7, 1993.

[122] P. J. Lemaire, R. Atkins, V. Mizrahi, *et al.*, "High pressure h2 loading as a technique for achieving ultrahigh uv photosensitivity and thermal sensitivity in geo2 doped optical fibres," *Electronics Letters*, vol. 29, no. 13, pp. 1191–1193, 1993.

[123] G. Meltz, W. Morey, and W. Glenn, "Formation of bragg gratings in optical fibers by a transverse holographic method," *Opt. Lett.*, vol. 14, no. 15, pp. 823–825, 1989.

[124] E. Born, Max Wolf, "Principles of optics," *Pergamon Press*, p. 188, 1987.

[125] W. W. Morey, G. Meltz, and W. H. Glenn, "Fiber optic bragg grating sensors," in *OE-FIBERS'89*. International Society for Optics and Photonics, 1990, pp. 98–107.

[126] F. M. M. Araújo, "Redes de bragg em fibra óptica," Ph.D. dissertation, Faculty of Sciences of University of Porto, 1999.

[127] K. Hill, B. Malo, F. Bilodeau, *et al.*, "Bragg gratings fabricated in monomode photosensitive optical fiber by uv exposure through a phase mask," *Applied Physics Letters*, vol. 62, no. 10, pp. 1035–1037, 1993.

[128] C. Giles, "Lightwave applications of fiber bragg gratings," *Lightwave Technology, Journal of*, vol. 15, no. 8, pp. 1391–1404, 1997.

[129] T. A. Berkoff and A. D. Kersey, "Fiber bragg grating array sensor system using a bandpass wavelength division multiplexer and interferometric detection," *Ieee Photonics Technology Letters*, vol. 8, no. 11, pp. 1522–1524, 1996.

[130] W. W. Morey, J. R. Dunphy, and G. Meltz, "Multiplexing fiber bragg grating sensors," pp. 216–224, 1992.

[131] L. Ferreira, F. Araujo, A. Maia, *et al.*, "Redes de bragg em fibra óptica-contribuições para o desenvolvimento de uma tecnologia revolucionária em monitorização estrutural," *Betão Estrutural*, vol. 2004, 2004.

[132] R. Kashyap, *Fiber bragg gratings*. Academic Press, 2009.

[133] K. O. Hill and G. Meltz, "Fiber bragg grating technology fundamentals and overview," *Lightwave Technology, Journal of*, vol. 15, no. 8, pp. 1263–1276, 1997.

[134] A. Iadicicco, A. Cusano, S. Campopiano, *et al.*, "Thinned fiber bragg gratings as refractive index sensors," *Ieee Sensors Journal*, vol. 5, no. 6, pp. 1288–1295, 2005.

[135] A. P. Zhang, X. M. Tao, W. H. Chung, *et al.*, "Cladding-mode-assisted recouplings in concatenated long-period and fiber bragg gratings," *Opt Lett*, vol. 27, no. 14, pp. 1214–6, 2002.

[136] M. Fu, "Refractive index sensing based on the reflectivity of the backward cladding-core mode coupling in concatenated a fiber bragg gratin and a long period grating," *IEEE Sensors Journal*, no. 99, pp. 1–1, 2011.

[137] Y. Ma, X. Qiao, T. Guo, *et al.*, "Reflective fiber-optic refractometer based on a thin-core fiber tailored bragg grating reflection," *Opt Lett*, vol. 37, no. 3, pp. 323–5, 2012.

[138] T. Erdogan and J. E. Sipe, "Tilted fiber phase gratings," *J. Opt. Soc. Am. A*, vol. 13, no. 2, pp. 296–313, Feb 1996.

[139] S. Savin, M. Digonnet, G. S. Kino, *et al.*, "Tunable mechanically induced long-period fiber gratings," *Opt Lett*, vol. 25, no. 10, pp. 710–712, 2000.

[140] Y. Kondo, K. Nouchi, T. Mitsuyu, *et al.*, "Fabrication of long-period fiber gratings by focused irradiation of infrared femtosecond laser pulses," *Opt Lett*, vol. 24, no. 10, p. 646, 1999.

[141] D. D. Davis, T. K. Gaylord, E. N. Glytsis, *et al.*, "Long-period fibre grating fabrication with focused co2 laser pulses," *Electronics Letters*, vol. 34, no. 3, pp. 302–303, 1998.

[142] S. Greenberg Kosinski, A. M. Vengsarkar, and G. A. Ten Eyck, "Method for making long-period fiber gratings," Patent, 1998.

[143] M. Fujimaki, Y. Ohki, J. Brebner, *et al.*, "Fabrication of long-period optical fiber gratings by use of ion implantation," *Opt Lett*, vol. 25, pp. 88–89, 2000.

[144] K. Okamoto, "Chapter 4 - coupled mode theory," in *Fundamentals of Optical Waveguides (Second Edition)*, second edition ed. Burlington: Academic Press, 2006, pp. 159 – 207.

[145] T. Erdogan, "Fiber grating spectra," *Journal of Lightwave Technology*, vol. 15, no. 8, pp. 1277–1294, 1997.

[146] D. Baptista, "Simulação do comportamento espectral de redes de período longo em fibra óptica," Master's thesis, University of Madeira, 2009.

[147] X. Shu, L. Zhang, and I. Bennion, "Sensitivity characteristics near the dispersion turning points of long-period fiber gratings in b/ge codoped fiber," *Opt Lett*, vol. 26, no. 22, pp. 1755–7, 2001.

[148] V. Grubsky and J. Feinberg, "Long-period fiber gratings with variable coupling for real-time sensing applications," *Opt Lett*, vol. 25, no. 4, pp. 203–5, 2000.

[149] I. Bennion, J. A. R. Williams, L. Zhang, *et al.*, "Uv-written in-fibre bragg gratings," *Opt. Quantum Electron.*, vol. 28, pp. 93–135, 1996.

[150] L. Zhang, Y. Liu, L. Everall, *et al.*, "Design and realization of long-period grating devices in conventional and high birefringence fibers and their novel applications as fiber- optic load sensors," *Journal of Selected Topics in Quantum Electronics*, vol. 5, pp. 1373–1378, 1999.

[151] B. O. Guan, H. Y. Tam, S.-L. Ho, *et al.*, "Growth of long-period gratings in h2-loaded fibre after 193 nm uv inscription," *Ieee Photonics Technology Letters*, vol. 12, pp. 642–4, 2000.

[152] K. P. Chen, P. R. Herman, J. Zhang, *et al.*, "Fabrication of strong long-period gratings in hydrogen free fibers with 157 nm f2-laser radiation," *Opt Lett*, vol. 26, pp. 771–3, 2001.

[153] G. Kakarantzas, T. Birks, and P. Russell, "Structural long-period gratings in photonic crystal fibers," *Optics Letters*, vol. 27, pp. 1013–1015, 2002.

[154] C.-S. Kim, Y. Han, B. H. Lee, *et al.*, "Induction of the refractive index change in b-doped optical fibers through relaxation of the mechanical stress," *Optics Communications*, vol. 185, pp. 337 – 342, 2000.

[155] L. Stensland, "Long-period fibre gratings written by co2 exposure of h2-loaded, standard fibres," *Electronics Letters*, vol. 36, pp. 742–744(2), April 2000.

[156] Y. Wang, "Review of long period fiber gratings written by co2 laser," *Journal of Applied Physics*, vol. 108, no. 8, p. 081101, 2010.

[157] G. Rego, O. Okhotnikov, E. Dianov, *et al.*, "High-temperature stability of long-period fiber gratings produced using an electric arc," *Journal of Lightwave Technology*, vol. 19, no. 10, pp. 1574–1579, 2001.

[158] I. K. Hwang, S. H. Yun, and B. Y. Kim, "Long-period fiber gratings based on periodic microbends," *Opt Lett*, vol. 24, no. 18, pp. 1263–5, Sep 1999.

[159] E. Dianov, V. I. Karpov, A. Kurkov, *et al.*, "Long-period fiber gratings and mode-field converters fabricated by thermodiffusion in phosphosilicate fibers," in *Optical Communication, 1998. 24th European Conference on*, vol. 1, 1998, pp. 395–396.

[160] K. Morishita and Y. Miyake, "Fabrication and resonance wavelengths of long-period gratings written in a pure-silica photonic crystal fiber by the glass structure change," *J. Lightwave Technol.*, vol. 22, no. 2, p. 625, Feb 2004.

[161] V. Karpov, M. Grekov, E. Dianov, *et al.*, "Mode-field converters and long-period gratings fabricated by thermo-diffusion in nitrogen-doped silica-core fibers," in *Optical Fiber Communication Conference and Exhibit, 1998. OFC '98., Technical Digest*, 1998, pp. 279–280.

[162] H. Y. Wang, S. M. Chuo, C. Y. Huang, *et al.*, "Embedded corrugated long-period fiber gratings for sensing applications," *Appl Opt*, vol. 51, no. 10, pp. 1453–8, 2012.

[163] L. A. Wang, C. Y. Lin, and G. W. Chern, "A torsion sensor made of a corrugated long period fibre grating," *Measurement Science and Technology*, vol. 12, no. 7, pp. 793–799, 2001.

[164] W. Bock, J. Chen, P. Mikulic, *et al.*, "A novel fiber-optic tapered long-period grating sensor for pressure monitoring," *Instrumentation and Measurement, IEEE Transactions on*, vol. 56, no. 4, pp. 1176–1180, 2007.

[165] L.-Y. Shao, J. Zhao, X. Dong, *et al.*, "Long-period grating fabricated by periodically tapering standard single-mode fiber," *Appl. Opt.*, vol. 47, no. 10, pp. 1549–1552, Apr 2008.

[166] Y. Jeong, B. Yang, B. Lee, *et al.*, "Electrically controllable long-period liquid crystal fiber gratings," *Photonics Technology Letters, IEEE*, vol. 12, no. 5, pp. 519–521, 2000.

[167] G. Rego, J. Fernandes, J. Santos, *et al.*, "New technique to mechanically induce long-period fibre gratings," *Optics Communications*, vol. 220, pp. 111 – 118, 2003.

[168] H. Sakata and T. Iwazaki, "Sensitivity-variable fiber optic pressure sensors using microbend fiber gratings," *Optics Communications*, vol. 282, no. 23, pp. 4532 – 4536, 2009.

[169] Q. Li, C. Lin, A. Au, *et al.*, "Compact all-fibre on-line power monitor via core-to-cladding mode coupling," *Electronics Letters*, vol. 38, no. 18, pp. 1013–1015, 2002.

[170] V. Bhatia, "Applications of long-period gratings to single and multi-parameter sensing," *Opt Express*, vol. 4, no. 11, pp. 457–66, 1999.

[171] V. Bhatia, D. K. Campbell, D. Sherr, *et al.*, "Temperature-insensitive and strain-insensitive long-period grating sensors for smart structures," *Optical Engineering*, vol. 36, no. 7, pp. 1872–1876, 1997.

[172] K. S. Chiang, Y. Q. Liu, M. N. Ng, *et al.*, "Analysis of etched long-period fibre grating and its response to external refractive index," *Electronics Letters*, vol. 36, no. 11, pp. 966–967, 2000.

[173] I. Del Villar, I. Matias, F. Arregui, *et al.*, "Optimization of sensitivity in long period fiber gratings with overlay deposition," *Opt Express*, vol. 13, no. 1, pp. 56–69, 2005.

[174] A. Cusano, A. Iadicicco, P. Pilla, *et al.*, "Cladding mode reorganization in high-refractive-index-coated long-period gratings: effects on the refractive-index sensitivity," *Opt Lett*, vol. 30, no. 19, pp. 2536–8, 2005.

[175] A. Cusano, P. Pilla, M. Giordano, *et al.*, *Modal Transition in Nano-Coated Long Period Fiber Gratings: Principle and Applications to Chemical Sensing.* Springer New York, 2009, ch. 3, pp. 35–75.

[176] P. Pilla, M. Giordano, M. L. Korwin-Pawlowski, *et al.*, "Sensitivity characteristics tuning in tapered long-period gratings by nanocoatings," *Photonics Technology Letters, IEEE*, vol. 19, no. 19, pp. 1517–1519, 2007.

[177] Z. Gu, Y. Xu, and K. Gao, "Optical fiber long-period grating with solgel coating for gas sensor," *Opt Lett*, vol. 31, no. 16, pp. 2405–7, 2006.

[178] K. Okamoto, "Chapter 3 - optical fibers," in *Fundamentals of Optical Waveguides (Second Edition)*, second edition ed. Burlington: Academic Press, 2006, pp. 57 – 158.

[179] O. Frazao, J. M. Baptista, and J. L. Santos, "Recent advances in high-birefringence fiber loop mirror sensors," *Sensors*, vol. 7, no. 11, pp. 2970–2983, 2007.

[180] M. Sudo, M. Nakai, K. Himeno, *et al.*, "Simultaneous measurement of temperature and strain using panda fiber grating," in *OFS*, vol. 12, 1997, pp. 170–173.

[181] L. A. Ferreira, F. M. Araujo, J. L. Santos, *et al.*, "Simultaneous measurement of strain and temperature using interferometrically interrogated fiber bragg grating sensors," *Optical Engineering*, vol. 39, no. 8, pp. 2226–2234, 2000.

[182] O. Frazao, T. Martynkien, J. M. Baptista, *et al.*, "Optical refractometer based on a birefringent bragg grating written in an h-shaped fiber," *Opt Lett*, vol. 34, no. 1, pp. 76–8, 2009.

[183] C. M. Lawrence, D. V. Nelson, and E. Udd, "Measurement of transverse strains with fiber bragg gratings," *Proc. SPIE Smart Structures and Materials 1997: Smart Sensing, Processing, and Instrumentation*, vol. 3042, 1997.

[184] C. Caucheteur, S. Bette, R. Garcia-Olcina, *et al.*, "Transverse strain measurements using the birefringence effect in fiber bragg gratings," *Photonics Technology Letters, IEEE*, vol. 19, no. 13, pp. 966–968, 2007.

[185] E. T. Fogg, A. N. Hixson, and A. R. Thompson, "Densities and refractive indexes for ethylene glycol-water solutions," *Analytical Chemistry*, vol. 27, no. 10, pp. 1609–1611, 1955.

[186] H. El-Kashef, "The necessary requirements imposed on polar dielectric laser dye solvents," *Physica B: Condensed Matter*, vol. 279, no. 4, pp. 295 – 301, 2000.

[187] E. Chehura, S. W. James, and R. P. Tatam, "Temperature and strain discrimination using a single tilted fibre bragg grating," *Optics Communications*, vol. 275, no. 2, pp. 344–347, 2007.

[188] N. J. Alberto, C. A. Marques, J. ao L. Pinto, *et al.*, "Three-parameter optical fiber sensor based on a tilted fiber bragg grating," *Appl. Opt.*, vol. 49, no. 31, pp. 6085–6091, Nov 2010.

[189] C. Caucheteur, K. Chah, F. Lhomme, *et al.*, "Simultaneous bend and temperature sensor using tilted fbg," *17th International Conference on Optical Fibre Sensors, Pts 1 and 2*, vol. 5855, pp. 707–710, 2005.

[190] L. Y. Shao, A. Laronche, M. Smietana, *et al.*, "Highly sensitive bend sensor with hybrid long-period and tilted fiber bragg grating," *Optics Communications*, vol. 283, no. 13, pp. 2690–2694, 2010.

[191] T. Guo, L. Shao, H. Y. Tam, *et al.*, "Tilted fiber grating accelerometer incorporating an abrupt biconical taper for cladding to core recoupling," *Opt Express*, vol. 17, no. 23, pp. 20 651–60, 2009.

[192] Y. Huang, T. Guo, C. Lu, *et al.*, "Vcsel-based tilted fiber grating vibration sensing system," *Photonics Technology Letters, IEEE*, vol. 22, no. 16, pp. 1235–1237, 2010.

[193] T. Guo, A. Ivanov, C. Chen, *et al.*, "Temperature-independent tilted fiber grating vibration sensor based on cladding-core recoupling," *Opt Lett*, vol. 33, no. 9, pp. 1004–6, 2008.

[194] T. Guo, H. Y. Tam, P. A. Krug, *et al.*, "Reflective tilted fiber bragg grating refractometer based on strong cladding to core recoupling," *Opt Express*, vol. 17, no. 7, pp. 5736–42, 2009.

[195] Y. X. Jin, C. C. Chan, X. Y. Dong, *et al.*, "Temperature-independent bending sensor with tilted fiber bragg grating interacting with multimode fiber," *Optics Communications*, vol. 282, no. 19, pp. 3905–3907, 2009.

[196] D. Saez-Rodriguez, J. L. Cruz, A. Diez, *et al.*, "Coupling between counterpropagating cladding modes in fiber bragg gratings," *Optics Letters*, vol. 36, no. 8, pp. 1518–1520, 2011.

[197] G. Rego, "Arc-induced long-period fibre gratings fabrication and their applications in optical communications and sensing," Ph.D. dissertation, Faculty of Sciences of University of Porto, 2006.

[198] P. Caldas, "Fiber optic sensing by evanescent field interaction," Ph.D. dissertation, Faculty of Sciences of University of Porto, 2011.

[199] I. M. White and X. Fan, "On the performance quantification of resonant refractive index sensors," *Opt Express*, vol. 16, no. 2, pp. 1020–8, 2008.

[200] R. Falate, O. Frazao, G. Rego, *et al.*, "Refractometric sensor based on a phase-shifted long-period fiber grating," *Appl Opt*, vol. 45, no. 21, pp. 5066–72, 2006.

[201] H. W. Fang, K. Y. Li, T. L. Su, *et al.*, "Dip coating assisted polylactic acid deposition on steel surface: Film thickness affected by drag force and gravity," *Materials Letters*, vol. 62, no. 21-22, pp. 3739–3741, 2008.

[202] A. Cusano, A. Iadicicco, P. Pilla, *et al.*, "Coated long-period fiber gratings as high-sensitivity optochemical sensors," *Journal of Lightwave Technology*, vol. 24, no. 4, pp. 1776–1786, 2006.

[203] D. Hage, "Immunoassays," *Analytical Chemistry*, vol. 65, no. 12, pp. 420–424, 1993.

[204] A. Warshawsky, R. Kalir, and A. Patchornik, "Functionalization of polystyrene .1. alkylation with substituted benzyl halide and benzyl alcohol compounds," *Journal of Organic Chemistry*, vol. 43, no. 16, pp. 3151–3157, 1978.

[205] R. Green, J. Davies, M. Davies, *et al.*, "Surface plasmon resonance for real time in situ analysis of protein adsorption to polymer surfaces," *Biomaterials*, vol. 18, no. 5, pp. 405 – 413, 1997.

[206] P. C. Jeronimo, A. N. Araujo, and B. S. M. M. M. Conceicao, "Optical sensors and biosensors based on sol-gel films," *Talanta*, vol. 72, no. 1, pp. 13–27, 2007.

[207] G. J. Mohr, "Materials and polymers in optical sensing," *Institute of Physical Chemistry*, 2002.

[208] P. A. S. Jorge, P. Caldas, J. C. G. E. Da Silva, *et al.*, "Luminescence-based optical fiber chemical sensors," *Fiber and Integrated Optics*, vol. 24, no. 3-4, pp. 201–225, 2005.

[209] E. Davies, R. Viitala, M. Salomäki, *et al.*, "Sol–gel derived coating applied to long-period gratings for enhanced refractive index sensing properties," *Journal of Optics A: Pure and Applied Optics*, vol. 11, no. 1, p. 015501, 2009.

[210] J.-F. Ding, A. P. Zhang, L.-Y. Shao, *et al.*, "Fiber-taper seeded long-period grating pair as a highly sensitive refractive-index sensor," *Photonics Technology Letters, IEEE*, vol. 17, no. 6, pp. 1247–1249, 2005.

[211] D. W. Kim, Y. Zhang, K. L. Cooper, *et al.*, "In-fiber reflection mode interferometer based on a long-period grating for external refractive-index measurement," *Appl Opt*, vol. 44, no. 26, pp. 5368–73, 2005.

[212] A. P. Zhang, L. Y. Shao, J. F. Ding, *et al.*, "Sandwiched long-period gratings for simultaneous measurement of refractive index and temperature," *Ieee Photonics Technology Letters*, vol. 17, no. 11, pp. 2397–2399, 2005.

[213] C. Lam, R. Mandamparambil, T. Sun, *et al.*, "Optical fiber refractive index sensor for chloride ion monitoring," *Sensors Journal, IEEE*, vol. 9, no. 5, pp. 525–532, 2009.

[214] Y. E. Fan, T. Zhu, L. Shi, *et al.*, "Highly sensitive refractive index sensor based on two cascaded special long-period fiber gratings with rotary refractive index modulation," *Appl Opt*, vol. 50, no. 23, pp. 4604–10, 2011.

[215] G. A. Cardenas-Sevilla, D. Monzon-Hernandez, I. Torres-Gomez, *et al.*, "Tapered mach-zehnder interferometer based on two mechanically induced long-period fiber gratings as refractive index sensor," *Optics and Laser Technology*, vol. 44, no. 5, pp. 1516–1520, 2012.

[216] A. van Brakel, "Temperature-compensated optical fiber michelson refractometer," *Optical Engineering*, vol. 44, no. 2, p. 020504, 2005.

[217] Y. J. Rao and D. A. Jackson, "Recent progress in fibre optic low-coherence interferometry," *Measurement Science and Technology*, vol. 7, no. 7, pp. 981–999, 1996.

[218] J. Yang, Y. G. Yuan, A. Zhou, *et al.*, "A novel quasi-distributed sensing network based on non-balance mach-zehnder autocorrelator," *21st International Conference on Optical Fiber Sensors*, vol. 7753, p. 24, 2011.

[219] M. Jiang, Z. G. Guan, and S. He, "Multiplexing scheme for self-interfering long-period fiber gratings using a low-coherence reflectometry," *Ieee Sensors Journal*, vol. 7, no. 11-12, pp. 1663–1667, 2007.

[220] A. P. Zhang, Z. G. Guan, and S. He, "Optical low-coherence reflectometry based on long-period grating mach-zehnder interferometers," *Appl Opt*, vol. 45, no. 22, pp. 5733–9, 2006.

[221] Z.-G. Guan, A. P. Zhang, M. Jiang, *et al.*, "Low-coherence interrogation scheme for multiplexed sensors based on long-period-grating mach-zehnder interferometers," *Photonics Technology Letters, IEEE*, vol. 18, no. 7, pp. 832–834, 2006.

[222] P. Caldas, P. A. S. Jorge, F. M. Araujo, *et al.*, "Geometrical effects on the refractive index sensitivity of mach-zehnder fibre modal interferometers based on long-period gratings," *Measurement Science and Technology*, vol. 20, no. 7, pp. –, 2009.

[223] J. H. Osório, L. Mosquera, C. J. Gouveia, *et al.*, "High sensitivity lpg mach–zehnder sensor for real-time fuel conformity analysis," *Measurement Science and Technology*, vol. 24, no. 1, p. 015102, 2013.

[224] F. Baldini, A. Falai, A. R. De Gaudio, *et al.*, "Continuous monitoring of gastric carbon dioxide with optical fibres," *Sensors and Actuators B-Chemical*, vol. 90, no. 1-3, pp. 132–138, 2003.

[225] O. S. Wolfbeis, "Fiber-optic chemical sensors and biosensors," *Anal Chem*, vol. 80, no. 12, pp. 4269–83, 2008.

[226] A. Mills, *Optical sensors for carbon dioxide and their applications.* Springer, 2009, pp. 347–370.

[227] T. J. Pfeiffer, S. T. Summerfelt, and B. J. Watten, "Comparative performance of co2 measuring methods: Marine aquaculture recirculation system application," *Aquacultural Engineering*, vol. 44, no. 1, pp. 1–9, 2011.

[228] M. T. Borges, J. O. Domingues, J. M. Jesus, *et al.*, "Direct and continuous dissolved co2 monitoring in shallow raceway systems: From laboratory to commercial-scale applications," *Aquacultural Engineering*, vol. 49, pp. 10–17, 2012.

[229] H. Segawa, E. Ohnishi, Y. Arai, *et al.*, "Sensitivity of fiber-optic carbon dioxide sensors utilizing indicator dye," *Sensors and Actuators B-Chemical*, vol. 94, no. 3, pp. 276–281, 2003.

[230] Y. Amao and N. Nakamura, "Optical co2 sensor with the combination of colorimetric change of alpha-naphtholphthalein and internal reference fluorescent porphyrin dye," *Sensors and Actuators B-Chemical*, vol. 100, no. 3, pp. 347–351, 2004.

[231] F. Charpentier, J. Troles, Q. Coulombier, *et al.*, "Co2 detection using microstructured chalcogenide fibers," *Sensor Letters*, vol. 7, no. 5, pp. 745–749, 2009.

[232] R. Orghici, U. Willer, M. Gierszewska, *et al.*, "Fiber optic evanescent field sensor for detection of explosives and co2 dissolved in water," *Applied Physics B*, vol. 90, no. 2, pp. 355–360, 2008.

[233] R. B. Queiros, "Biosensors for the detection and quantification of aquatic bacterial contamination in waters for human use," Ph.D. dissertation, Faculty of Sciences of University of Porto, 2013.

[234] R. Slavík, J. Homola, J. Ctyroky, *et al.*, "Novel spectral fiber optic sensor based on surface plasmon resonance," pp. 106–111, 2001.

[235] S. Silva, E. G. Pachon, M. A. Franco, *et al.*, "Ultrahigh-sensitivity temperature fiber sensor based on multimode interference," *Appl Opt*, vol. 51, no. 16, pp. 3236–42, 2012.

[236] P. Wang, G. Brambilla, M. Ding, *et al.*, "High-sensitivity, evanescent field refractometric sensor based on a tapered, multimode fiber interference," *Opt Lett*, vol. 36, no. 12, pp. 2233–5, 2011.

[237] O. Frazao, L. M. Marques, S. Santos, *et al.*, "Simultaneous measurement for strain and temperature based on a long-period grating combined with a high-birefringence fiber loop mirror," *Ieee Photonics Technology Letters*, vol. 18, no. 21-24, pp. 2407–2409, 2006.

[238] O. Frazao, P. A. S. Jorge, J. M. Baptista, *et al.*, "Optical refractometer based on a hi-bi d-type fiber loop mirror," *Sensors, 2008 IEEE*, pp. 957–960, 2008.

[239] P. Gao, X. Chen, and W. Feng, "Simultaneous measurement of external refractive index and temperature based on long-period-grating-inscribed sagnac interferometer and fiber bragg grating," *Review of Scientific Instruments*, vol. 83, no. 10, pp. 105 001–105 001, 2012.

[240] C. Zhong, C. Y. Shen, Y. You, *et al.*, "A polarization-maintaining fiber loop mirror based sensor for liquid refractive index absolute measurement," *Sensors and Actuators B-Chemical*, vol. 168, pp. 360–364, 2012.

[241] D. B. Mortimore, "Fiber loop reflectors," *Lightwave Technology, Journal of*, vol. 6, no. 7, pp. 1217–1224, 1988.

[242] P. Urquhart, "Fiber lasers with loop reflectors," *Applied optics*, vol. 28, no. 17, pp. 3759–3767, 1989.

[243] X. Fang and R. O. Claus, "Polarization-independent all-fiber wavelength-division multiplexer based on a sagnac interferometer," *Optics letters*, vol. 20, no. 20, pp. 2146–2148, 1995.

[244] J. Noda, K. Okamoto, and Y. Sasaki, "Polarization-maintaining fibers and their applications," *Lightwave Technology, Journal of*, vol. 4, no. 8, pp. 1071–1089, 1986.

[245] B. Culshaw, "The optical fibre sagnac interferometer: an overview of its principles and applications," *Measurement Science and Technology*, vol. 17, no. 1, p. R1, 2006.

[246] M. Campbell, G. Zheng, A. Holmes-Smith, *et al.*, "A frequency-modulated continuous wave birefringent fibre-optic strain sensor based on a sagnac ring configuration," *Measurement Science and Technology*, vol. 10, no. 3, pp. 218–224, 1999.

[247] A. Starodumov, L. Zenteno, D. Monzon, *et al.*, "Fiber sagnac interferometer temperature sensor," *Applied Physics Letters*, vol. 70, no. 1, pp. 19–21, 1997.

[248] B. Dong, Q. Zhao, F. Lvjun, *et al.*, "Liquid-level sensor with a high-birefringence-fiber loop mirror," *Applied Optics*, vol. 45, no. 30, pp. 7767–7771, 2006.

[249] Y. Liu, B. Liu, X. Feng, *et al.*, "High-birefringence fiber loop mirrors and their applications as sensors," *Applied Optics*, vol. 44, no. 12, pp. 2382–2390, 2005.

[250] O. Frazão, L. Marques, and J. Baptista, "Fibre bragg grating interrogation based on high-birefringence fibre loop mirror for strain temperature discrimination," *Microwave and optical technology letters*, vol. 48, no. 11, pp. 2326–2328, 2006.

[251] A. M. Hatta, "Singlemode-multimode-singlemode optical fibre structures for optical sensing," Ph.D. dissertation, Faculty of Engineering Faculty of Engineering of Dublin Institute of Technology, 2009.

[252] Q. Wang, G. Farrell, and W. Yan, "Investigation on single-mode–multimode–single-mode fiber structure," *Journal of Lightwave Technology*, vol. 26, no. 5, pp. 512–519, 2008.

[253] W. S. Mohammed, P. W. Smith, and X. Gu, "All-fiber multimode interference bandpass filter," *Optics letters*, vol. 31, no. 17, pp. 2547–2549, 2006.

[254] Q. Wang and G. Farrell, "Multimode-fiber-based edge filter for optical wavelength measurement application and its design," *Microwave and optical technology letters*, vol. 48, no. 5, pp. 900–902, 2006.

[255] A. M. Hatta, Y. Semenova, Q. Wu, *et al.*, "Strain sensor based on a pair of single-mode-multimode-single-mode fiber structures in a ratiometric power measurement scheme," *Applied optics*, vol. 49, no. 3, pp. 536–541, 2010.

[256] Q. Wu, Y. Semenova, P. Wang, *et al.*, "Experimental demonstration of a simple displacement sensor based on a bent single-mode–multimode–single-mode fiber structure," *Measurement Science and Technology*, vol. 22, no. 2, p. 025203, 2011.

[257] J. G. Aguilar-Soto, J. E. Antonio-Lopez, J. J. Sanchez-Mondragon, *et al.*, "Fiber optic temperature sensor based on multimode interference effects," *Journal of Physics: Conference Series*, vol. 274, p. 012011, 2011.

[258] S. Silva, O. Frazão, J. Viegas, *et al.*, "Temperature and strain-independent curvature sensor based on a singlemode/multimode fiber optic structure," *Measurement Science and Technology*, vol. 22, no. 8, p. 085201, 2011.

[259] P. J. Henderson, Y. J. Rao, D. A. Jackson, *et al.*, "Simultaneous multi-parameter monitoring using a serial fibre-fabry-perot array with low-coherence and wavelength-domain detection," *Measurement Science and Technology*, vol. 9, no. 11, pp. 1837–1839, 1998.

[260] L. Ferreira, A. L. Ribeiro, J. Santos, *et al.*, "Simultaneous displacement and temperature sensing using a white light interrogated low finesse cavity in line with a fiber bragg grating," *Smart materials and structures*, vol. 7, no. 2, p. 189, 1998.

[261] A. D. Kersey, T. A. Berkoff, and W. W. Morey, "High-resolution fiber-grating based strain sensor with interferometric wavelength-shift detection," *Electronics Letters*, vol. 28, no. 3, pp. 236–238, 1992.

[262] A. Kersey, "Fiber-optic bragg-grating differential-temperature sensor," *Photonics Technology Letters*, 1992.

[263] L. C. Goncalves, G. Gonzalez-Aguilar, O. Frazao, *et al.*, "Chemical sensing by differential thermal analysis with a digitally controlled fiber optic interferometer," *Rev Sci Instrum*, vol. 84, no. 1, p. 015002, 2013.

[264] Y. L. Lo, H. Y. Lai, and W. C. Wang, "Developing stable optical fiber refractometers using pmdi with two-parallel fabry-perots," *Sensors and Actuators B-Chemical*, vol. 62, no. 1, pp. 49–54, 2000.

[265] Y. L. Lo and C. H. Chuang, "Differential optical fiber refractometer based on a path-matching differential interferometer with temperature compensation," *Appl Opt*, vol. 40, no. 21, pp. 3518–24, 2001.

[266] S. M. Murtry, J. D. Wright, and D. A. Jackson, "Sensing applications of a low-coherence fibre-optic interferometer measuring the refractive index of air," *Sensors and Actuators B-Chemical*, vol. 72, no. 1, pp. 69–74, 2001.

[267] C. Delisle and P. Cielo, "Application de la modulation spectrale à la transmission de l'information," *Canadian Journal of Physics*, vol. 53, no. 11, pp. 1047–1053, 1975.

[268] P. Cielo and C. Delisle, "Multiplex optical communication based on large-path-length interferometry in white light," *Canadian Journal of Physics*, vol. 54, pp. 2322–2331, 1976.

[269] S. Al-Chalabi, B. Culshaw, and D. Davies, "Partially coherent sources in interferometric sensors," in *First International Conference on Optical Fibre Sensors*, 1983, pp. 26–28.

[270] T. Bosselmann and R. Ulrich, "High-accuracy position-sensing with fiber-coupled white-light interferometers," pp. 361–364, 1984.

[271] J. W. Goodman, "Statistical optics," *New York, Wiley-Interscience, 1985, 567 p.*, vol. 1, 1985.

[272] A. Ribeiro, "White-ligth interferometry: Applications to fibre optic sensors for ac and dc mesurands," Master's thesis, University of Kent, 1992.

[273] A. L. Ribeiro, "Esquemas de multiplexagem de sensores de fibra óptica," Ph.D. dissertation, Faculty of Sciences of University of Porto, 2002.

[274] B. Lee and Y. Jeong, "Interrogation techniques for fiber grating sensors and the theory of fiber gratings," *Fiber Optic Sensors*, pp. 295–381, 2002.

[275] *Workshop on Sigle Mode Optical Fiber Sensor Technology.* University of Kent, UK, Lecture Notes, 1985.

[276] J. Velosa, "Controlo automático de um interferómetro para monitorização e caracterização de sensores interferométricos," Master's thesis, University of Madeira, 2009.

[277] L. C. Gonçalves, "Configuração interferómetrica diferencial para medição de deformação e temperatura," Master's thesis, University of Madeira, 2010.

[278] W. Henry, "Evanescent field devices: a comparison between tapered optical fibres and polished or d-fibres," *Optical and quantum electronics*, vol. 26, no. 3, pp. S261–S272, 1994.

[279] F. Gonthier, S. Lacroix, X. Daxhelet, *et al.*, "Broadband all-fiber filters for wavelength division multiplexing application," *Applied Physics Letters*, vol. 54, no. 14, pp. 1290–1292, 1989.

[280] G. Pendock, H. MacKenzie, and F. Payne, "Dye lasers using tapered optical fibers," *Applied optics*, vol. 32, no. 27, pp. 5236–5242, 1993.

[281] S. Leon-Saval, T. Birks, W. Wadsworth, *et al.*, "Supercontinuum generation in submicron fibre waveguides," *Optics Express*, vol. 12, no. 13, pp. 2864–2869, 2004.

[282] J. Villatoro, V. P. Minkovich, and D. Monzon-Hernandez, "Compact modal interferometer built with tapered microstructured optical fiber," *Photonics Technology Letters, IEEE*, vol. 18, no. 11, pp. 1258–1260, 2006.

[283] J. Mora, J. Villatoro, A. Dıez, *et al.*, "Tunable chirp in bragg gratings written in tapered core fibers," *Optics communications*, vol. 210, no. 1, pp. 51–55, 2002.

[284] J. Villatoro, D. Monzón-Hernández, and E. Mejía, "Fabrication and modeling of uniform-waist single-mode tapered optical fiber sensors," *Applied optics*, vol. 42, no. 13, pp. 2278–2283, 2003.

[285] K. Kieu and M. Mansuripur, "Tuning of fiber lasers by use of a single-mode biconic fiber taper," *Optics letters*, vol. 31, no. 16, pp. 2435–2437, 2006.

[286] P. E. Ciddor, "Refractive index of air: new equations for the visible and near infrared," *Appl Opt*, vol. 35, no. 9, pp. 1566–73, 1996.